MSc Francesca Canyelles i Font

Development of dual-analyte fluorescent probes for the detection of hypoxia in cellular models

Doctoral dissertation

Supervisor: dr hab. Jacek Ł. Kolanowski

Poznań, August 2024

Department of Molecular Probes and Prodrugs

Laboratory of Molecular Assays and Imaging

Institute of Bioorganic Chemistry Polish Academy of Sciences

INSTITUTE OF BIOORGANIC CHEMISTRY
Polish Academy of Sciences

I would like to dedicate this manuscript to my parents Elies and Maria Montserrat.

Acknowledgements

It is my great pleasure to thank Jacek Ł. Kolanowski for giving me the opportunity to work on this project, which gave me a lot of satisfaction and enabled my scientific development. I am extremely grateful for the understanding, encouragement, kindness, intellectual stimulation (mainly in the form of inspiring discussions), patience, among many other things, that I have received in all these years.

I would like to thank all the co-workers from the Department of Molecular Probes and Prodrugs and the Laboratory of Molecular Assays and Imaging, IBCH PAS. First of all, the most experienced members, for their invaluable help and good humour: Michał Gładysz, Dorota Kwiatek, Dorota Jakubczyk, Michał Jakubczyk. It was a pleasure as well to perform fluorescence measurements at WCZT in the company of Joanna Kosman, Krzysztof Żukowski, Magdalena Otrocka, Monika Pyc, and Natalia Karczewska. I would also like to thank other members that stayed for a shorter time, but nevertheless left an impression on me: Damien Baud, Katarzyna Wodecka, Karolina Konsewicz, Aleksandra Bigos, Piotr Michałowski, Katarzyna Zielezińska. All of you made such an enjoyable work place possible and helped make my stay in Poland a truly blessed time.

My warmest thanks to Ania, Linh, Kinga, Masroor, and Adrian with whom I could share the pleasant and not so pleasant moments of the life of the PhD student.

I would like to thank Magdalena Otrocka and Katarzyna Zielezińska for the fluorescence confocal microscopy studies in 3D models (spheroids).

I am also really grateful to Monika Pyc, Esther Masiá Sanchis, and María J. Vicent Docón for the fluorescence confocal microscopy and flow cytometry studies carried out in the Polymer Therapeutics Laboratory and Screening Platform, Centro de Investigación Príncipe Felipe (CIPF) and Centro de Investigación Biomédica en Red Cáncer (CIBERONC), Spain.

I would like to express my gratitude to Prof. Mariola Dutkiewicz and Ms. Małgorzata Dąbkiewicz for their help and patience during my doctoral studies. I would also like to acknowledge the help received and thank the Laboratory of NMR.

Last but not least, I would like to express my gratitude to my family and close friends, but in particular my parents, Elies and Maria Montserrat, who were always showing their love and support even from the distance.

The main experimental work described in this manuscript was carried out at the Institute of Bioorganic Chemistry Polish Academy of Sciences in Poznan under the supervision of dr. hab Jacek Kolanowski and within a project entitled “MultiGATE: Dual-analyte responsive fluorescent probes for a real-time multi-parametric sensing in cellular models” funded within HOMING programme by Foundation for Polish Science (agreement no: Homing/2017-4/33).

Parts of the work were also additionally supported by the funding from the National Science Centre of Poland (NCN, SONATA grant no *2017/26/D/NZ1/01234* and OPUS grant no. 2018/29/B/ST4/01498) and the Polish Ministry of Education and Science (previously MNiSW, decision no DIR/WK/2018/06) for involvement in the joint international project entitled European Infrastructure of Open Screening Platforms of Chemical Biology European Research Infrastructure Consortium UU-OPENSCREEN ERIC).

Selected experiments reported in this work, as explicitly indicated in the text, were carried out in collaboration with Centro de Investigación Príncipe Felipe (CIPF) and CIBERONC (Spain) within funding of Generalitat Valenciana (APOSTD/2021/239) and the Fondo Europeo de Desarrollo Regional (FEDER) included in the Operative Program FEDER of the Valencian Community 2014–2020.

ABSTRACT **1-9**

ABSTRAKT **1-11**

ABBREVIATIONS **1-13**

1. INTRODUCTION **1-15**

1.1. PHOTOPHYSICAL PRINCIPLES OF FLUORESCENCE 1-16

1.1.1. Jablonski diagram *1-16*

1.1.2. Stokes shift and the mirror image rule *1-17*

1.1.3. Extinction coefficient, fluorescence quantum yield, brightness, and fluorescence lifetime *1-18*

1.1.4. Quenching *1-20*

1.2. FLUORESCENCE TECHNIQUES FOR BIOLOGICAL INVESTIGATIONS 1-23

1.2.1. Autofluorescence *1-23*

1.2.2. Fluorescent tools in cellular imaging *1-24*

1.3. DESIGN OF FLUORESCENT RESPONSIVE PROBES 1-25

1.3.1. Modes of response of fluorescent probes to analytes *1-26*

1.3.2. Fluorophore selection *1-27*

1.3.3. Reversibility of probes *1-30*

1.3.4. Dual-analyte probes *1-31*

1.4. THE IMPORTANCE OF REDOX HOMEOSTASIS AND INTRACELLULAR pH IN CELL FUNCTION 1-33

1.4.1. Redox Balance and Reactive Oxygen Species *1-33*

1.4.2. Hypoxia in tumour microenvironments *1-34*

1.4.3. Acidosis in hypoxic tumour microenvironments *1-39*

2. AIM AND OBJECTIVES **2-41**

3. RESULTS AND DISCUSSION **3-42**

3.1. DESIGN STRATEGY 3-42

3.2. TOWARDS IMPROVED STABILITY OF HEMICYANINES 3-43

3.2.1. Design *3-44*

3.2.2. Synthesis *3-45*

*3.2.3. Spectroscopic characterisation of **HCy-OMe**, **HCy-NEt$_2$**, and **HCy-Jul** in solution* *3-47*

3.2.4. Stability against nucleophiles *3-69*

3.2.5. Cellular behaviour *3-80*

3.2.6. Summary *3-87*

3.3. INTENSITY-BASED DUAL-ANALYTE PROBE FOR HYPOXIA 3-89

3.3.1. Design *3-89*

3.3.2. Synthesis ... *3-90*
3.3.3. Spectroscopic characterisation ... *3-91*
3.3.4. Cellular behaviour ... *3-97*
3.3.5. Summary ... *3-105*
3.4. RATIOMETRIC DUAL-ANALYTE PROBE FOR HYPOXIA ... 3-108
3.4.1. Design ... *3-108*
3.4.2. Synthesis ... *3-109*
3.4.3. Spectroscopic characterisation ... *3-113*
3.4.4. Cellular behaviour ... *3-116*
3.4.5. Summary ... *3-121*
4. CONCLUSIONS AND OUTLOOK ... 4-123
5. METHODOLOGY ... 5-125
5.1. GENERAL ... 5-125
5.2. SYNTHESIS AND CHARACTERISATION ... 5-126
5.3. NMR ANALYSIS OF NUCLEOPHILIC ADDITION TO HEMICYANINE DERIVATIVES ... 5-134
5.4. FLUORESCENCE MEASUREMENTS ... 5-135
5.5. BIOLOGY ... 5-140
5.5.1. General cell lines information and cell culture conditions ... *5-140*
5.5.2. Fluorescence Confocal Microscopy experiments ... *5-140*
5.5.3. Flow cytometry ... *5-157*
5.5.4. Cytotoxicity ... *5-158*
6. APPENDIX ... 6-159
6.1. NMR SPECTROSCOPY ... 6-159
6.1.1. NMR spectra of synthesised compounds ... *6-159*
6.1.2. NMR spectra of titrations ... *6-176*
7. BIBLIOGRAPHY ... 7-250

Abstract

This work concerns the development and characterisation of fluorescent probes that respond to two chemical species concurrently by turning from a quenched to a fluorescent state (off-on mode response).

The aim of this thesis was to develop stable dual-analyte fluorescent probe for visualising hypoxia in cellular environments. This goal was achieved through a comprehensive approach from initial probes' design through synthesis and characterisation, culminating in the validation of these probes in biological systems. The conceptual design of probes capable of multiparametric sensing of hypoxic state involved careful selection of the fluorophore core (hemicyanine dye) and the responsive moieties for the corresponding target analytes – pH and reducing environment (nitroreductase activity), which would serve as proxies for hypoxia.

Following the design phase, a new hemicyanine-based fluorescent scaffold, **HCy-Jul**, that is more robust and resistant to biological interferents than other commonly used hemicyanines was synthesized, characterised and successfully validated. Subsequently, using this scaffold, two new dual-analyte responsive probes, **NHCy** and **NHCy-C** were synthesized, characterised to confirm their structure and purity, and tested for photophysical response to target analytes. Finally, the developed probes were validated *in vitro* and *in cellulo* to determine their performance, sensitivity, reliability and effectiveness in biological environments.

Critically, **NHCy** successfully reported on hypoxia cells through a fluorescence turn-on response to bio-reduction and low pH, two hallmarks of hypoxia, but its residual fluorescence in the off state (common for most turn-on probes) limited the reliability of detection. **NHCy-C probe,** on the other hand, demonstrated a ratiometric response to the presence of both hypoxia surrogate analytes that allowed for reliable hypoxia detection in cells via fluorescence microscopy and flow cytometry.

Designs and methodologies (synthesis, spectroscopic characterisation, live-cell imaging) described herein enabled the development and validation of new fluorescent probes for reliable multiparametric sensing of hypoxia in cancer cell models. This constitutes a major advancement

in the field of cellular imaging since a dual-analyte detection with a single probe allows for a more extensive and comprehensive monitoring of biological processes occurring in cells. This knowledge key in the better understanding of diseases, discovery of new functional biomarkers and drug targets and validation of new therapies.

Keywords: responsive fluorescent probes · dual-analyte · hemicyanine dye · hypoxia · pH · nitroreductase activity · cancer

Abstrakt

Niniejsza praca dotyczy opracowania i charakterystyki sond fluorescencyjnych, które reagują na dwa związki chemiczne jednocześnie, przechodząc ze stanu wygaszonego do stanu fluorescencyjnego (odpowiedź w trybie włącz-wyłącz).

Celem tej pracy było stworzenie stabilnej fluorescencyjnej sondy dwuanalitowej do wizualizacji hipoksji w środowisku komórkowym. Cel ten został osiągnięty przez kompleksowe podejście począwszy od zaprojektowania sond, poprzez syntezę i charakteryzację, aż po walidację tych sond w systemach biologicznych. Zaprojektowanie sond zdolnych do wieloparametrowego wykrywania hipoksji wymagało starannego doboru rdzenia fluoroforu (barwnik hemicyjaninowy) oraz elementów odpowiedzialnych za reakcję na odpowiednie anality docelowe – pH oraz środowisko redukcyjne (aktywność nitroreduktazy) jako biomarkerów hipoksji.

Po fazie projektowej zsyntetyzowano, scharakteryzowano i pomyślnie zwalidowano nowy szkielet fluorescencyjny oparty na hemicyjaninie, **HCy-Jul**, który jest bardziej stabilny i odporny na niespecyficzne działanie środowiska biologicznego niż inne powszechnie stosowane hemicyjaniny. Następnie w oparciu o tę strukturę zsyntetyzowano dwie nowe sondy dwuanalitowe, **NHCy** i **NHCy-C**, scharakteryzowano je w celu potwierdzenia ich struktury i czystości oraz zbadano ich odpowiedź fotofizyczną na docelowe anality. Ostatecznie, opracowane sondy zostały zwalidowane *in vitro* i *in cellulo* w celu określenia ich wydajności, czułości, niezawodności i skuteczności działania w środowisku biologicznym.

Co istotne, sonda **NHCy** umożliwiła skuteczną detekcję hipoksji w komórkach poprzez odpowiedź fluorescencyjną typu "turn-on" na bioredukcję i niskie pH, dwa wyznaczniki hipoksji, jednak śladowa fluorescencja w stanie wyłączonym (powszechna dla większości sond typu "turn-on") ograniczała wiarygodność detekcji. Z drugiej strony, sonda **NHCy-C** wykazała odpowiedź typu „ratiometric” (zmiana stosunku intensywności fluorescencji w dwóch różnych długościach fali) na obecność obu analitów charakterystycznych dla hipoksji, co pozwoliło na niezawodną detekcję hipoksji w komórkach za pomocą mikroskopii fluorescencyjnej i cytometrii przepływowej.

Koncepcje i metodologie (synteza, charakterystyka spektroskopowa, obrazowanie żywych komórek) opisane w niniejszej pracy umożliwiły opracowanie i walidację nowych sond fluorescencyjnych do niezawodnego, wieloparametrycznego wykrywania hipoksji w modelach komórek nowotworowych. Jest to znaczący postęp w dziedzinie obrazowania komórkowego, ponieważ dwuanalitowa detekcja z wykorzystaniem pojedynczej sondy pozwala na bardziej rozległe i kompleksowe monitorowanie procesów biologicznych zachodzących w komórkach. Ta wiedza jest kluczowa dla lepszego zrozumienia chorób, odkrywania nowych funkcjonalnych biomarkerów i celów molekularnych dla leków oraz walidacji nowych terapii.

Słowa kluczowe: responsywne sondy fluorescencyjne · dwuanalitowe · barwnik hemicyjaninowy · hipoksja · pH · aktywność nitroreduktazy · nowotwór

Abbreviations

Textual abbreviations

ACN	Acetonitrile
anh	Anhydrous
Ar atm	Argon atmosphere
A549	Adenocarcinomic human alveolar basal epithelial cells isolated from lung tissue
cat.	Catalyst
$CDCl_3$	Deuterated chloroform
CD_3CN	Deuterated acetonitrile
COSY	Correlation spectroscopy (2D NMR)
CPB	Citrate-Phosphate buffer
DCM	Dichloromethane
DIPEA	(N,N-diisopropyl-N-ethylamine – Hunig base
DMEM	Dulbecco's Modified Eagle's Medium
DMF	Dimethylformamide
DMSO	Dimethylsulfoxide
DU145	Cell line with epithelial morphology isolated from the brain of male with prostate cancer
D_2O	Deuterium oxide
d_6-DMSO	Deuterated dimethylsulfoxide
EDC·HCl	1-Ethyl-3-(3-dimethylaminopropyl)carbodiimide hydrochloride
EDG	Electron-donating group
EWG	Electron-withdrawing group
EtOAc	Ethylacetate
EtOH	Ethanol
FRET	Förster Resonance Energy Transfer
GSH	Glutathione
HCy	Hemicyanine
HEK	Cells originated from a human embryonic kidney
HEPES	(4-(2-Hydroxyethyl)-1-piperazineethanesulfonic acid)
Hex	Hexane
HMBC	Heteronuclear multiple-bond correlation spectroscopy (2D NMR)
HOMO / LUMO	Highest / lowest unoccupied molecular orbital
HR-MS	High Resolution Mass spectrometry
HSQC	Heteronuclear single-quantum correlation spectroscopy (2D NMR)
ICT	Intramolecular charge transfer

LT-DR	Lysotracker Deep-Red
MeOH	Methanol
MT-DR	Mitotracker Deep-Red
MS	Mass spectrometry
MCF7	Cell line derived from a human mammary adenocarcinoma
MeOD	Deuterated methanol
NMR (1D and 2D)	Nuclear Magnetic Resonance (one- and two-dimensional techniques)
NTR	Nitroreductase
PB	Phosphate buffer
PBS	Phosphate buffer saline
PLC	Preparative Layer Chromatography
ROS	Reactive oxygen species
r.t.	Room temperature
TBET	Through-bond Energy Transfer
TLC	Thin-layer Chromatography
TRIS·HCl	Tris(hydroxymethyl)aminomethane hydrochloride
UV-Vis	Ultraviolet-visible light

Analytical variables and parameters

Abs [a.u.]	Absorbance or absorption
B [M^{-1} cm^{-1}]	Brightness
$E_T(30)$ [kcal mol^{-1}]	Reichardt polarity parameter
Ɛ [M^{-1} cm^{-1}]	Molar absorptivity or molar extinction coefficient
l [cm]	Light path, from the Beer-Lamber equation $A = Ɛ \cdot l \cdot c$
I_{em} [RFU or a.u.]	Fluorescence intensity of emission
λ_{em} [nm]	Wavelength of fluorescence emission
$\lambda_{em,max}$ [nm]	Wavelength of maximum fluorescence emission
λ_{exc} [nm]	Wavelength of fluorescence excitation
$\lambda_{exc,\ max}$ [nm]	Wavelength of maximum fluorescence excitation
pK_a	Negative decimal logarithm from the thermodynamic constant of acid dissociation reaction: K_a = [A][H]/[AH] of the reaction $HA \Leftrightarrow A^- + H^+$
pH	Negative decimal logarithm of the hydrogen ion concentration in moles per litre (M).
ϕ_F	Quantum yield

1. Introduction

Biological processes involve a wide range of molecules in a variety of settings, which can be difficult to detect directly without the use of spectroscopic and microscopic techniques. Cell-imaging methods that use luminous molecular probes are essential for tracking biological molecular behaviour and improving our understanding of molecular cell biology. Among the various luminescent probes discovered, including nanoparticles, polymers, and genetically encoded tags, small organic compounds with fluorescent properties are particularly appealing because of their biocompatibility, ease of modification, and diversity of available structures. Extensive efforts in recent decades have increased the use of functionalised fluorescent probes for selective visualisation of physical-chemical characteristics within cellular microenvironments. [1–4]

Fluorescence microscopy is an optical imaging technique widely used in fundamental research as well as clinical medicine. Its widespread application can be attributed to its non-invasive nature, high sensitivity and spatio-temporal resolution. To take advantage of these properties, researchers have focused on the development of chemical tools, in particular, fluorescent responsive probes that enable visualisation of physiological and pathological processes. These fluorescent probes enable the detection and monitoring of biologically relevant species' subcellular localization and concentration in cells and living organisms, facilitating the determination of their biological roles and contributions to disease progression, which can lead to new approaches for disease diagnosis and treatment. [1,2,5–9]

Fluorescent probes can be observed in optical microscopy as they emit detectable electromagnetic signal usually within UV-VIS or near IR regions. This can be a result of a variety of different physico-chemical processes collectively called photoluminescence with fluorescence relying on the interaction between electrons and the light that is absorbed and subsequently emitted from the quantum existed state of the same spin multiplicity as the initial ground state. [10]

1.1. Photophysical principles of fluorescence

1.1.1. Jablonski diagram

When a molecule interacts with electromagnetic radiation and absorbs an appropriate photon of energy, an electron is promoted to an electronically excited state. The subsequent relaxation of this electron to the electronically ground state can occur through various mechanisms. The Jablonski diagram (***Figure 1***) illustrates the energy transfer between energetic levels involving photoluminescence and other mechanisms. The transitions between states are depicted as vertical lines indicating that electronic transitions occur within the same set of vibrational states. This is true under the assumption of the Frank-Codon principle that since electronic transitions are much faster than nuclear ones, no movement of the nucleus occurs during these transition.[10]

Upon the absorption of a photon, an electron of the molecule (usually at a ground state S_0 of a single spin multiplicity aka. highest occupied molecular orbital, HOMO) adopts an excited state (e.g. S_1 or higher energy levels) of the same spin multiplicity. The electronic state then relaxes relatively quickly to the lowest vibrational energy state of the excited states (before transition called lowest unoccupied molecular orbital, LUMO) through internal charge transfer. Then, the electron from that lowest energy level of the excited state can relax to the singlet ground state. This process is defined by the Kasha's rule stating that the emitting electronic level of a given multiplicity is the lowest excited level of that multiplicity.[11] A rapid relaxation process (10^{-12} s) from a higher electronic level to the lowest vibrational level of S_1 follows photoexcitation. This fast relaxation is believed to take place because of a strong overlap of numerous states of nearly equal energy. The few exceptions to this rule include rare molecules capable of emitting from the S_2 state and fluorophores that possess two ionization states, displaying distinct absorption and emission spectra depending on the ionization state.[12]

The relaxation to the ground state can occur through various radiative and non-radiative pathways The non-radiative pathways of relaxation primarily involve quenching or intersystem crossing mechanisms. Quenching allows the non-radiative loss of energy through vibrations, collisions, chemical reactions or other mechanisms explained in *1.1.1.5. Quenching*. Alternatively, an electron in the excited state can change its spin multiplicity in a process called intersystem

crossing (ISC) that usually leads to a formation of a triplet state T_1 that is significantly longer-lived than singlet spin state. Triplet state is usually also prone to variable chemical reactions or other non-radiative mechanisms of energy loss, leading back to the molecule (same as before or changed if undergone reaction) to the ground state. When an electron from the lowest excited energy state S_1 returns to the ground state by the emission of a photon (i.e. radiative relaxation) without a change of the electronic spin state, the process is called fluorescence, and the molecule undergoing it is referred to as a fluorophore. When the electron undergoes intersystem crossing (change in the spin state) before emission of energy in a form of light, the process is called phosphorescence and is significantly longer than fluorescence.

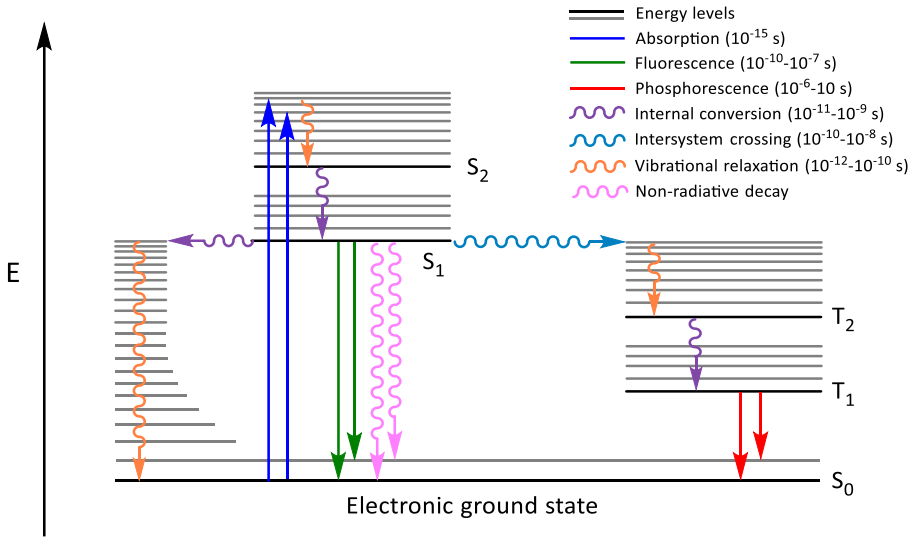

***Figure 1**. Jablonski diagram. Adapted from*[13].

1.1.2. Stokes shift and the mirror image rule

By examining the Jablonski diagram (***Figure 1***), it can be concluded that the energy of the emission should be lower than that of absorption, and thus it should occur at longer wavelengths at temperatures above absolute zero (where multiple vibronic states can occur). This phenomenon was first observed by Sir G. G. Stokes in 1852.[12]

The energetic gap between the maxima of absorption and fluorescence spectra of a fluorophore is known as the Stokes shift (***Figure 2***), which is typically expressed in cm^{-1}. The Stokes shifts rule states that the peak emission wavelength appears at longer wavelengths with respect to the peak

absorption wavelength since the excited state dye molecule can lose energy through vibrational relaxation and collisional quenching with the solvent. [10,14] The emission spectrum of a dye molecule is usually a mirror image of its absorption spectrum; such phenomenon is known as the mirror image rule, a consequence of Kasha's rule and the Franck-Condon principle.[10] It is also worth to point out that the existence of the Stokes shift requires the occurrence of the near-overlapping vibrational energy states allowing for fast non-radiative partial relaxation of the electrons in the excited state. Since no variable vibrational states occur at the temperatures of absolute zero, in this state, the excitation and emissions would then be of exactly the same energy.

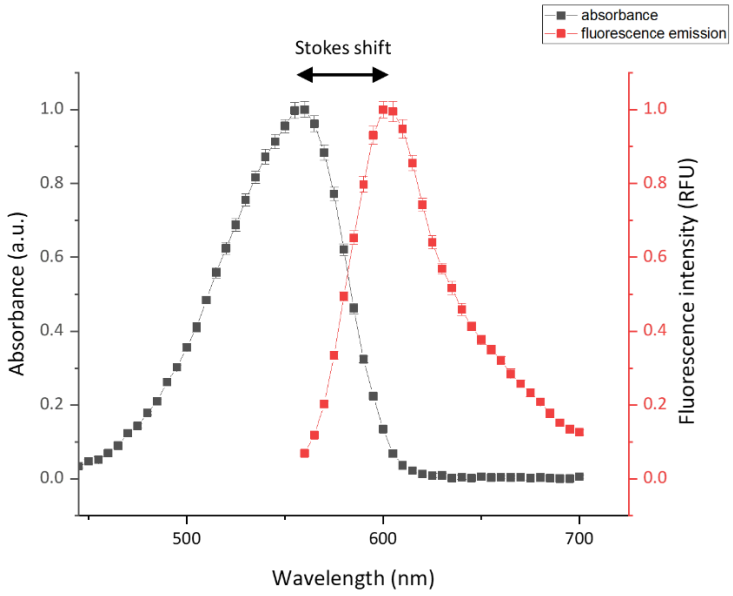

***Figure 2**. Absorption (black squares) and emission spectra (red squares) and corresponding Stokes shift.*

1.1.3. Extinction coefficient, fluorescence quantum yield, brightness, and fluorescence lifetime

A fundamental part of fluorescence spectroscopy comprises the measurement of absorbance, which is defined via the incident intensity (I_0) of electromagnetic irradiation and the transmitted intensity (I) of an absorber. The Beer-Lambert law (equation 2) is the linear relationship between the absorbance and the concentration of a given absorber of electromagnetic irradiation, where where l is the light path (in cm), ε is the molar extinction coefficient (in M^{-1} cm^{-1}) and c is the

concentration (in moles · L^{-1}). Thus, the molar extinction coefficient ε gives the relationship between the absorbed light and concentration of fluorophore in solution at a given wavelength.[10]

$$log_{10}\frac{I_0}{I} = A = \varepsilon \cdot I \cdot c \quad (1)$$

Fluorescence quantum yield Φ_0 can be defined as the efficiency of a fluorophore to emit a quant of light upon photoexcitation, and can be calculated as the quotient of photons emitted from the fluorophore over the photons initially absorbed. Moreover, in agreement with Kasha-Valivov's rule[11], fluorescence quantum yield is usually not affected by the wavelength of exciting radiation.

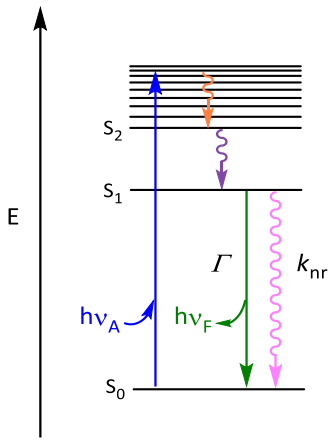

***Figure 3**. Amplified Jablonski diagram. Adapted from*[10].

Zooming into the Jablonski diagram (***Figure 3***), it can be inferred that the depopulation of the excited state depends on both the emissive rate (Γ) and the rate of non-radiative decay to S_0 (k_{nr}). Thus, the fluorescence quantum yield can be calculated with equation 2. The fluorescence quantum yield can be close to unity if the k_{nr} is much smaller than Γ. [10]

$$Q = \frac{\Gamma}{\Gamma + k_{nr}} \quad (2)$$

Apart from fluorescence quantum yield, there is another important parameter called brightness *B*, which is the product of the fluorescence quantum yield Φ_0 and the molar extinction coefficient ε of a fluorophore (equation 3).

$$B = \varepsilon \cdot \phi \quad (3)$$

Fluorescence lifetime (τ) is defined as the average time in which a fluorophore remains in its excited state before its radiative relaxation to the ground state following photoexcitation. This lifetime can be calculated by the following expression:

$$\tau = \frac{1}{\Gamma + k_{nr}} \quad (4)$$

1.1.4. Quenching

The phenomenon involving a decrease in the intensity of fluorescence is referred to as quenching. Quenching can occur by a wide variety of mechanisms, including vibrations, collisions, Förster Resonance Energy Transfer, Photoinduced electron Transfer, and Dexter electron Transfer, among others. A molecule or a motif that leads to the decrease in fluorescence intensity of a fluorophore is called a quencher, which will be elaborated on below. [15]

Photoinduced electron transfer (PeT) is the dynamic or static transfer of an electron from a donor to an acceptor (quencher) upon irradiation with light.[16,17,18] In dynamic quenching, PeT occurs through molecular collisions, while in static quenching, PeT occurs in a stable donor-acceptor complex with the potential to undergo multiple excitation-emission cycles. PeT quenching efficiency is distance dependent, and increases as the distance between quencher and fluorophore decreases.[10]

The electron transfer in static PeT can occur through donor-excited PeT (d-PeT) mechanism, from the fluorophore excited state to the acceptor, or acceptor-excited (a-PeT) mechanism, from the acceptor excited state to the fluorophore. [16]

In d-PeT, the electron from photoexcited donor molecule is transferred to LUMO of the acceptor exothermically, generating a radical-ion pair (***Figure 4a***). Back electron transfer then occurs from the LUMO of the acceptor to its lower semi-occupied orbital, re-establishing the original electronic state of the system.

In a-PeT, the electron in the ground state of the donor is transferred to the vacancy in the HOMO of the photoexcited acceptor exothermically, generating the radical-ion pair (***Figure 4b***). Back electron transfer then occurs from the LUMO of the acceptor to the vacancy in the HOMO of the donor, re-establishing the original electronic state of the system.

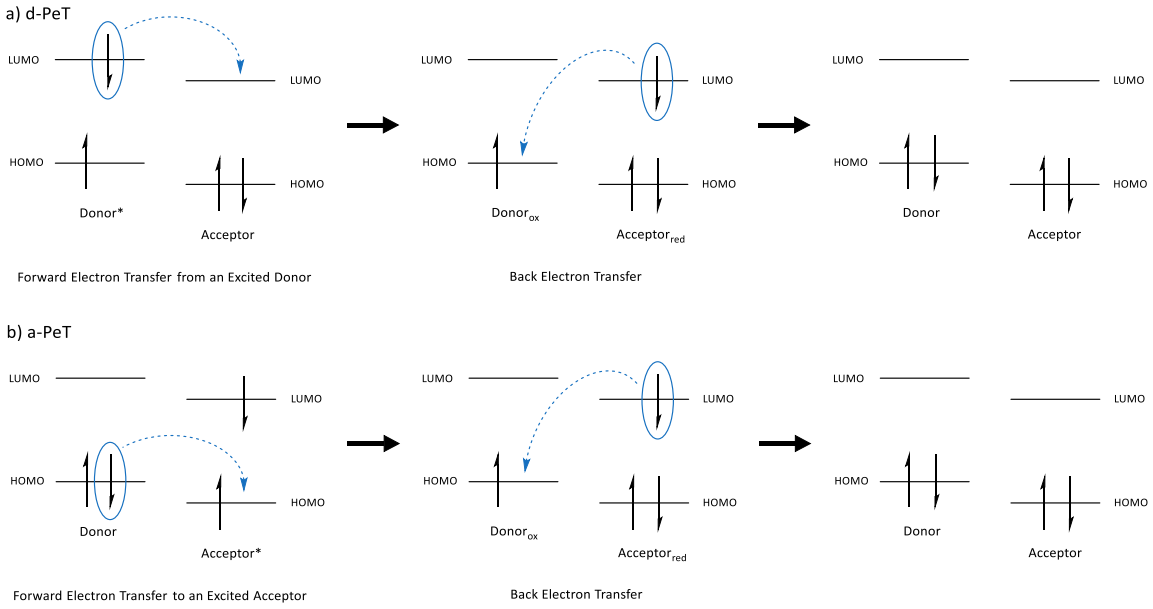

Figure 4*. Forward and back electron transfer in (a) d-PeT, (b) a-PeT, adapted from* [17].

The **Förster Resonance Energy Transfer** (***Figures 5*** and ***6a***) refers to the phenomenon that occurs due to long-range dipole-dipole resonance interaction between fluorophores if some conditions (orientation of dipoles, distance) are met and thus, it is considered a through-space process. In particular, such mechanism takes place in the range of 10 and 100 Angstroms. One molecule (donor) absorbs radiation of a certain wavelength and in its excited state transfers energy to the other molecule (acceptor), which can subsequently relax to the ground state through radiative or non-radiative pathways. Quenching occurs when the acceptor returns to the ground state through non-radiative relaxation pathways. In the case both donor and acceptor are fluorophores, the donor is excited when irradiated at a certain wavelength and the observed emission at a longer wavelength corresponds to the acceptor. [10]

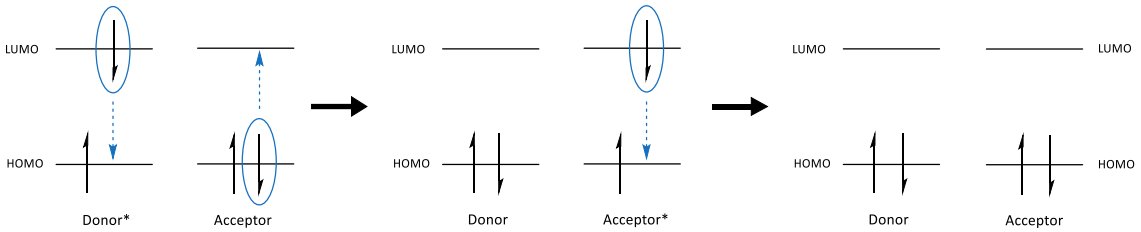

***Figure 5**. Singlet-singlet FRET mechanism.*

Intramolecular energy transfer can also occur through bonds even if there is no finite spectral overlap between the emission spectrum of the donor and the absorption spectrum of the acceptor. This pathway is called **Through-Bond Energy Transfer** (TBET) and it occurs when energy is transferred from a donor group to an acceptor group through a non-flexible conjugated π-system linker that twists both groups out of co-planarity (***Figure 6b***).[19] TBET is faster and hence, can be distinguished from FRET through energy transfer kinetics using ultrafast spectroscopy studies. [20]

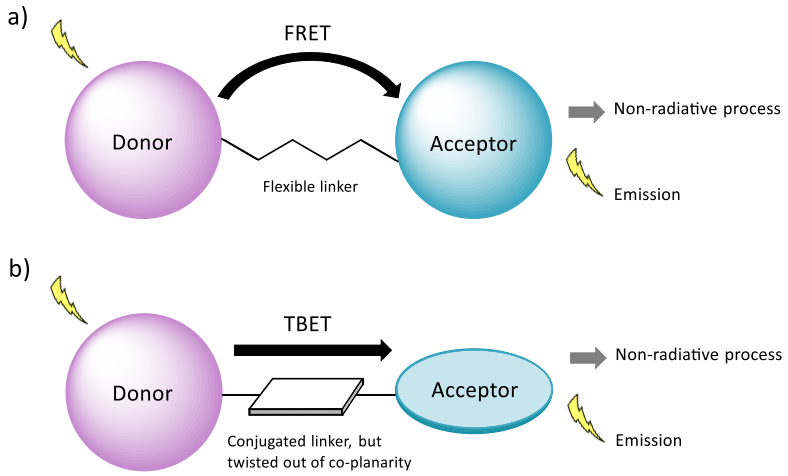

***Figure 6**. (a) Through-space and (b) through-bond energy transfer, adapted from[19].*

Internal charge transfer (ICT) occurs in so-called push-pull fluorophores,[21] which contain both an electron-donating groups (e.g. amino group[22]) with free electron pairs and electron-withdrawing groups joined together via the system of conjugated double bonds.[23] During ICT electrons, which are not directly involved in chemical bonds, are transferred from the donor to the acceptor (it must have unoccupied orbitals of appropriately low energy levels to be able to receive electrons).[23] As a result, dipole moment and emission intensity change [4,22] (***Figure 7***). Due

to a change of the dipole moment, the available energy levels of the electrons during ICT are particularly sensitive to the environment. The lowest excited energy state can be determined by the fluorophore's environment, for instance, due to the solvent's polarity. If the resulting excited chemical species presents large charge separation, then it can become the lowest energy state in a polar solvent. Whilst a chemical species with no charge separation will present the lowest energy excited state in apolar solvents. Such fluorescent probes are characterised by large Stokes shift.[24]

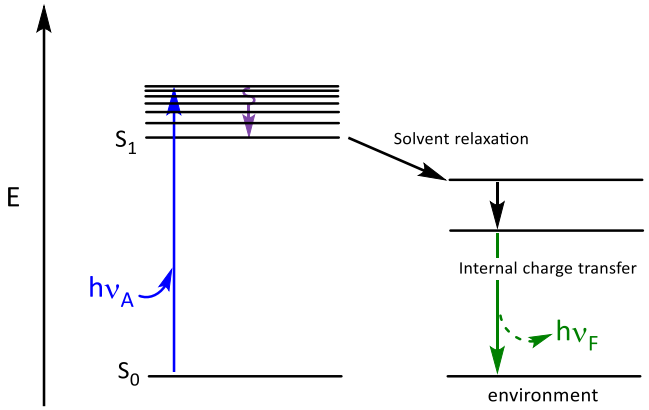

***Figure 7**. Internal charge transfer scheme. The dashed arrows indicate the fluorophore can display fluorescence emission. Adapted from[10].*

1.2. Fluorescence techniques for biological investigations

1.2.1. Autofluorescence

Prokaryotic and eukaryotic cells display an intrinsic natural fluorescence emission at short wavelengths (blue-orange region) when excited by UV-Vis radiation of suitable wavelength. This native fluorescence or "autofluorescence" in cells arises from endogenous fluorophores (***Figure 8***), comprising fluorescent cellular structural components and metabolites such as aromatic amino acids, lipo-pigments, pyridinic (NADPH) and flavin coenzymes. The cytoplasm's autofluorescence is mainly due to NAD(P)H and flavins. [25–28] The physiological and/or pathological processes occurring in the cells can alter the physicochemical properties of their microenvironment as well as affect the amount and distribution of these endogenous

fluorophores. Therefore, autofluorescence can be a means for discerning the physiological and/or pathological state of the cells.[27] On the other hand, exogenous fluorophores that emit at red or far-red wavelengths are of interest when considering biological applications, as eukaryotic cells and tissues display reduced autofluorescence at these longer wavelengths and as such are also more permeable to light in these frequencies enabling deeper and more reliable imaging.

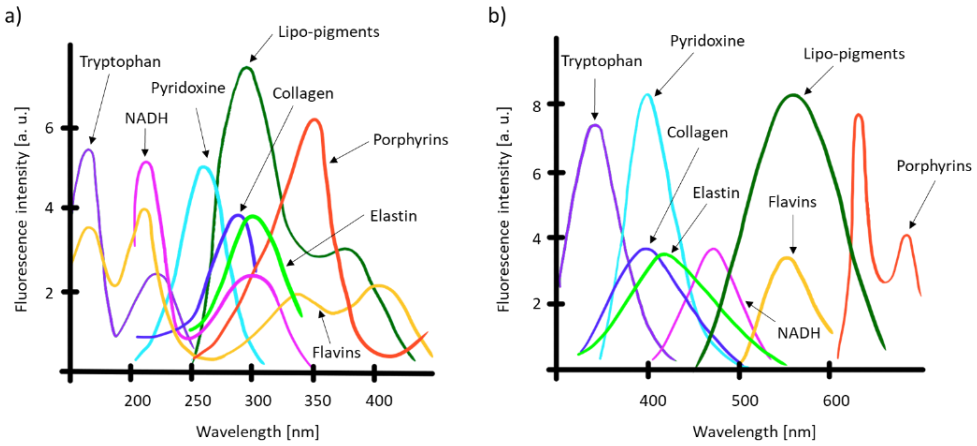

***Figure 8**. Excitation (a) and emission spectra (b) of the principal endogenous fluorophores. Spectral shapes are shown for the best relative excitation/emission conditions. Adapted from* [25].

1.2.2. Fluorescent tools in cellular imaging

Fluorescent probes present the ability to emit light in response to desired targets or phenomena, and hence are widely used in chemical, biochemical and biological research. [29] Such exogenous fluorescent compounds can be added and used in live cell imaging to visualize targets. These tools can be divided into two types: tags (or labels) and fluorescent responsive probes. Fluorescent tags (***Figure 9a***) exhibit constant fluorescence regardless of their local environment and often exhibit a targeting group or have genetically controlled expression. In contrast, fluorescent responsive probes (***Figure 9b***) exhibit changes in fluorescence intensity, wavelength, or fluorescence lifetime upon interaction with a specific analyte, and they can be small molecule, polymer, or nanoparticle based. Ideally, the signal generated by the probe upon interaction with an analyte should be unambiguously discernible from the signal in the absence of the analyte and should not be affected by the differences in local probe's concentration, eliminating the need for washing away of the remaining probes. Such response ensures reliability of analyte's detection

especially in more complex environments like biological models. [30] This can usually be achieved if the analyte's interaction with the probe leads to a fluorescent activation of previously non-fluorescent species (fluorogenic), significant change of colour or clearly measurable change in fluorescence lifetime. Details of optimal modes of response that affect this reliability are also discussed in the following chapter.

Thanks to the above-mentioned Conventionally, fluorescent probes consist of a fluorescent reporter or fluorophore and a sensing motif, making them versatile and convenient to use thanks to the design flexibility according to one's needs. By applying principles of organic chemistry and spectroscopy, scientists can design probes to detect single or multiple analytes simultaneously, with emission at desired wavelengths. [23]

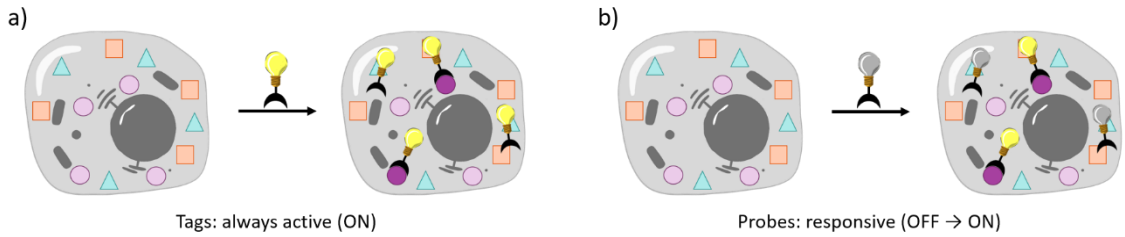

***Figure 9**. Visualization tools: tags (a) and probes (b).*

1.3. Design of fluorescent responsive probes

Observation of biological processes in real time is usually challenging due to the amount and diversity of endogenous species – target molecules – involved and a lack of unique and detectable signal emitted by these targets directly (i.e. most are "dark" to the majority of live cell analytical methods). A reliable fluorescent probe should possess some properties, including solubility in aqueous media, chemical "inertness" except in relation to the analyte, photostability, high brightness[31] and sensitivity.[32]Fluorescent probes can be used to detect and monitor such target molecules in the cell, via their chemical reaction or interaction with the target and/or sensitivity to physico-chemical parameters of the environment (mainly polarity and viscosity).[33] However, a fluorescent probe has to be designed in the way, which emits an unequivocal signal output upon the interaction with a target (specificity/selectivity), as well as meet the requirements for

reliability, robustness and biocompatibility to ensure unambiguous interpretation of experimental data.

1.3.1. Modes of response of fluorescent probes to analytes

One of the key features of reliable fluorescent probes is to emit a signal that can be unambiguously interpreted as coming from the presence of (interaction with) the analyte. Mode of response to the analyte of interest, usually classified as turn-on, turn-off or ratiometric, is, next to the type of fluorescent parameter (e.g. intensity / lifetime), key in ensuring this unambiguity. In case of turn-on / turn-off response, analyte's presence leads to a change in emission intensity at a given wavelength, while ratiometric probes achieve this through changes in emission colour (or more specifically: change in the ratio of emission intensity at two distinct wavelengths).[34]

Turn-on probes (***Figure 10a***) exhibit an increase in fluorescence emission upon photoexcitation in the presence of said analyte.[35,36] In contrast, for turn-off probes (***Figure 10b***), interaction with an analyte leads to decrease in fluorescence intensity. The use of turn-off probes is therefore usually more challenging, because a lack of fluorescence emission is ambiguous as it can be attributed to either the absence of analyte and/or absence of functional probe. Turn-on probes are therefore more desirable, since they ensure the presence of analyte by an increase in the fluorescent emission intensity. Ideally, turn-on response is truly fluorogenic, i.e. the probe before interaction of the analyte remains completely non-fluorescent. However, in practice, almost all probes exhibit a residual fluorescence in the off state. Therefore, in biological studies the response of intensity-based sensors can be difficult to interpret as the uptake, accumulation and local distribution will strongly affect its absolute intensity and can be confounded with the presence of the analyte.

On the other hand, ratiometric fluorescent probes change their relative intensities at multiple wavelengths in the presence of the analyte, allowing an internal standardisation of the response to give a measurable ratio of fluorescence that is independent of probe concentration (***Figure 10c***). Some fluorescent scaffolds can be made intrinsically ratiometric (changing colour upon a change in the structure or the environment). However, a more generalisable strategy for introduction of ratiometricity that is also compatible with virtually all fluorophores is linking a

fluorophore with an analyte-specific sensing group to another fluorophore to provide an internal control of fluorescence emission intensity. [37] Ratiometric probes are generally more desirable than turn-off and turn-on ones, since the relationship between the fluorescence emission intensity of both the responsive and the non-responsive fluorophore can be obtained, which is independent of the probe's concentration and correlates with the presence of the analyte.

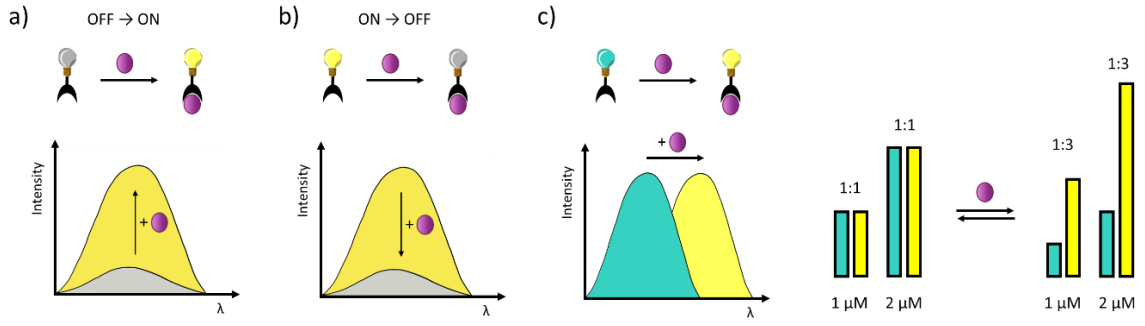

***Figure 10**. Schematic representation of (a) turn-on, (b) turn-off, and (c) ratiometric probes. Adapted from.*[38]

1.3.2. Fluorophore selection

Examples of fluorophore cores (scaffolds) most commonly used in the construction of fluorescent responsive probes for biological applications are shown in ***Figure 11***. Two main classes of fluorophores can be distinguished – endogenous (their presence in cells is natural) and exogenous. Flavins and aromatic amino acids can serve as examples of the former group, while rhodamines and coumarins find their place among representatives of the latter (at least as far as human cells are concerned).[10] Rhodamines, coumarins, BODIPYs, hemicyanines, and flavins are widely used in design and development of fluorescent probes. In those compounds the emission of light occurs because of intramolecular charge transfer – ICT. During this process, upon excitation the electron is transferred through conjugated system of π-bonds from the functional group that acts as electron donor to the acceptor group leading to a a charge separation in the excited state.[39,40,38] This mechanism of fluorescent response has made these fluorescent scaffolds broadly used in probe's development.[36]

In this work we focussed on using coumarins and hemicyanines as the scaffold for creation of responsive probes and so the following subchapters will introduce these two classes of fluorophores in more details.

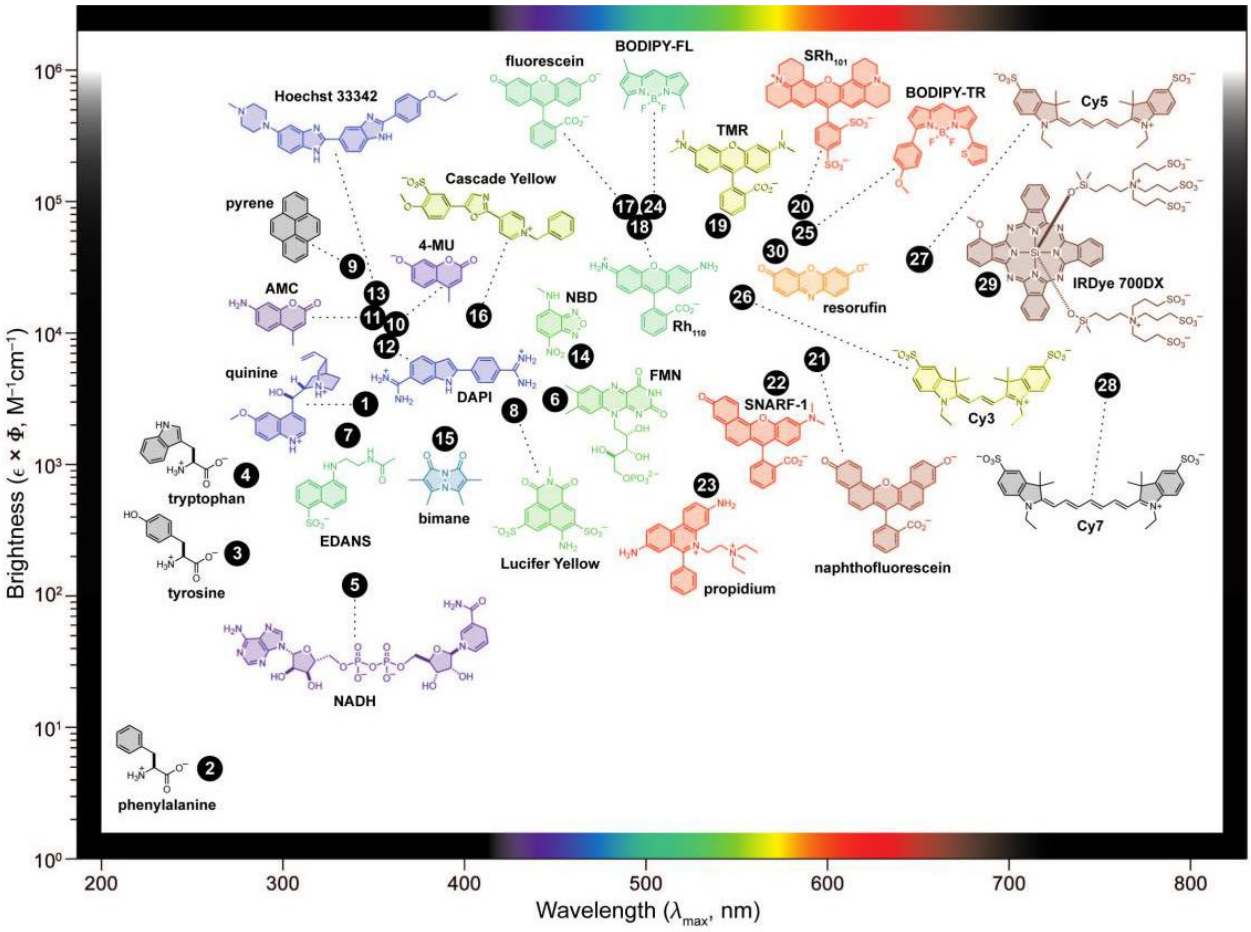

***Figure 11**. Scheme presenting the plot of fluorophore brightness and wavelength of maximum absorption λ_{max}. The wavelength of maximum emission λ_{em} is indicated through the colour of the structure. Copied from* [41]

Hemicyanine dyes

Hemicyanine dyes (***Figure 12***) are closely related to a broader class of cyanine fluorophores (fluorophore number 26 in ***Figure 11***) that are widely used in broad range of applications, including as a scaffold of fluorescent responsive probes for sensing and imaging. Hemicyanines, in particular, are of interest due to their extended π-conjugation and thus, most typically visible absorbance (400-500 nm) and fluorescence emission at long wavelengths (500-600 nm)[2], but also

displaying near-Infrared emission in some cases[42]. These dyes are commonly used also in ratiometric probes design due to their relative facility of conjugation with other fluorophores [1,43]. The lipophilic cationic nature of indolinium ion can also be exploited for mitochondria targeting in cells[7,44] The hemicyanine scaffold (***Figure 12a***) has been also used in the development of fluorescent probes to sense pH and viscosity[6,7,44]. More information on hemicyanine dyes for the development of fluorescent probes can be found in the following recent reviews: [42,43,45].

Styrylindolium dyes are arguably a subclass of hemicyanines that is most commonly selected for the development of responsive fluorescent probes. They are known for their chemical reactivity and instability upon exposure to many reactive biological endogenous compounds, which is their main caveat. They consist of an unsaturated iminium ion, which electrophilic behaviour towards several nucleophilic analytes (CN^-, HS^-, $HSO3^-$) [46–51] has been previously studied. Nucleophilic addition to the styrylindolium core (***Figure 13b***) predominantly occurs in 1,2- and 1,4-positions. [52] Thus, some hemicyanine-based probes employ this charged iminium ion as the responsive moiety for sensing of biologically and environmentally relevant [46–51,53] changes. However, this chemical reactivity makes hemicyanine-based probes susceptible to potential undesired interactions and/or reactions with biological analytes other than the one the probe was designed to sense. Such interactions and/or reactions could lead to changes in the fluorescent output signal of the probe and interfere with accurate bioimaging, leading to confounding data interpretation. However, there have been attempts in the literature to obtain more stable hemicyanine dyes for yielding chemically resilient dyes for the development of fluorescent probes.[54]

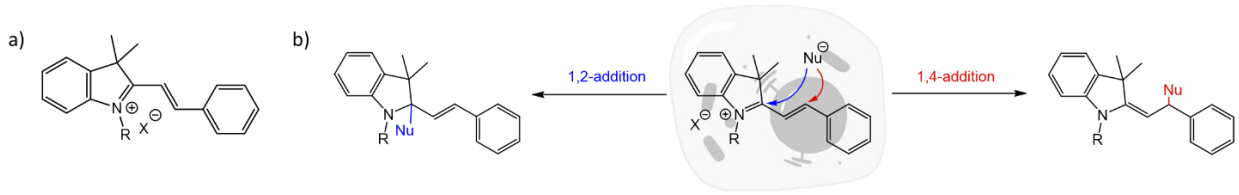

Figure 12*. Styrylindolium core (a) and modes of nucleophilic addition (b).*[52]

Coumarin dyes

Coumarins are classified as phytochemicals, or naturally occurring substances. Their name comes from the name of the bean from which they were originally collected. They are characterized by an absorption in the range of 300-450 nm and thus, they usually exhibit a blue fluorescence emission.[55]

The coumarin core (***Figure 13a***) can be furnished with a variety of functional groups virtually at every position in the ring. To impart a favourable fluorescent properties to the coumarin scaffold, the most common substitution is an introduction of electron-donating functionality (commonly amino group) in position 7 of the ring (***Figure 13b***). [30] This enables an internal or intramolecular charge transfer (ICT) phenomenon to occur between the electron-donor motif in position 7 and electron acceptor lactone motif and as such forms the basis for the fluorescence of coumarins. This substitution pattern is the most common one in the design and synthesis of coumarin fluorescent probes and one of the most common in all probes reported.[9,56,57] Substitutions at other positions of the ring have been extensively studied as they enable a fine tuning of the fluorescent properties of these scaffolds.[58] The fluorophore emits light when atoms can transfer electrons through the conjugated system of double bonds while exhibiting the roles of donor and acceptor. The fluorescence is quenched when the lone pair is not accessible for the electron transfer.[36] Another example of 7-amino-substituted coumarin is the scaffold that constitutes coumarin 343[36] (***Figure 13c***), with a more rigid structure.

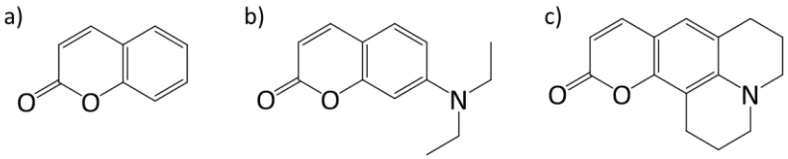

Figure 13*. Coumarin dye a) core; b) 7-diethylamino-coumarincore used in literature for designing fluorescent probes; c) core for coumarin 343.*

1.3.3. Reversibility of probes

Another important aspect of the probes' response to the presence of analyte is physico-chemical form of interaction and corresponding reversibility. Reversible probes form a transient complex

which depends on the concentration of the analyte and microenvironment (intermolecular interactions – interaction by "association") or is a result of a reversible reaction (covalent bonds formation). Probes exhibiting reversible interaction with the target analytes enable sensing dynamic changes pertaining to biological processes occurring in cells. Reversible probes are mainly used to detect the presence of cations, anions as well as changes in pH, viscosity, and polarity changes (***Figure 14a,b***). Contrary to reversible probes, irreversible ones remain permanently altered after reacting with the analyte usually via cleavage and separation of the part of the molecules from the rest (***Figure 14c***) or addition that is practically irreversible in the conditions of cellular environment (***Figure 14d***).

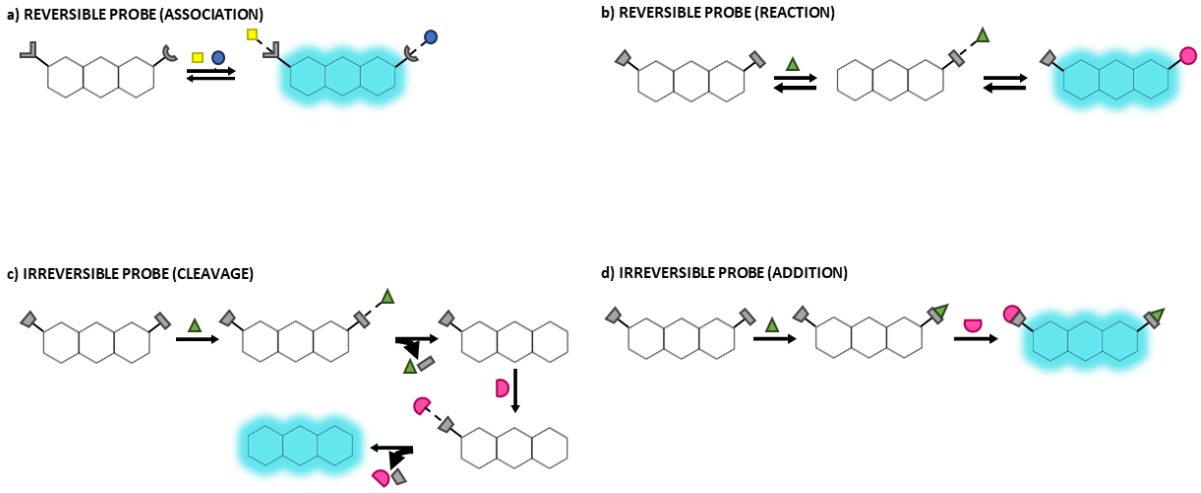

Figure 14*. Schematics showing different types of dual-analyte probes in respect to the type of interaction with the analyte. Reversible probes by (a) intramolecular interaction, (b) reversible reaction; irreversible probes by (c) cleavage, and (d) addition). The fluorophore is represented as three connected hexagons, coloured white to indicate quenched fluorescence emission (inactive form), and coloured blue for when the fluorophore displays fluorescence emission (active form). The grey shapes attached to the sides are the responsive groups and the coloured shapes symbolize molecular targets (analytes) recognised by the corresponding responsive groups. Adapted from* [59].

1.3.4. Dual-analyte probes

While a lot of applications of fluorescent probes up to date have been based on visualisation of a single analyte, ability to monitor multiple analytes simultaneously in the same sample provides much more information about the studied system. It also enables the understanding of the interdependencies between different targets and allows for much deeper understanding of

biological processes. Up to date, measurement of two analytes simultaneously has been most commonly realised by using two separate selective probes, but a more robust approach would be to do so with a use of one dual(multi)-analyte probes. By doing so, data interpretation would not be compromised by the potential differences in uptake, localization, and retention of the two probes. [60]

Owing to the above-mentioned advantages and an increasing need of looking into multiple analytes simultaneously, recent years have seen a logarithmic increase in the numbers of dual-analyte probes.[59,61,62] As single analyte probes typically contain a fluorophore and a responsive sensing group for the selected analyte of interest, dual-analyte probes require merging of two sensing elements into a single probe. This, in turn, leads to a potentially significantly more complex changes to the signal that the probe generates. In order to ensure unambiguity of detection in a biological complex system, a dual-analyte probe need to function like an AND logic gate able to interact with two analytes (inputs, e.g. A and B) and being able to generate a distinct signal specific when both are present. Some dual-analyte probes might also be able (but do not need to be to act as reliable dual-analyte probes) to report simultaneously on the presence of one of the analytes separately (only A or only B), but it is critical these signals are clearly distinguishable from the unique signal generated in the presence of both analytes (A+B). [60]

An example of a dual-analyte fluorescent probe is **RTFt1** (***Figure 15***), which detects simultaneously both ferrous iron and H_2O_2. Both iron-dependent reactive oxygen species (ROS) producing enzymes and labile iron are thought to contribute to ROS-dependent cell damage and death.[63] Taking into account the role of the Fenton reaction in ferroptosis (specific mechanism of the cell death with increasing diagnostic and therapeutic potential), sensing its endogenous reactants (Fe^{2+}, H_2O_2) and relevant product (hydroxyl radical) would be optimal. However, sensing the hydroxyl radical is challenging with its extremely short half-life (10^{-10} s), low intracellular concentrations, and production by Haber–Weiss reaction[64], Fenton reaction[65] or by decomposition of peroxynitrite[66]. **RTFt1** probe has been designed to detect Fe and H_2O_2 using a short-lived nature of hydroxyl-radical as a product of their reaction. The detection event involves the initial chelation step of Fe(II) ion in the spirolactam ring-open form through hydrazide and thiol groups. A second reaction step involves the hydrolysis of the amide bond *in situ* in the

presence of H_2O_2, that would generate OH^- and $OH^{\cdot}$, as well as release the fluorescent Rhodamine B (which would exhibit the maximal fluorescence intensity (200-fold increase), when compared to the unreacted probe (unchelated and/or chelated). There is a possible interference with hypochlorous acid, so studies should be supplemented with OCl^- sensor. [67]

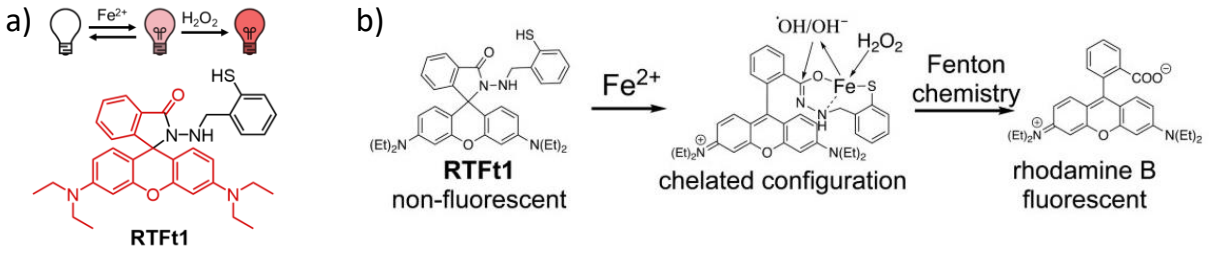

***Figure 15**. (a) Fluorescence response of RTFt1 in the presence of iron(II) and hydrogen peroxide, and (b) proposed mechanism by which **RTFt1** detects the Fenton chemistry. Adapted from [59] and [67].*

1.4. The importance of redox homeostasis and intracellular pH in cell function

1.4.1. Redox Balance and Reactive Oxygen Species

The maintenance of redox balance and adequate intracellular pH is essential for cell homeostasis, and its perturbation can have profound effects on the onset of disease and the efficacy of therapeutic interventions.[63] Human cells' redox balance is influenced by a variety of elements, the most important of which are reactive oxygen species (ROS – $O_2^{\bullet-}$, H_2O_2, HClO…), reactive nitrogen species (RNS – $ONOO^-$, NO…), oxygen levels, and redox-active metal ions, especially iron (II).

Reactive oxygen species (ROS) are mainly produced by enzymes (e.g. NADPH oxidases, xanthine oxidase, nitric oxide synthase, and peroxisomal constituents)[68] or by mitochondrial respiration as natural by-products[69]. They are unstable, highly reactive chemical molecules which arise from the univalent reduction of O_2 occurring in all kinds of cells [70]: superoxide anion ($^{\bullet}O_2^-$), hydrogen peroxide (H_2O_2), hydroxyl radical ($^{\bullet}OH$), and singlet oxygen ($^1O_2^-$).[68] Adequate levels of ROS are needed for diverse cellular responses essential for normal cell signalling and homeostasis.[71] However, when ROS are above the level required for normal cellular homeostasis and/or persist for prolonged periods of time, and the adequate concentration fails to be re-established,

oxidative stress (OS) / damage occurs.[72,73] The harmful effects of ROS in the cell include, among others, (i) damage to DNA or RNA[74]; (ii) lipid peroxidation of polyunsaturated fatty acids (such as membrane phospholipids)[73]; and (iii) oxidation of proteins[75]. The irreversible damage caused to DNA, lipids, and enzymes present in cells may result in functional impairment or even cell death leading to the development of diseases.[68]

Altered levels of redox agents and ROS are present in hypoxic microenvironments since various reductive species, e.g. flavin adenine dinucleotide ($FADH_2$) and nicotinamide adenine dinucleotide (NADH), accumulate due to the low molecular oxygen concentration. Moreover, these species contribute to the reduction of the remaining oxygen, producing an excess of ROS.[76,77]

1.4.2. Hypoxia in tumour microenvironments

Hypoxia (***Figure 16***) refers to a localised state of oxygen deficiency resulting from an imbalance between oxygen delivery and consumption. [78–80] This condition is particularly prevalent in some solid tumour regions distant from the arteriolar source. The cells in these hypoxic regions are resistant to nonsurgical anticancer therapies which are directly or indirectly oxygen dependent, or both.[81–83] In addition, hypoxia has also been associated with increased metastatic potential[81,84–86] which all together leads to usually poor prognosis. Therefore, the development of reliable methods to detect and monitor hypoxia level in tumour cells is of great importance for understanding the molecular mechanisms underpinning the formation, maintenance and alterations of hypoxia and informing the design of better therapies.

One of the most distinctive features of hypoxia in human and animal models is the increase in nitroreductase-like activity, which becomes more pronounced in oxygen-poor states.[87] This activity is responsible for the reduction of nitroaromatic compounds (***Figure 17***), which can occur through one- or two-electron mechanisms. The best studied examples of this activity are processes catalysed by two types of bacterial nitroreductases, bacterial oxygen-insensitive or type I nitroreductases (two-electron mechanism), and bacterial oxygen-sensitive or type II nitroreductases (one-electron mechanism), that are also often used as proxies of hypoxia for validation of fluorescent probes in vitro. [81,88–91]

Nitroreductases are flavoenzymes that catalyse the NAD(P)H-dependent reduction of the nitro groups on nitroaromatic and nitroheterocyclic compounds (**1**).[89] Type I nitroreductases produce amines (**5**) through sequential two-electron reduction of nitro groups via nitroso (**3**) and hydroxylamine (**4**) intermediates. The initial nitroaromatic molecules and final amine-like products of this process are relatively stable in live cells. However, reaction of the nitroso and hydroxylamine intermediates with biomolecules can cause toxic and mutagenic effects.[92,93] Type II nitroreductases produce an unstable nitro radical anion (**2**) through one-electron reduction in aerobic conditions, which are characteristic of normoxic cells. This anion can get re-oxidised back to a nitro group by molecular oxygen, which is in turn reduced to superoxide anion (**6**) and thus, a futile cycle takes place. In hypoxic cells where anaerobic conditions are met, two nitro radical anions can undergo a disproportionation reaction, obtaining the nitroso intermediate and the corresponding nitro compound.[89,90]

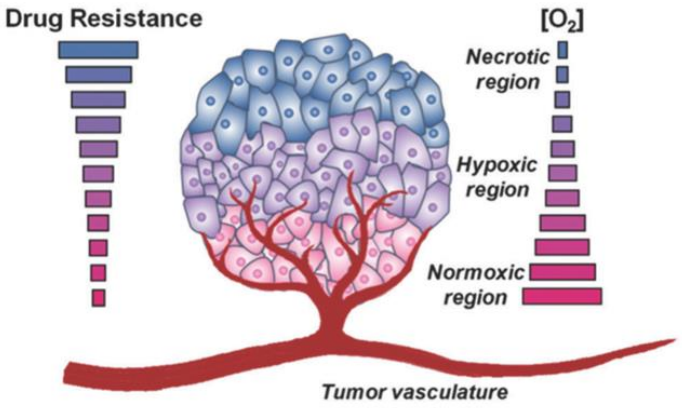

***Figure 16**. Representation of hypoxia in tumour environment (from [86]). A tumour includes three main regions due to increasing distance to the tumour vasculature: normoxic, hypoxic, and necrotic. The further away from the tumour vasculature, the more limited is the accessibility of nutrients and the oxygen level.*

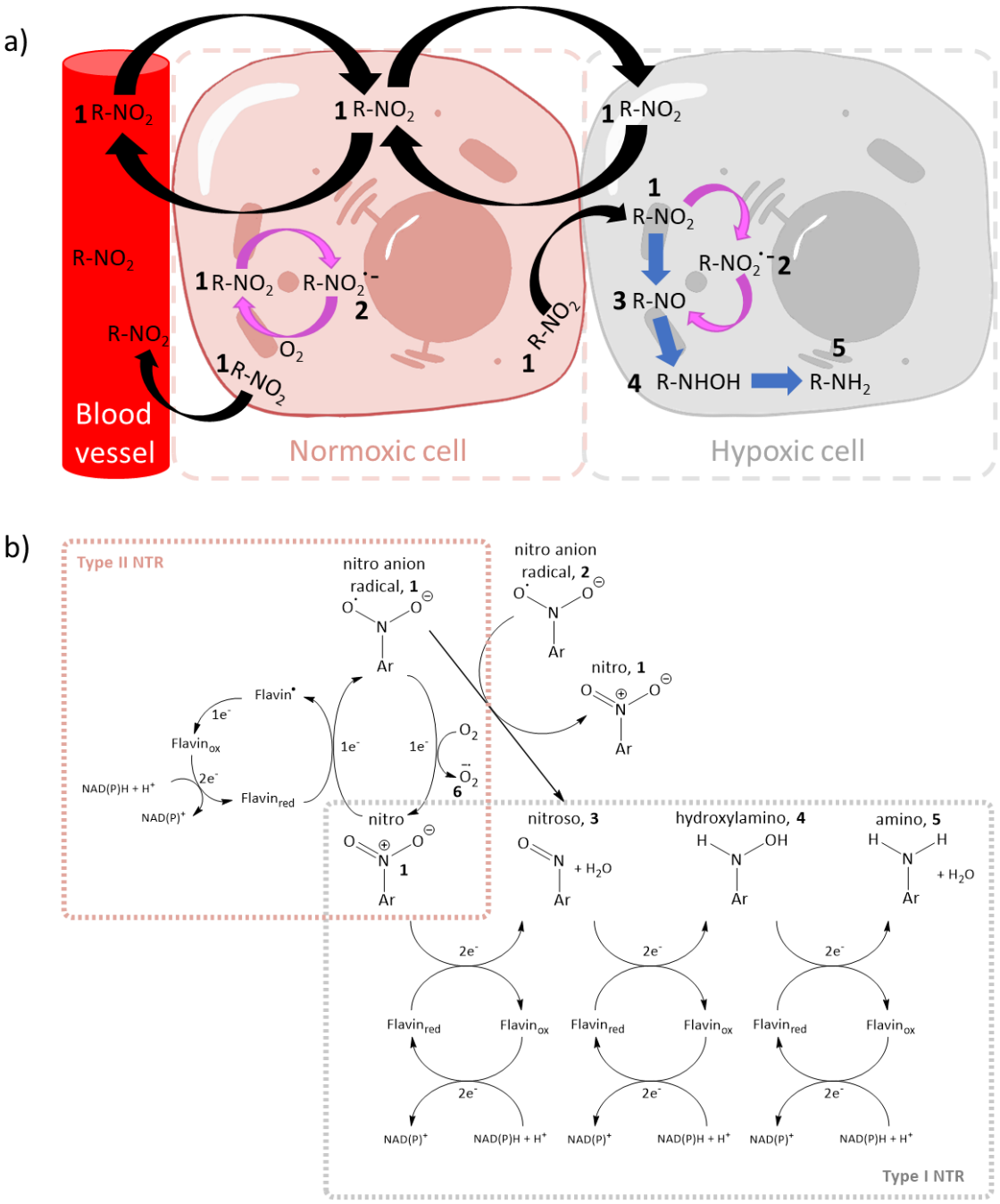

***Figure 17**. (a) Schematics and (bI mechanism of bioreduction of nitroaromatic compounds by types I and II of bacterial nitroreductase in normoxic and hypoxic conditions. Adapted from* [94].

1.4.2.1. Existing fluorescent probes for hypoxia

The most common fluorescent probes developed for sensing hypoxia typically contain nitro, azo or quinone groups, which act as hypoxia sensitive moieties based on their hypoxia-triggered

molecular cleavage character. [95] There are plenty of single-analyte probes for sensing hypoxic state; an example would be the reversible turn-on probe **RHyCy5** (***Figure 18***), which allows the monitoring of hypoxia-normoxia cycles in live cells. The fluorescence off-on mechanism is based on a FRET process between an acceptor (rhodamine moiety) and donor (cyanine moiety). Under normoxic conditions, **RHyCy5** showed extremely weak fluorescence due to FRET mechanism. Under hypoxic conditions, the rhodamine moiety undergoes one-electron bio-reduction to its radical form, then, a decrease in absorbance at 660 nm is observed and FRET can no longer occur. The cyanine moiety becomes then strongly fluorescent, increasing the fluorescent emission 7- to 8-fold. Upon recovery of normoxic conditions, the radical is re-oxidized and FRET is restored, causing the decrease in fluorescent emission to the initial state. [96]

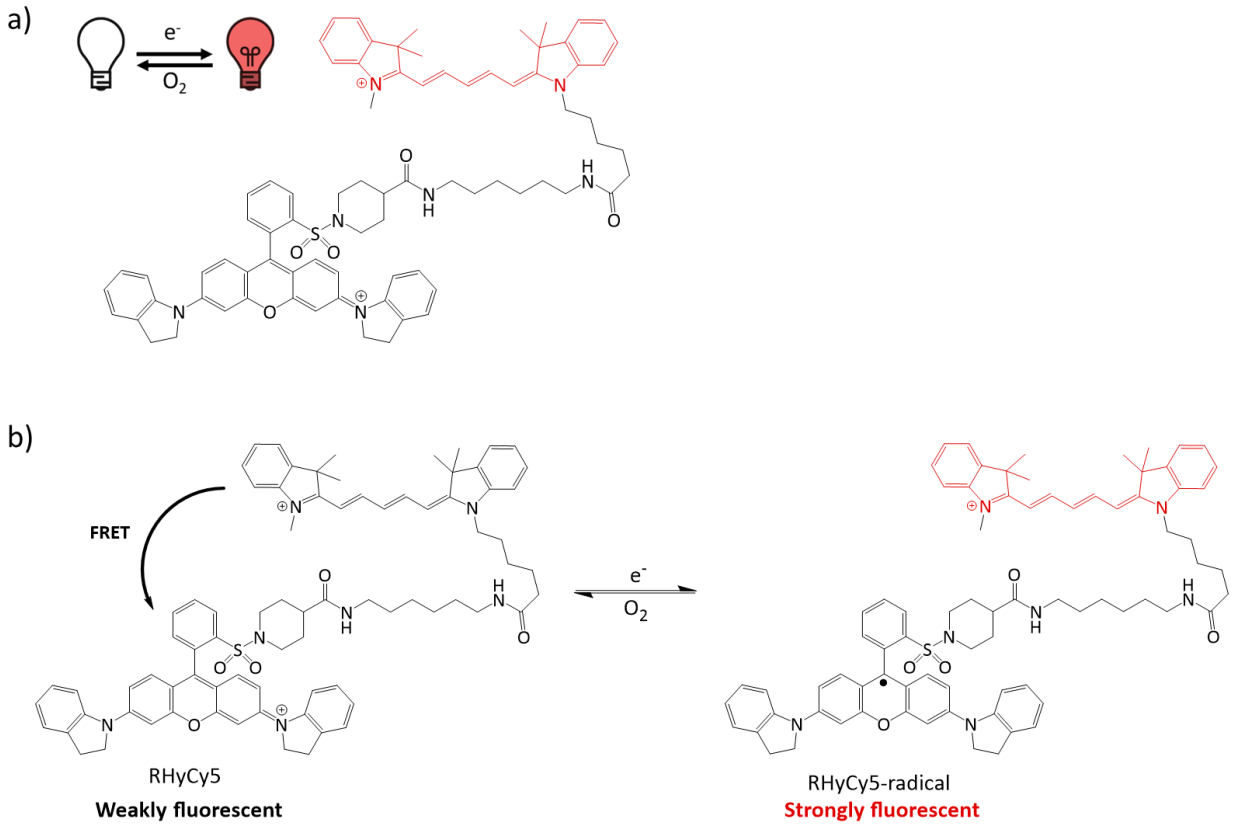

***Figure 18**. Fluorescence response of RHyCy5 in hypoxic state: (a) General scheme of the probe's response; (b) proposed mechanism of reversible detection of hypoxia. Adapted from [96].*

The changes in the redox capacity in hypoxia is one of the key markers of this state, but similar changes might also take place as a result of other conditions. In addition, the molecular processes

leading to the pathological effects of hypoxia are the effect of the interplay of multiple factors. Therefore, to improve reliability of monitoring hypoxia and its understanding, multiple biomarkers and/or molecular targets should be visualised at the same time.

Despite this and the importance of hypoxia, only one dual-analyte fluorescent probe designed to sense hypoxic state has been reported in the literature.[97] This probe detects NTR activity (common proxy of reducing capacity in hypoxia) irreversibly and adenosine triphosphate (ATP – indicator of metabolic activity of the cells) in a reversible fashion (***Figure 19***). Since a decrease in oxygen levels may result in changes in the metabolic rates, the authors designed the probe to be able to study the interplay between the hypoxia and the ATP. The probe was designed with two fluorophores (naphthalimide and Rhodamine B derivatives) linked together via a diethylenetriamine-based chain. The responsive moieties for NTR and ATP were a nitro group and a diethylenetriamine groups, respectively. The probe would present no fluorescent emission as it would be quenched for both fluorophores due to the interrupted aromaticity in the rhodamine via closed ring, and the nitro group in the naphthalimide via PeT quenching. However, the nitro moiety would react irreversibly with NTR in the presence of NADH and give the corresponding amino, eliminating quenching and thus, displaying fluorescence of emission in the naphthalimide region. Rhodamine is in equilibrium between its open (extended conjugated system, fluorescent) form and its closed form (interrupted aromatic system, non-fluorescent). The equilibrium is shifted towards the open form when diethylenetriamine interacts with ATP through multiple hydrogen bonding and due to proximity, there is also π–π stacking interaction between the rhodamine and the adenine part of ATP. [97] The findings revealed an exponential decrease of ATP in hypoxic cells and though further research is needed, the authors propose ATP as a potential biomarker for hypoxia.

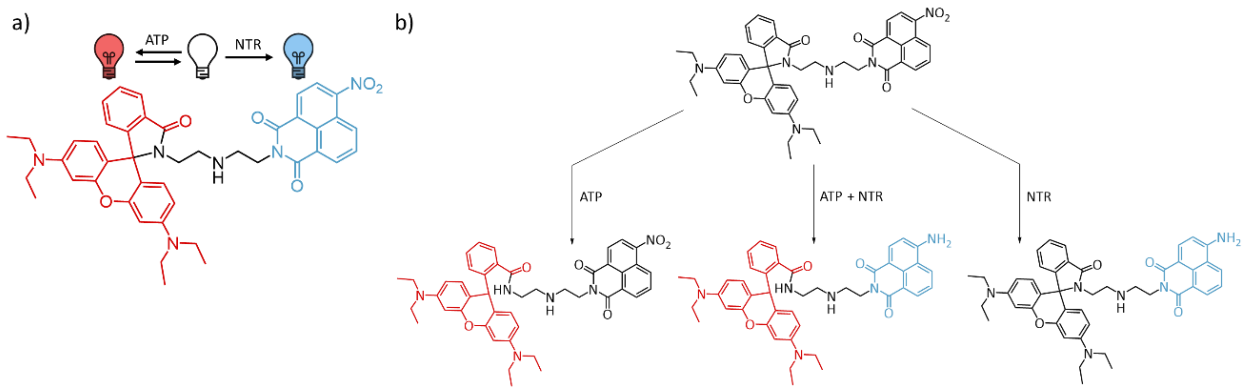

***Figure 19**. Fluorescence response of dual-analyte probe for NTR and ATP as a means of sensing hypoxic state. a) General scheme of the probe's response to each of the analytes; b) change in fluorescent emission of the fluorophores depending on the reaction of the probe with only ATP, only NTR, or both. Adapted from [59] and [97].*

1.4.3. Acidosis in hypoxic tumour microenvironments

Apart from the reducing capacity, hypoxic microenvironments are also characterised by acidosis. In hypoxia, the low molecular oxygen concentration forces a shift from aerobic to anaerobic glycolysis, leading to increased lactate production from glucose.[98,99] This metabolic change results in an acidification of extracellular microenvironment (pH: 6.5−6.9) due to the increased production of lactic acid that can also affect intracellular homeostasis.[100] The acidification is further enhanced by the less effective removal of the catabolites (waste products) from the hypoxic environment that is usually caused by a lack of the well-developed vasculature.

While aliphatic carboxylic acids and unsubstituted benzoic acid motifs have pK_a values too low to generally experience protonation/deprotonation equilibrium in most cellular conditions, unsubstituted phenol, aliphatic alcohols and simple aliphatic amines all have pK_a values too high for it.[101,102] This limitation can be overcome by incorporating carboxylic and phenolic groups directly into the (hetero)aromatic systems with extended aromatic conjugation. These are often found in fluorophores and characterised by pK_a values below 7 but higher than carboxylic acids and so still within that biologically relevant range.

Multiple fluorescent probes have been developed to sense pH within the relevant biological range, many of which contain the above-mentioned carboxylic and/or hydroxyl groups on (hetero)aromatic and/or multicyclic systems.[9,36,103–110] If these groups are incorporated into the

fluorescent scaffolds in the appropriate positions, to detect the pH changes, the protonated and unprotonated forms should present different fluorescent properties.

Multiple mechanisms can lead to switching between two differently protonated forms that also differ in their fluorescence. One of such mechanisms that has been explored especially for rhodamine (***Figure 20a***) and hemicyanine-based (***Figure 20b***) pH probes involves a carboxylic or phenolic group on extended conjugated aromatic systems. [9,103] If positioned at the right distance and orientation, these groups upon deprotonation can act as nucleophiles in an intramolecular ring-closure (cyclisation) reaction that disturbs the conjugated aromatic system of a chromophore (***Figure 20***). [9,36,103–110] A significant advantage of this approach in comparison to commonly employed PeT or ICT-based mechanisms in which pH-sensitive moiety act as electron donor with protonation-dependent donating capacity, is the complete disappearance of the chromophore in deprotonated state potentially promising a true turn-on/turn-off response with a firmly "dark" off state.

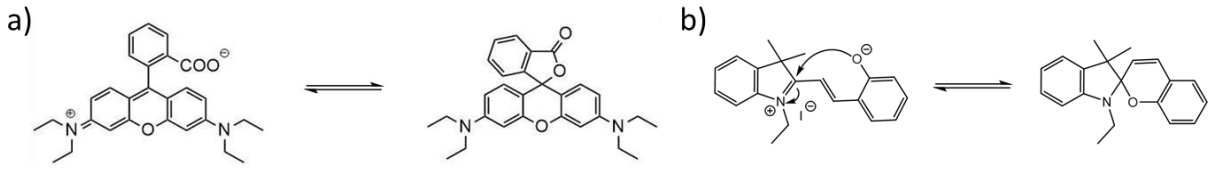

Figure 20. *The open-close equilibrium in (a) rhodamine and (b) hemicyanine derivatives. Adapted from*[9,103].

2. Aim and objectives

The overarching aim of this thesis was to develop stable dual-analyte fluorescent probe for visualising hypoxia in cellular environments. This goal encompassed a comprehensive approach; from initial probe design through synthesis and characterisation, culminating in the validation of these probes in biological systems. The development of such dual-analyte probes represents a significant advancement in the field of cellular imaging, as it offers the potential for multiparametric and therefore more reliable sensing of the hypoxic state.

The multiparametric capability of dual-analyte fluorescent probes is of particular importance as it promises to provide a more nuanced and comprehensive understanding of complex biological systems. By simultaneously detecting multiple analytes associated with hypoxia, these probes can offer a more complete picture of cellular conditions than single-analyte probes. This insight could prove invaluable in the development of more accurate cancer monitoring tools, potentially leading to more reliable and robust methods for cancer models profiling and studying of their response to treatment.

To achieve this goal, the research was conducted towards three main objectives:

1. **Design of reliable dual-analyte fluorescent probes for hypoxia:** this would require a development of a robust fluorescent scaffold stable in biological environment as well as selection of the type and position of introduction of responsive moieties for the corresponding target analytes – pH and reducing environment, which would serve as proxies for hypoxia.
2. **Synthesis and characterisation of reliable dual-analyte fluorescent probe for hypoxia**: implementation of the design by synthetic introduction of the selected responsive motifs to a robust fluorescent scaffold followed by characterization to confirm their structure and purity.
3. **Validation of dual-analyte fluorescence probe for hypoxia in cellular models:** testing of the performance of the developed probe in biologically relevant settings, involving both *in vitro* and *in cellulo* validation of fundamental spectroscopic properties, probe responsiveness and compatibility with biological settings.

3. Results and discussion

3.1. Design strategy

As mentioned in the introduction, hypoxia is one of the critically important states in pathology of cancer development and its response to treatment. In order to reliably investigate the changes in the hypoxic state, a fluorescent probe that emits robust and hypoxia-specific signal is required. Most previously reported probes for hypoxia in fact respond to only one hypoxia biomarker, usually reducing capacity. Instead, our aim was to develop a probe that responds to two most characteristic parameters of hypoxia – reducing capacity and low pH. This not only would allow for increased reliability of hypoxia monitoring in cellular models but would also enable studying of the interplay between these parameters for a better understanding of processes underlying cancer progression and response to treatment.

The first step in designing a reliable and robust probe is a selection of the appropriate fluorescent scaffold. The fluorophore scaffold chosen in this dissertation for the design of dual-analyte probes for hypoxia was the hemicyanine core, given its desirable features[2,7,42,44] including their photostability, orange-red emission and possibility of conjugation, among other important characteristics. [2,7,36, 42,44]

In order to equip hemicyanine with pH sensitivity, a hydroxyl group in *ortho*- position of the phenyl ring of the hemicyanine can be introduced, forming the corresponding 2-hydroxystyrylindolium cation (***Figure 21a***). The introduction of intrinsic pH-sensitivity onto the hemicyanine scaffold can also be used for the design and development of dual-analyte probes by a direct masking of the phenolic oxygen with the responsive moiety for the second analyte (***Figure 21***). For hypoxia sensing, as explained also in the chapter above, this could mean an introduction of the p-nitrobenzyl motif that undergoes reduction to aniline in hypoxic but not in normoxic conditions.[35,91,111–113] If this motif is placed on the hydroxyl group of hemicyanine, only upon its cleavage would the fluorescence response be pH dependent. The nitro moiety that would allow the detection of NTR could potentially also act as a PeT quencher[111,113], making the probe relatively non-fluorescent unless cleaved off by NTR-like activity as proxy for hypoxia

(***Figure 21b***). After bio-reduction (by NTR and NADH) of the nitro moiety connected to the benzylic position of the HC scaffold and its subsequent cleavage, a pH-sensitive form of the probe (styrylindolium cation) would be obtained. This cation can adopt two forms depending on the pH of the environment: spiropyran (ring-closed) and merocyanine (ring-opened) forms (***Figure 21b***), which exhibit different fluorescence properties. The merocyanine form (open ring) is highly fluorescent in orange-red range, while virtually no orange-red fluorescence can be observed in a spiropyran form due to interruption of aromatic conjugated system and therefore a factual lack of the long-emission chromophore. Additionally, such hemicyanine could possess another linker-like moiety that enables an introduction of additional fragment responsible for targeting or modification of the fluorescent properties of the probe (e.g. via conjugation to other fluorophores).

All of the elements demonstrated on the figure below have been explored in the design of the probes described in this dissertation and the details of these designs will be discussed in more depth in the subsequent chapters.

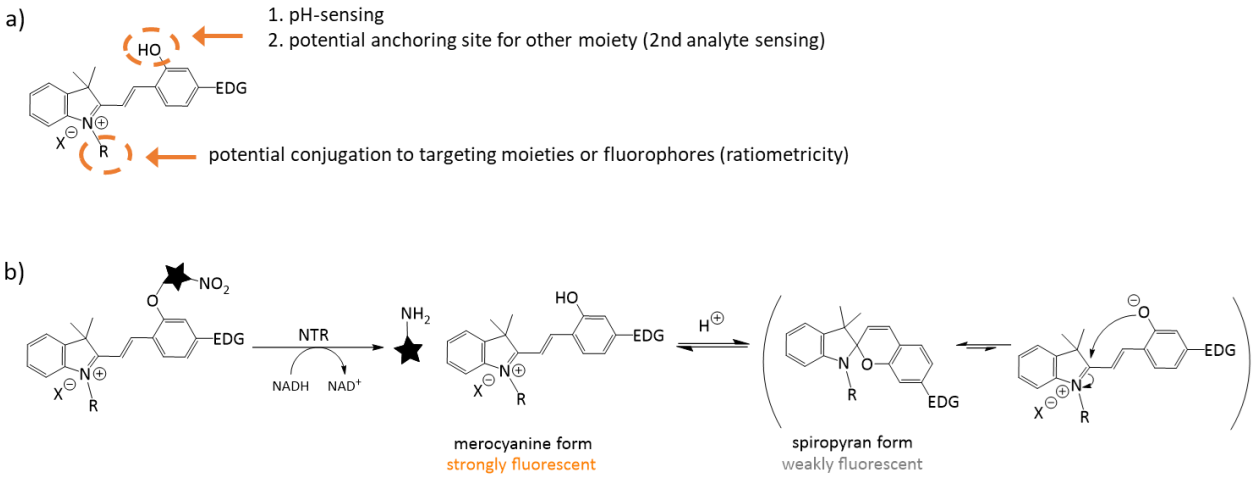

Figure 21*. (a) Proposed design of a dual-analyte probe based on a hemicyanine structure with a pH-sensitive moiety, which can act as an anchoring site for another moiety (2nd analyte sensing), and a second anchoring point for targeting or ratiometricity purposes. (b) Fluorescence response mechanism driven by the cleavable nitro moiety connected to the benzylic position of the hemicyanine scaffold and its subsequent cleavage, the obtained pH-sensitive molecule is in equilibrium between its merocyanine (acidic pH – fluorescent) and spiropyran (basic pH – non-fluorescent) form.*

3.2. Towards improved stability of hemicyanines

3.2.1. Design

A key characteristic of the reliable probe is its specificity for targeted analytes and subsequent robustness of the signal in complex biological environments, but off-target reactivities are often not comprehensively tested. As mentioned in section **Error! Reference source not found.**, the m ajor concern regarding fluorescent probes based on hemicyanine dyes and styrylindolium cations in particular, is their propensity to undergo nucleophilic addition in the presence of certain chemical species which can lead to a change in their fluorescent properties.[52,114,115] Since yielding a resilient probe against biological interferents different than the target analytes, the identification of a stable hemicyanine scaffold is desired. The key vulnerability of the electron-poor electrophilic hemicyanine scaffold is the susceptibility to nucleophilic addition. One can hypothesise that when the 2-hydroxystyrylindolium cation adopts its spiropyran form in basic conditions, it could potentially be protected from nucleophilic attack. However, this form is non-fluorescent and prevalent in more basic pH. We hypothesized that we can decrease the electrophilicity of the fluorescent, open-form hemicyanine and therefore increase its stability by increasing the electron density in the conjugated system. This could potentially be achieved by an introduction of variable electron-donating groups (EDG) into the aromatic ring of the fluorophore. As indicted by the Hammett and Hansen parameters that help predict the relative propensity of nucleophilic addition to aromatic systems, the highest stabilisation (i.e. highest increase in electron density) can be achieved by placing the EDG in *para* position in respect to the potential place of the nucleophilic addition.[116] The presence of EDGs in the para position in respect to the conjugated system has also been shown to increase fluorescence of hemicyanines due to an improved ICT-type processes between the EDG and the cationic motif on the other side of the molecule.

With this aim in view, in order to explore the relative influence of different substituents, three derivatives with various EDGs in *para* position of the ring were synthesised: previously reported **HCy-OMe**, reference **HC-NEt$_2$** (the scaffold that has been used for hemicyanine-based probes)[9], and a newly designed at the time of development **HCy-Jul**. **HCy-OMe** contains a methoxy group in *para* position, while **HCy-NEt$_2$** and **HCy-Jul** contain an alkylamino group in the same position. **HCy-Jul** presents more rigidity and delivers additional EDG contribution given by alkyl groups in

meta positions. [116] Upon the design and successful synthesis, their fluorescence emission signal stability was tested in various solvents, buffers, and against interferents to determine the most stable core.

3.2.2. Synthesis

Three hemicyanine dye derivatives (***Scheme 1***) have been synthesized by adaptation of existing protocols of condensation reactions between **1** and corresponding benzaldehyde derivatives. [117,118] The main challenge encountered was the effective purification of such derivatives, as they are positively charged and exhibit high retention on silica gel regardless of the mobile phase used.

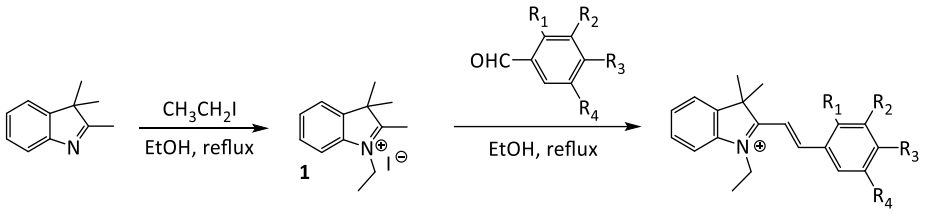

HCy-OMe, **2** R_1,R_2,R_4: H, R_3: OMe
HCy-NEt$_2$, **3** R_1,R_2,R_4: H, R_3: NEt_2
HCy-Jul, **4** R_1: H, R_2: CH_2R, R_3: NCH_2R'

***Scheme 1**. Synthetic scheme of hemicyanine derivatives. Yields: **1**, 48.8%; **2**, 34.2%; **3**, 98.5%; **4**, 99.2%.*

The synthesis of hemicyanine derivatives starts with the alkylation of heteroaromatic moiety to generate the styrylindolinium cation. The electron pair on the sp^2 orbital of the nitrogen atom of the 2,3,3-trimethylindolenine can act as a nucleophile. In this case it has been reacted with the carbon of the alkyl chain with sp^3 hybridization next to the iodide or bromide, which acts as the leaving group leading to a formation of **1**.

Then, as presented on the ***Scheme 2***, in the presence of base, the obtained 1,2,3,3-tetramethyl-3H-indolium iodide (**1**) is deprotonated, leading to a tautomeric equilibrium that stabilises a potentially nucleophilic carbanion. This, in turn, can nucleophilically attack carbonyl group of the aldehyde, generating an alkoxide followed by dehydration and a formation of the stable conjugated π-system across the majority of the resulting hemicyanine scaffold.

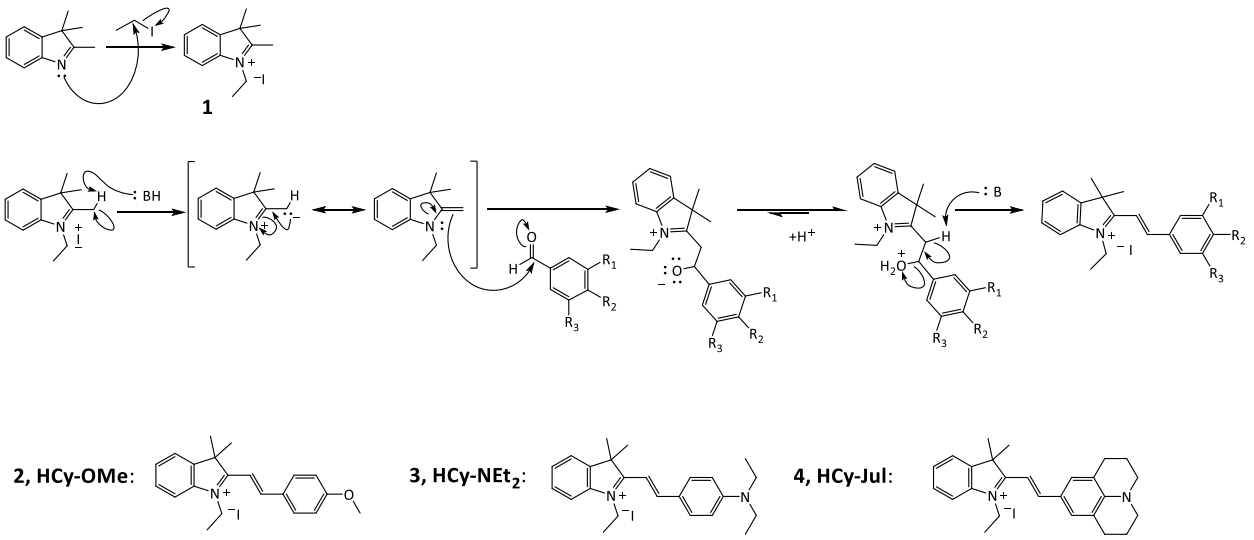

***Scheme 2**. Mechanisms of the reaction leading to the formation and of hemicyanine derivatives **2-4** from common **precursor 1**.*

The products' purity and identity were confirmed through two main spectroscopic techniques mainly NMR spectroscopy (^{1}H NMR, ^{13}C NMR, COSY, …), and mass spectrometry (HR-MS). All relevant spectra can be found in the Appendix (subchapter 6.1.1). Compounds **2** (**HCy-OMe**)[119] and **3** (**HCy-NEt$_2$**) [114,120] have already been reported and signals in obtained NMR and MS spectra correlate to those found in the literature.

Compound **4** (**HCy-Jul**) is a novel hemicyanine derivative, which was hoped to be a better candidate for yielding stable fluorescent probes than its more used counterpart (compound **3**) due to a presence of the motifs with higher electron donating on the phenyl residue. One of the most common ways to describe the electron-donating / electron withdrawing character of aryl substituents is the use of Hammett parameters.[116] These parameters also known as substituent constants were initially established to empirically relate reaction rates with equilibrium constants for reactions of substituted benzoic acid analogues. Since then, they have been found to be largely generalisable to a wide range of groups as determinants of electron-withdrawing group (EWG) / EDG character of the aromatic substituents in relation to H (value of 0). Therefore, EDGs have usually values < 0 and EWGs values above 0. Hammett parameter for -OMe group (-0.27) in position para in respect to the substituent of interest (here: conjugated π-system through alkene bridge) is larger (less electron donating) than the one for dimethylamino substituent (-0.88)

resembling groups in **HCy-NEt$_2$** and **HCy-Jul**. The latter in addition, possesses two alkyl groups in positions meta in respect to the π-conjugated system (for -Me meta parameter is -0.07) that cumulatively lead to -1.02 overall Hammett parameter-defined EDG contribution from Julolidine substituent (highest of all). This theoretical order of EDG character (**HCy-OMe** weaker than **HCy-NEt$_2$** weaker than **HCy-Jul**) is also confirmed experimentally for the investigated compounds by the chemical shifts of aromatic protons in the conjugated π-system (***Figure 22***). In general, **NCy-OMe** exhibits most down-field shifts, followed by **NCy-NEt$_2$**, with **HCy-Jul** exhibiting most up-field shifts indicating highest electron shielding (i.e. higher electron density). In particular, it is usually protons in position *meta* to the changing substituents that are often used as diagnostic ones for evaluation of electron density in aromatic systems due to a lack of resonance contributions that might distort the trends. For those (3' and 5') the values decrease from 8.15 ppm (**HCy-OMe**) > 8.00 ppm (**HCy-NEt$_2$**) > 7.48 ppm (**HCy-Jul**) indicating increase in the shielding ad therefore EDG in the opposite order (***Figure 22***) further confirming the achievement of the designed effect.

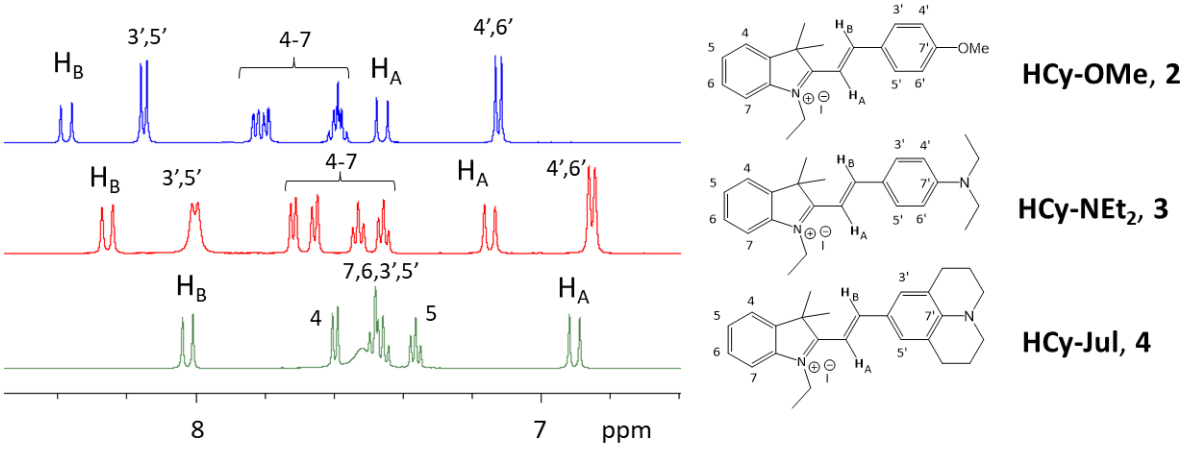

Figure 22. *^{1}H-NMR of the aromatic region of **HCy-OMe** (blue), **HCy-NEt$_2$** (red), and **HCy-Jul** (green) in d_6-DMSO/D_2O (80:20).*

3.2.3. Spectroscopic characterisation of **HCy-OMe**, HCy-NEt$_2$, and **HCy-Jul** in solution

3.2.3.1. Fluorescence properties in DMSO

The absorbance and emission spectra of **HCy-OMe**, **HCy-NEt$_2$** and **HCy-Jul** were collected in DMSO as a solvent and normalised to the maximum absorbance or fluorescence output for a

given hemicyanine derivative (***Figure 23a-c***). **HCy-OMe** presents a green emission ($\lambda_{exc\ max/em\ max}$ = 430/530) with relatively large Stokes shift, whereas **HCy-NEt$_2$** ($\lambda_{exc\ max/em\ max}$ = 560/600) and **HCy-Jul** ($\lambda_{exc\ max/em\ max}$ = 585/615) present a more red-shifted fluorescence emission with Stokes shifts relatively similar to each other but significantly lower than the one of **HCy-OMe**, suggesting a structure-dependent shift in emission wavelength. Such measured spectroscopic properties are in accordance with the ones reported in the literature.[84,119]

Hemicyanine derivatives with substituent in *para* position possessing an electron-donating character are known for their ICT mechanism (***Figure 23d***), in which the "push-pull"-like intramolecular electron transfer processes give rise to other resonance structures, contributing to further stabilisation and causing a red shift in fluorescence emission. The existence of the donor-acceptor motif pair that remains in the electronic communication (conjugation) is responsible for the appearance of the long wavelength absorption charge transfer band (CT) that is usually assigned to π–π* transition .[121] According to the ICT mechanism of fluorescence, in the excited state the electronic charge is transferred from the methoxy- or alkylamino-substituent of the phenyl ring to the nitrogen atom of the indolium ring. Interestingly, relative excitation and emission wavelengths of in the series in the series of **HCy-OMe**, **HCy-NEt$_2$**, and **HCy-Jul** can be directly correlated with the electron donating character of the substituents (Hammett parameters). The greater the electron donating character of the motifs on phenyl ring, the more red shifted (lower energies) their excitation and emission spectra but also the smaller the Stokes shifts.[46] The latter (including significantly larger Stokes shift for **HCy-OMe** vs two other compounds) might be attributed particularly to a much more energetically demanding electron/charge transfer (bigger energy loss) due to a lower propensity of the oxygen to release electrons (and lower electron donating character of -OMe substituent) than it is for nitrogen. All of these dependencies, stemming from the changes in the electron donating character of the substituents, highlight the possibility of fine-tuning the spectral properties of hemicyanine derivatives through strategic structural modifications.

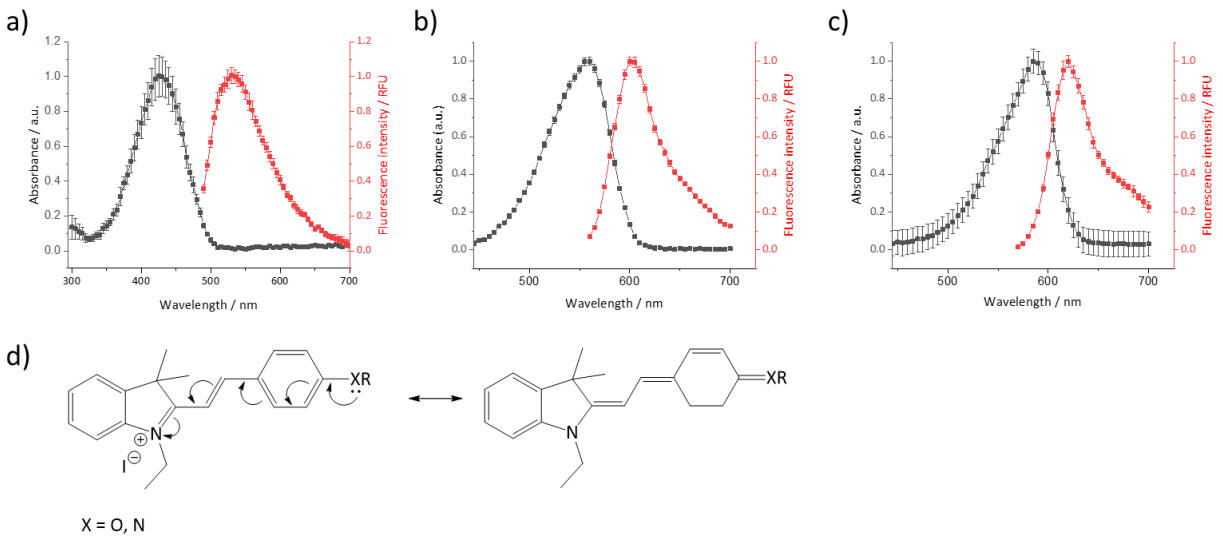

***Figure 23**. Normalised absorbance (black dots) and fluorescence emission (red dots) spectra for (a) **HCy-OMe** (5 µM), (b) **HCy-NEt₂** (2.5 µM), (c) **HCy-Jul** (2.5 µM) hemicyanine derivatives in DMSO. For **HCy-OMe**, $\lambda_{exc/em}$ = 430/490-700 nm, for **HCy-NEt₂**, $\lambda_{exc/em}$ = 530/560-700 nm, and for **HCy-Jul**, $\lambda_{exc/em}$ = 530/560-700 nm. N = 3 (d) Movement of electrons in ICT mechanism expected for hemicyanine derivatives with EDG substituents containing oxygen or nitrogen as heteroatoms in para position.* [45,119,122]

Once their maxima of absorbance and fluorescence emission was determined, their dependence on the concentration was studied. An enhancement of both the absorbance and the intensity of emission of all derivatives was observed with the gradual increase of concentration (***Figure 24***). Hence, the increase in concentration has no interfering effect nor in the absorbance nor the fluorescence emission processes. The obtained linear relationship between concentration and absorbance (as well as intensity of emission) for all derivatives suggests nor solubility nor aggregation effects within the investigated range of concentrations (2.5 – 10 µM **HCy-OMe**, 0.5 – 2.5 µM for **HCy-NEt₂**, and 0.5 – 2.5 µM for **HCy-Jul**).

The molar extinction coefficients (ε), fluorescence quantum yields (Φ_F), and brightness (B) for the hemicyanine derivatives were determined via a comparative method developed by Williams et al. Reference molecule **HCy-NEt₂** presents approximately 2-3 times higher relative molar extinction coefficients, quantum yield and brightness than **HCy-Jul** in DMSO that aligns well with the common trend in increased non-radiative relaxation towards longer wavelengths due to closer proximity of excited and ground states).

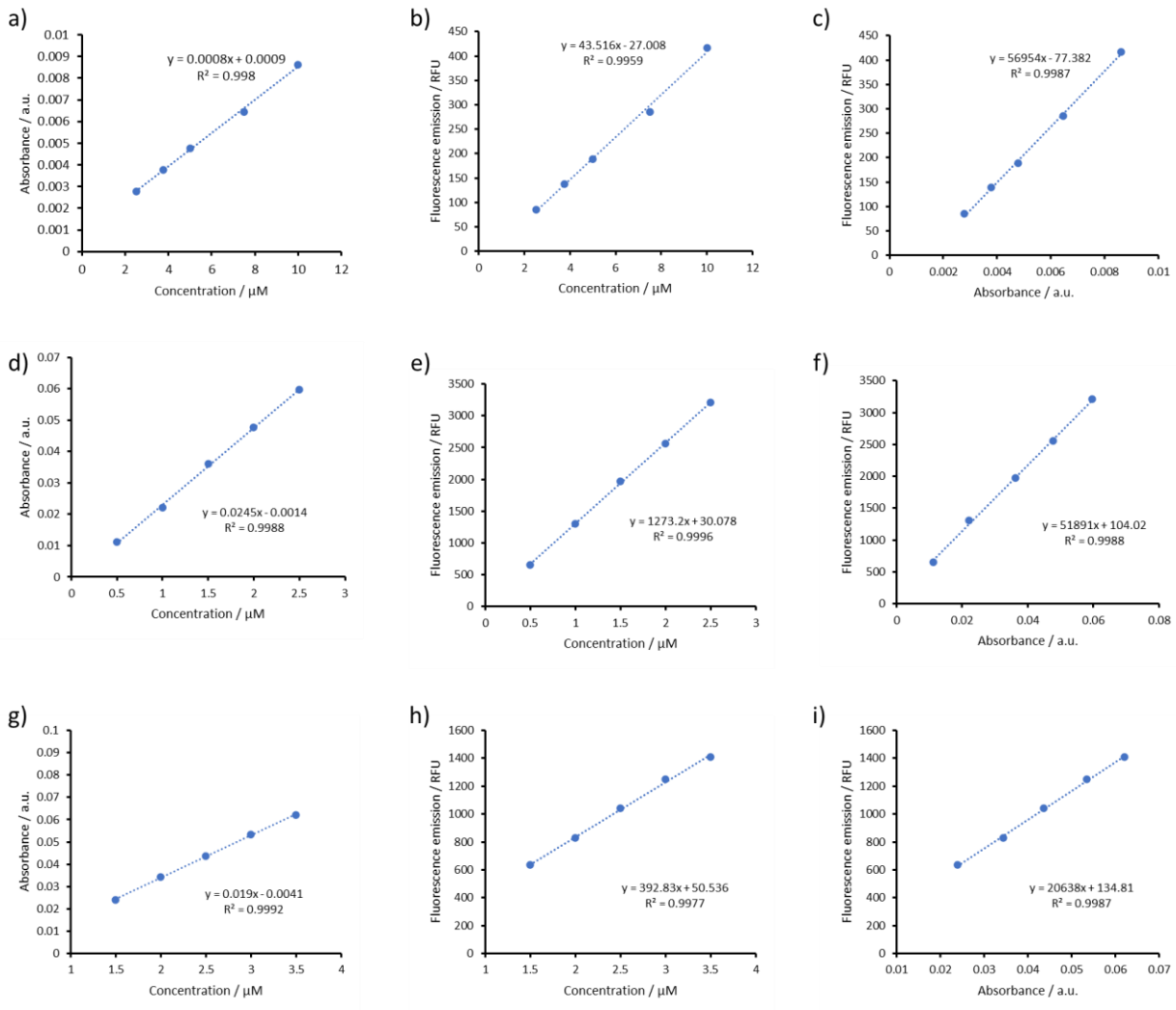

Figure 24. *(a,d,g) Absorbance vs concentration, (b,e,h) fluorescence emission vs concentration, (c,f,i) fluorescence emission vs absorbance for (a-c)* ***HCy-OMe*** *(range 2.5 – 10 µM), (d-f)* ***HCy-NEt₂*** *(range 0.5 – 2.5 µM), (g-i)* ***HCy-Jul*** *(range 0.5 – 2.5 µM) hemicyanine derivatives in DMSO. Collection of fluorescence emission spectra:* ***HCy-OMe****,* $\lambda_{exc/em}$ *= 450/480-700 nm;* ***HCy-NEt₂****,* $\lambda_{exc/em}$ *= 530/560-700 nm;* ***HCy-Jul****,* $\lambda_{exc/em}$ *= 530/560-700 nm. Fluorescence emission vs concentration for (b)* ***HCy-OMe*** *(*$\lambda_{exc/em}$ *= 450/524), (e)* ***HCy-NEt₂*** $\lambda_{exc/em}$ *= 515/601), (h)* ***HCy-Jul*** *(*$\lambda_{exc/em}$ *= 515/619). N = 3*

Table 1: Calculated spectroscopic properties of the hemicyanine scaffolds (**HCy-NEt$_2$** and **HCy-Jul**) measured in DMSO. Values were calculated based of the results averaged over 3 separate repeats. Extinction coefficient values rounded to a full 10s. Quantum yields were measured by a relative method[123] comparing to the standard (ϕ_F = 0.95 for Rhodamine 6G in EtOH[124]) for **HCy-NEt$_2$** and **HCy-Jul**). N = 3

Compound	$\lambda_{exc}/\lambda_{em}$	Ɛ / [M^{-1} cm^{-1}]	Quantum yield (ϕ_F)	Brightness [M^{-1} cm^{-1}]
HCy-NEt$_2$	560/605	43770	0.024	1050
HCy-Jul	584/623	33990	0.009	300

3.2.3.2. Fluorescence in a buffer at different pH values

The use of buffer solutions that replicate biological environments is fundamental in validation of probes and prodrugs.[125,126] There is a wide selection of buffers that are used depending on the pH range of interest, as well as buffering capacity and temperature dependence, among other properties.[127,128] As a preliminary investigation these hemicyanine derivatives were tested for their pH sensitivity. The dependence of their spectroscopic properties was studied for a pH range of 4 – 8: from an acidic pH to a slightly basic pH. However, such a range cannot be achieved via one single buffer agent, but requires at least two of them. To account for potential chemical differences between the buffers, for at least one pH value the measurements have been done for multiple buffers. The buffers selected for this work, based on previous literature in the field, were citrate-phosphate (CPB; pH values of 4, 5, 6), and phosphate (PB; pH values of 6, 7, 7.5, 8) buffers with pH 6 as a common value of pH.[129]

The fluorescent emission signal of the hemicyanine derivatives was recorded in pH values ranging from 4 – 8 in two solutions (Figure 25). None of the synthesised hemicyanine derivatives showed any statistically significant pH dependency of fluorescence emission (***Figure 25***), which is consistent with the absence of pH-sensitive substituent in the styrylindolium core in this pH range (pK_a for tertiary amines is above the highest tested pH value[101] – relevant for **HCy-NEt$_2$** and **HCy-Jul**).

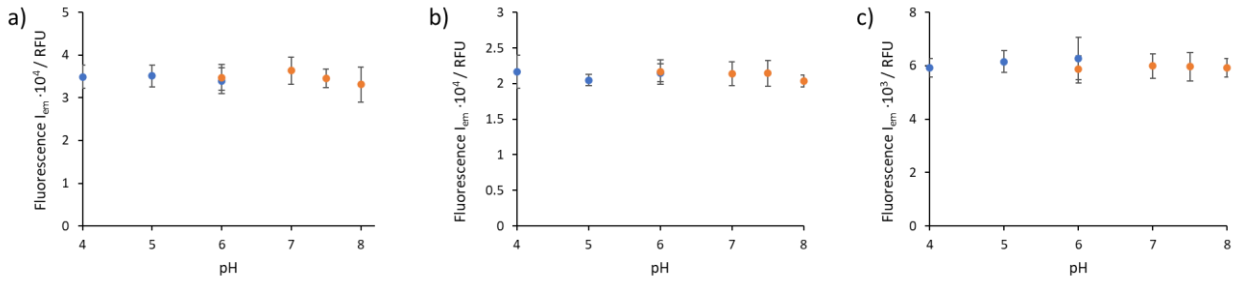

***Figure 25**. pH dependency of fluorescent emission signal for (a) **HCy-OMe** (5 µM), (b) **HCy-NEt₂** (2.5 µM), (c) **HCy-Jul** (2.5 µM) hemicyanine derivatives. Two different buffer solutions were used for the pH range of 4-8: citrate-phosphate buffer (CPB, blue dots) and phosphate buffer (PB, orange dots). For **HCy-OMe**, $\lambda_{exc/em}$ = 430/530 nm, for **HCy-NEt₂**, $\lambda_{exc/em}$ = 530/595 nm, and for **HCy-Jul**, $\lambda_{exc/em}$ = 530/615 nm. N = 3*

3.2.3.3. Fluorescence in in buffers of variable chemical nature

Ideally, the nature, composition, and/or concentration of the buffer in which the hemicyanine derivatives are dissolved should not cause perturbances in spectroscopic properties to prove the robustness of the scaffold. The first study involved the spectroscopic characterisation of these dyes in selected buffers (most commonly used in bioanalytical applications) [125] of the same pH value but at a range of different buffer concentrations spanning micromolar ranges. For this work, the model buffers selected included phosphate buffer (PB, proxy for the phosphate buffer saline, PBS), TRIS·HCl and HEPES at pH 7.4 and concentrations of 50, 100, 150, 200, 250, and 500 µM.

The hemicyanine derivatives were tested in these buffer conditions (***Figure 26 a-f***, ***Figure A1*** in Appendix in subchapter 6.3), and in general for all three dyes fluorescence emission intensity remained relatively unperturbed for PB and TRIS·HCl at different buffer concentrations (***Figure 26a-c***; PB, grey dots and trendline; TRIS·HCl, orange dots and trendline). However, changes in HEPES buffer could be observed with a gradual enhancement in fluorescence intensity with increasing buffer concentration, becoming more significant at the highest concentration (***Figure 26a-c,*** blue dots and trendline). Moreover, when comparing the fluorescence emission of the same compound in these three different buffers at the same value of pH (physiological, 7.5), all derivatives exhibited decreasing emission in the following order: HEPES > TRIS·HCl > PB, with less difference between last two (***Figure A1 j-l*** in Appendix).

In the attempt to try and verify whether the fluorescence changes in different buffers come from the differences in the chemical nature of the buffers (e.g. their nucleophilicity) or it is the effect of physico-chemical parameters of the buffers, the correlation between fluorescence changes and conductivity of the solution (which is a proxy of the ionic strength) was analysed. The conductivity of PB and TRIS·HCl buffers were relatively similar at the same concentrations, while the same concentrations of HEPES buffer led to much smaller changes in conductivity (***Figure A1m*** in Appendix subchapter 6.3.). In order to assess such interdependence, the fluorescence intensity was plotted against the conductivity of a given buffer and concentration (***Figure 26d-f***), which presented a linear trend fitting for all compounds. Slope values for PB and TRIS·HCl are comparable and rather small suggesting little buffer effect, while for HEPES slope value is higher by an order of magnitude indicating that the chemical nature of HEPES may play more important role than conductivity or ionic strength. These findings indicate that as the fluorescence signal increases with increasing conductivity, collisional quenching does not significantly influence the fluorescence in the tested buffer solutions. [130]

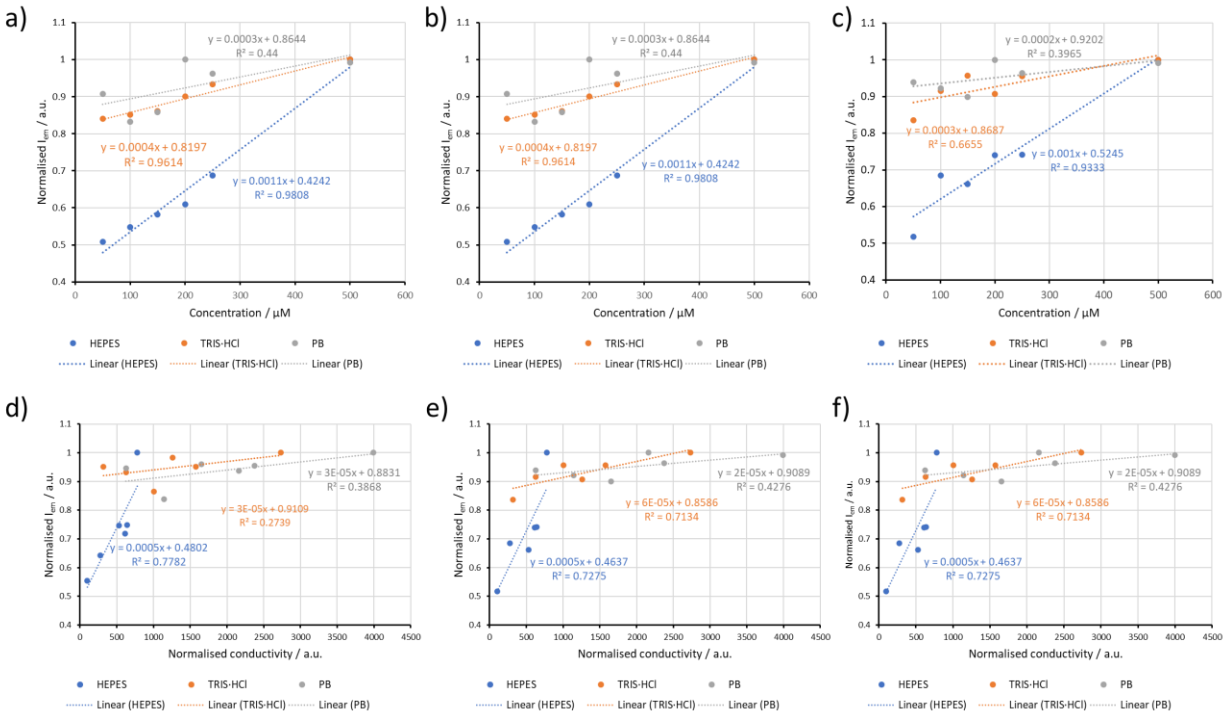

Figure 26*. (a-c) Plots of normalised fluorescence emission of (a,d)* ***HCy-OMe*** *(5 µM), (b,e)* ***HCy-NEt₂*** *(2.5 µM), (c,f)* ***HCy-Jul*** *(2.5 µM) hemicyanine derivatives at the maximum wavelength of emission in three different buffer solutions (PB, grey dots and trendlines; TRIS·HCl, orange dots and trendlines; HEPES, blue dots and*

trendlines) vs the concentration of the buffer(50, 100, 150, 200, 250, and 500 µM) of pH 7.4, with a final 1% of DMSO. Normalisation of the fluorescent output signal was carried out within a given compound and buffer solution. For ***HCy-OMe****, $\lambda_{exc/em}$ = 430/530, for* ***HCy-NEt$_2$****, $\lambda_{exc/em}$ = 530/595 and* ***HCy-Jul*** *hemicyanines at $\lambda_{exc/em}$ = 530/615. To be normalised within a given compound.For* ***HCy-OMe*** *hemicyanine, spectra were collected at λ_{exc} = 430 nm, λ_{em} = 460-700 nm, Gain 120, and for* ***HCy-NEt$_2$*** *and* ***HCy-Jul*** *hemicyanines at λ_{exc} = 530 nm, λ_{em} = 560-700 nm. (m) Plot of normalised electric conductivity vs concentration (50, 100, 150, 200, 250, and 500 µM) of PB (blue dots and trendline), TRIS·HCl (orange dots and trendline), HEPES (grey dots and trendline) buffers at pH 7.5. Conductivity was normalised to the output value given by 500 µM PB. N = 3*

3.2.3.4. Fluorescence changes at different viscosity and polarity

Polarity and viscosity are two key physical factors influencing biological processes within an organism and thus, are usually linked with the genesis of various diseases.[131,132] At the same time, those parameters can vary significantly across cells. Therefore, understanding the relationship between the fluorescence of the dyes and the changes in viscosity and polarity of the environment is important to enable reliable interpretation of biological data.[2] The hemicyanine derivatives were dissolved in solutions containing different ratios of either 1,4-dioxane/water (imitating changes in polarity) or glycerol/water solutions (changes in viscosity). All derivatives showed sensitivity of the fluorescence intensity to both viscosity (***Figure 27a,c,e***) and polarity (***Figure 27b,d,f***).

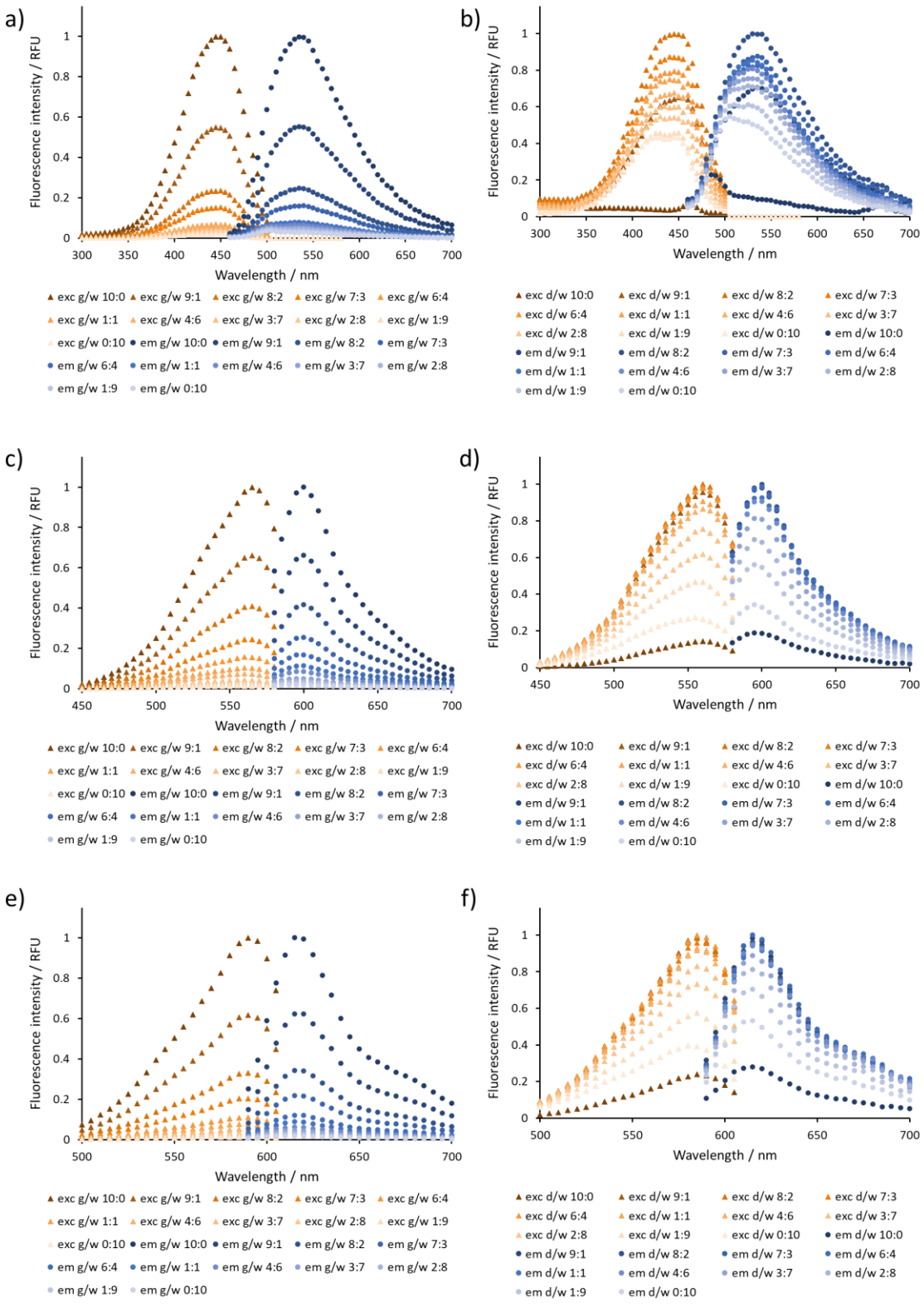

***Figure 27**. Fluorescence measurements of hemicyanine derivatives in solutions of different viscosity (a,c,e) and polarity (b,d,f). (a,b) **HCy-OMe** (5 µM), (c,d) **HCy-NEt₂** (2.5 µM), (e,f) **HCy-JuI** (2.5 µM) hemicyanines in*

(a,c,e) glycerol/water or (b,d,f) 1,4-dioxane/water solutions of different ratios (10:0, 9:1, 8:2, 7:3, 6:4, 1:1, 4:6, 3:7, 2:8, 1:9, 0:10) with a final 1% DMSO. The blank samples consisted in the corresponding solution of glycerol/water or 1,4-dioxane/water of a given ratio with the same final %DMSO. Excitation spectra are represented in orange triangles, while emission spectra are in blue dots. For ***HCy-OMe****, excitation spectra were collected at* λ_{em} *= 530 nm,* λ_{exc} *= 300-500 nm, and emission spectra at* λ_{exc} *= 430 nm,* λ_{em} *= 460-700 nm. For HCy-*NEt_2*, excitation spectra were collected at* λ_{em} *= 610 nm,* λ_{exc} *= 300-580 nm, and emission spectra at* λ_{exc} *= 550 nm,* λ_{em} *= 580-700 nm. For* ***HCy-Jul****, excitation spectra were collected at* λ_{em} *= 635 nm,* λ_{exc} *= 300-605 nm, and emission spectra at* λ_{exc} *= 570 nm,* λ_{em} *= 600-700 nm. Normalisation was carried out given the solution that displayed the maximum fluorescence intensity within a given compound. N = 3*

The viscosity-dependent fluorescence increase observed in ***Figure 27a-c*** was quantified via calculating the integrated intensity of emission (as well as the relative one for easier comparison) of each compound for each glycerol/water mixture (***Tables 2*** and ***3***). Then the resulting integrated intensity of emission was plotted against the dynamic viscosity[133] for a given percentage of glycerol in water and the fitting of such plot was done into a natural logarithmic scale trend to give ***Figure 28 a,c,e***. A second plot for each compound was created for the logarithmic integrated emission against the logarithmic dynamic viscosity, and a linear fitting was applied (***Figure 28b,d,f***). Considering the obtained tables and plots, it can be confirmed that all compounds present an enhancement of the fluorescence emission with the increasing viscosity of the mixture with similar extent, as the constants (slopes) of the fittings are of the same magnitude for all three compounds.

The observed viscosity-sensitivity can be attributed to the molecular rotor nature of merocyanine dyes extensively studied in the literature[119,134]. Generally, a molecular rotor consists of two symmetric small π- conjugations in which the electron acceptor and the electron donor moieties are connected by a rotatable bond to form a D−π−A structure. In more viscous environments, restriction of intramolecular rotation inhibits nonradiative decay pathways, such as twisted intramolecular charge transfer, which enhances the fluorescence emission. Such fluorescence response is observed for the three hemicyanine derivatives, confirming correlation with previous literature studies[119,134].

Table 2. **HCy-OMe** (5 μM) in various glycerol/water solutions of different ratios (10:0, 9:1, 8:2, 7:3, 6:4, 1:1, 4:6, 3:7, 2:8, 1:9, 0:10) with a final 1% DMSO. The blank samples consisted in the corresponding solution of glycerol/water of a given ratio with the same final %DMSO. λ_{em} - maximum of emission for a chosen glycerol/water mixture; $\lambda_{em\text{-}max}$ – maximum of emission spectrum value in a chosen glycerol/water mixture; Integrated I_{em} – sum of emission given in a chosen glycerol/water mixture; Relative integrated I_{em} – sum of emission given in a chosen solvent or buffer, where values were normalized to the highest value (for glycerol/water mixture 10:0). N = 3

Glycerol % in water	Dynamic viscosity at 20°C [133] [cP=mPa·s]	**HCy-OMe** $\lambda_{em,max}$ [nm]	**HCy-OMe** Integrated I_{em}	**HCy-OMe** Relative integrated I_{em}
100	1412	540	802450	1.00
90	219.0	540	450511	0.56
80	60.1	540	201448	0.25
70	22.5	540	133815	0.17
60	10.8	535	66632	0.08
50	6.00	535	67786	0.08
40	3.72	530	55965	0.07
30	2.50	530	44575	0.06
20	1.76	505	39634	0.05
10	1.31	505	31414	0.04
0	1.005	505	27155	0.03

Table 3. **HCy-NEt$_2$** (2.5 µM) and **HCy-Jul** (2.5 µM) in various glycerol/water solutions of different ratios (10:0, 9:1, 8:2, 7:3, 6:4, 1:1, 4:6, 3:7, 2:8, 1:9, 0:10) with a final 1% DMSO. The blank samples consisted in the corresponding solution of glycerol/water of a given ratio with the same final %DMSO. λ_{em} - maximum of emission for a chosen glycerol/water mixture; $\lambda_{em\text{-}max}$ – maximum of emission spectrum value in a chosen glycerol/water mixture; Integrated I_{em} – sum of emission given in a chosen glycerol/water mixture; Relative integrated I_{em} – sum of emission given in a chosen solvent or buffer, where values were normalized to the highest value (for glycerol/water (10:0)). N = 3

Glycerol % in water	Dynamic viscosity at 20°C [133] [cP=mPa·s]	**HCy-NEt$_2$** $\lambda_{em,max}$ [nm]	**HCy-NEt$_2$** Integrated I_{em}	**HCy-NEt$_2$** Relative integrated I_{em}	**HCy-Jul** $\lambda_{em,max}$ [nm]	**HCy-Jul** Integrated I_{em}	**HCy-Jul** Relative integrated I_{em}
100	1412	600	972096	1.00	620	916281	1.00
90	219.0	600	643797	0.66	620	574212	0.63
80	60.1	600	406867	0.42	620	316944	0.35
70	22.5	600	250466	0.26	620	203369	0.22
60	10.8	600	166379	0.17	620	113462	0.12
50	6.00	600	112089	0.12	620	83028	0.09
40	3.72	595	84082	0.09	620	58917	0.06
30	2.50	595	50395	0.05	620	42196	0.05
20	1.76	595	37468	0.04	620	30101	0.03
10	1.31	595	27846	0.03	620	21834	0.02
0	1.005	595	19100	0.02	620	17286	0.02

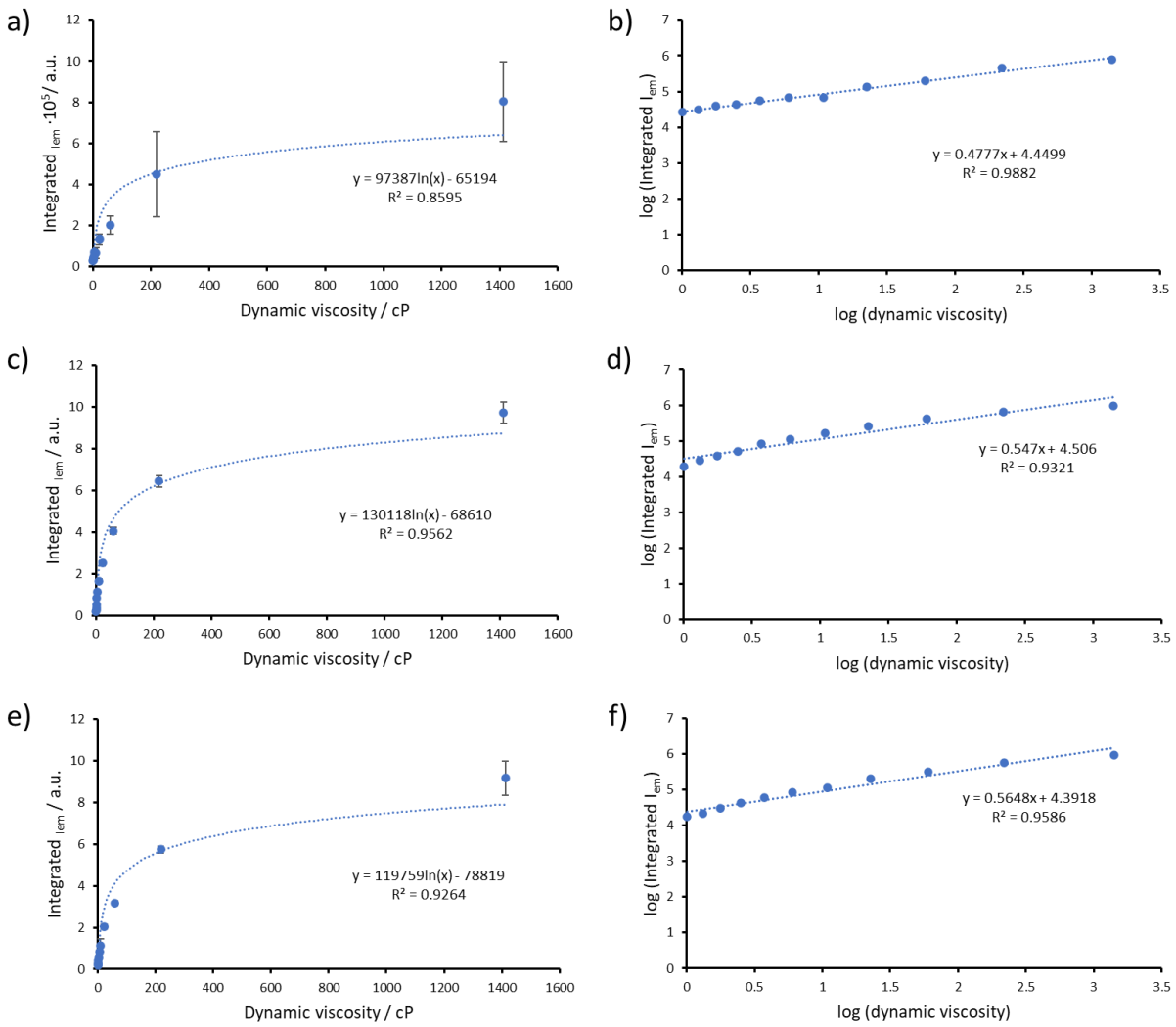

Figure 28. *(a,c,e) Plotting of the integrated intensity (sum) of the fluorescence emission as a function of the dynamic viscosity for glycerol/water mixtures and (b,d,f) plotting of the log(Integrated I_{em}) as a function of the log(dynamic viscosity) of the hemicyanine derivatives (a,b)* ***HCy-OMe*** *(5 µM), (c,d) HCy-NEt$_2$ (2.5 µM), (e,f) HCy- Jul (2.5 µM). log(Integrated I_{em}) – logarithm of the integrated emission of the corresponding hemicyanine derivative; log(dynamic viscosity) – logarithm of the viscosity of glycerol/water mixtures. N = 3*

The Reichardt polarity parameter, based on the empirical measurement of molar transition energy using the betaine B30 indicator (2,6-diphenyl-4-(2,4,6-triphenyl-1-pyridinio)-phenolate, $E_T(30)$), is widely regarded as one of the most dependable and essential scales for assessing the polarity of binary mixtures or pure solvents. Thus, for the quantification of polarity sensing of the hemicyanine derivatives, each solvent combination has been described by the $E_T(30)$ value and an integrated fluorescence emission intensity has been assigned to it for each compound (***Tables 4*** and ***5***). In generally, increasing the polarity of the environment (increasing water percentage)

causes a decrease in both fluorescence excitation and emission intensity (spectra in Figure 27d-f) with the exception of high dioxane concentrations where the effect seems opposite. In fact, all three dyes in pure 1,4-dioxane exhibit the most significant quenching from all the tested conditions. This can be attributed to solubility issues or the formation of secondary species, such as π-π stacking in apolar solvents, may be occurring in the ground or excited states. This is particularly likely to happen when attempting to dissolve polar (charged) molecules, such as these hemicyanine derivatives, in less polar media, where the molecules may preferentially interact with each other rather than with the solvent, leading to the formation of stacks that self-quench. The presence of a small amount of water might be sufficient to disrupt these π-π stacks, allowing more traditional effects to dominate, which could explain the fluorescence behaviour for all compounds from mixtures with increasing percentage of water (in particular, from1,4-dioxane/water (8:2)).

To investigate the relationships closer, data presented in ***Figure 27d-f*** have been transformed and plotted as integrated fluorescence emission against Reichardt polarity parameter for a given percentage of 1,4-dioxane in water (***Figure 29a,c,e***). From these clear trends emerge with pure dioxane and dioxane:water 9:1 being outliers (as discussed above). Interestingly, fitting of the data into a linear trend (after discarding 1,4-dioxane/water (10:0) and (9:1) mixtures - ***Figure 29b,d,f***) revealed decreasing values of slopes for the compounds in the following order: **HCy-OMe**> **HCy-NEt$_2$** > **HCy-Jul**. In addition, when investigated more closely, **HCy-OMe** fit could be separated into two linear fits one for data for dioxane/water ratios of 8:2 to 6:4 and then the other from 1:1 to pure water. These biphasic fit is not as clear for other two compounds potentially indicating a presence of more pronounced additional fluorescence mechanism in **HCy-OMe** but not in chemically more similar **HCy-NEt$_2$** and **HCy-Jul**.

Moreover, only **HCy-OMe** presented a significant hypsochromic shift of the emission spectra (from 535 to 505 nm, for 1,4-dioxane/water (9:1) to (0:10), respectively) with other two exhibiting virtually no change in the wavelength of emission maximum (**HCy-NEt$_2$** only a 5 nm hypsochromic shift from 40 to 30 % of 1,4-dioxane in water). These distinct behaviours suggest that polarity sensitivity is highly dependent on the specific substituents.

Table 4. **HCy-OMe** (5 μM) in various glycerol/water solutions of different ratios (10:0, 9:1, 8:2, 7:3, 6:4, 1:1, 4:6, 3:7, 2:8, 1:9, 0:10) with a final 1% DMSO. The blank samples consisted in the corresponding solution of glycerol/water or 1,4-dioxane/water of a given ratio with the same final %DMSO. λ_{em} - maximum of emission for a chosen glycerol/water mixture; $\lambda_{em\text{-}max}$ – maximum of emission spectrum value in a chosen glycerol/water mixture; Integrated I_{em} – sum of emission given in a chosen glycerol/water mixture; Relative integrated I_{em} – sum of emission given in a chosen solvent or buffer, where values were normalized to the highest value (for glycerol/water mixture 80:20). N = 3

Dioxane % in water	Polarity $E_T(30)$ [135] [kcal mol^{-1}]	Relative polarity E_T^N [136]	**HCy-OMe** λ_{em} [nm]	**HCy-OMe** Integrated I_{em}	**HCy-OMe** Relative integrated I_{em}
100	37.1	0.197	485	56948	0.16
90	40.2	0.293	535	257771	0.73
80	46.0	0.472	530	351513	1.00
70	46.6	0.490	530	307252	0.87
60	47.3	0.513	530	279642	0.80
50	48.1	0.538	530	280932	0.80
40	49.5	0.580	530	266053	0.76
30	51.1	0.629	530	249805	0.71
20	53.5	0.705	505	235165	0.67
10	57.1	0.815	530	201433	0.57
0	62.5	0.982	505	172210	0.49

Table 5. **HCy-NEt$_2$** (2.5 µM) and **HCy-Jul** (2.5 µM) in various 1,4-dioxane/water solutions of different ratios (10:0, 9:1, 8:2, 7:3, 6:4, 1:1, 4:6, 3:7, 2:8, 1:9, 0:10) with a final 1% DMSO. The blank samples consisted in the corresponding solution of 1,4-dioxane/water of a given ratio with the same final %DMSO. λ_{em} - maximum of emission for a chosen glycerol/water mixture; $\lambda_{em\text{-}max}$ – maximum of emission spectrum value in a chosen glycerol/water mixture; Integrated I_{em} – sum of emission given in a chosen glycerol/water mixture; Relative integrated I_{em} – sum of emission given in a chosen solvent or buffer, where values were normalized to the highest value (for glycerol/water mixture (80:20) for **HCy-NEt$_2$**, and (10:0) for **HCy-Jul**). N = 3

Dioxane % in water	Polarity $E_T(30)$ [135] [kcal/mol]	**HCy-NEt$_2$** $\lambda_{em,max}$ [nm]	**HCy-NEt$_2$** Integrated I_{em}	**HCy-NEt$_2$** Relative integrated I_{em}	**HCy-Jul** $\lambda_{em,max}$ [nm]	**HCy-Jul** Integrated I_{em}	**HCy-Jul** Relative integrated I_{em}
100	37.1	600	10705	0.19	620	8936	0.28
90	40.2	600	55735	0.99	620	31677	0.99
80	46.0	600	56564	1.00	620	30853	0.96
70	46.6	600	55650	0.98	620	30446	0.95
60	47.3	600	56041	0.99	620	32042	1.00
50	48.1	600	52623	0.93	620	29743	0.93
40	49.5	600	51433	0.91	620	30287	0.95
30	51.1	595	45965	0.81	620	28294	0.88
20	53.5	595	38916	0.69	620	26174	0.82
10	57.1	595	31202	0.55	620	22369	0.70
0	62.5	595	19100	0.34	620	17286	0.54

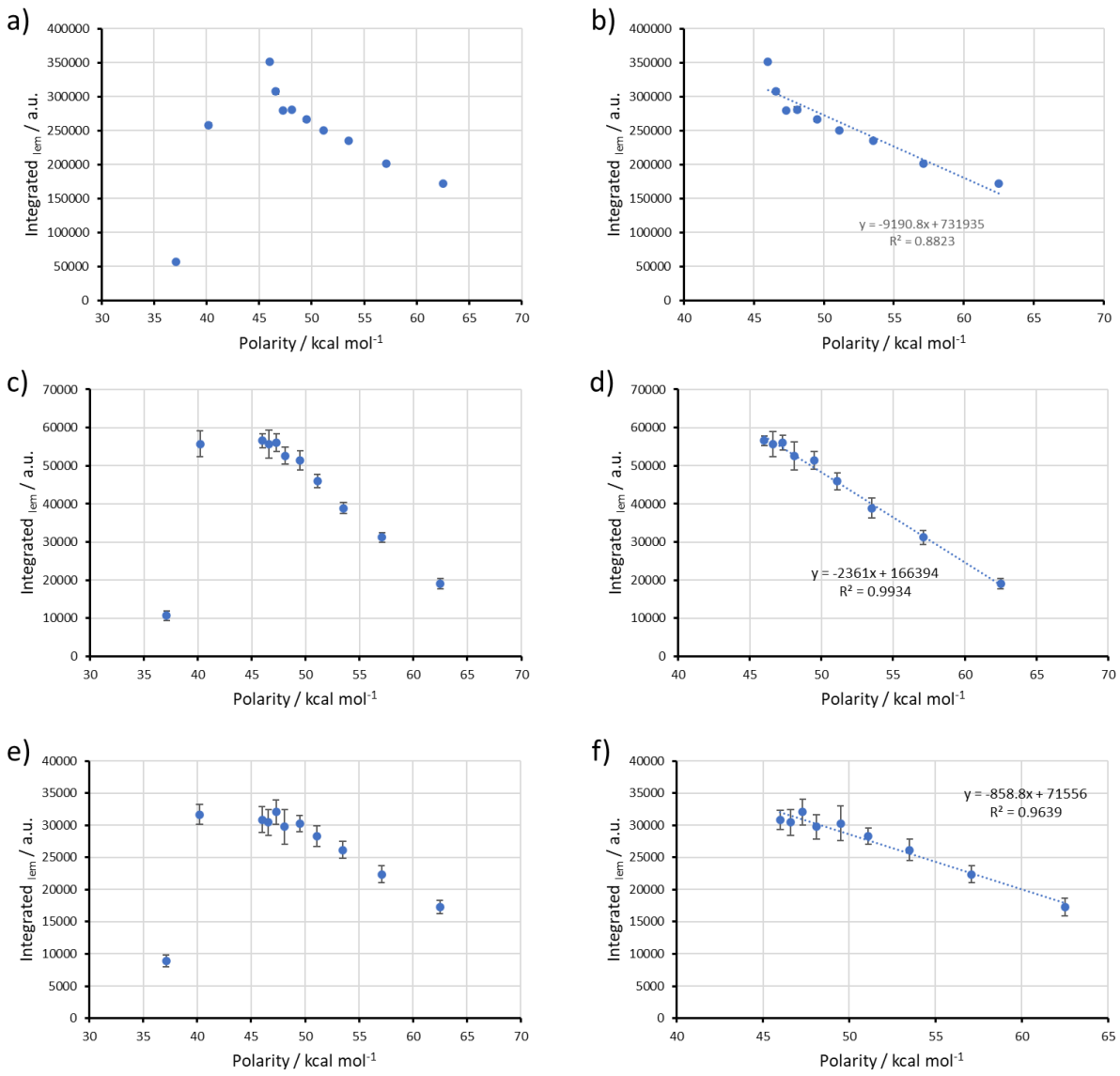

***Figure 29**. Plots of the integrated intensity (sum) of the fluorescence emission as a function of the polarity for 1,4-dioxane/water mixtures) of (a,b) **HCy-OMe** (5 µM), (b,c) **HCy-NEt₂** (2.5 µM), (e,f) **HCy-Jul** (2.5 µM). (b,d,f) Linear fitting was carried out after discarding mixtures 1,4-dioxane/water (10:0) and (9:1). N = 3*

3.2.3.5. Fluorescence in cell culture media

Considering that these hemicyanine derivatives are intended for the development of fluorescent probes in cellular models, their stability in cell culture media is relevant. The most common procedures of cell treatment with fluorescent probes involve the following main steps: probe addition (in cell growth medium containing no more than 1% DMSO), incubation (optimal exposure time should be determined), rinsing (to get rid of the excess of probe and of any

interferents found in the cell culture medium), and addition of cell culture medium suitable for live cell imaging. For many mammalian adherent cell lines, Dulbecco's Modified Eagle's Medium (DMEM) High Glucose supplemented with Fetal Bovine Serum (FBS) is used as cell growth medium [137]. The main components of this cell medium include aminoacids, vitamins, and inorganic salts. Hence, cell medium incorporates potential interferents that may affect the probe's integrity and compromise the fluorescence response in case the probe is not stable enough. However, this medium is known to present high autofluorescence background given its composition (mainly due to FBS and phenol red indicator), which would lead to a high fluorophore signal-to-noise ratio – undesirable for cell imaging. [138] This the main reason why fluorescence confocal live cell imaging is most commonly carried out in FluoroBrite™, a special cell culture medium based on DMEM formulation, which is known for its minimal fluorescent output and no light scattering, as it does not contain any interfering components, but still possesses the required nutrients for long-term cell health. [138] However, the autofluorescence arising from the medium components can be minimised by using fluorescent probes that would get excited and emit at long wavelengths. Therefore, the fluorescent signal stability of the HCy derivatives was studied in regular supplemented DMEM High Glucose and in FluoroBrite™, as one would be the medium in which the probe will be dissolved for cell treatment, and the other the one in which cell imaging would be performed, respectively.

Fluorescence spectroscopic studies of **HCy-OMe**, **HCy-NEt$_2$**, and **HCy-Jul** in supplemented DMEM High Glucose with phenol red pH indicator and in analogous Fluorobrite™ medium (***Figure 31***). The measurements of fluorescence intensities were taken at different time points after the addition of the corresponding hemicyanine derivative (0 min, 15 min, 1 h, 6 h, 24 h). **HCy-OMe**'s stability could not be tested in supplemented DMEM as it presents an absorbance in the same region as phenol red indicator present in the cell medium. Interestingly, no significant loss of signal intensity could be observed within the first 15 min of exposure to the cell media. Nevertheless, in Fluorobrite™ medium **HCy-OMe** signal quenching appeared already 1h after exposure and was the most significant of all three dyes after 1h, with fluorescence being largely totally quenched within 24h of the media exposure (if compared with control of the medium with 1% DMSO final – ***Figure 30 e***). **HCy-Jul**, on the other hand, presents generally the highest stability

of fluorescent signal throughout, with particularly significant difference at 1 and 6h timepoints where no significant decrease in **HCy-Jul** is detected ***Figure 30a,c*** while HCy-NEt_2 shows more significant depletion already at 1h and onwards ***Figure 30b,d***. The perturbance of the fluorescence output signal may arise from the components of the cell growth medium, in particular inorganic salts and aminoacids (which can contain potentially nucleophilic groups). For instance, nucleophilic aminoacids such as lysine[139,140] and the reduced form of cystine (cysteine)[141,142], which present an amino and a thiol group, respectively.

This is of importance since confocal imaging experiments of a well within a 4-compartment dish performed in this dissertation take no longer than 1.5 h each. As long as the derivatives' fluorescence emission will remain unperturbed within the time frame of the experiment, they can be considered a good scaffold for the development of fluorescent probes.

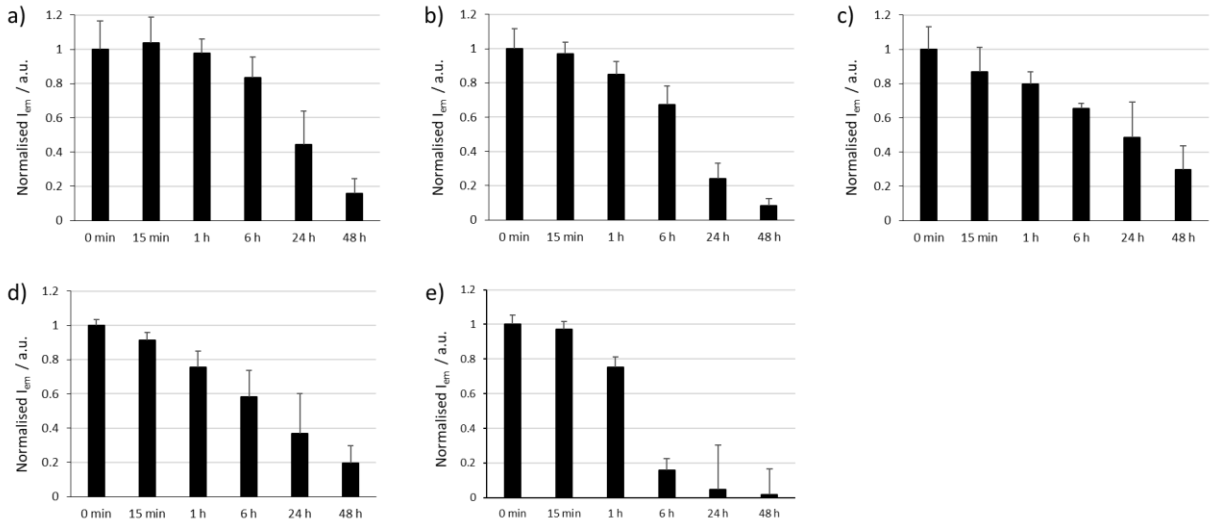

Figure 30*. Normalised fluorescence emission of (a,c)* ***HCy-Jul*** *(2.5 µM), (b,d)* ***HCy-NEt₂*** *(2.5 µM), (e)* ***HCy-OMe*** *(5 µM) in (a-b) supplemented cell medium (DMEM High Glucose with 10% Fetal Bovine Serum, 1% penicillin-streptomycin) and in (c-e) Fluorobrite™ with a final 1% DMSO at different time points: 0 min, 15 min, 1 h, 6 h, 24 h, 48 h. The blank sample contained the same final %DMSO. Emission spectra were collected at λ_{exc} = 430 nm, λ_{em} = 490-700 nm for* ***HCy-OMe****, and λ_{exc} = 530 nm, λ_{em} = 560-700 nm for* ***HCy-NEt₂*** *and* ***HCy-Jul****. The output values at the maximum of fluorescence emission intensity ($\lambda_{exc/em}$ = (430/535) nm for* ***HCy-OMe****; $\lambda_{exc/em}$ = (530/600) nm for* ***HCy- NEt₂****; $\lambda_{exc/em}$ = (530/620) nm for* ***HCy-Jul****) were normalized to the value given at time 0 min of the corresponding HCy derivative. N = 3*

3.2.3.6. Fluorescence In the presence of inorganic salts

Taking into consideration the above results of the hemicyanine derivatives in cell media and that the composition of DMEM medium consists of several inorganic salts, fluorescence signal output was studied against several metal salts. The inorganic salts present in DMEM medium are comprised of Ca^{2+}, Fe^{3+}, K^{+}, Mg^{2+}, and Na^{+} as metal cations and chlorides, nitrates, and sulphates as the main counterions. [137]

For that reason, the hemicyanine derivatives were tested in the presence of 2.5 and 25 µM (higher concentration than that present in cell medium) of inorganic salts in MilliQ water (1% DMSO final). The selected salts included biologically relevant metal ions (Ca^{2+}, Co^{2+}, Cu^{+}, Cu^{2+}, Fe^{2+}, Fe^{3+}, K^{+}, Mg^{2+}, Na^{+}, Ni^{2+}), including the ones found in the formulation, and in the case of the anions, and depending on salts availability and solubility, three different counterions were present among tested compounds, that possess also biological significance (Cl^{-}, NO_3^{-}, SO_4^{2-}).

HCy-OMe derivative was tested despite being weakly fluorescent in these conditions, which gave rise to considerable error bars, as its fluorescence intensity was almost as low as the blank sample (MilliQ water with 1% DMSO final). Nevertheless, none of the three compounds presented any significant differences in fluorescence emission signal in the presence of these metal ion salts at time points of 0 and 1 h after exposure (***Figure 31***). This is likely due to the fact that tested dyes do not contain any moieties that would exhibit significant metal ion binding and/or complexation. This outcome ensures that the fluorescent signal from tested dyes in biological systems would not be disturbed by fluctuations in metal ion concentrations.

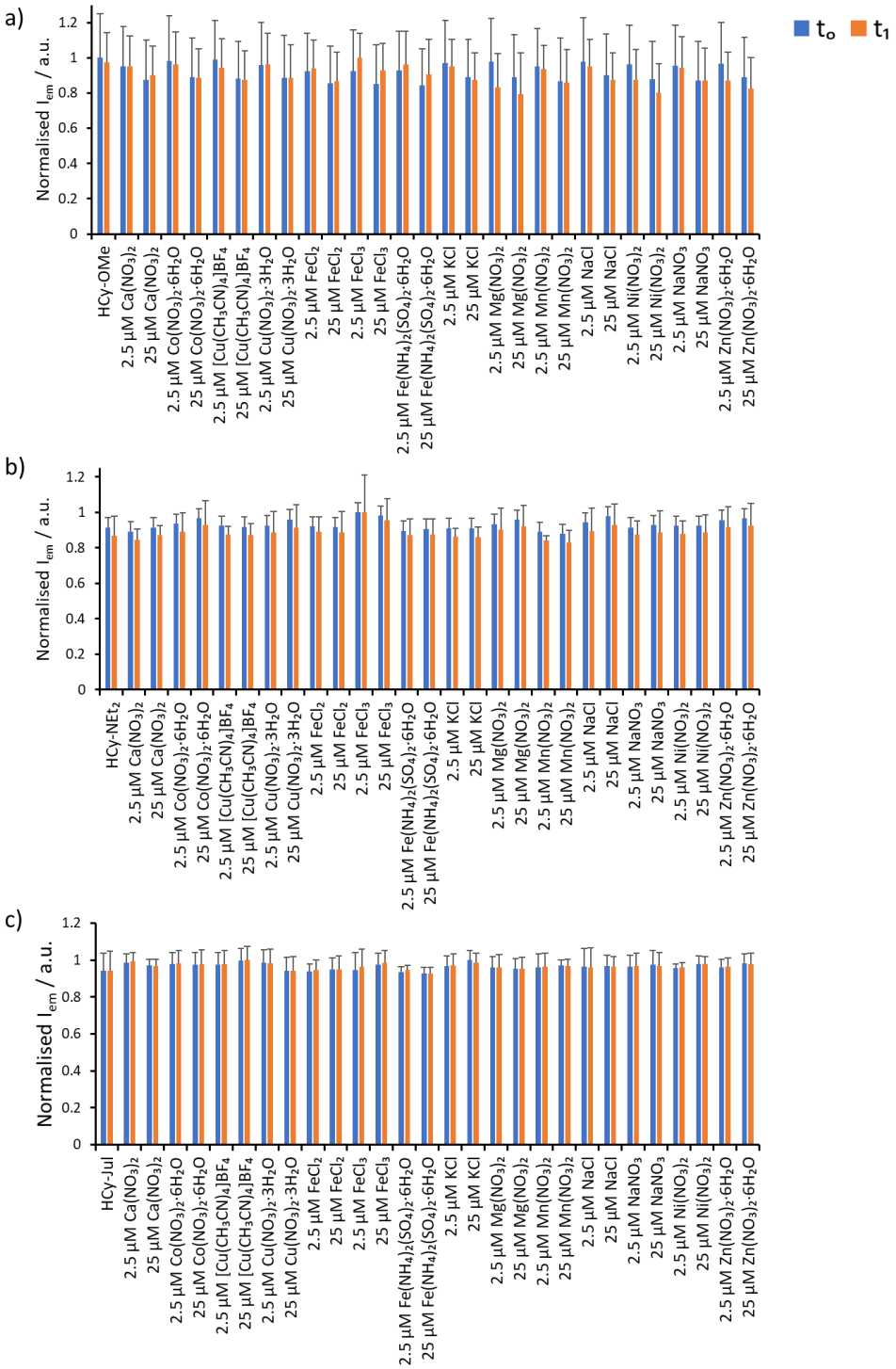

Figure 31. *Normalised fluorescence emission of (a)* ***HCy-OMe*** *(2.5 µM), (b) HCy-NEt₂, (2.5 µM), (b)* ***HCy-JuI*** *(2.5 µM) in the absence (column referred as* ***HCy-OMe****, HCy-NEt₂, and* ***HCy-JuI*** *in the corresponding plot) and presence of either 2.5 µM or 25 µM of metal ion salts at 0 min (t_0; blue columns) and 1 h (t_1; orange columns) timepoints after exposure. $\lambda_{exc/em}$ **HCy-OMe** = 490/530; $\lambda_{exc/em}$ HCy-NEt2 = 550/600; $\lambda_{exc/em}$ **HCy-JuI** = 550/615. N = 3*

3.2.3.7. Summary

A wide array of experiments were carried out testing spectral properties of the derivatives in different buffers, polarity, viscosity and against metal ion interferents, in order to perform a reliable assessment of their fluorescent signal stability. All derivatives presented a fluorescence emission that would be dependent on the polarity and viscosity of the environment, which behaviour correlates to hemicyanine-based probes published in the literature[6,7,44,134]. Considering firstly **HCy-OMe**, this derivative presents the lowest fluorescence emission intensity and lowest stability in all the studied conditions and thus, this scaffold was concluded unsuitable for probe development. When it comes to **HCy-NEt$_2$**, an extensively used scaffold for fluorescent probe development, it presented an adequate stability and it possessed the highest QY and brightness in DMSO out of all derivatives. However, **HCy-Jul**, while presenting a lower QY, it also presents a remarkable fluorescent signal output stability, and shows a somewhat superior performance in the cell culture media tested. Importantly, **HCy-Jul**'s integrity in cell culture media would not be a concern even if imaging process would take place for longer live-cell imaging studies than the ones carried out in this thesis (approximately 1-1.5 h duration).

Given the results above, **HCy-OMe**, **HCy-NEt$_2$** and **HCy-Jul** scaffolds have been progressed to further testing against variable nucleophiles to verify whether new substitution pattern of **HCy-Jul** would further prove to be more robust than the two previously reported ones.

3.2.3.8. Future directions and potential applications

The synthesis and characterisation of these hemicyanine derivatives provides valuable insights for potential application and future developments:

- The tunable spectral properties through structural modifications offer opportunities for developing a palette of fluorescent probes with distinct emission wavelengths.
- The viscosity and polarity sensitivity of these compounds could be exploited for studying specific cellular compartments or during cellular events.

- The stability of **HCy-Jul** in cell culture media makes it a promising candidate for extended live-cell imaging studies. Further investigation into the structural features contributing to this stability could guide the design of even more robust fluorescent probes.

3.2.4. Stability against nucleophiles

A critical aspect in the development of robust hemicyanine probes is the assessment of their stability in the presence of nucleophiles. The reliability and efficacy of these probes in biological systems are contingent upon their ability to withstand nucleophilic attack, which could lead to undesired reactivity and compromise their performance. The results of the experiments performed above suggest already that the stability of the hemicyanines in different media can be compromised and that this might potentially be caused, among others, by the susceptibility to nucleophiles. This hypothesis is also supported by previous literature reports that looked into the detailed mechanisms of the nucleophilic addition to hemicyanines and even explored that susceptibility for sensing nucleophiles of biological significance. [52,114,115] Therefore, this section aims at investigating this susceptibility and presents the stability studies conducted on the abovementioned hemicyanine derivatives, using Nuclear Magnetic Resonance (for more structural / mechanistic information) and fluorescence spectroscopy (for more biologically-relevant validation).

3.2.4.1. Stability of dye scaffolds against nucleophiles by NMR spectroscopy

The hemicyanine derivatives were tested against model nucleophiles and their corresponding NMR spectroscopic characterisation was done using a main methodology previously published [114] as a baseline reference for my investigation. ^{1}H, COSY, HMBC, HSQC, ^{13}C NMR spectra obtained during the titration of these derivatives were analysed in hope that they would allow the determination of their stability and their potential resilience in biological context.

In particular, the three hemicyanines were exposed to model nucleophiles cyanide (CN^-) and methanethiolate (CH_3S^-) for 1,2-addition and 1,4-addition, respectively. Given the HSAB theory, one would expect that a soft nucleophile/Lewis base such as a sulphur-based anion (MeS^-) would attack the alkene part – the soft electrophile/Lewis acid. As for cyanide, although it is a borderline

nucleophile (neither a classical hard nor soft Lewis base), it has been empirically proved that it preferentially attacks the charged iminium ion. [52,114,115]

The nucleophilic addition of cyanide to hemicyanine derivatives **HCy-OMe**, **HCy-NEt$_2$**, **HCy-Jul** was studied and the site of addition in all derivatives was confirmed by HMBC spectra in DMSO-d_6/D_2O (80:20). The mode of nucleophilic addition of to all HC derivatives was confirmed to give the corresponding 1,2-adduct. In ^{1}H NMR the disruption of aromaticity in the **HCy-OMe** adduct can be observed through the general upfield shifts due to the increasing shielding of the unsaturated protons (***Figure 32a***) and HMBC shows the correlation between the alkene proton and the carbon atom in cyanide (***Figure 32b***). The same position of addition has been observed for two other hemicyanines and the respective NMR spectra of these dyes upon the addition of CN^- can be found in the Appendix (subchapter 6.1.2.). Such results confirm previously reported mode of addition in the literature[52,114,115].

The experiments with methanethiolate (1 eq) were performed to investigate the position of addition. In case of **HCy-OMe**, the formation of 1,4-adduct was elucidated from ^{1}H NMR spectra in DMSO-d_6/D_2O (80:20) solvent (***Figure 33a***) based on the general upfield shifts pointing and the disturbance of the π-π conjugated system of the molecule. The HMBC spectra (***Figure 33b***) revealed a correlation (coupling through 4- bonds) between the methine carbon atom in HC and the H_3CS protons. Such results are in accordance to previously nucleophilic addition studies [109]. As for **HCy-NEt$_2$** and **HCy-Jul**, a typical 1,4-addition of CH_3S^- was not observed (***Figure 34***). Therefore, it could be speculated that both **HCy-NEt$_2$** and **HCy-Jul** indeed display a higher stability against sulphur-based nucleophiles possibly thanks to the nature of their substituents.

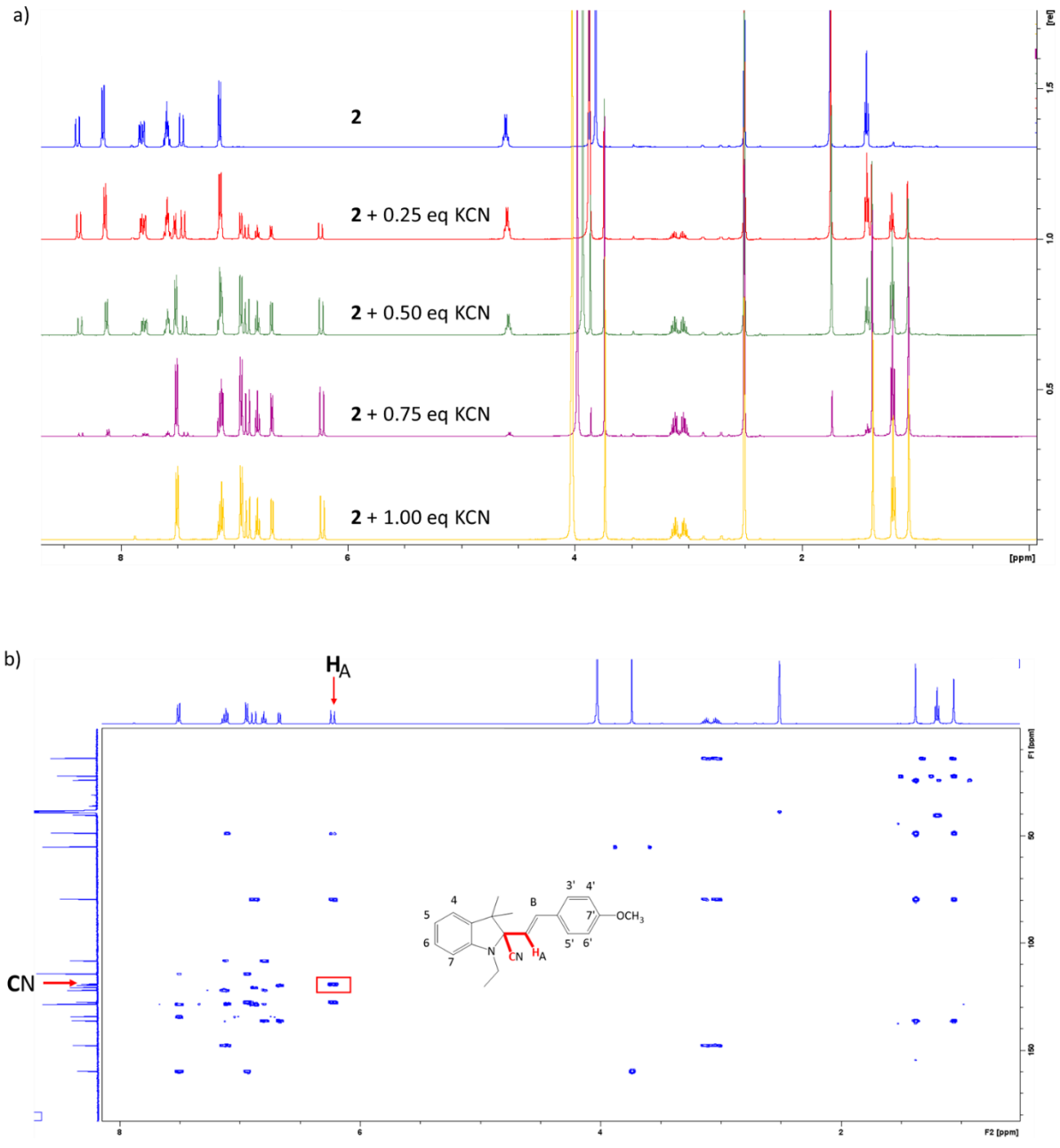

***Figure 32**. (a) [1]H NMR spectra of **HCy-OMe** (**2**) titration with 0 eq (blue), 0.25 eq (red), 0.50 eq (green), 0.75 eq (purple), 1 eq (yellow) of CN^-. To solutions of **2** (0.0125 mmol) in DMSO-d_6/D_2O (85:15) (500 µL) in NMR tubes was added a solution of sodium methanethiolate (0.25 M in D_2O). Additions were made in 0.25 eq increments (i.e. 12.5 µL of 0.25 M solution, 0.00313 mmol) up to 1 eq total (with a final 20% D_2O), allowing 30 minutes between additions. (b) HMBC NMR spectrum of 1,2-adduct of compound **2** formed upon reaction of 1 eq of KCN in DMSO-d_6/D_2O (80:20).*

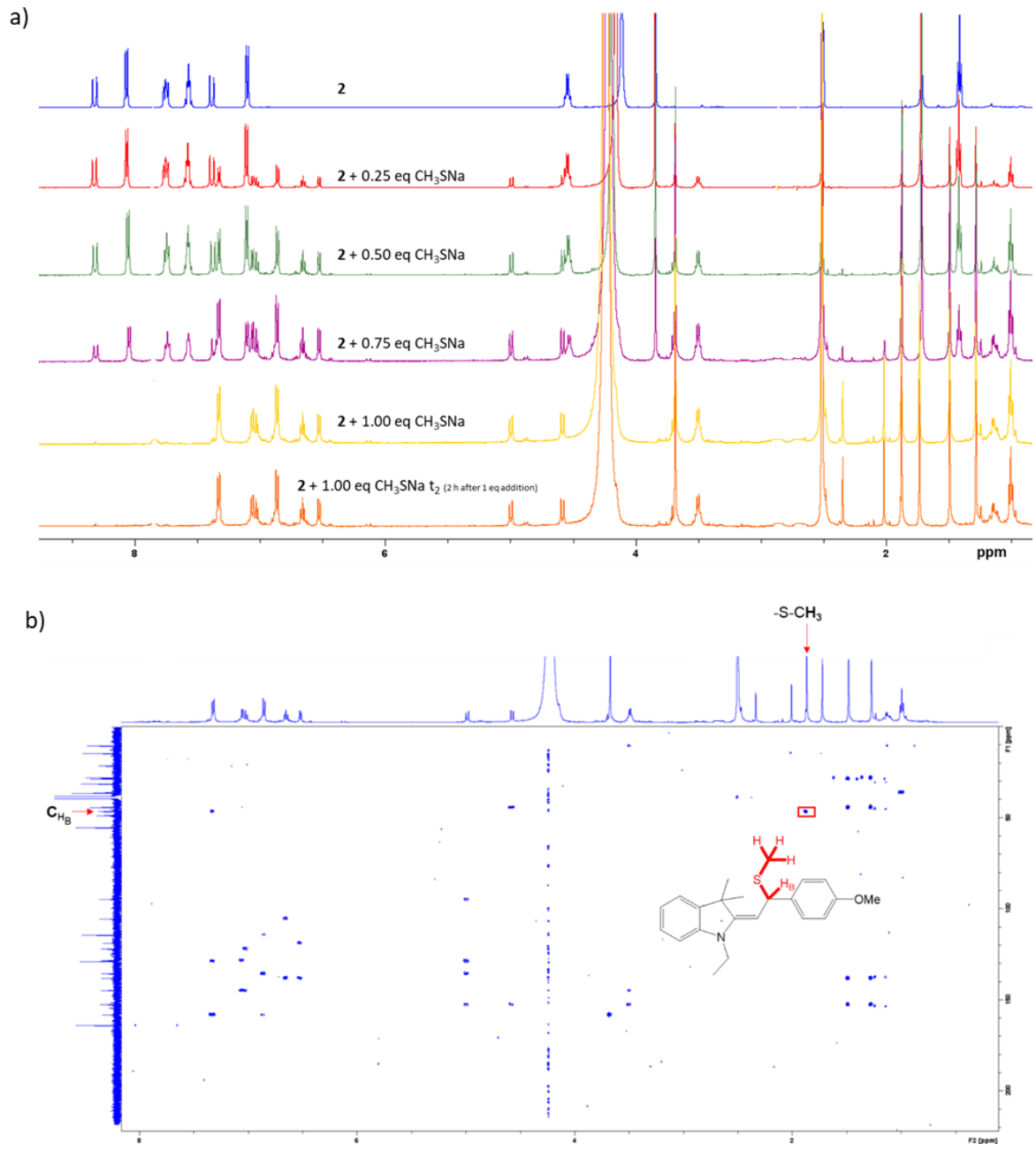

Figure 33. *(a) ^{1}H NMR spectra of **HCy-OMe** (**2**) titration with 0 eq (blue), 0.25 eq (red), 0.50 eq (green), 0.75 eq (purple), 1 eq (0 min, yellow; 2 h, orange) of CH_3S. To solutions of **2** (0.0125 mmol) in DMSO-d_6/D_2O (85:15) (500 µL) in NMR tubes was added a solution of sodium methanethiolate (0.25 M in D_2O). Additions were made in 0.25 eq increments (i.e. 12.5 µL of 0.25 M solution, 0.00313 mmol) up to 1 eq total (with a final 20% D_2O), allowing 30 minutes between additions. (b) HMBC NMR spectrum of 1,2-adduct of compound **2** formed upon reaction of 1 eq of CH_3SNa in DMSO-d_6/D_2O (80:20).*

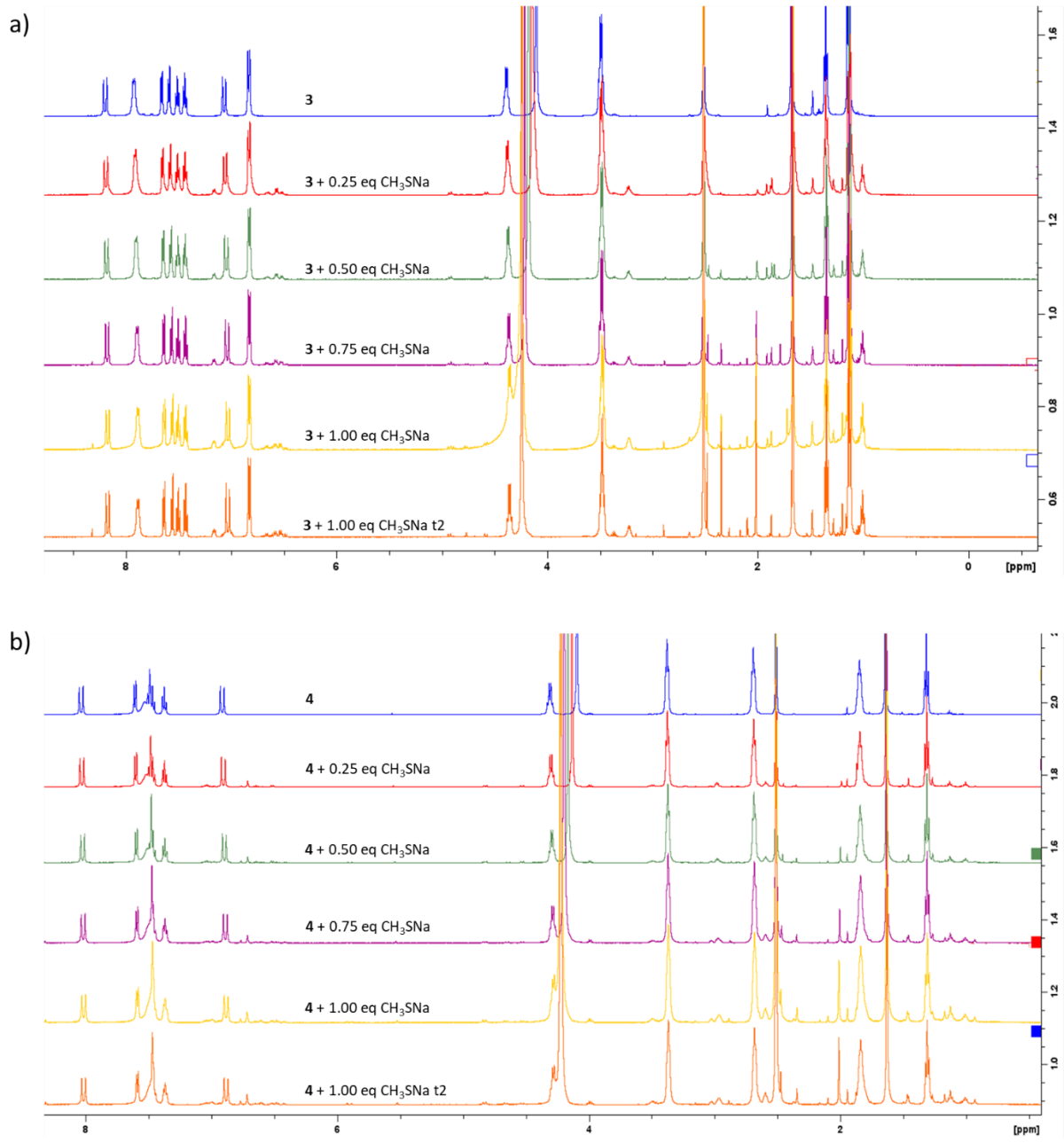

Figure 34. *^{1}H NMR spectra of (a) **HCy-NEt$_2$** (**3**) and (b) **HCy-Jul** (**4**) titration with 0 eq (blue), 0.25 eq (red), 0.50 eq (green), 0.75 eq (purple), 1 eq (0 min, yellow; 2 h, orange) of CH_3S. To solutions of **2** or **4** (0.0125 mmol) in DMSO-d_6/D_2O (85:15) (500 µL) in NMR tubes was added a solution of sodium methanethiolate (0.25 M in D_2O). Additions were made in 0.25 eq increments (i.e. 12.5 µL of 0.25 M solution, 0.00313 mmol) up to 1 eq total (with a final 20% D_2O), allowing 30 minutes between additions.*

Finally, the susceptibility of tested dyes towards glutathione (GSH), common biological nucleophile, was then studied in DMSO-d_6/D_2O (80:20). For **HCy-OMe** and **HCy-NEt$_2$**, ^{1}H NMR revealed that a signal from H_A proton is no longer present and H_B becomes a singlet (***Figure 35a***

and ***35b***, respectively). As all other signals have not been changed, rather than deprotonation, an intermolecular interaction (maybe of a H-bonding type) could instead lead to a more efficient nuclear spin relaxation of H_A upon interaction with GSH, leading to its disappearance from the spectrum. In the case of **HCy-Jul**, the signals from H_A and H_B remain unperturbed throughout the treatment (***Figure 35c***).

Nevertheless, it is important to note that in the selected experimental conditions, GSH addition to the hemicyanine core of the derivatives could not be confirmed by HMBC analysis as no correlation between the $H_2C_\beta S$ protons from cysteine aminoacid (potential stronger nucleophile in GSH) and the methine C atom in HC could be found for any of the derivatives. Thus, the interaction between the derivatives and GSH remained inconclusive in these conditions.

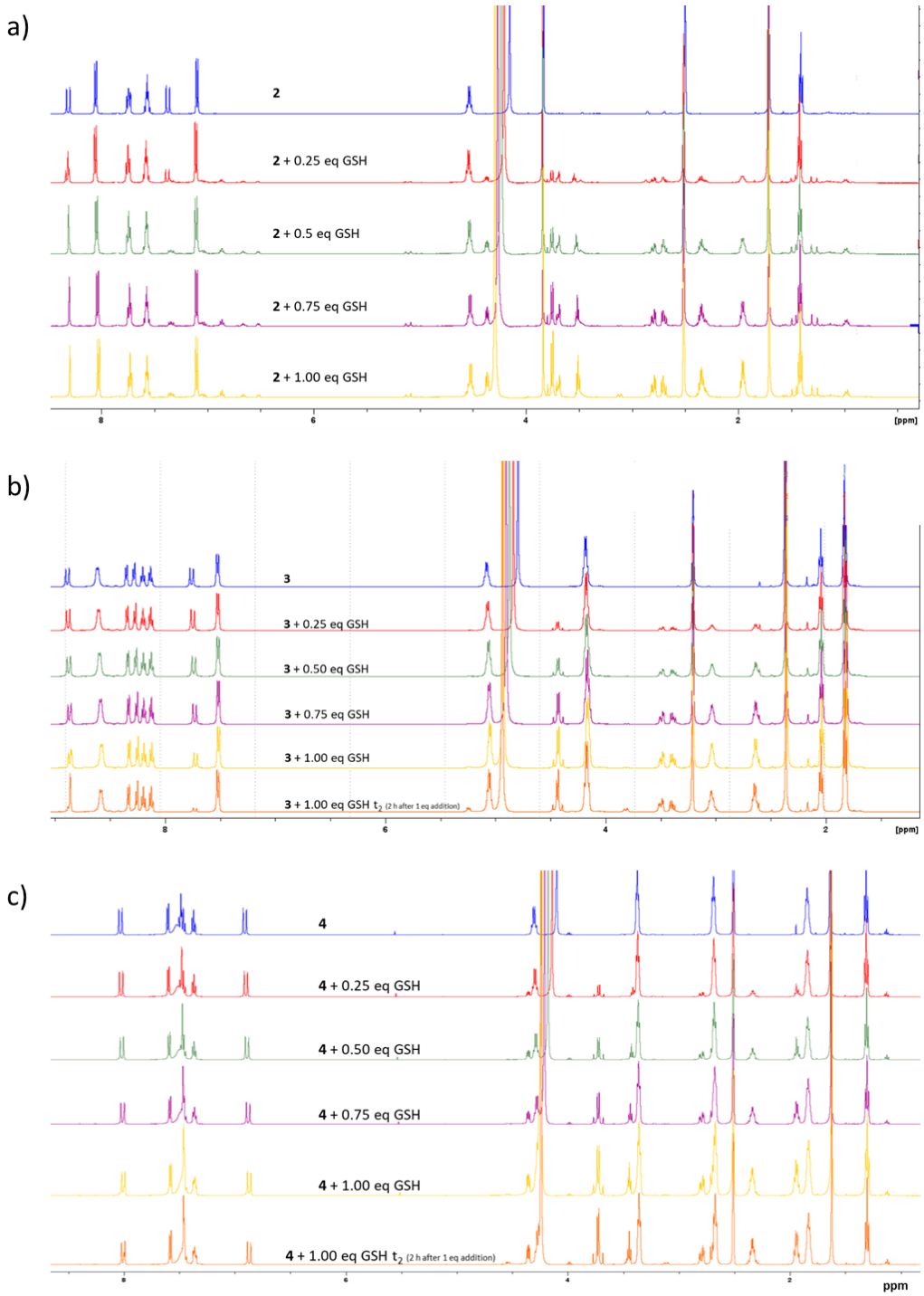

Figure 35. *^{1}H NMR spectra of (a)* ***HCy-OMe*** *(**2**), (b)* ***HCy-NEt$_2$*** *(**3**), and (c)* ***HCy-Jul*** *(**4**) titration with 0 eq (blue), 0.25 eq (red), 0.50 eq (green), 0.75 eq (purple), 1 eq (0 min, yellow; 2 h, orange) of GSH. To a solution of hemicyanine derivative (0.0125 mmol) in DMSO-d$_6$/D$_2$O (85:15) (500 µL) in NMR tubes were added a solution of glutathione (0.25 M in D$_2$O). Additions were made in 0.25 eq increments (i.e. 12.5 µL of 0.25 M solution, 0.00313 mmol) up to 1 eq total (with a final 20% D$_2$O), allowing 30 minutes between additions.*

3.2.4.2. Stability of dye scaffolds against nucleophiles by NMR spectroscopy

After investigating the pathways of nucleophilic addition and/or interaction via NMR spectroscopic studies with the model nucleophiles, I proceeded to compare these results to fluorescence emission data obtained by analogous nucleophile treatment but in buffered solutions better representing biologically-relevant media (DMSO/HEPES mixture instead of DMSO/water ones used for NMR investigations). First of all, the stability of **HCy-OMe**, **HCy-NEt$_2$**, and **HCy-Jul** fluorescent signal was studied in DMSO/HEPES (80:20 with HEPES at final 100 mM concentration) at different pH values (***Figure 36***), as HEPES itself could most likely act as a nucleophile (given population of the deprotonated form would be higher [143]). Interestingly, these experiments revealed that with increasing pH of the buffer, signal intensities decreased most significantly for **HCy-OMe** (blue bars in ***Figure 36***), with **HCy-NEt$_2$** and **HCy-Jul** being relatively similar and stable even at pH 9. Slight but not statistically significant decrease in the signal of **HCy-Et$_2$** vs **HCy-Jul** at pH 8 could be observed and the decrease was to the level that has been observed for **HCy-Jul** only at pH 9.

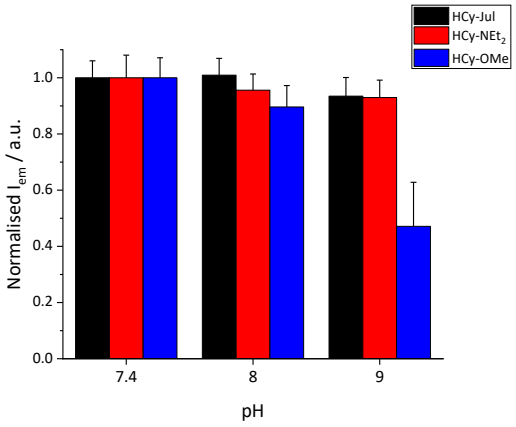

***Figure 36**. Fluorescence studies of **HCy-Jul** (black column), **HCy-NEt$_2$** (red column), and **HCy-OMe** (blue column) in DMSO/HEPES (80:20) with pH values of 7.4, 8, 9. $\lambda_{exc/em}$ **HCy-OMe** = 430/530; $\lambda_{exc/em}$ HCy-NEt2 = 550/600; $\lambda_{exc/em}$ **HCy-Jul** = 550/615.*

Subsequently, I have proceeded to investigate the addition of exogenous nucleophiles to the DMSO/HEPES media. Evaluation of cyanide addition effects on fluorescence of the derivatives was performed in buffered solutions (DMSO/HEPES 80:20, at pH 7.4) at different time points. Fluorescence emission of **HCy-OMe** (5 µM) in such conditions was fully quenched upon cyanide

treatment (25 µM) even after 15 minutes of exposure (***Figure 37a***, blue bars). When comparing **HCy-NEt$_2$** and **HCy-Jul** fluorescence for untreated solutions (full bars in Figure 35a – concentration of dyes at 2.5 µM) and treated with cyanide (25 µM – ***Figure 37a***, dashed bars) little to no effect was observed with **HCy-Jul**, while **HCy-NEt$_2$** fluorescence was quenched already at 15 min post exposure, with the effect plateauing at approx. 35-40% quenching at 45 min mark. When additional equivalents of cyanide are used (100 eq – 250 µM, with respect to **HCy-NEt$_2$** and **HCy-Jul**) for the treatment of **HCy-NEt$_2$** and **HCy-Jul**, the same tendency can be noted (Fig 35b) although with somewhat more visible quenching of **HCy-Jul** fluorescence (to approx. 80% of initial fluorescence by 2 h mark – ***Figure 37b*** – black bars) and still stronger quenching for **HCy-NEt$_2$** (about 60% of residual fluorescence at 1 h mark – ***Figure 37b*** red bars). Detailed analysis of absorbance and fluorescence spectra of the dyes (full set available in the appendix in subchapter 6.3.) in the presence of cyanide anions revealed an appearance of the new band in absorbance spectrum at shorter wavelengths for both **HCy-OMe** and **HCy-NEt$_2$**, indication interruption of aromaticity. No such change could be observed for **HCy-Jul** spectrum confirming the hypothesis that **HCy-Jul** presents the most stable fluorescent output signal, followed by **HCy-NEt$_2$**, and **HCy-OMe**.

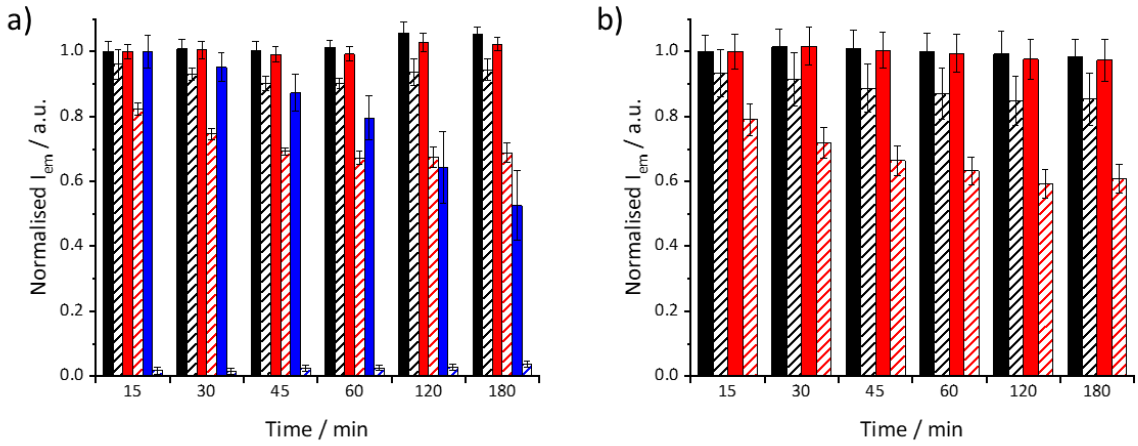

Figure 37*. Fluorescence studies of hemicyanine derivatives and their treatment with cyanide (a) 25 µM and (b) 250 µM in DMSO/HEPES (80:20) with a pH value of 7.4 at different timepoints. Normalised fluorescence emission of* ***HCy-Jul*** *untreated (black columns) and treated (dashed black columns);* ***HCy-NEt$_2$*** *untreated (red columns) and treated (dashed red columns);* ***HCy-OMe*** *untreated (blue columns), and treated (dashed blue columns).* $\lambda_{exc/em}$ ***HCy-OMe*** *= 430/530;* $\lambda_{exc/em}$ *HCy-NEt2 = 550/600;* $\lambda_{exc/em}$ ***HCy-Jul*** *= 550/615.*

In attempt to further investigate the stability of hemicyanine derivatives against biologically relevant GSH, fluorescence spectroscopic measurements were performed, as GSH NMR titrations were inconclusive. Fluorescence measurements of the derivatives in the absence and presence of GSH (2 mM – biologically relevant intracellular concentrations) were performed at different pH values and at several timepoints (***Figure 38***). **HCy-OMe** fluorescence emission was already perturbed at pH 7.4 in the presence of GSH (Figure 36a) even at 3 min mark, and the quenching was near complete at higher pH. **HCy-NEt$_2$** showed slight quenching of the fluorescent signal throughout all pH values, but it became particularly apparent at pH 9 (Figure 36 c – residual fluorescence intensity of approx. 40% at 1h mark onwards). This pH-enhanced quenching might result from a stronger nucleophilic character of unprotonated GSH that is more abundant at higher pH. However, a contribution from HEPES buffer itself that also reveals higher nucleophilicity at higher pH cannot be excluded [143]. **HCy-Jul** only showed slight quenching of signal at pH 9 (***Figure 38c***), confirming the hypothesis that indeed stronger EDG in the phenyl ring confers higher stability and additionally, the particular substitution pattern of **HCy-Jul** is sufficient to ensure stability in these conditions that mimic biological media. Additional absorbance and fluorescence spectra can be found in the appendix in subchapter 6.3.

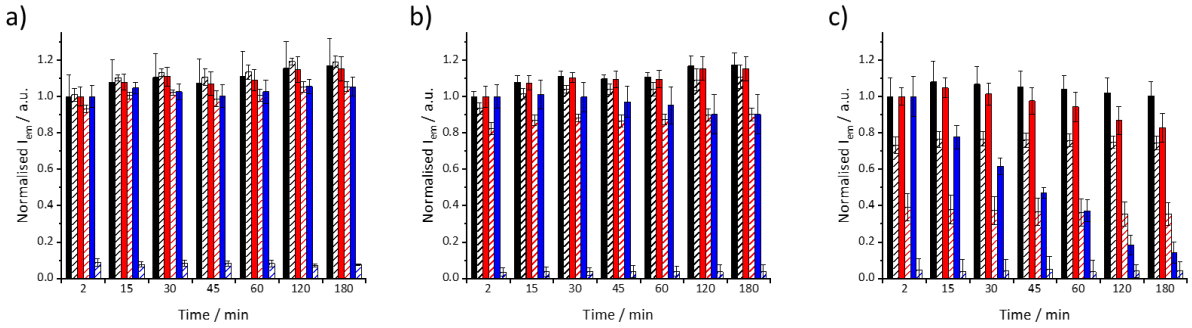

***Figure 38**. Fluorescence studies of hemicyanine derivatives and their treatment with GSH (2 mM) in DMSO/HEPES (80:20) with a pH value of (a) 7.4, (b) 8, (c) 9 at different timepoints. Normalised fluorescence emission of **HCy-Jul** untreated (black columns) and treated (dashed black columns); **HCy-NEt$_2$** untreated (red columns) and treated (dashed red columns); **HCy-OMe** untreated (blue columns), and treated (dashed blue columns). $\lambda_{exc/em}$ **HCy-OMe** = 430/530; $\lambda_{exc/em}$ HCy-NEt2 = 550/600; $\lambda_{exc/em}$ **HCy-Jul** = 550/615.*

3.2.4.3. Summary

Three hemicyanine derivatives with different substituents in *para* position were synthesised and their stability against nucleophiles was studied via two spectroscopic techniques. Generally, the derivatives display the following gradual order when it comes to enhanced stability against interferents: **HCy-OMe** < **HCy-NEt$_2$** < **HCy-Jul**.

Exposure of these derivatives to a few model nucleophiles was initially monitored by NMR spectroscopy and the site of nucleophilic addition after exposure with the model nucleophiles, as previously reported in literature. The mode of nucleophilic addition of CN^- to all HC derivatives was confirmed to give the corresponding 1,2-adduct. The formation of 1,4-adduct upon exposure to CH_3S^- was only confirmed for **HCy-OMe**, as it was not observed for neither **HCy-NEt$_2$** nor **HCy-Jul**. Hence, it could be speculated that they indeed display a higher stability.

Analysis of ^{1}H NMR spectra upon titration with GSH revealed that H_A proton signal is no longer present and H_B becomes a singlet only for **HCy-OMe** and **HCy-NEt$_2$** potentially due to an increased efficiency of spin relaxation of that proton as an effect of intermolecular interactions rather than covalent addition. In the case of **HCy-Jul**, the signals from H_A and H_B remain unperturbed throughout the treatment suggesting no such interaction (or less intense). No covalent addition of GSH addition to any of the three derivatives could be observed by HMBC spectra.

Further investigation of nucleophile susceptibility of the derivatives was performed using fluorescent spectroscopy. In solvent conditions analogous to those In NMR studies, but using HEPES buffer pH 9 (instead of deuterated water), a significant drop of fluorescence intensity of **HCy-OMe** was observed suggesting HEPES buffer acting as nucleophile (given population of the deprotonated form would be higher [143]). Subsequent exposure of the derivatives to exogenous nucleophiles confirmed the effects observed with NMR, revealing a decrease in fluorescence intensity for **HCy-OMe** and **HCy-NEt$_2$**, and an appearance of new band at shorter wavelengths of the absorbance spectra appeared. Interestingly, **HCy-Jul**'s fluorescence was not significantly perturbed.

Fluorescence measurements of the derivatives in the absence and presence of GSH (2 mM) at different pH revealed quenching of **HCy-OMe** fluorescence emission intensity already at pH 7.4, with the effect increasing with higher pH (possibly due to a stronger nucleophilic character of unprotonated GSH, more abundant at higher pH). **HCy-NEt$_2$** showed slight quenching of the fluorescent signal throughout all pH values, particularly at pH 9, potentially due to HEPES extra contribution as a nucleophile. Little to no quenching of **HCy-Jul** fluorescence (with only some at pH 9) confirmed the improved nucleophilic resistance of **HCy-Jul** and validated the hypothesis of the stabilising influence of designed substitution pattern, better suited for biological applications than commonly used **HCy-NEt$_2$** or **HCy-OMe**.

In summary, results confirmed that introduction of electron donating groups to the phenylic substituent increases the stability of the hemicyanine core. Moreover, **HCy-OMe** was not selected for cell studies considering its low stability and low fluorescence emission intensity. Therefore, from this section onwards, only **HCy-NEt$_2$** and **HCy-Jul** were continued to be tested in cellular models.

3.2.5. Cellular behaviour

To assess the performance and suitability of the hemicyanine derivatives for cellular applications, a series of fluorescence confocal imaging experiments and cell viability tests were conducted.

The selection of cell lines was done considering several factors: broad use in the literature, high growth rates, adherent growth, and epithelial morphology. Two representative cell lines were chosen: a disease-free one that would serve as a baseline (HEK239), and a cancer one that has also been previously used in studying effects of hypoxia (DU145). HEK239 (or HEK) originates from a human embryonic kidney[144,145] and DU145 from a metastatic site of human prostate carcinoma in the brain[146]. For fluorescent experiments, cells were seeded in supplemented DMEM High Glucose medium (300 µL) into CellView cell culture dish with 4 compartments (or wells). To obtain approximately 90-95% coverage in the well for 4 compartments dish 48 h after cell seeding, 75000 cells/well was chosen as the optimal concentration for both cell lines. The concentration of cells/well for both cell line was the same, even if the coverage would be slightly

different since their size and way of attachment to the surface differ: flatness, proximity to other cells.

3.2.5.1. Fluorescent properties in live cells

For fluorescence confocal microscopy experiments, the setting of the instrument selection of conditions was done initially based on the fluorescence spectra obtained in buffer (without cells). The probe concentration and time of exposure were selected inspired by literature[87,96,112,147,148] – that is in the single micromolar range. The initial plate with concentration-dependent staining was used to determine the minimal concentration (2 µM) that would give a significant signal difference from the blank (autofluorescence signal - well containing only DMSO). Subsequently HEK and DU145 cells were treated with the same concentration of each of hemicyanine (2 µM) with the same exposure time (15 min). Microscope settings (including the range of channels as well as their laser power, detector gain and threshold) were set to be the same for all samples; and the same thresholding method was used for the collected fluorescence confocal images during data analysis. Such settings would allow the comparison of the fluorescence intensity across all samples.

Intensity-based analysis using the same threshold of fluorescence confocal images obtained from cells (DU145 or HEK) treated with either **HCy-NEt$_2$** or **HCy-Jul** (***Figure 39***) showed that both present a higher fluorescence intensity of emission than that of the blank sample in both cell lines. Moreover, **HCy-NEt$_2$** fluorescent output is higher than that of **HCy-Jul**: these results correspond to the difference in fluorescence intensity of emission observed in buffer solutions in previous experiments mentioned during the initial spectroscopic characterisation studies. Since these derivatives show a reliable fluorescence emission output in fluorescence confocal microscopy, they can be used for the design of fluorescent probes.

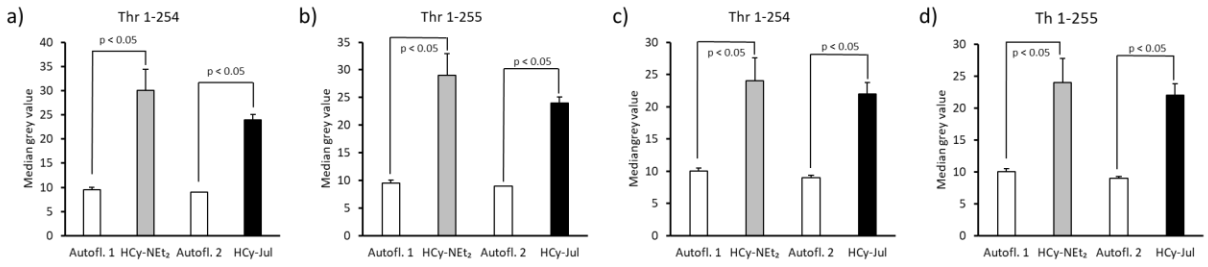

***Figure 39**. Quantification of median grey value of **HCy-NEt₂** (2 µM, a,c) and **HCy-Jul** (2 µM, b,d) via fluorescence confocal microscopy studies in (a,b) DU145 and (c,d) HEK cell lines under normoxic conditions with a final 1% of DMSO. Channel: λ_{exc} = 530 nm, λ_{em} = 580 - 700 nm. ImageJ was used for thresholding (Threshold 1-254 – left; Threshold 1-255 - right), selection of regions of interest (ROI), and measurement of median grey values. N = 3*

Additional experiments via fluorescence confocal microscopy were carried out to further confirm that the collected fluorescent output truly arises solely from the dye and that it did not correspond to the change in autofluorescence induced by the presence of dye. Spectral scan of DU145 and HEK cells treated with either **HCy-NEt₂** or **HCy-Jul** was collected during fluorescence confocal experiments (***Figure 40***) in the same conditions (channel wavelength range, laser power, gain). The relevant information from such spectral scan is the shape of the emission spectra and the corresponding fluorescence emission maxima, which were at around 600 and 620 nm for **HCy-NEt₂** and **HCy-Jul**, respectively. Both the shape of the emission spectra and the corresponding fluorescence emission maxima obtained in cells treated with **HCy-NEt₂** and **HCy-Jul** is comparable to the one observed in organic solvents and buffer solutions from previous spectroscopic characterisation. Therefore, the obtained spectral scans confirmed the presence of the corresponding hemicyanine derivatives in both cell lines upon treatment.

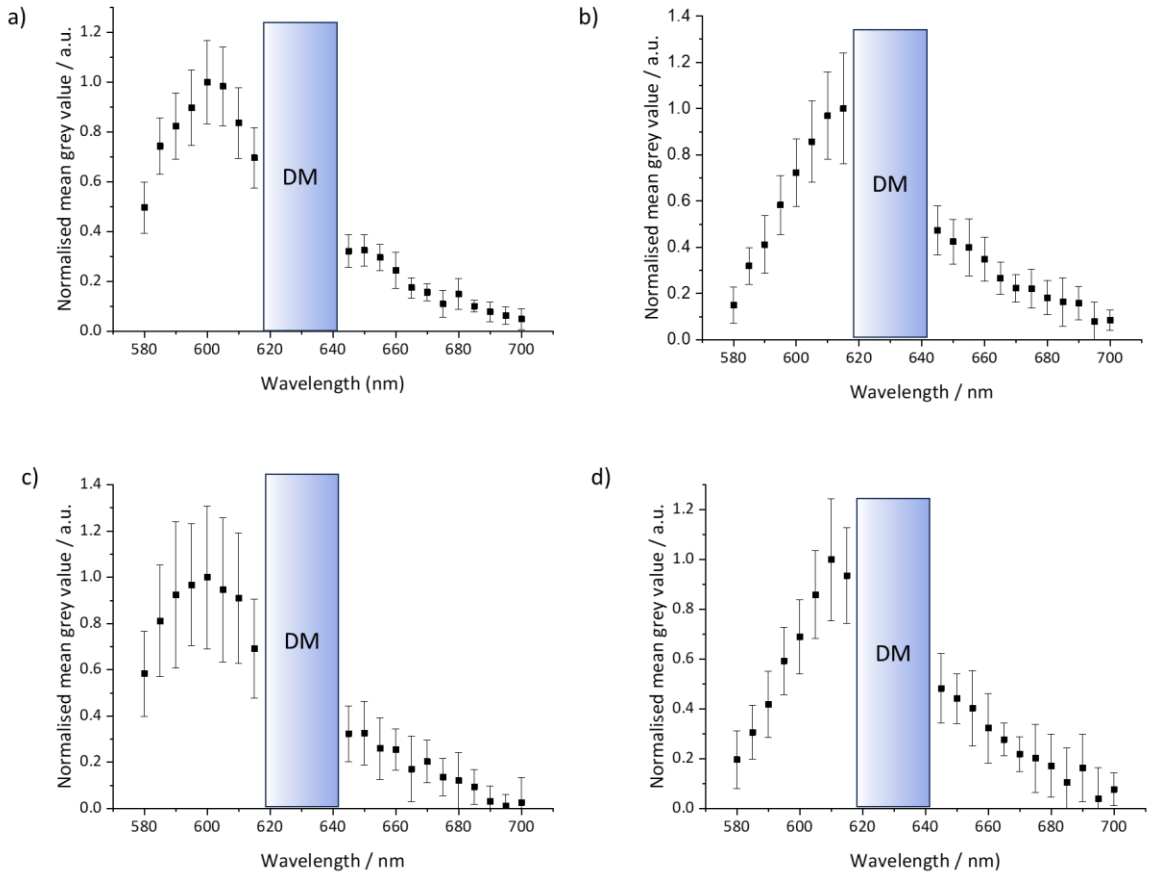

***Figure 40**. Spectral scan of **HCy-NEt₂** (2 µM, a,c) and **HCy-Jul** (2 µM, b,d) in (a) DU145 and (b) HEK cell lines under normoxic conditions with a final 1% of DMSO. Conditions for spectrum collection: λ_{exc} = 530 nm, λ_{em} = 580 - 700 nm (with 5 nm steps). DM: schematic representation of the dichroic mirror in the fluorescence confocal microscope settings. N = 3*

3.2.5.2. Intracellular localisation of hemicyanines

In order to better understand an intracellular behaviour of these derivatives, co-localisation experiments with organelle-specific stains (so called Mitotracker-Deep Red MT-DR and Lysotracker Deep Red – LT-DR) were carried out in HEK and DU145 cell lines (***Figure 41***). Subsequently, Pearson's coefficients (***Table 6***) were calculated based on obtained images. These revealed a slight co-localisation with MT-DR (an approximate coefficient value of 0.5), suggesting some signal partition to this organelle. This result is in line with previous reports that extensively demonstrate a use of lipophilic cations (and hemicyanines have those) as targeting motifs for ensuring mitochondrial localisation of probes and drugs via an electrostatic interactions with

negatively charged mitochondrial membranes.[2,6,7,37] This suggests that both **HCy-NEt$_2$** and **HCy-Jul** can be found in mitochondria as well as in other regions in the cell (especially cytoplasm - ***Figure 41c,d,g,h***). Importantly, neither **HCy-NEt$_2$** nor **HCy-Jul** localise in lysosomes in neither of the cell types (low Pearson's coefficients values, ***Table 6***). For the purpose of sensing hypoxic acidosis, lysosomal localisation is unwanted due to the potential toxicity of the probe (sequestration and degradation in the lysosomes, commonly leading to autophagy) and the natural intrinsic low pH of lysosomes that would "artificially" indicate an existence of an acidosis even if the cytoplasmic pH was not affected. These sub-cellular localisation patterns make the scaffolds suitable development of fluorescent probes to sense hypoxia-specific intracellular low pH.

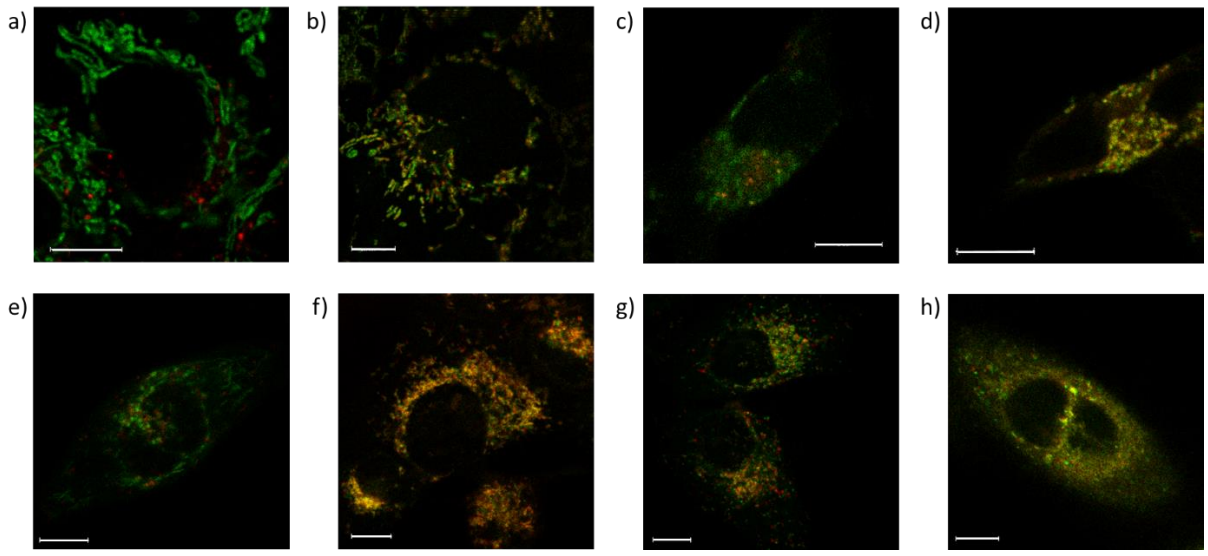

***Figure 41**. Hemicyanine derivative (2 µM, green channel) co-localisation experiments in (a-d) HEK and in (e-h) DU145 cells lines. LT-DR (50 nM, red channel) co-staining with (a,e) HCy-NEt$_2$ or (c,g) **HCy-Jul**; MT-DR (100 nM, red channel) co-staining with (b, f) **HCy-NEt$_2$** or (d,h) **HCy-Jul**. All samples contained with a final 1% of DMSO. Green channel: λ_{exc} = 550 nm and $\lambda_{em\ HCy\text{-}NEt2}$ = 560 nm - 630 nm and $\lambda_{em\ \mathbf{HCy\text{-}Jul}}$ = 630 nm - 700 nm. Red channel: λ_{exc} = 644 nm, λ_{em} = 654 nm - 700 nm). Scale bar: 10 µm. N = 3*

Table 6. Pearson's coefficient from images of DU145 and HEK cell lines stained with either **HCy-NEt_2** or **HCy-Jul**, and Lysotracker or Mitotracker Deep Red. N = 3

Cell line	Tracker (Deep Red)	**HCy-NEt_2**	**HCy-Jul**
DU145	Lysotracker	0.24 ± 0.04	0.25 ± 0.08
	Mitotracker	0.55 ± 0.06	0.52 ± 0.02
HEK	Lysotracker	0.25 ± 0.08	0.09 ± 0.05
	Mitotracker	0.45 ± 0.06	0.50 ± 0.02

3.2.5.3. Biocompatibility of hemicyanine scaffolds

Additional validation of the fluorescent dyes consisted in cell viability studies to ensure that the observed fluorescent output is not an artefact caused by the probe's influence on the cells. Cytotoxicity studies were carried out in the format of 384-well plates due to several factors: high number of samples, lower concentration of cells, low volumes of media and reagents (DMSO, resazurin, staurosporine[149], HCy) solutions. A concentration of 2500 cells/well would give a similar coverage to the one chosen for imaging conditions. Considering that cell treatment in 4 compartments format was with a hemicyanine derivative solution to yield a final concentration of 2 µM (0.0667 nmols) in supplemented DMEM High Glucose (300 µL, 1% DMSO), the appropriate derivative mol equivalents to 2500 cells/well in the 384-well plate format would be 0.0222 nmols. Since cell treatment in the 384 well-plate format would be in supplemented DMEM High Glucose (30 µL, 1% DMSO), the corresponding concentration of hemicyanine derivative would be 0.74 µM (giving the same value of mols per cell). Consequently, a concentration of 0.74 µM in the 384-well format would be equivalent to a concentration of 2 µM in 4 compartments one in terms of the amount of probe per cell. IC_{50} curves can be found in appendix in the subchapter 6.4.

Typically, cell exposure with the corresponding hemicyanine derivative for fluorescence imaging studies were 15 min long, followed by rinsing the well, addition of cell medium without the probe, and imaging with this whole process lasting no longer than 1.5 h. In the performed cytotoxicity

studies, the cells were exposed to the probe for 1 h (longer than 15 min exposures during the imaging) before rinsing and addition of cell media, making it a more extreme condition that during imaging experiments. The reasoning behind that is to be on the safe side since the effects would be lower in the imaging conditions. Measurements of cell viability were performed 48 h after cell exposure and the results (***Table A1*** in Appendix in subchapter 6.4) were plotted (***Figure 42***). **HCy-NEt$_2$** and **HCy-Jul** present IC_{50} values higher than 0.74 µM in 384 well-plate format. Importantly, IC_{50} for **HCy-NEt$_2$** could not be calculated because the upper limit value given by a 10 µM was too low and no inflexion point was present suggesting low toxicity. Nevertheless, all cell viability fitting parameters are shown in ***Table A2*** in Appendix in subchapter 6.4. A final 0.74 µM concentration in 384-well plate (that corresponded to the amount of probe per cell found in imaging conditions at 2 µM concentration) was deemed suitable for imaging. However, some long-term concentration can still cause some long-term effect in the cells viability as assessed by the cell death observed after 48 h after 1h exposure (4 times longer than the exposure during the imaging).

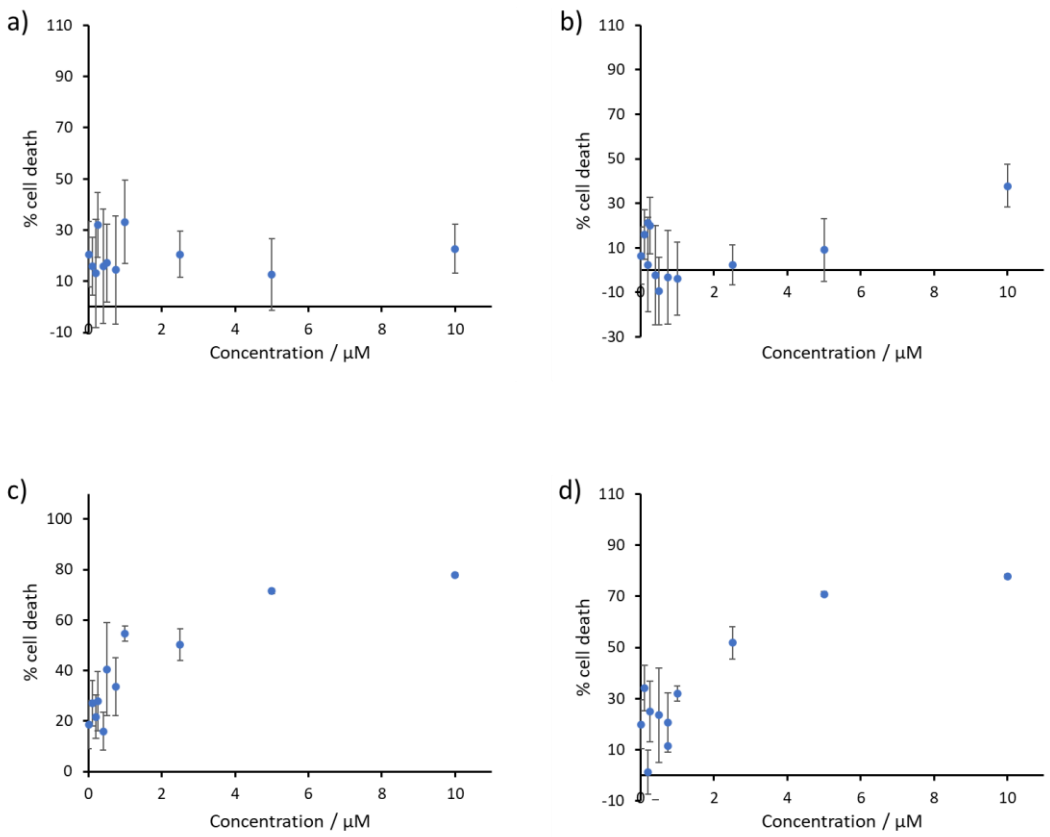

***Figure 42**. Plots of cell death (%) vs the concentration (µM) of (a,b) **HCy-NEt₂** and (c,d) **HCy-Jul** in (a,c) DU145 and (b,d) HEK cell lines.*

3.2.6. Summary

A new hemicyanine scaffold was designed with an aim to improve its stability to various interferents in comparison to other commonly used hemicyanine scaffolds. The robustness of these derivatives was investigated in a range of experiments and variety of interferents and environments.

HCy-OMe presented a green fluorescence emission and was deemed the least stable, followed by **HCy-NEt₂**, and then by **HCy-Jul** (both with orange-red emission) in terms of fluorescent signal stability against nucleophiles and other potential signal interferents. All derivatives presented a fluorescent output signal independent of the pH (range 4-8), but dependent on the nature of the buffer (related to their conductivity), and dependent on the viscosity and polarity of the solvent to which they were exposed. Importantly, further exploration yielded independence of

fluorescence output signal in the presence of selected inorganic salts. Finally, **HCy-OMe** revealed signal instability in cell growth (DMEM High Glucose) and imaging (Fluorobrite^{TM}) media with other two being significantly more robust.

Subsequently, the stability of the signal against the presence of nucleophiles have been investigated. The mode of addition to **HCy-OMe** was confirmed via NMR spectroscopy following using 1,2- and 1,4-addition model nucleophiles already reported in the literature, while the **HCy-Jul** and **HCy-NEt$_2$** were more stable in NMR conditions. Parallel fluorescent studies confirmed higher susceptibility of **HCy-OMe** fluorescence intensity to nucleophiles and buffers that lead to its quenching, with the **HCy-NEt$_2$** being more robust but still suffering from quenching especially in the presence of glutathione and at higher pH values. Importantly, newly designed **HCy-Jul** scaffold showed highest robustness with little to no change in fluorescence intensity in the presence of biologically relevant nucleophiles or buffers.

Once the *in vitro* spectroscopic characterisation was finalised, **HCy-OMe** was not further investigated due to its poor stability and **HCy-NEt$_2$** and **HCy-Jul** behaviour was tested in 2D cellular models (HEK and DU145 cell lines). Spectral scans collected during imaging proved both the presence and integrity of the dyes in the treated cells and fluorescence confocal images with organelle markers revealed favourable (whole cell and non-lysosomal) localisation of both fluorophores. Cell viability studies confirmed that the concentrations used for fluorescence confocal microscopy experiments should not produce any artefacts, as cytotoxicity was only observed for a more extreme treatment (longer exposure time with the compounds) of the cells and prolonged time (48 hours after treatment).

All of the experimental evidence above confirmed that newly designed **HCy-Jul** is more robust than previously reported scaffolds (**HCy-NEt$_2$** and **HCy-OMe**), including a resistance to biologically relevant nucleophiles. This also demonstrated a successful rational approach to improvement of the stability of hemicyanines via an increase in the electron donating character of the substituents on phenyl moiety. Consequently, **HCy-Jul** was selected as the hemicyanine scaffold for a further development of dual-analyte fluorescent probes for hypoxia.

3.3. Intensity-based dual-analyte probe for hypoxia

3.3.1. Design

Previous chapter has yielded a new more robust fluorescent scaffold (**HCy-Jul**) with increased resistance to biologically-relevant nucleophiles. This chapter reports on the responsive dual-analyte probe for hypoxia that is based on the new **HCy-Jul** scaffold (***Figure 43***). Such probe should emit a distinct signal (different from other states) once both low pH and increased NTR activity, the combination used as proxies for hypoxia state, are present. As discussed in the introduction, a turn-on like response is preferred over turn-off to increase the reliability of detection. To best meet this criteria, the probe should have little-to-no fluorescence in normoxic conditions and increase it in hypoxia (low pH and high NTR-like activity). To ensure such a response, the probe was designed in a way that would allow a subsequent set of reactions with the target analytes. The probe should exhibit the maximum of fluorescence emission intensity only when hypoxic conditions are met, given that its pH sensitivity is only occurring after bio-reduction by NTR. In other words, the probe would operate as an NTR-activatable pH probe with turn-on response to acidic environments and so as tur-on probe for hypoxia.

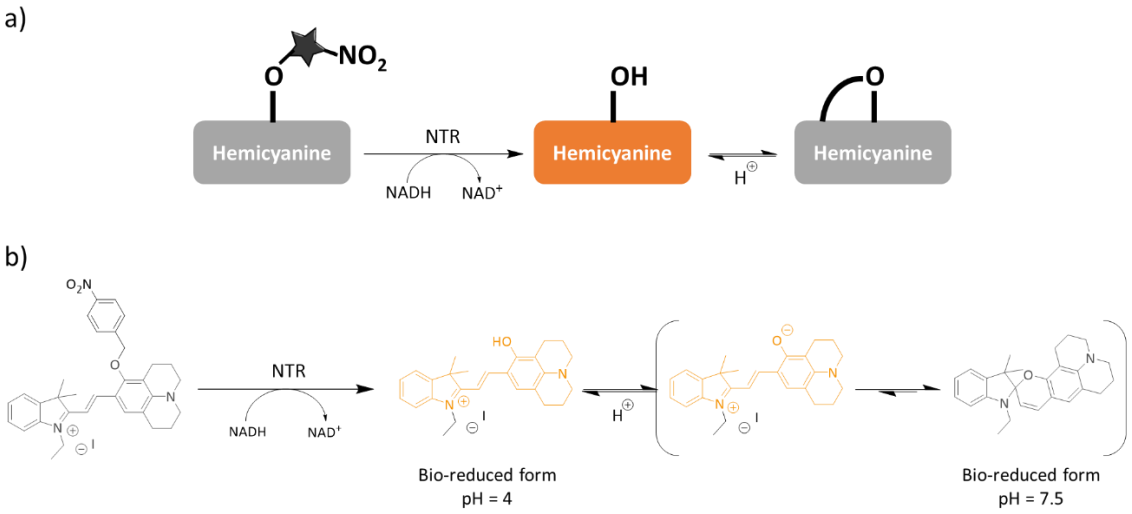

Figure 43. *(a) Schematics of **NHCy** fluorescence response upon bio-reduction via NTR-like activity in the presence of NADH. The grey boxes indicate the quenched hemicyanine fluorophore, which turns orange after bio-reduction and in low pH; the black star depicts the nitro-cleavable moiety. (b) Bio-reduction of **NHCy** in the presence of NTR and NADH and its corresponding merocyanine and spiropyran equilibrium depending on the pH.*

3.3.2. Synthesis

The simple retrosynthetic strategy for the synthesis of the probe and the corresponding synthons for each step is shown in **Scheme 3**. The synthesis of probe **NHCy** involves the connection of **1** and the benzaldehyde with a NTR-cleavable nitrobenzyl moiety. The reactions to obtain the two synthons and the final product (probe) were carried out via adapted protocols found in the literature. [117,118]

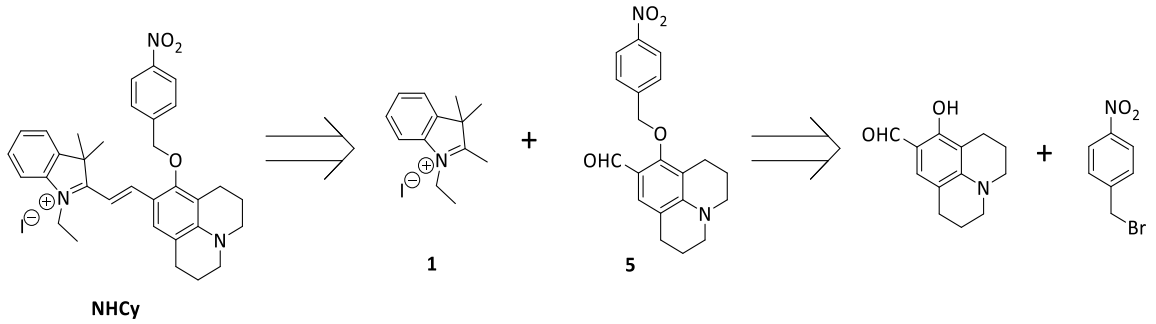

***Scheme 3**. Retrosynthetic analysis for the development dual-analyte fluorescent probe **NHCy**.*

The benzaldehyde with a NTR trigger moiety (p-nitrobenzyl) is obtained via a reaction of the 9-formyl-8-hydroxyjulolidine with 4-nitrobenzyl bromide in basic conditions. In this reaction environment, deprotonation of 9-formyl-8-hydroxyjulolidine ihelps generate nucleophile that is able to attack the benzylic carbon of 4-nitrobenzyl bromide, releasing Br^- as the leaving group.[113]

The synthesis of the dual-analyte fluorescent probe (**7**) and its active molecule counterpart, **5**, (***Scheme 4***) from this commercially available benzaldehyde derivative is carried out via a condensation reaction directly (**5**) or in the case of compound **7,** preceded by a preparation of aldehyde **6** via an alkylation of hydroxyl group on the aldehyde with p-nitrobenzyl bromide. A total conversion of aldehyde substrates in both reactions towards hemicyanine derivatives (**5** and **7)** was observed after 4 h of reflux. However, the isolated yield of desired compounds is low, mainly due to the complex purification by column chromatography. The difficulty in purification might stem from the fact that both **1** and the hemicyanine products present a similar retention factor due to them being tertiary amines, and their positive charge contributes to their high retention on silica gel.

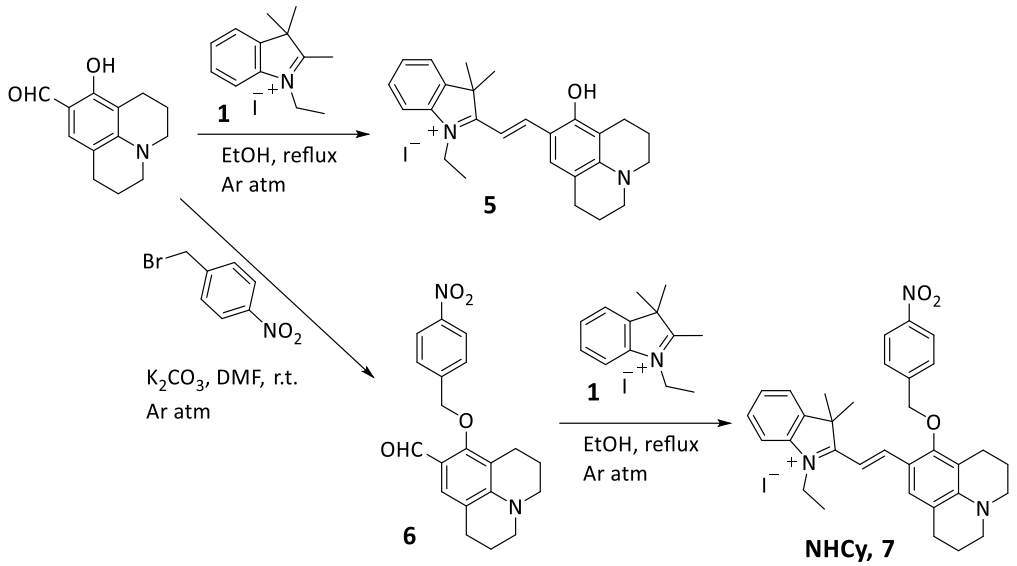

***Scheme 4**. Synthesis of dual-analyte probe **NHCy** (**7**) and of its corresponded bio-reduced form (**5**). Yields: **5**, 23.5%; **6**, 98.1; **NHCy** (**7**), 33.0%.*

The products' purity and identity were confirmed through NMR spectroscopy (mainly via ^{1}H NMR, ^{13}C NMR, COSY), and mass spectrometry (HR-MS). Corresponding ^{1}H NMR, ^{13}C NMR spectra can be found in the Appendix (subchapter 6.1.1). Compounds **6** and **NHCy** (**7**) are novel compounds, compound **5** was also novel at the time the studies started, but it has been unfortunately patented[150] this year.

3.3.3. Spectroscopic characterisation

The initial validation of the probe started with collection of absorbance and fluorescence emission spectra of **NHCy** in DMSO and in buffers (***Figure 44***). Spectra were normalised to the maximum absorbance or fluorescence output (***Figure 44a,d***). **NHCy** presents one absorption band and its corresponding orange-red fluorescence emission band ($\lambda_{exc\ max/em\ max}$ = 580/610 in PBS 7.4 100 mM; $\lambda_{exc\ max/em\ max}$ = 585/620 in DMSO) from the hemicyanine fluorophore. This orange-red emission corresponds to emissions from other hemicyanine derivatives containing an alkylamino group in *para* position[9], as well as **HCy-NEt$_2$** ($\lambda_{exc\ max/em\ max}$ = 560/605, in DMSO) and **HCy-Jul** ($\lambda_{exc\ max/em\ max}$ = 584/623, in DMSO) as reported in previous subchapters. After determining its absorption and fluorescence emission maxima, the concentration dependence of the signal in DMSO was investigated. A concentration range of 2 - 10 µM was chosen, as all

absorbance values at the excitation maximum were below 0.1 a.u. for all obtained solutions. A gradual increase in concentration led to higher absorbance and also higher emission intensity according to the linear trend. (***Figure 44b,c***). The linearity of this relationship between concentration and absorption as well as emission intensity of this compound indicates that such concentration range poses no problems regarding its solubility, aggregation and/or self-quenching. The fluorescence emission of **NHCy** and its corresponding bio-reduced form (**5**) was studied in pH values of 4 (citrate-phosphate buffer, CPB, 100 mM) and 7.5 (phosphate buffer, PB, 100 mM) (***Figure 44d***). The probe displays the same fluorescence of emission in both pH while **5** presents enhanced emission in acidic pH and a quenching in basic pH. The output signal of **NHCy** can be differentiated unequivocally at both pH from the output signal of **5** in on-state (merocyanine form, pH 4) and off-state (spiropyran form, basic pH).

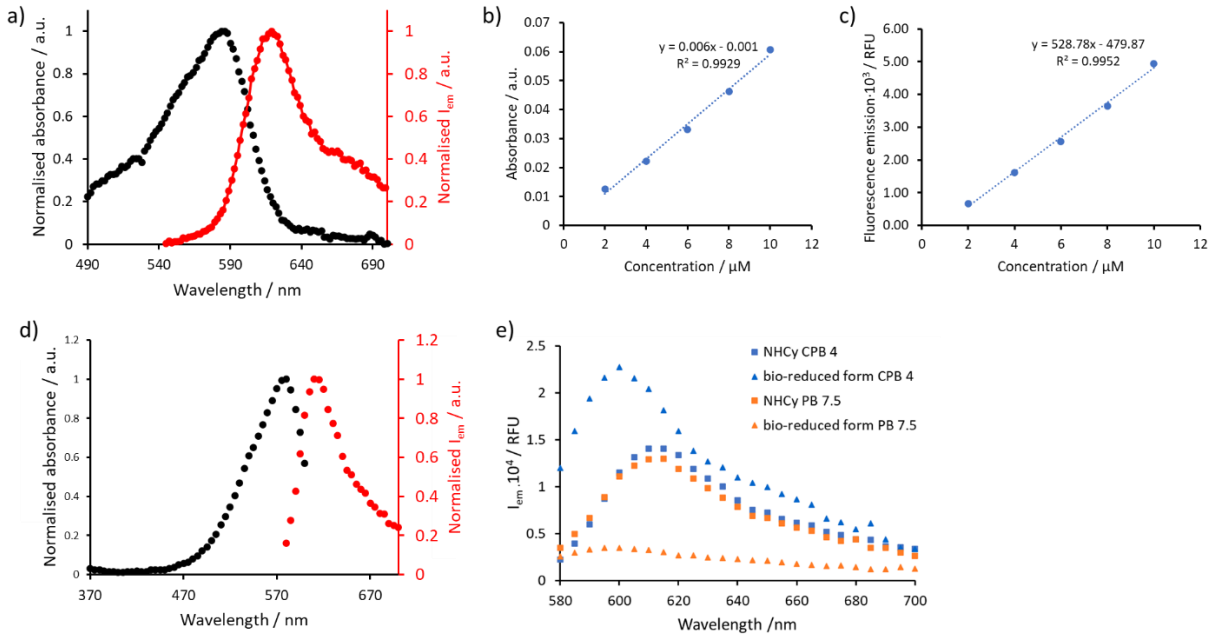

Figure 44*. Normalised (a) absorbance (black dots) and fluorescence emission (red dots) spectra of* ***NHCy*** *(2.5 µM) in DMSO. Plots of (b) absorbance vs concentration and (c) fluorescence emission ($\lambda_{exc/em}$ = 550/611) vs concentration for* ***NHCy*** *(range: 2 -10 µM) in DMSO. Emission spectra in DMSO was collected in the following condition: $\lambda_{exc/em}$ = 515/545-700 nm. (d) Normalised absorbance (black dots) and fluorescence emission (red dots) spectra for* ***NHCy*** *(2.5 µM) in PB 7.5 (1% DMSO final). (e) Fluorescence emission of bio-reduced form (****5,*** *triangles), and* ***NHCy*** *(squares) in acidic (4, citrate-phosphate buffer, CPB, 100 mM, blue) and physiological (7.5, phosphate buffer, PB, 100 mM, orange) pH (1% DMSO final). Emission spectra in buffer was collected in the following condition: $\lambda_{exc/em}$ = 550/580-700 nm. N = 3*

By using the same comparative method as in previous subchapter, the molar extinction coefficients (ε), fluorescence quantum yields (Φ_F), and brightness (B) for the hemicyanine derivatives were determined for **NHCy** (***Table 7***). Its relative Φ_F is comparable to the ones obtained for the other hemicyanines in the previous subchapter, and in particular presents a comparable brightness to **HCy-Jul** (same order of magnitude).

Table 7. Calculated spectroscopic properties of **NHCy** measured in DMSO. Values were calculated based of the results averaged over 3 separate repeats. Extinction coefficient values rounded to a full 10s. Quantum yields were measured by a relative method[123] comparing to the standard (Φ_F = 0.95 for Rhodamine 6G in EtOH[124]). Experiment was carried out in 384 well-plates with a final volume of 40 µL. The corresponding path length was estimated via N = 3

Compound	$\lambda_{exc}/\lambda_{em}$	Ɛ / [M^{-1} cm^{-1}]	Quantum yield (ϕ_F)	Brightness [M^{-1} cm^{-1}]
NHCy	515/619	19360	0.021	410

NHCy's (2.5 µM) fluorescence emission signal stability in the presence of biologically relevant nucleophiles was explored in TRIS·HCl 100 mM by comparing the signal of the probe in the presence of GSH (2 mM) and without GSH in the pH values of range of 7.5 and 9 (***Figure 45***). In those two different pH values, even given that at pH = 9 nucleophilicity of GSH increases, the probe's fluorescence emission did not significantly change with and without GSH, proving that the probe is stable against it. Indeed, as per design, **NHCy** should not be prone to undergo nucleophilic addition of GSH due to its decreased electrophilicity given by the **HCy-Jul** core (via EDG groups) as well as by the steric hindrance from the nitro-cleavable moiety in *ortho* position.

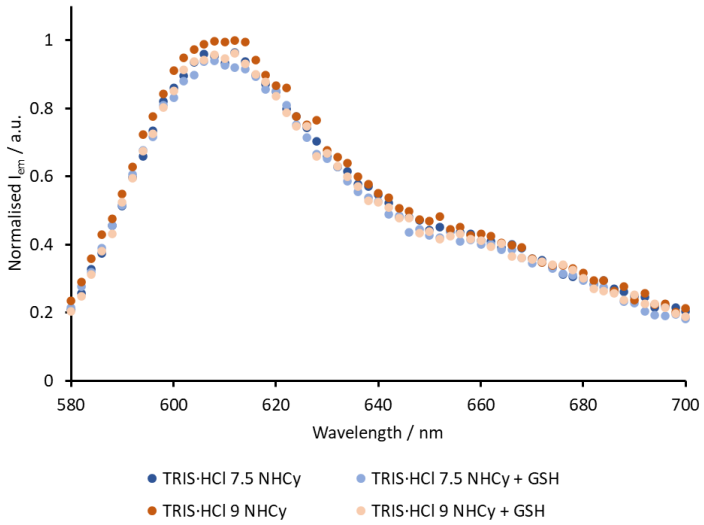

***Figure 45**. Normalised fluorescence emission of **NHCy** (2.5 µM) in TRIS·HCl buffer (100 mM pH 7.5 and 9) with 1% DMSO final in the absence (orange gradient dots) and presence (blue gradient dots) of GSH (2 mM). The blank samples presented the same %DMSO final. Fluorescence emission spectrum was collected at: λ_{exc} = 550 nm and λ_{em} = 580 – 700 nm. N = 3*

NHCy and its corresponding bio-reduced form (**5**) response to pH was studied via fluorescence spectroscopy (***Figure 46***). Two type of buffer solutions were used: phosphate buffer (PB) and citrate-phosphate buffer (CPB), each of them with the same pH value of 6 (to account for a possible pH-independent change in buffer chemical character) plus 7.5 and 4, respectively. Fluorescence emission signal of **NHCy** (***Figure 46a***) was not significantly perturbed in the studied pH range, while **5** (***Figure 46b***) presents a clear pH dependency, confirming that only the bio-reduced form exhibits pH-sensitivity, supporting the probe design.

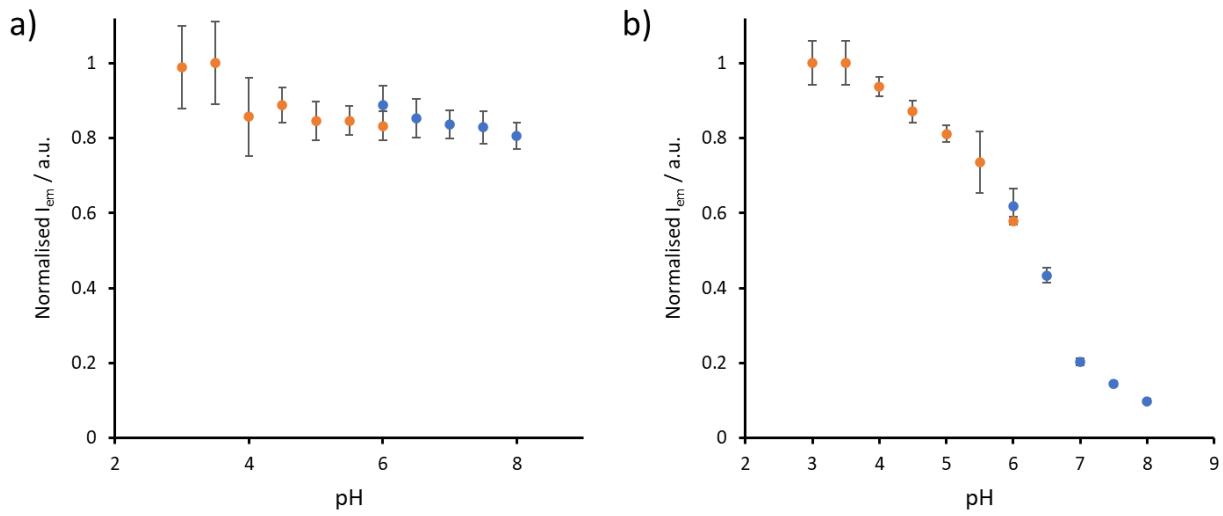

***Figure 46**. pH dependency of fluorescent emission signal for (a) **NHCy** (2.5 µM), (b) **5** (2.5 µM). Two different buffer solutions were used for the pH range of 3-8: citrate-phosphate buffer (CPB, blue dots) and phosphate buffer (PB, orange dots). $\lambda_{exc/em}$ = 550/600. N = 3*

Given the obtained pH curve in ***Figure 46b***, the estimation of the bio-reduced forms' pK_a was performed. In essence, the pK_a value defines the pH range (±1.5 pH units, equating to a thousandfold change in proton concentration) within which a probe modifies its optical properties or charge, making it useful for sensing applications [151]. Based of experimental data, the pK_a of the bioreduced form of **NHCy** was estimated to be 5.8, ± 0.1, calculated as an average of values obtained from fluorescence emission at 600 nm at different pH (***Figure 47***). This pK_a value fits well within the biologically-relevant pH range (usually 4 to 8), thus making it suitable for *in cellulo* applications. [152,153]

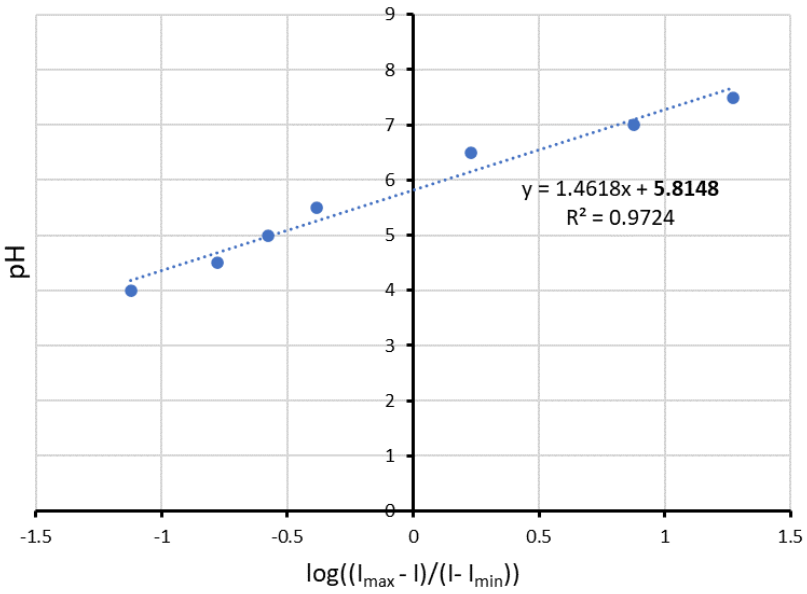

Figure 47. *Plot of pH vs log[(I$_{max}$-I)(I-I$_{min}$)], where I is the observed fluorescence intensity of* ***5*** *(2.5 µM) at 600 nm with* $\lambda_{exc/em}$ *= 550/600. The y-intercept is the* pK_a *value (5.8 ± 0.1) of an equilibrium between the protonated and non-protonated forms of* ***5****. 5 was dissolved with 100 mM ion concentration of CPB and PB buffers.*

Fluorescence spectroscopy was used to study the **NHCy** bio-reduction in the presence of NTR with NADH as a co-factor in acidic (4, citrate-phosphate buffer, CPB, 100 mM) and physiological (7.5, phosphate buffer, PB, 100 mM) pH (***Figure 48***). The probe displays the same fluorescence of emission in both pH 4 and 7.5 in the absence of NTR and NADH confirming lack of pH sensitivity. It is only upon bio-reduction that there is an increase (in acidic pH) or a quenching (in basic pH) of the output signal, as expected for the shifts in merocyanine-spiropyran equilibrium. Increased fluorescence intensity of the bioreduced form in acidic pH (protonated and open form) in comparison to the **NHCy** bearing nitrobenzyl moiety can be explained by the existence of the PeT quenching via p-nitrobenzyl[111,113] in **NHCy**. But not in its reduced form, as explained in subchapter 3.1. Some change in the emission wavelength maxima could be observed when moving from **NHCy** to its reduced form (***Figure 48b***), but the shift is minimal and in practice insufficient for application in ratiometric detection in cells.

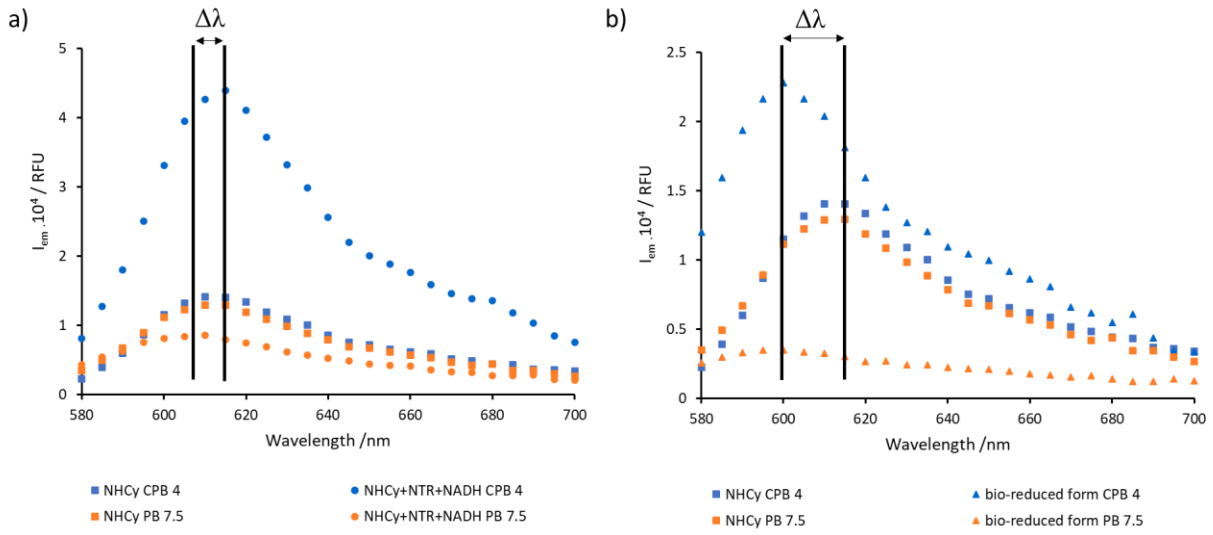

***Figure 48**. Fluorescence studies of bio-reduced form, and **NHCy** bio-reduction in the presence of NTR (10 µg mL^{-1}) and NADH (500 µM) in acidic (4, citrate-phosphate buffer, CPB, 100 mM, blue) and physiological (7.5, phosphate buffer, PB, 100 mM, orange) pH. Fluorescence emission comparison of NTR(+NADH) (a) untreated (squares) and treated (dots) **NHCy**; (b) untreated (squares) **NHCy** (off state control) and bio-reduced form (triangles, compound **5** – on state reference). N = 3*

3.3.4. Cellular behaviour

In order to evaluate the performance and compatibility of **NHCy** for cellular applications, several fluorescence confocal imaging experiments as well as cell viability studies were designed and performed.

The selection of cell lines for such studies was done analogously to previous experiments with the hemicyanine derivatives, but this time only focusing on widely used cancer cell lines: DU145[146] (already used for earlier hemicyanine derivatives validation) and A549 (cells derived from a human alveolar adenocarcinoma of the lung [154]. Both cell lines are commonly employed in cancer research, including studies of cancer progression, metastasis and therapy resistance,[155] as well as hypoxic studies [156–159]. Two different cell lines were used to account for potential differences in their biological behaviour and response to hypoxia.

Cell viability studies were carried out as described in an earlier section to determine if a final concentration of 2 µM would be appropriate for imaging purposes (i.e. 1 h exposure followed by washing off and waiting 48 hours to measure cell viability). IC_{50} fitting (**Figure 49**, ***Tables A3** and*

A4 in Subchapter 6.4 in Appendix) could only be carried out of D145 treated cells, as too low cytotoxicity was observed for treated A549 cells even in the highest concentration of probe tested (10 µM). **NHCy** presents IC_{50} values of 1.09 in DU145 cell line in 384 well-plate format experiments, respectively, which is the equivalent amount of probe (number of moles) as in the volume of 2.95 µM solution used in 4 compartments format of imaging experiments. In the case of A549, it can be concluded that, 2-2.5 µM concentration induced little to no cell death in the experimental conditions.

Therefore, while 2-2.5 µM concentration generates long-term toxicity in DU145 cells, its application in a short-term experiment (15 min exposure followed by immediate imaging rather than 1 h exposure and cell death observation within 48 h) or with a different cell line (A549) should still allow for reliable investigation of hypoxia.

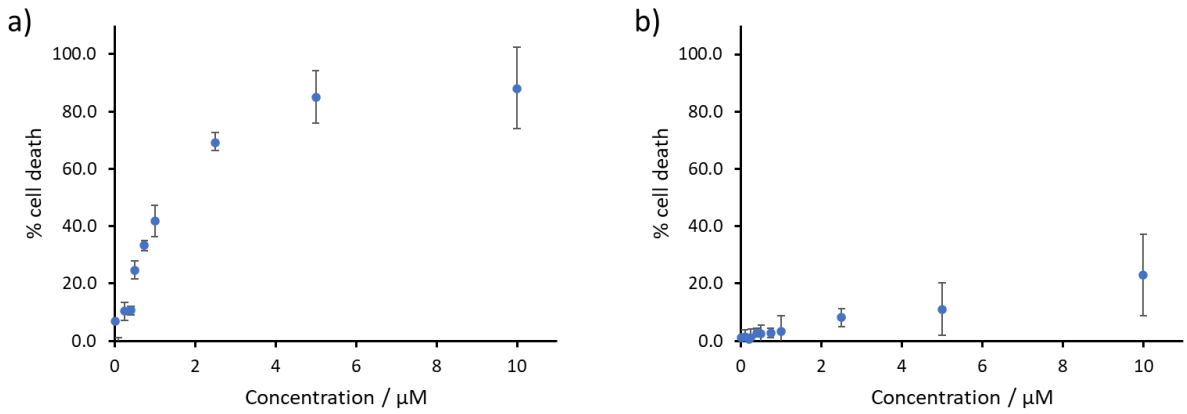

Figure 49*. Plots of cell death (%) vs the concentration (µM) for* ***NHCy****, in (a) DU145 and (b), A549 (cell lines. N = 3*

Fluorescence confocal microscopy studies were carried out taking into consideration the spectra collected in vitro in the buffer to choose the appropriate channels of fluorescence wavelength of excitation and corresponding emission ranges. The presence of the probe in cells upon treatment was verified (***Figure 50***) by a comparison of the fluorescence emission spectrum obtained from the treated cells under normoxic conditions and the one obtained from the probe dissolved in a buffer solution without cells but at physiological pH (phosphate buffer 100 mM, pH 7.5),

mimicking normoxic conditions. There was an overlap between the two spectra and the $\lambda_{em\ max}$ observed in cell culture normoxic conditions and in buffered conditions was 615 and 611 nm, respectively. The overlap between spectra suggests that, in fact, the fluorescent output signal from the cells is from the probe and thus, suggesting that the integrity of the probe is not compromised in cells.

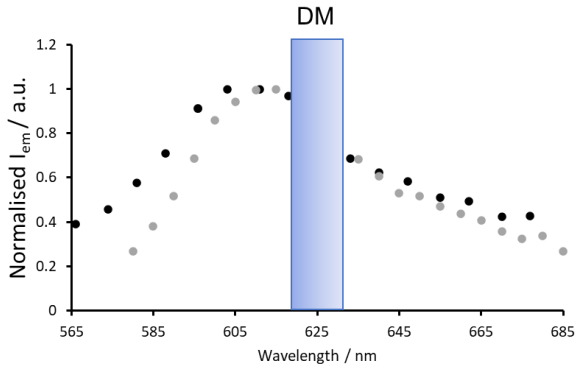

***Figure 50**. **NHCy** fluorescent probe in buffer conditions (grey, phosphate buffer 100 mM pH = 7.5, 1% DMSO) in DU145 cell culture under normoxic conditions (black, Fluorobrite™, 1% DMSO). Cell culture conditions for spectrum collection: λ_{exc} = 490 nm, λ_{em} = 565 -680 nm (with 7 nm steps). Buffer conditions for spectrum collection: λ_{exc} = 550 nm, λ_{em} = 580 - 700 nm (with 5 nm steps). DM: dichroic mirror. N = 2*

Fluorescence confocal microscopy studies of DU145 cell line treated with **NHCy** in normoxia and hypoxia (induction for 4 h at 1% O_2) were performed. Co-localisation studies with MT-DR (***Figure 51c-f***) yielded a Pearson's coefficient value range was of 0.5-0.7 (N = 3), confirming that the probe was mainly localising in mitochondria (as expected from lipophilic cationic structure), with some signal distribution across cytoplasm. However, intensity-based analysis of fluorescence of DU145 cells treated with **NHCy** (***Figure 51a,b***) in hypoxic and normoxic conditions showed no statistically significant difference between the two conditions. A lack of the difference in fluorescent signal between hypoxic and normoxic conditions in DU145 cells might stem from a variety of reasons, including an insufficient probe's sensitivity but also a potential higher redox buffering capacity of DU145 cells that might protect them against hypoxia even if exposed to hypoxic culture conditions.

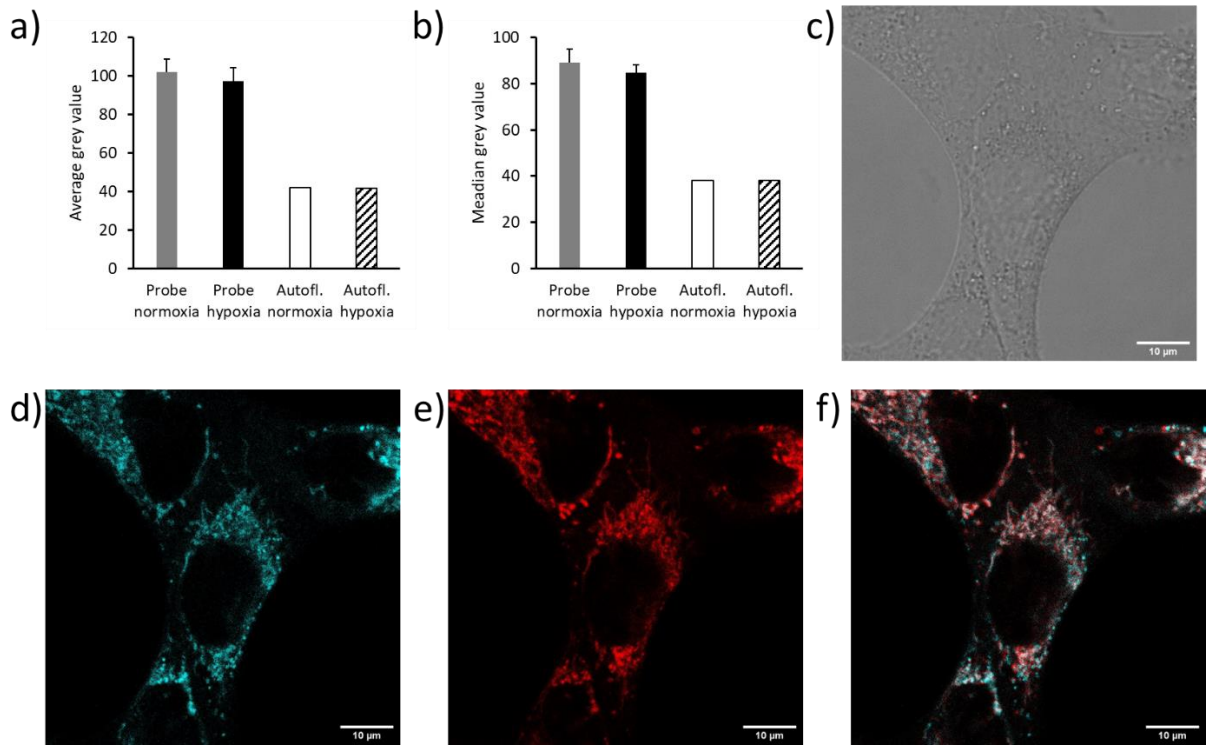

***Figure 51**. Quantification of hypoxic state via fluorescence confocal microscopy studies of **NHCy** in DU145 cell line: (a) average grey value, (b) median grey value. DU145 cell line untreated (1% DMSO) in normoxic (white columns), hypoxic (dashed columns); treated with **NHCy** (2.5 µM, 1% DMSO) in normoxic (grey columns), hypoxic (black columns) conditions. Channel: 490/600-650. Co-localisation experiments in DU145 cell line in normoxic conditions for **NHCy** (2.5 µM, 1% DMSO, cyan channel) with MT-DR (100 nM, 1% DMSO) red channel): (c) bright-field image, (d) cyan channel fluorescence image, (e) red channel fluorescence image, (f) overlay of channels. Cyan channel: λ_{exc} = 490 nm and λ_{em} = 600 nm - 650 nm. Red channel: λ_{exc} = 644 nm, λ_{em} = 654 nm - 700 nm. Scale bar: 10 µm. N = 5*

To investigate whether lack of detectable signal change in hypoxia vs normoxia in 2D layer of DU145 cells has biological origin or is an intrinsic deficit of the probe, another cancer cell line, A549, was also investigated. Fluorescence confocal microscopy studies of A549 cell line treated with **NHCy** revealed the presence of probe induced signal in both conditions (confirming probe's uptake). More importantly though, an analysis of differences in fluorescent signal intensity between **NHCy**-treated A549 cells in normoxia and hypoxia (induction for 4 h at 1% O_2) revealed a statistically significant increase in intensity in hypoxic conditions when compared to normoxic ones (***Figure 52a-b***). This experiment confirmed that the probe can indeed effectively detect hypoxia in cellular models via a turn-on response validating the design. Additionally, co-localisation experiments of **NHCy** with MT-DR in A549 (***Figure 52c-f***) demonstrated that the probe

is localised in mitochondria, (Pearson's coefficient value for the shown example had a value of 0.7-0.8 (N=3)).

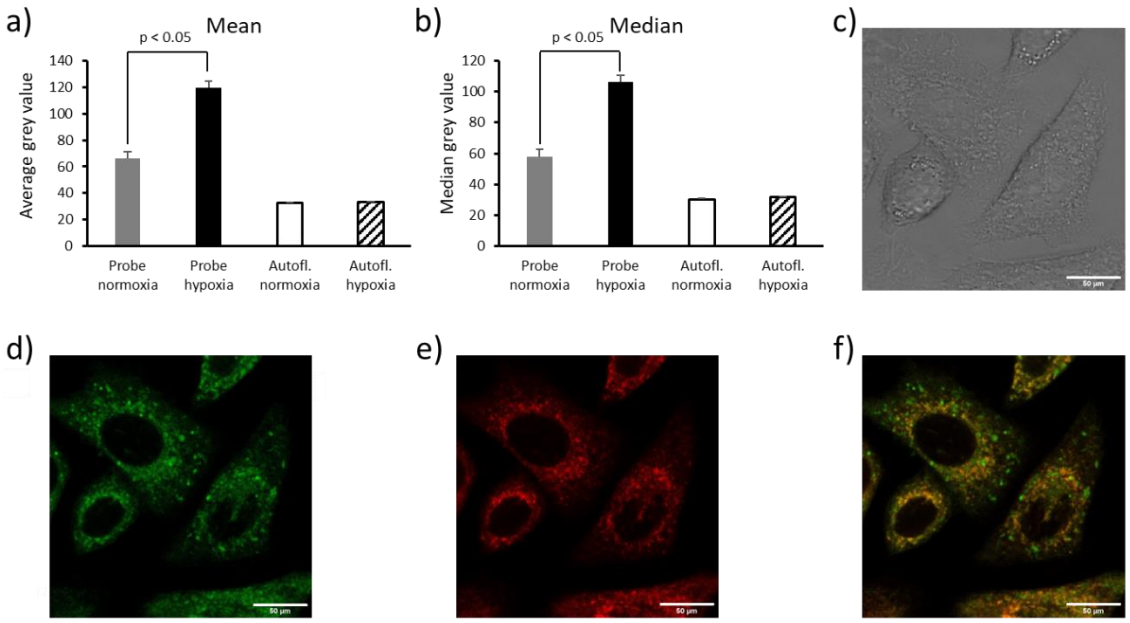

***Figure 52**. Quantification of hypoxic state via fluorescence confocal microscopy studies of **NHCy** in A549 cell line: (a) average grey value, (b) median grey value. A549 cell line untreated (1% DMSO) in normoxic (white columns), hypoxic (dashed columns); treated with **NHCy** (5 µM, 1% DMSO) in normoxic (grey columns), hypoxic (black columns) conditions. Channel: 490/590-620. Co-localisation experiments (c-f) in A549 cell line in normoxic conditions for **NHCy** (5 µM, green channel) with MT-DR (100 nM, red channel): (c) bright-field image, (d) green channel fluorescence image, e) red channel fluorescence image, (f) overlay of channels. All samples contained a final 1% of DMSO. Green channel: λ_{exc} = 490 nm and λ_{em} = 500 nm - 640 nm. Red channel: λ_{exc} = 644 nm, λ_{em} = 654 nm - 700 nm. Scale bar: 50 µm. N = 5*

Considering that the probe's response was confirmed in the 2D model cell culture of A549 cells in hypoxia, but remained inconclusive for DU145 cell line, it could be speculated that this second cell line requires a longer time of hypoxia induction than the first one. Alternatively, 3D cell culture model of DU145 cells (tumour spheroids) was used in order to mimic the hypoxia developing in tumour microenvironment. Spheroids are a broadly used models for inversed solid tumours and as them develop a changing gradient in respect to their oxygen level and efficiency of delivering nutrients and clearing out metabolites.[86,160] In spheroids with diameters in the range of 200-400 µm, this was reported to lead to observation of effectively two layers, normoxic (outer

shell), hypoxic (inner shell); when diameters reach 500 μm they can developing into three layers normoxic (outer shell), hypoxic (middle shell), necrotic (inner core).[161]

To perform these validation experiments, DU145 spheroids were prepared in a 96-well plate screening format. The experimental data was obtained by dr. Magdalena Otrocka and MSc Katarzyna Zielezinska, and was analysed by me. The cell culture plates were centrifuged for 5 min at 300g upon cell seeding (1000 cells/well), ensuring all cells were pelleted at the bottom of the well. DU145 formed regular and compacted spheroids spontaneously in suspension within a 24 h culture period. Fluorescence confocal microscopy studies of untreated (blank; final 1% DMSO; 8 repeats) and treated (and **NHCy**, 1 μM; final 1% DMSO; 8 repeats) DU145 spheroids were performed at two different channels: exc/em = 488/522 (channel measuring autofluorescence coming mainly from redox-sensitive flavins) and exc/em = 561/599 (probe-specific channel). A total of 25 z-stacks of thickness 15 μm were collected for each spheroid and a z-stack from the middle of the spheroid was selected for each sample (3 independent repeats for each condition). The obtained spheroids presented a diameter in the range of 310 to 410 μm, confirming the possibility of hypoxia sensing in the inner core.

Analysis of the profiles of emission intensity along the cross section of the confocal image of spheroid plane were plotted (representative sample plots presented in ***Figure 53*** and ***Figure 54***). Interestingly, an autofluorescence channel revealed a significant variation of intensity emission profiles with increased intensities localised mainly in the centre of spheroid (within 400 – 600 μm from the spheroid edge in case of untreated ones – ***Figure 53a-c***, and 600 – 800 μm from the edge for probe treated ones – ***Figure 53d-f***). Flavins that are the most probable source of this signal are well known to be redox active and their autofluorescence that increases upon increase in the oxidative stress has been previously used for the purposes of evaluating redox state of cellular models on multiple occasions [162].

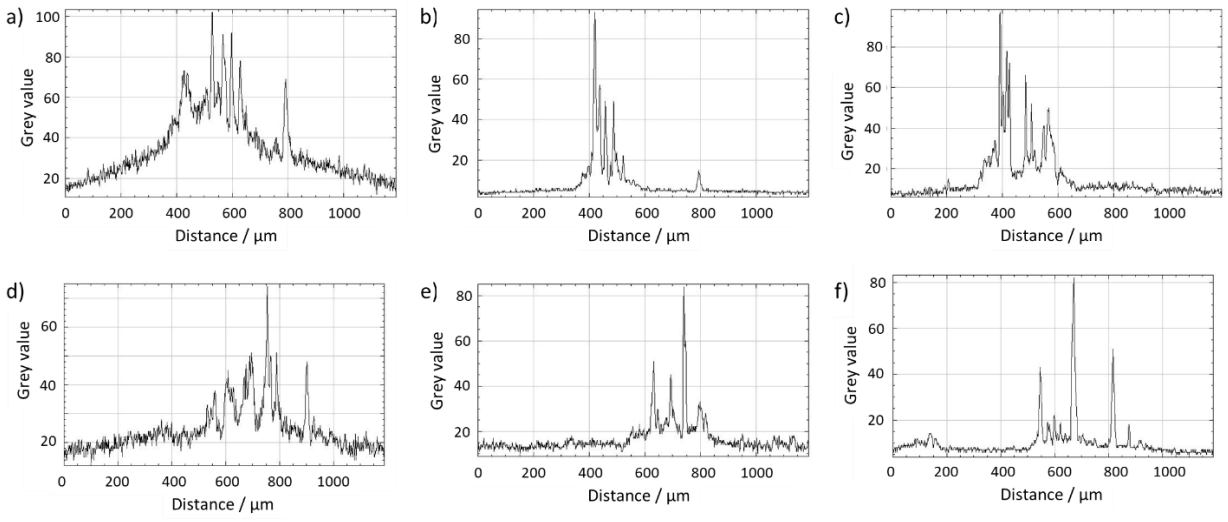

***Figure 53**. Profiles of grey value of autofluorescence channel ($\lambda_{exc/em}$ = 488/522) in fluorescence confocal images of 1000 cells DU145 spheroids (a-c) untreated (DMSO blank) and (e-f) treated with **NHCy** (1 µM). A line was drawn with the help of a script for ImageJ analysis at specific coordinates (54, 394, 1048, 394) as the ROI from which the profile of the grey value was plotted. A z-stack from the middle of the spheroid was selected for each spheroid sample.*

In the case of fluorescence confocal images obtained from the channel of exc/em of **NHCy**, profiles of untreated (***Figure 54a-c***) and treated (**NHCy**, ***Figure 54d-f***) spheroids with probe are similar, but higher intensities can be observed for the treated samples. This enhanced intensity in ***Figure 54e,f*** is especially observed in the outer layer (roughly within 150 - 200 µm away from the spheroid edge, marked in red) of the spheroids, potentially indicating the increased localisation of the probe in that region.

Further characterisation involved intensity-based analysis (***Figure 54***) of different regions of interest (ROI) in the cross-section images of the spheroids in the channel of exc/em of **NHCy**. To perform that analysis, each spheroid was segmented into three distinct regions of interest - ROI 1 whole spheroid (ROI 1), inner core (ROI 2), and outer part of the spheroid (ROI 3, with approximately 100 µm of width). Comparing the values of fluorescence intensity of untreated and treated samples (**NHCy**, 1 µM) there was a clear increase in fluorescence intensities in both outer and inner region of the spheroid suggesting that the probe can penetrate the spheroid. However, no significant enhancement in fluorescence emission in ROI 2 (potentially inner core, where hypoxic conditions would be expected) when compared to ROI 3 (outer part).

Unfortunately, since the probe responds to hypoxia in a turn-on intensity-based mode and in addition its off state (before bioreduction) remains relatively fluorescent in comparison to the active form (only approx. 2-fold increase in signal after bioreduction and in low pH in vitro) the results cannot be reliably interpreted. The change in the intensity can come from either an activation of the probe or a larger accumulation of an off state of the probe. Therefore, the signal in the outer part may arise from a high concentration of non-bio-reduced probe, while the signal from the inner core would come from bio-reduced probe in hypoxic conditions (merocyanine form). In the result, the probe cannot be reliably used to detect hypoxic states in these 3D models and it also demonstrates the intrinsic limitations of any intensity-based probes in the reliable detection of bioanalytes, especially in complex systems.

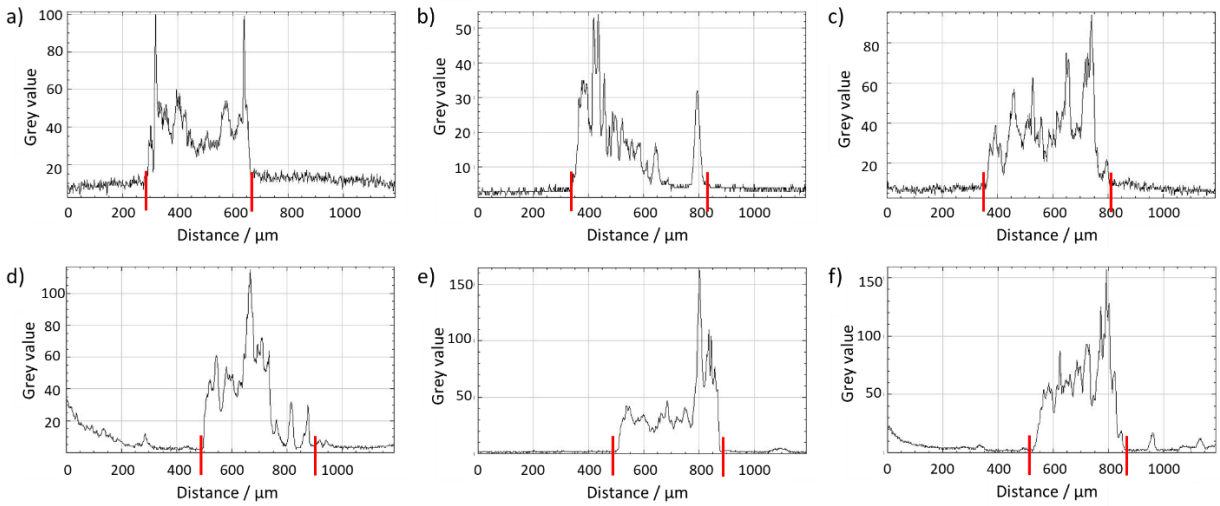

***Figure 54**. Profiles of grey value of fluorescence channel ($\lambda_{exc/em}$ = 561/599) in fluorescence confocal images of 1000 cells DU145 spheroids (a-c) untreated (DMSO blank) and (e-f) treated with **NHCy** (1 µM). A line was drawn with the help of a script for ImageJ analysis at specific coordinates (54, 394, 1048, 394) as the ROI from which the profile of the grey value was plotted. A z-stack from the middle of the spheroid was selected for each spheroid sample.*

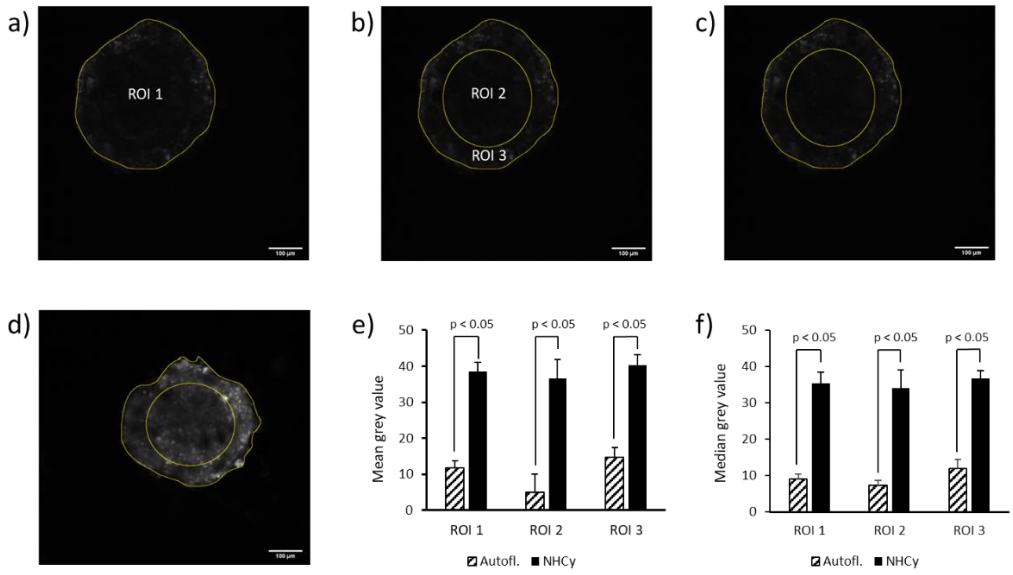

***Figure 55**. Exemplary selection of regions of interest in DU145 spheroids: (a) ROI 1 (whole spheroid), (b) ROI 2 (inner core), ROI 3 (outer part). Fluorescence confocal images of DU145 spheroids (c) untreated (DMSO blank) and (d) treated with **NHCy** (1 µM). Intensity-based analysis (3 images for each condition) and resulting (e) average, (f) median grey values. ROI 1: whole spheroid. ROI 2: inner core of the spheroid. ROI 3: outer part of the spheroid (ROI 2 was subtracted from ROI 1). The background value for each image was subtracted. Scale bar: 100 µm. N = 3*

3.3.5. Summary

NHCy exhibits one absorption band and one main orange-red fluorescence emission band from the hemicyanine fluorophore, which is in accordance to other HCy derivatives presenting an alkylamino group in *para* position found in the literature[9], and exhibits similar brightness to HCy-Jul.

Before investigating the fluorescence response mechanism of **NHCy**, an initial validation of the probe's stability in the presence of a biologically relevant interferent was conducted. This probe was expected to resist nucleophilic addition by GSH, as previously indicated in Subchapter 3.2, where **HCy-Jul** demonstrated a more robust structure against the tested interferents. Such resilience was confirmed by examining the stability of **NHCy-C**'s fluorescence emission signal, which remained unperturbed in the presence of GSH at pH values of 7.5 and 9.

Fluorescence response of the probe towards desired analytes 9pH and nitroreductase-like activity) was confirmed via testing **NHCy** in different pH and in the absence or presence of NTR

and NADH. The probe exhibits the same intensity of fluorescence emission in both acidic and physiological pH when there are no NTR nor NADH present (due to the probe being masked by a PeT quencher[111,113]). However, in the presence of the analyte and the co-factor, the fluorescence emission signal is dependent on the pH, showing a turn-on response only when the pH is acid Such results indicate that bio-reduction takes place and thus, the obtained hemicyanine is in equilibrium between its merocyanine (fluorescent) and spiropyran (non-fluorescent) forms. A minute change in the wavelength of fluorescence maximum could be used for ratiometric detection in a spectral-based fluorescent plate reader measurements but in practice, in practice the Δλ is not enough for adapting ratiometric-type readout in biological applications.

Parallel to imaging experiments with the hemicyanine derivatives, the same type of data were collected, including spectral scan, and fluorescence confocal (and corresponding brightfield) images. The two selected cell lines included A549 (previously used for scaffolds in chapter 3.2) and another cancer cell line, DU145, commonly used as a model of drug-resistant disease. The presence and stability of the probe in treated cells was confirmed via the overlap between the fluorescence emission spectrum obtained from spectral scan in fluorescence confocal microscope under normoxic conditions (*in cellulo*) and the one obtained in buffer solution at physiological pH (phosphate buffer 100 mM, pH 7.5) without cells (*in vitro*). Analogously to the results obtained for the hemicyanine derivatives in chapter 3.2, **NHCy** presents a mitochondrial localisation in both tested cell lines.

In A549 cells, **NHCy** probe exhibited low toxicity and allowed for a detection of hypoxic changes in the cells by monitoring of the increase in probe's fluorescence intensity in cell images. However, in the same experimental conditions, no change in fluorescence signal could be observed in DU145 cells exposed to hypoxic vs normoxic conditions. Since hypoxic-to-normoxic difference could be observed in A549, the most probable reason for a lack of change in DU145 is ineffective induction of hypoxia in this model and/or better redox buffering capacity of DU145 cells that prevents them from experiencing hypoxic conditions.

In the attempt to address an insufficient hypoxia induction in DU145 cells, a 3D spheroid model was employed to naturally replicate the tumour microenvironment and hypoxia state. Despite

the presence of the signal across the whole spheroid, the intensity of fluorescence in the outer regions was larger and/or similar to the one observed in the inner region, expected to exhibit hypoxic states. This contradicts the assumption that the hypoxic inner core would exhibit stronger fluorescence due to **NHCy** bio-reduction and pH-dependent equilibrium shift. The discrepancy may stem from probe penetration issues, with high concentrations of non-bio-reduced probe in the outer region masking the signal from the bio-reduced probe in the hypoxic core. However, the inability to quantify probe distribution in different regions limits the effectiveness of **NHCy** in detecting hypoxia in this 3D cell culture model and represents well the intrinsic limitations of virtually every intensity-based probe.

To sum up, cross-experimental validation of **NHCy** *in vitro* and *in cellulo* allowed confirmed the assumptions of the design that probe acted as a dual-analyte probe for hypoxia. The probe turned out to be also suitable for application in cellular imaging of hypoxia at least in A549 cells thanks to a sufficiently high fluorescence intensity (especially compared to autofluorescence), clear intensity-based response and non-lysosomal localization (avoiding capturing in naturally acidic environments that could lead to false positive readouts of cellular acidosis). However, inability to quantify and account for variation in intracellular accumulation (as it is for turn-on probes) might compromise the reliability and capacity to detect hypoxia in some models as demonstrated by 2D and 3D cellular models based on DU145 cell line.

Considering this demonstrated, intrinsic limitation of turn-on intensity-based response, a new approach was taken to develop another probe that would overcome such issues. The main aim was to develop a probe based on the same resilient scaffold, exhaustively studied in the earlier chapter) and same fluorescence response mechanism, but with some alterations which would allow for a ratiometric response.

3.4. Ratiometric dual-analyte probe for hypoxia

3.4.1. Design

The probe described in the previous chapter exhibited largely turn-on type of response to hypoxia, i.e. the intensity of fluorescence increased in hypoxic conditions. However, the interpretation of the results using this type of probes is ambiguous, since the increase in the fluorescence intensity might come both, from the actual existence of hypoxia and/or from simply higher local concentration of the off form probe accumulated in the given area of the cell. Therefore, to address this challenge, an alternative probe has been designed in a way to exhibit a ratiometric fluorescence response. To achieve it, a new probe was designed that would consist of the same responsive motif and fluorescent scaffold but additionally linked to another fluorophore with different colour of emission that is less or even non-sensitive to the analyte (hypoxia). With such design, even though individual fluorescent intensities would be dependent on probe concentration, the ratio between them would not and it would only be correlating with the level of the analyte.

Following these considerations, the new design consisted of the same structure of **NHCy** (***Figure 56a***), but linked to a hypoxia-insensitive coumarin fluorophore instead of an ethyl group to yield a ratiometric probe for pH and NTR activity (***Figure 56b***). The linker is based on an alkyl chain and the connection point is via an amide bond, deemed highly stable in the context of biological systems (***Figure 56c***). [163–166] The detailed bio-reduction mechanism of the probe is shown in ***Figure 56c***. Analogously to **NHCy**, the nitro moiety in **NHCy-C** would be protecting the hydroxyl group and, hence, only upon its cleavage would the fluorescence response be pH dependent. The coumarin fluorophore should remain largely unaltered even in hypoxic conditions, serving as the reference fluorophore. Hence, this probe should enable a ratiometric-based response and readout, increasing the reliability of data interpretation.

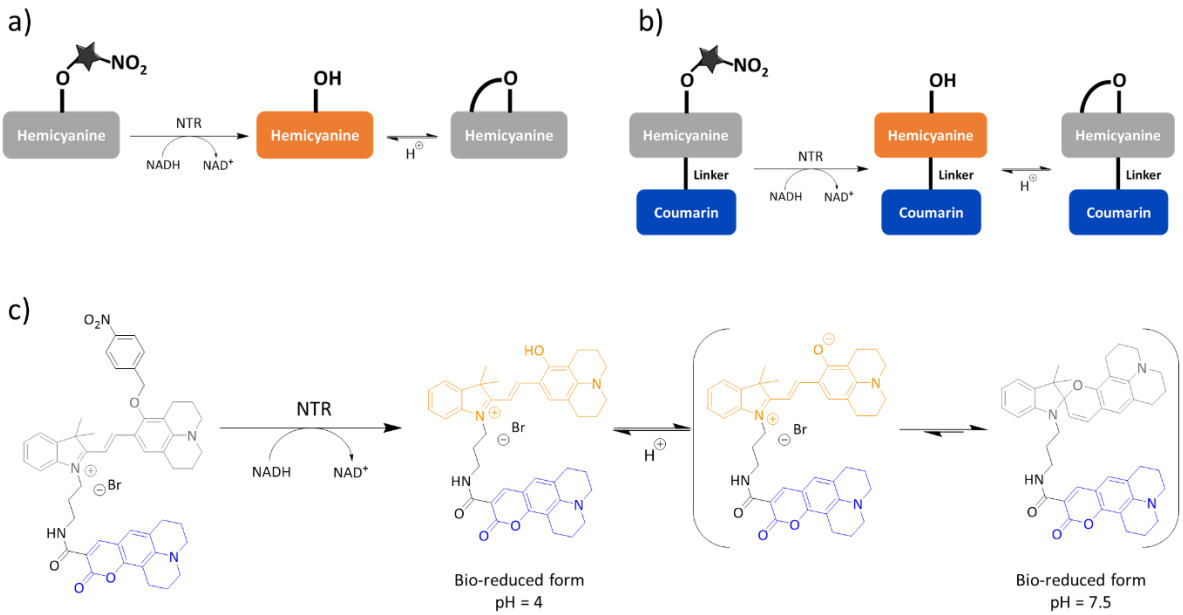

***Figure 56**. Schematics of (a) **NHCy** intensity-based and (b) **NHCy-C** ratiometric-based fluorescence response upon bio-reduction via NTR and NADH. The grey boxes indicate the quenched hemicyanine fluorophore, which turns orange after bio-reduction and in low pH; the black star depicts the nitro-cleavable moiety; the blue box represents the always fluorescent coumarin fluorophore. (c) Bio-reduction of **NHCy-C** in the presence of NTR and NADH and its corresponding merocyanine and spiropyran equilibrium depending on the pH.*

3.4.2. Synthesis

The synthesis of probe **NHCy-C** involves the connection of two fluorophores ("blocked" hemicyanine and coumarin). The retrosynthetic strategy for the synthesis of the probe and the corresponding synthons for each step is shown in ***Scheme 5***. From a theoretical organic synthetic perspective, two approaches can be used to prepare a synthon **11**, comprised of a positively charged indolenine moiety linked to a derivative of coumarin via an amide bond.

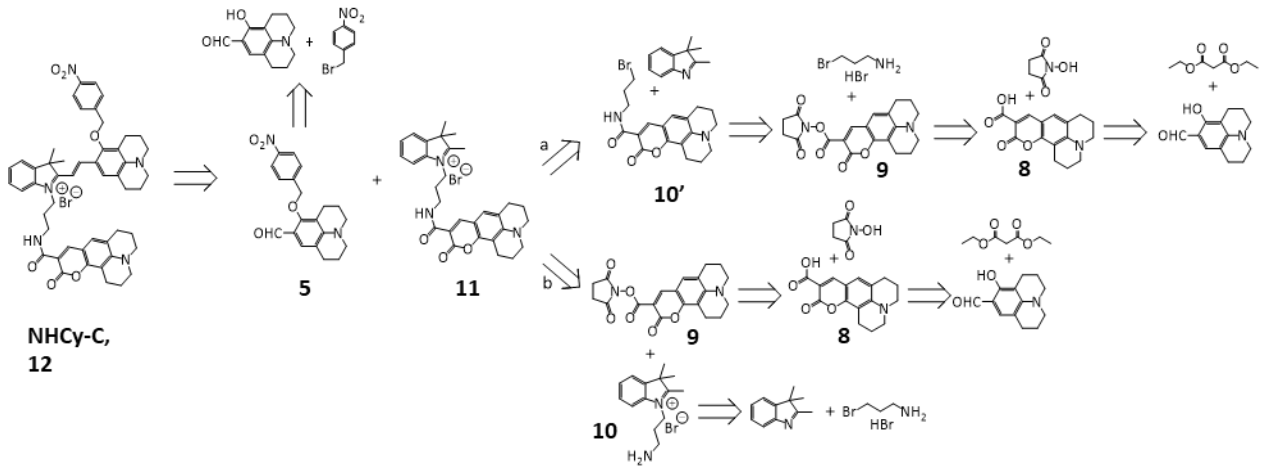

***Scheme 5**. Retrosynthetic analysis for the development ratiometric fluorescent probe **NHCy-C**.*

After extensive literature search, it was concluded that the most used approach for amide bond formation with similar substrate synthons consisted in reacting the activated ester (**9**) with the amide (**10'**) synthons. Thus, I proceeded with the synthesis of this probe considering the approach a from the retrosynthetic strategy mentioned above. The corresponding initial synthetic pathway (***Scheme 6***) was designed and reactions were carried out via adapted protocols found in the literature.[37,56,117,118,167]

A previously reported derivative of coumarin (**8**) was prepared by the Knoevenagel condensation of a diethyl malonate and commercially available derivative of *o*-hydroxy-benzaldehyde. proceeding through the mechanism presented on ***Scheme 7***. In particular, diethyl malonate loses an acidic proton in the presence of a base (piperidine) and thus, can attack the electrophilic carbonyl group of the other substrate, generating an alkoxide, which can be protonated and act as a leaving group when the proton of the adjacent carbon atom is subtracted, giving the expected coumarin via an intramolecular cyclisation / condensation reaction.

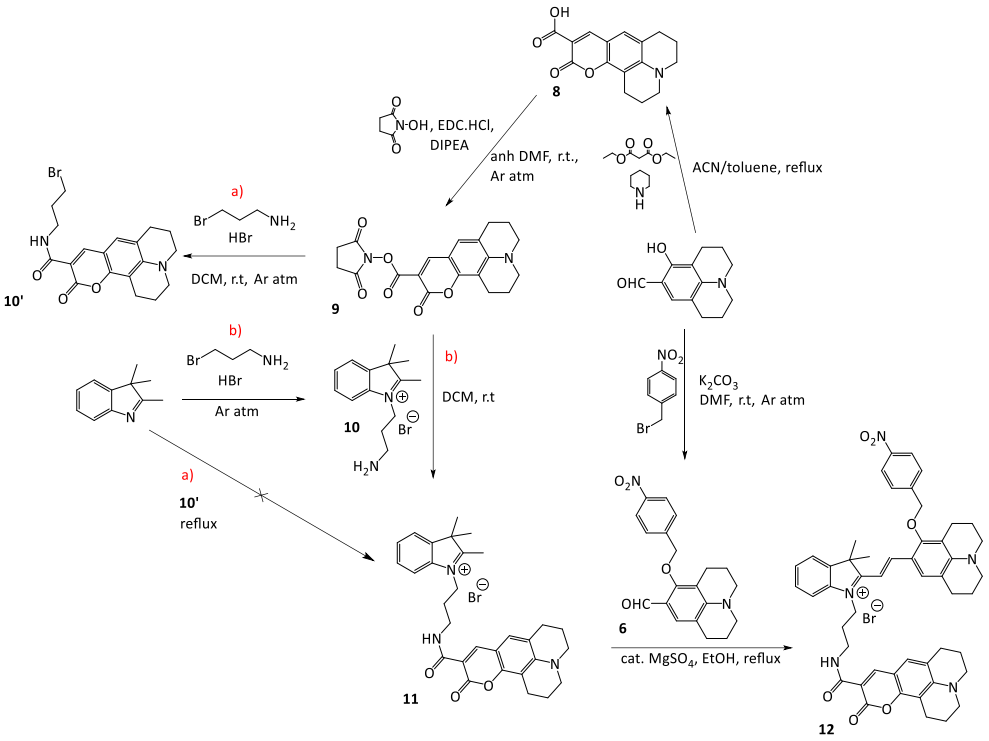

***Scheme 6**. Synthesis of pH and NTR activity responsive ratiometric fluorescent probe **NHCy-C**, **12**. Yields: **6**, 98.1%; **8**, 48.5%; **9**, 71.9; **10'**: 47.1%;**10**, 78.2%; **NHCy-C**, **12**, 3.0%.*

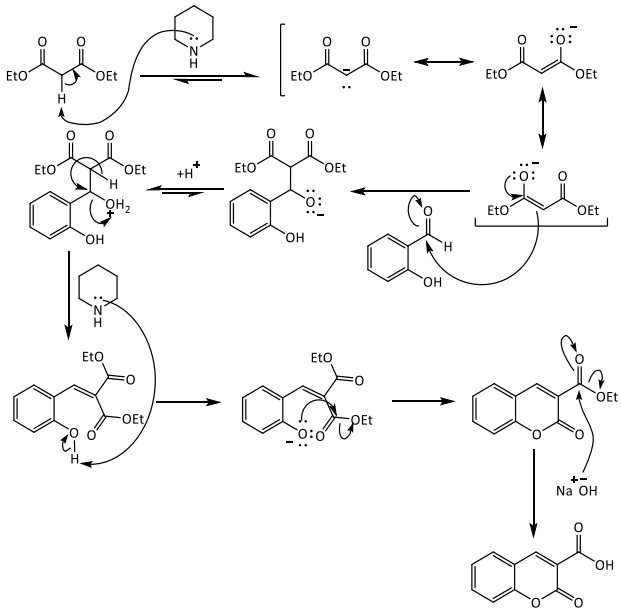

***Scheme 7**. Coumarin synthesis by Knoevenagel condensation.*

The mechanism of the formation of N-hydroxysuccinimide ester **9** and the corresponding amide compound **10** is presented on ***Scheme 8***. In particular, the carboxylic acid from the derivative of coumarin reacts with the electrophilic centre of the carbodiimide to form an O-acylisurea intermediate, which reacts with N-hydroxysuccinimide to give a more stable N-hydroxysuccinimide ester (**9**). An amide compound (**10**) is formed in the presence of a primary amine through a nucleophilic attack of the carbonyl group of the ester by the lone pair on the amine and the subsequent departure of the N-hydroxysuccinimide moiety as the leaving group. The formation of the N-hydroxysuccinimide esters can be confirmed by the addition of 4 more protons and by the change of chemical shift of the protons near the ester in the ^{1}H NMR.

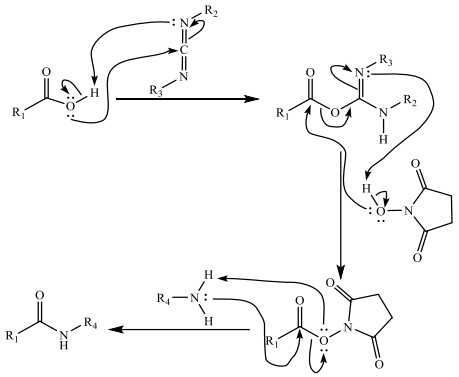

Scheme 8*. Synthesis of amide compounds by the formation of a N-hydroxysuccinimide ester.*

Unfortunately, failure to succeed with a formation of compound **10'** from **9** (no substrate conversion) led to exploring alternative synthetic route (approach b, ***Scheme 6***). In this alternative approach, the alkylamino linker is first introduced onto the indolenine synthon via a nucleophilic substitution with 3-bromopropan-1-amine hydrobromide (***Scheme 6***, compound **10**). This is then reacted with the NHS ester to obtain amide compound **11**. Subsequent reaction of 11 with the aldehyde via a condensation reaction (according to mechanism in Scheme 8) to yield the ratiometric dual-analyte probe **NHCy-C** (**12**).

The products' purity and identity were confirmed by NMR spectroscopy (^{1}H NMR, ^{13}C NMR, COSY), and mass spectrometry (HR-MS). Relevant spectra can be found in the Appendix. Compounds **6**, **10'**, **11**, and **12** are novel compounds.

3.4.3. Spectroscopic characterisation

The absorbance and fluorescence emission spectra of **NHCy-C** were collected in PBS pH 7.4 as a solvent and normalised to the maximum absorbance or fluorescence emission output (***Figure 57***). In such conditions, **NHCy-C** presents two absorption bands: a band from the coumarin fluorophore[36] and a second one from the hemicyanine fluorophore (due to the alkylamino group in *para* position[9], analogous to **NHCy**). It displays a green emission and a minimal red emission when excitation is done on the coumarin fluorophore (***Figure 57a***). It also presents a red emission when excitation takes place on the hemicyanine fluorophore (***Figure 57b***). The red emission signal in both cases is rather dim, as this fluorophore should be PeT quenched by the nitrobenzyl reduction-cleavable moiety.

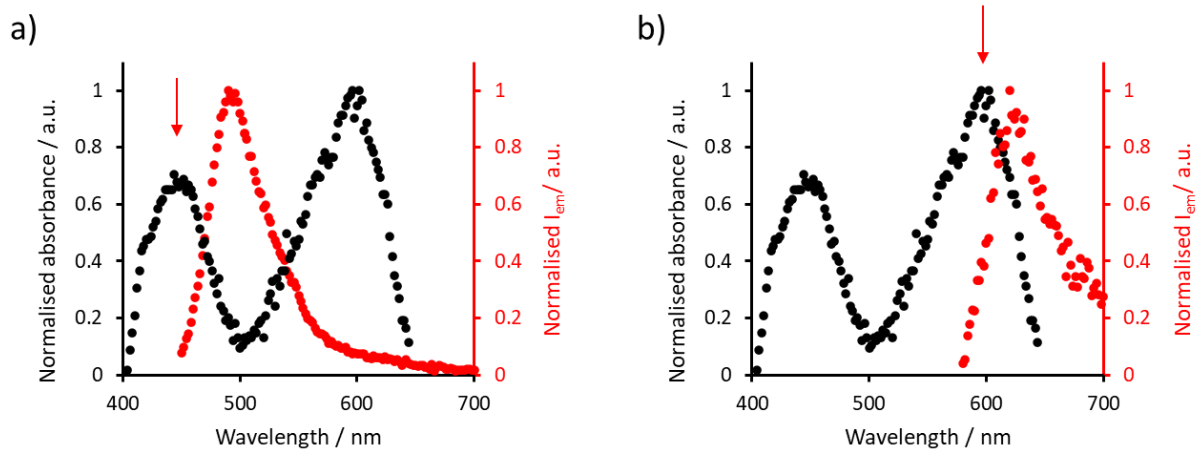

***Figure 57**. Normalised absorbance (black dots) and fluorescence emission (red dots) spectra for **NHCy** (2.5 µM) in PBS 7.4 (1% DMSO final): (a) $\lambda_{exc/em}$ = 420/450-700 nm, (b) $\lambda_{exc/em}$ = 550/480-700 nm. The red arrows mark the wavelength of excitation for the corresponding fluorescence emission spectrum collected. N = 3*

A concentration range of 2 - 16 µM was chosen, as all absorbance values at the excitation maximum were below 0.1 a.u. for all obtained solutions. A gradual rise in concentration consistently resulted in increased absorbance and emission intensity, according to the linear trend (***Figure 58 a-d***). The linearity of this relationship between concentration and absorption as well as emission intensity of this compound indicates that such concentration range poses no problems regarding its solubility, aggregation and/or self-quenching.

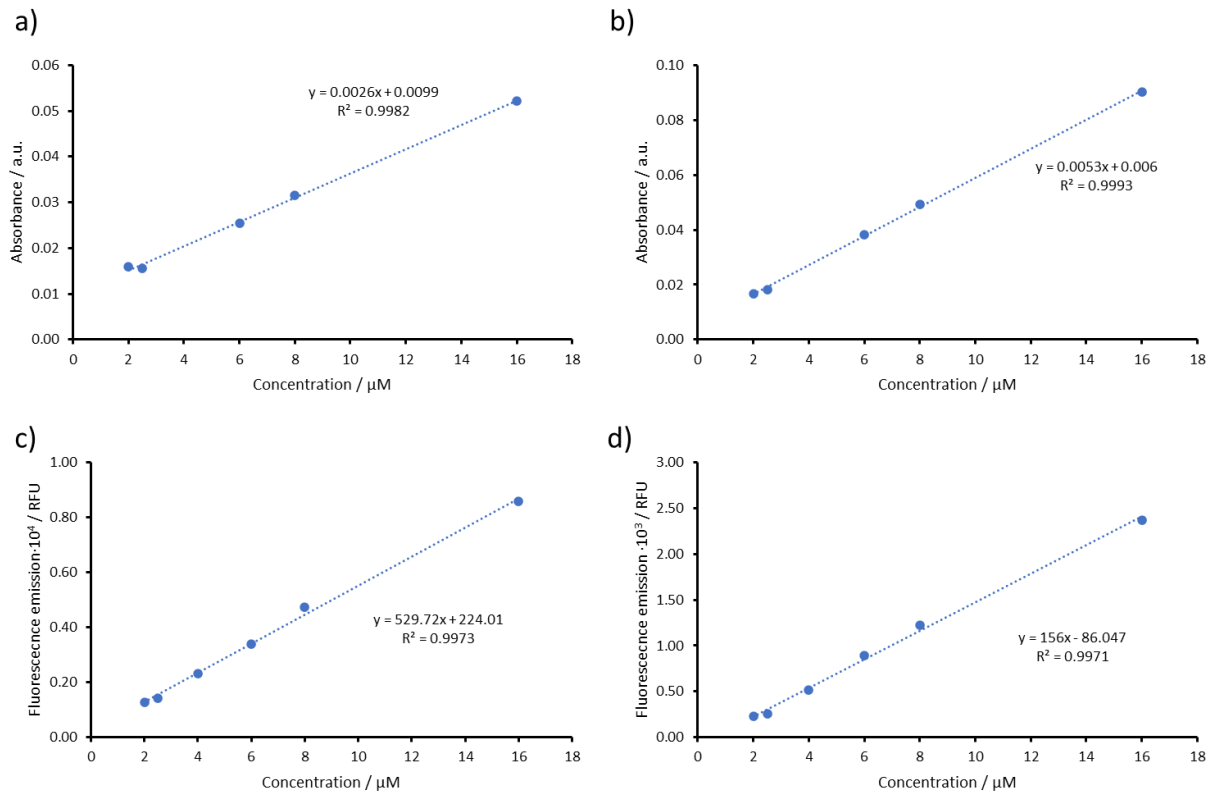

***Figure 58**. Plots of (a-b) absorbance vs concentration and (c,d) fluorescence emission vs concentration for N**HCy-C** (range 2-16 µM) in DMSO. (a,c) for coumarin region, $\lambda_{exc/em}$ = 450/486 nm, (b,d) for hemicyanine region, $\lambda_{exc/em}$ = 516/621 nm.*

Fluorescence spectroscopic studies of **NHCy-C** untreated and treated with NTR with NADH as co-factor in a range of pH buffered solution were carried out (***Figure 59***). Similarly to the experiments carried out in subchapter 3.2.3.2, two buffer solutions were selected: citrate-phosphate (CPB; pH values of 4, 6), and phosphate (PB; pH values of 6, 7.5) buffers with pH 6 as a common value of pH to account for potential buffer chemical nature-specific effects.[129] Untreated **NHCy-C** presents no significant difference in fluorescence of emission throughout both buffer solutions at all pH values when excited both at 550 nm (hemicyanine region) and at 420 nm (coumarin region). It must be mentioned that untreated **NHCy-C** presents some initial fluorescence emission in the hemicyanine region, as commented in Figure 52. When **NHCy-C** is excited in the hemicyanine absorbance region, a turn-on intensity-based response (6-fold increase) can be observed in the hemicyanine emission region in the presence of NTR and NADH at acidic pH (***Figure 59d***). Such mechanism of response is analogous to **NHCy**.

When **NHCy-C** is excited in the coumarin absorbance region, the probe presents two emission bands: a more intense one from the coumarin ($\lambda_{em,max}$ = 500 nm), and a significantly less intense one from the hemicyanine ($\lambda_{em,max}$ = 620 nm) (***Figure 59e-h***), that remains largely quenched. It is only in the presence of NTR (with NADH) in low pH that the emission band from the hemicyanine fluorophore presents a higher fluorescence emission signal (***Figure 59h***). Given the two possible bands of fluorescence excitation and the two bands emission, the probe indeed exhibits a ratiometric response. The ratio $\lambda_{em,max}$(hemicyanine)/$\lambda_{em,max}$(coumarin) can be calculated for untreated and treated samples of **NHCy** at different pH values. At pH 7.5, the ratios of untreated and treated probe are both within the range of 0.11 to 0.16, while the average ratios at pH 4 are 0.16 and 0.72, respectively (with standard deviation being significant on the third decimal digit). Given that the difference in ratios is significant, the observed fluorescence response of **NHCy-C** is encouraging for the validation of its use *in cellulo*. It should be mentioned that in the samples treated with NADH (***Figure 56e-h***) there is a contribution in the emission range of 450-550 nm due to the excitation of the co-factor in the wavelength of excitation of the coumarin fluorophore[26,27,28], and for this reason, blank subtraction was dine with blank sample containing these additives (in the same concentrations and %DMSO final). As for the fluorescence mechanism behind the fluorescence response of **NHCy-C**, an intramolecular energy transfer from coumarin emission to hemicyanine excitation could be speculated. Such energy transfer (e.g. FRET) would be possible since there is an overlap between the left tail of emission spectrum of the coumarin (donor) and the right tail absorption spectrum of the hemicyanine (acceptor) molecule.[10] Such hypothesis would be possible, considering that in the absorbance spectrum of the dual-analyte probe from the previous subchapter, **NHCy**, (***Figure 44d***) no absorbance band in the wavelength range of 370 – 470 nm (region of coumarin excitation band) can be observed.

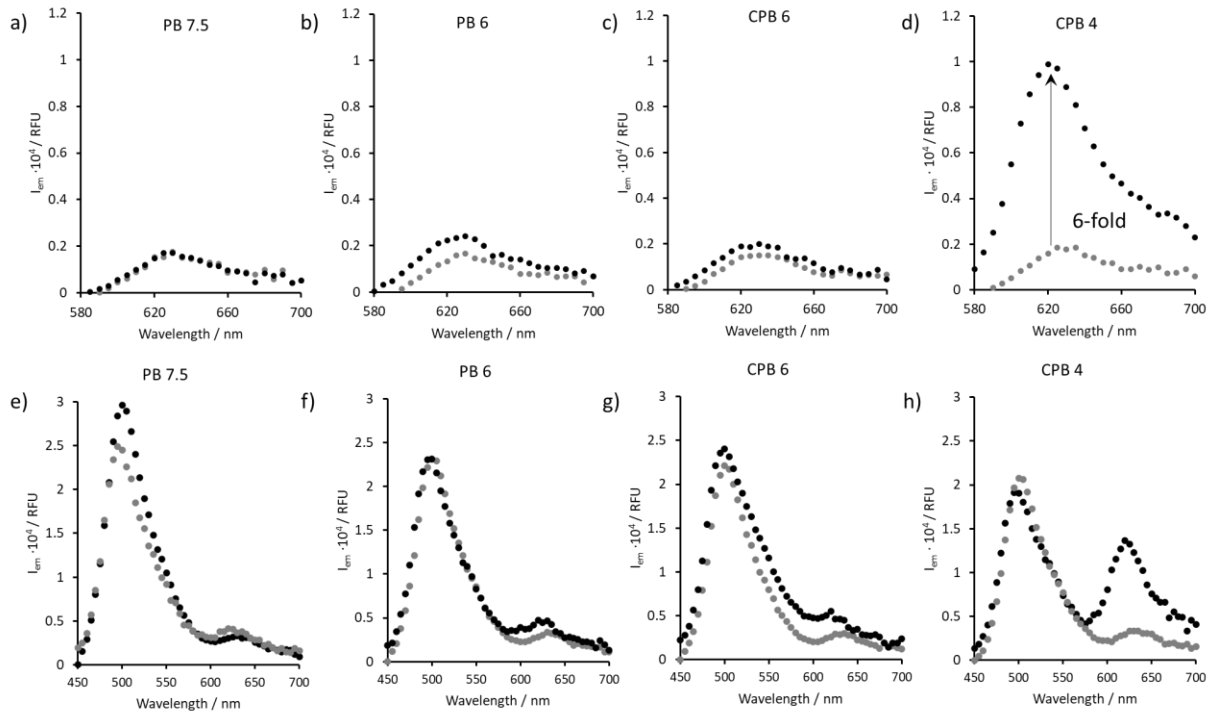

***Figure 59**. **NHCy-C** (2.5 uM) in PBS 1x pH 7.4 with 1% DMSO final in the absence (grey dots) and presence (black dots) of NTR (10 µg mL^{-1}) and NADH (500 µM) after 1 h of treatment. The blank samples presented the same %DMSO final. The blank sample for NHCy-C treated with NTR and NADH also contained the same concentration of these additives. Fluorescence emission spectra were collected at: (a-d) λ_{exc} = 550 nm and λ_{em} = 580 – 700 nm; (e-h) λ_{exc} = 420 nm and λ_{em} = 450 – 700 nm. PB, phosphate buffer; CPB, phosphate citrate buffer. N = 3*

3.4.4. Cellular behaviour

The prove has been validated in the experiments with three of the most widely used cancer cell lines in literature, including A549 (lung cancer) and DU145 (prostate cancer)[146], both previously used in experiments with **NHCy** probe and additionally also MCF-7 cell line (breast cancer, low metastatic potential)[168,169].

Cell viability studies were carried out to select the optimal concentration of **NHCy-C** fluorescent probe in all of the cell lines (***Figure 60***, ***Tables A5** and **A6*** in Subchapter 6.4 in Appendix). While cytotoxicity in DU145 and A549 cell lines was carried out according to the protocol described above for **NHCy** probe (1 h exposure, washing and cell death evaluation after 48 h), a toxicity against MCF7 cell lines was measured using MST assay (Promega kit) simply by exposing cells to

the probe for 24 h followed by cell viability evaluation. **NHCy-C** probe presents an IC_{50} value of 3.09 µM for DU145 in 384 well-plate format experiments, which is the equivalent to the absolute amount of probe contained in the volumes of 8.35 µM solution used in 4 compartments format imaging experiments. Little to no cell death was registered for A549 and MCF7 cells up to even 5 µM concentration of the probe. Therefore, given that cytotoxicity experiments were performed with 1 h exposure and then cell death evaluation after 48 h, a 2 µM concentration should be suitable for imaging in all of the cell lines both exposure time and experimental times are shorter than the ones used for cell viability studies. However, one needs to bear in mind that the probe still causes some long-term effect in DU145 cells viability.

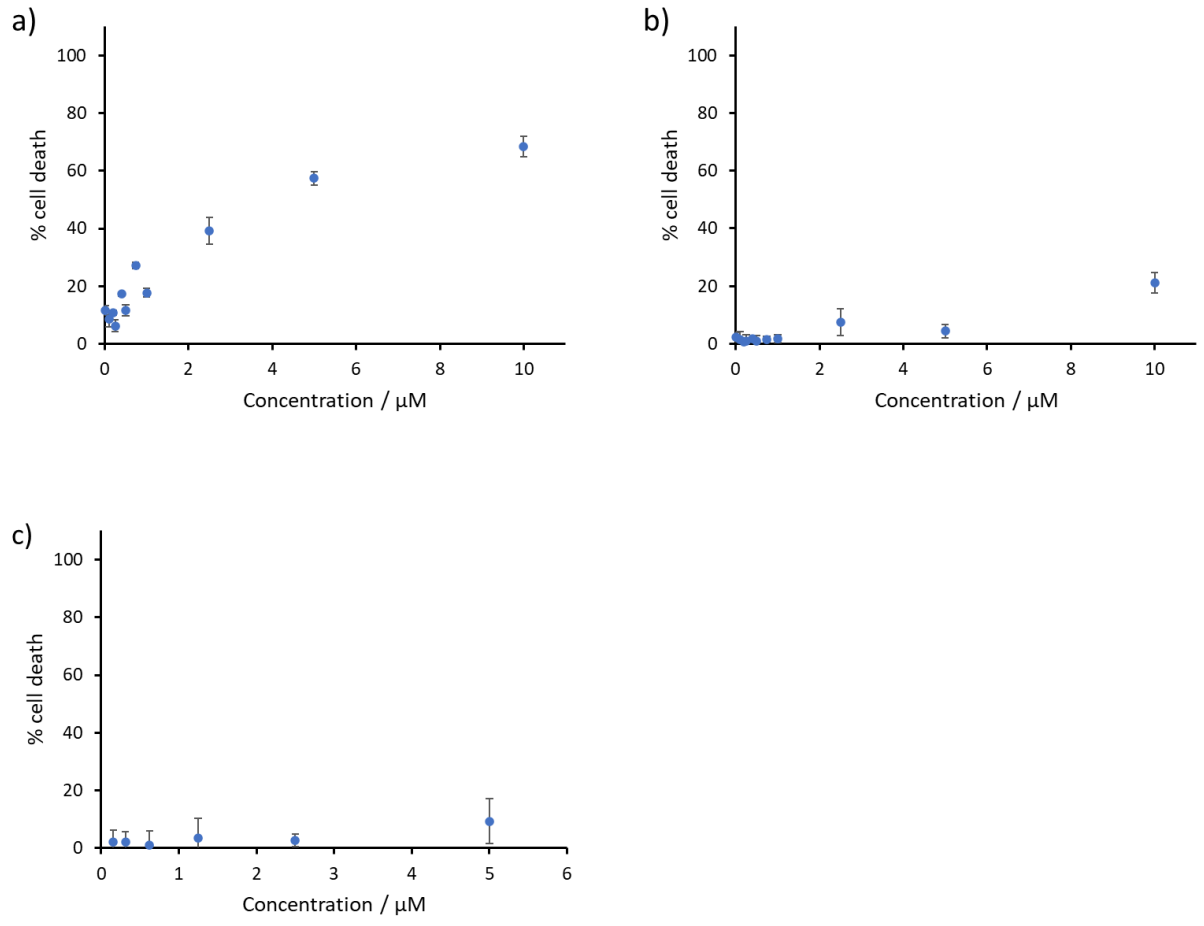

Figure 60. *Plots of cell death (%) vs the concentration (µM)* ***NHCy-C*** *in (a) DU145, (b) A549, and (c) MCF7 cell lines. N = 3*

Generally, fluorescence confocal microscopy experiments were carried out taking into consideration spectra presented on panel h from ***Figure 59*** to choose the appropriate channels of fluorescence wavelength of excitation and corresponding emission ranges. The emission ranges were divided into 4 channels (***Figure 61)***: coumarin emission (ch1), intersection emission (ch2), hemicyanine emission (ch3), and MT-DR or LT-DR emission (intended for co-localisation experiments).

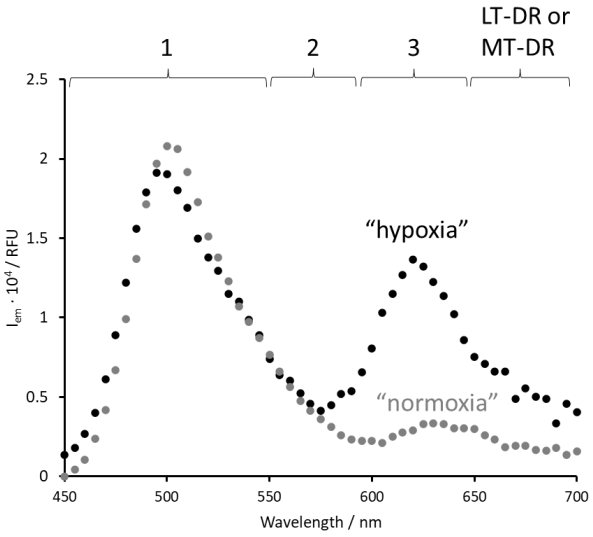

channel	exc/em
1	405/450-550
2	405/550-600
3	405/600-650
LT-DR/ MT-DR	640/660-700

Figure 61*. Selected channels for fluorescence confocal microscopy studies to determine hypoxic state in cells. Plot extracted from* ***Figure 57h****.*

Exposure of DU145 cell line treated with **NHCy-C** to normoxia and hypoxia for a previously used time (4 h) did not lead to significant change in fluorescence (data not shown). Only when hypoxia induction time was longer (10 h at 1% O_2), the fluorescence probe response was observed (***Figure 62***). Autofluorescence signal in both channels 1 and 3 (and for both normoxia and hypoxia conditions) is rather high, but it is considerably lower than that of the stained samples for channel 3 (as well as the ch3/ch1 ratio). Hypoxia induction did not cause significant change in fluorescent signal from ch1 (***Figure 62a,d***), but a statistically significant intensity increase in ch3 (***Figure 62b,e***), and so also the ratios of ch3 / ch1 (***Figure 62c,f***).

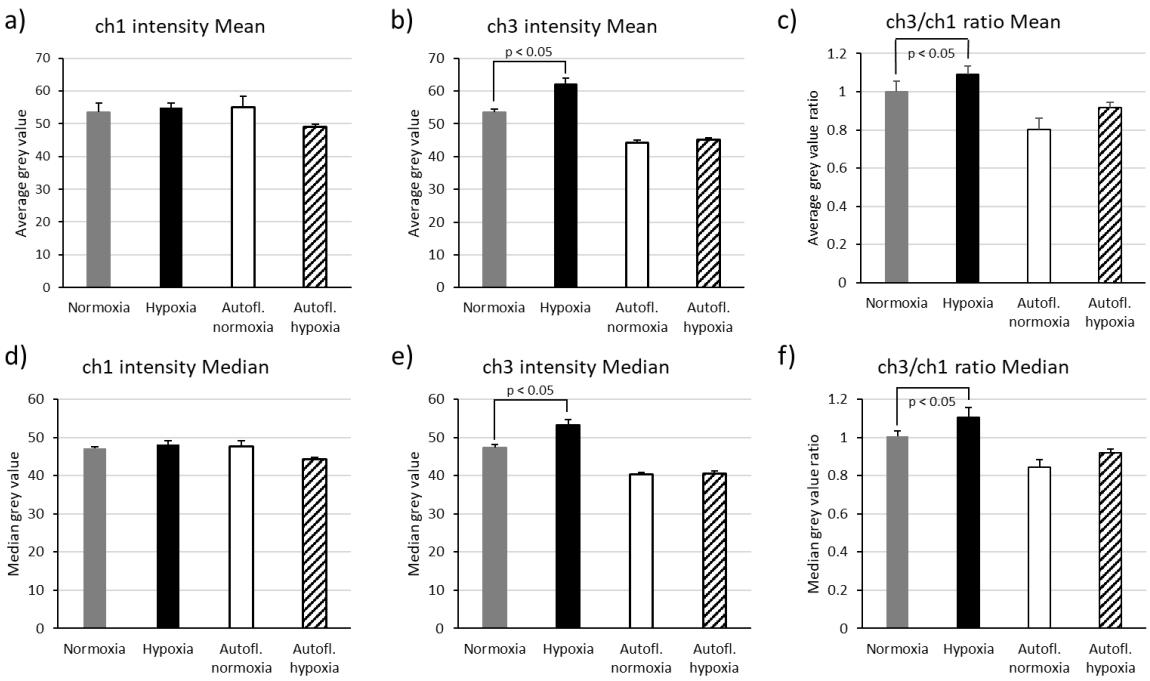

***Figure 62**. Quantification of hypoxic state via fluorescence confocal microscopy studies. DU145 cell line untreated in normoxic (white columns), hypoxic (dashed columns), treated with **NHCy-C** (2 µM) in normoxic (grey columns), hypoxic (black columns) conditions. All samples contained a final 1% of DMSO. (a-c) Average grey, (d-f) median grey value. Channels and ratio: ch1 (405/450-550); ch3 (405/600-650); ratio ch3/ch1. Shown for threshold 3 in ImageJ script. N = 5*

Co-localisation studies of **NHCy-C** with Lysotracker-Deep Red (LT-DR) were carried out in DU145 cell line. According to Pearson's Coefficient value (an approximate value of 0.23 ± 0.05, N = 3), **NHCy-C** does not localise in lysosomes and its fluorescent signal is spread out throughout the cytoplasm (***Figure 63a1-b2***). Co-localisation of these hemicyanine derivatives with lysotracker is unwanted due to the potential toxicity of the probe and the natural intrinsic low pH of lysosomes that can lead to false positive signal despite the lack of hypoxia-specific acidosis.

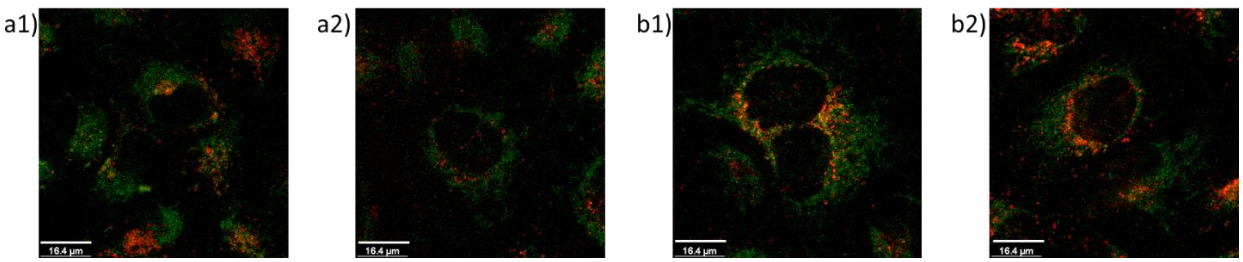

***Figure 63**. Overlay of green and red channels from co-localisation experiments of **NHCy-C** (2 µM, green channel) with LT-DR (50 nM, red channel) in DU145 cell line in (a1-2) normoxia and (b1-2) hypoxia. All*

samples contained a final 1% of DMSO. Green channel: λ_{exc} = 450 nm, λ_{em} = 500 nm - 550 nm. Red channel: λ_{exc} = 644 nm, λ_{em} = 654 nm - 700 nm). Scale bar: 16.4 µm. N = 3

The probe was further validated in MCF7 cells via fluorescence microscopy and flow cytometry by MSc Monica Pyc and collaborators in Spain (Centro de Investigación Príncipe Felipe (CIPF), Centro de Investigación Biomédica en Red Cáncer (CIBERONC)). Both fluorescence confocal microscopy and flow cytometry are techniques that rely on the fluorescence output for cellular and/or subcellular quantification and visualisation. Fluorescence confocal microscopy is superior when it comes to high-resolution imaging and spatial analysis of small cell populations, whereas flow cytometry is optimal for rapid, quantitative analysis of large cell populations (high throughput context).[170–172] The sample preparation is similar when it comes to staining and hypoxia induction, but flow cytometry often requires single-cell suspensions (contracted and round shaped cells); their detachment from the wells usually involves mechanic (scrapping) or enzymatic treatment.[154,172,173]

The first validation step was to study the localisation of **NHCy-C** in the cell. 2D cell cultures of MCF7 cell line were incubated in hypoxic conditions (induction for 24 h at 1% O_2), treated with **NHCy-C** (2.5 µM) and stained with MT-DR (***Figure 64a-d***). The obtained Pearson's coefficient has a value of 0.68 ± 0.02 (N = 3), hence it can be stated that the probe can be found in mitochondria as well as in other regions in the cell (especially cytoplasm – ***Figure 64a)*** and its fluorescence response is due to hypoxic state sensing.

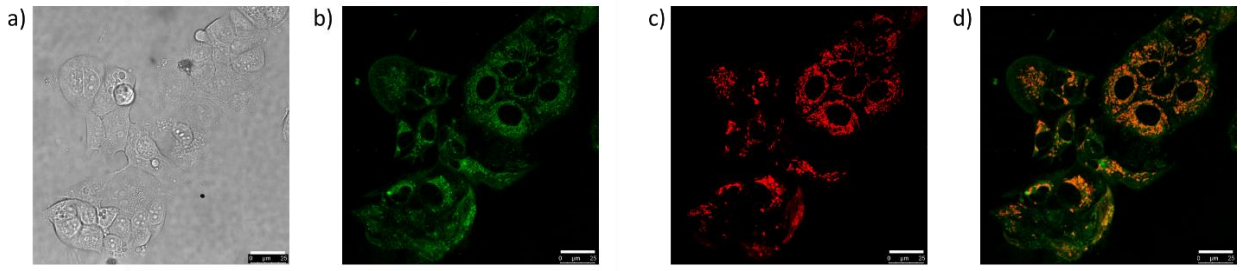

Figure 64*. Co-localisation experiments* ***NHCy-C*** *(2.5 µM, green channel) with MT-DR (100 nM, red channel) in MCF-7 cell line in hypoxic conditions via fluorescence confocal microscopy: (a) brightfield, (b) green channel, (c) red channel, (d) overlay of channels. Green channel: λ_{exc} = 450 nm, λ_{em} = 500 nm - 550 nm. Red channel: λ_{exc} = 644 nm, λ_{em} = 654 nm - 700 nm). Scale bar: 25 µm.*

2D cell cultures of MCF7 cell line incubated in normoxic and hypoxic conditions (induction for 24 h at 1% O_2) were treated with **NHCy-C** (2.5 µM), washed, and scratched manually before their subsequent injection to the flow cytometer. Flow cytometry scatter plots can be found in the Appendix subchapter 6.5. Flow cytometry studies of 2D cell cultures of MCF7 cell line incubated in normoxic and hypoxic conditions (**Figure 65a-c**) present similar results as in the fluorescence confocal microscopy mentioned above: intensity-based response in channel 3 (hemicyanine emission), and ratiometric response. However, the difference for both intensity- and ratiometric-based channels obtained for normoxia and hypoxia from flow cytometry presents a higher statistical significance than results from confocal microscopy. That is mainly due to the fact that the autofluorescence signal for both channels (but substantially for channel 3), is significantly lower in flow cytometry than the one obtained from fluorescence confocal microscopy studies. Therefore, it can be concluded that flow cytometry offers a better statistical power in this application.

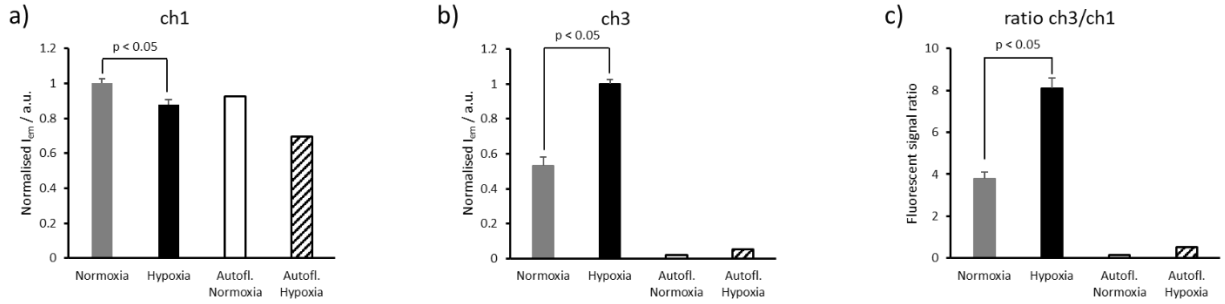

***Figure 65**. Flow cytometry experiment of MCF7 cells treated with **NHCy-C** fluorescent probe in normoxic and hypoxic conditions (a-c). MCF7 cells incubated in (grey column) normoxic, (black column) hypoxic conditions with **NHCy-C** (2.5 µM). The blank samples contained 1% final DMSO and were incubated in (white column) normoxic, (dashed column) hypoxic conditions. The samples were manually scratched. The fluorescence emission of all samples was collected in two channels (a) ch1, exc/em = 405/525; (b) ch3, exc/em = 405/610; and the corresponding (c) ch3/ch1 ratio was calculated. N = 1 for autofluorescence samples, and N = 4 for the rest.*

3.4.5. Summary

The spectroscopic characterisation of **NHCy-C** involved the collection of absorbance and emission spectra in several buffers and solvents. The probe presented two absorption bands, given by the two fluorophores linked via amide bond: coumarin (blue region), and hemicyanine (orange-red).

Upon excitation of the coumarin fluorophore, two emission bands can be observed in both the coumarin (green emission - intense) and the hemicyanine region (red emission - dim); while the excitation of the hemicyanine fluorophore gives a low intensity red emission. This low red emission observed in both cases is due to the unreacted hemicyanine form (before bio-reduction) quench via PeT mechanism by niotrobenzyl moiety.

Before delving into the fluorescence mechanism of response of **NHCy-C**, an initial validation step of the probe's integrity towards a biologically relevant interferent, GSH, was done. Neither **NHCy-C** nor its bio-reduced form should be prone to undergo nucleophilic addition of GSH, as one would expect from earlier results in chapter 3.2, where **HCy-Jul** was confirmed to present a more robust scaffold against the tested interferents. Such hypothesis was confirmed via exploration of **NHCy-C** fluorescence emission signal stability against GSH in the pH range of 7-9 also for coumarin band.

Validation *in vitro* was performed to test the probe's activation via treatment with NTR and NADH at different pH values. Bio-reduction of **NHCy-C** occurs analogously to **NHCy** and thus, a similar fluorescence response in the red emission is observed, while the emission from the coumarin fluorophore remained largely unperturbed. Therefore, as expected by the design, the probe exhibited a fluorescence ratiometric response. Such findings were correlated to results from *in cellulo* characterisation via both confocal microscopy and flow cytometry techniques confirming that the probe can indeed report on hypoxia in cellular models in unambiguous way in multiple cell types.

It can be concluded that **NHCy-C** usage for a ratiometric sensing of hypoxic state is suitable for both fluorescence confocal microscopy and flow cytometry techniques. Such suitability comes from a robust ratiometric-type response, no lysosomal localisation, **NHCy-C**'s fluorescence intensity significantly higher than the autofluorescence signal and minimal cytotoxicity within the time frame of the imaging experiment.

Thus, the rationally designed **NHCy-C** after the issues encountered with **NHCy**, mainly due to its intensity-based fluorescence response, has proved to be more reliable. Moreover, it would be the first reported dual-analyte ratiometric probe for hypoxia by surrogate sensing of two characteristic parameters of such state (NTR activity and pH).

4. Conclusions and outlook

Hypoxia state is characterised by several altered features and/or levels of chemical species caused by oxygen deficit, but many of these altered levels of chemical species have been associated to other diseases or medical conditions as well. It is only when several of them are present, that it can be unequivocally linked to hypoxia state. Most previously reported probes for hypoxia in fact respond to only one hypoxia biomarker, usually reducing capacity. For this reason, the main aim of this thesis was to develop stable dual-analyte fluorescent probes for sensing two characteristic parameters – reducing capacity and low pH.

The fluorophore core selection involved a rational design, synthesis and validation of the new hemicyanine-based scaffold, **HCy-Jul** for improved robustness and to limit off-target reactivities. **HCy-Jul** been extensively validated in vivo against various biologically interferents and showed superior stability, especially towards biorelevant nucleophiles, than the previously used hemicyanine scaffolds.

Once the new more stable core was developed, a dual-analyte fluorescent probe, **NHCy**, based on this scaffold and including two responsive moieties was designed, synthesized and and validated *in vitro* and *in cellulo*. The probe has been successfully used to distinguish between hypoxia and normoxia-exposed A549 cells via an increase in probe specific fluorescence. However, a turn-on mechanism of response did not allow for a reliable conclusion on the existence or a lack of hypoxic conditions in 3D cellular model of DU145 tumour spheroids.

Considering its inherent limitations due to its fluorescence response being intensity-based, **NHCy-C**, an analogous dual-analyte (pH and bioreduction) fluorescent probe that exhibited a ratiometric response was developed and its reliability was validated *in vitro* and *in cellulo*. The probe has proven to reliably report on the hypoxic conditions in both DU145 and MCF7 cells and showed compatibility with both fluorescent imaging and flow cytometry.

To the best of our knowledge, **NHCy** and **NHCy-C** are the first examples of dual-analyte probes that were sown to being able to detect hypoxia in cellular models based on response to two surrogate conditions (rather than single analyte). Compared to single-analyte probes, these

probes can provide a more extensive and comprehensive view of biological processes occurring in cells by concurrently detecting several analytes linked to hypoxia state. The ratiometric response of **NHCy-C** to both analytes positions it as a reliable tool to detect hypoxia in a wide range of biological models and with unmatched robustness. The knowledge gained by the use of these new tools may be extremely helpful in a better understanding of the diseases and facilitate development of new predictive biomarkers and better treatments.

5. Methodology

5.1. General

Milli-Q water was used to prepare all aqueous solutions. Commercially available chemicals were were of analytical grade and used without further purification. Solvents, salts, acids, bases and drying agents were collected from the warehouse (POCH, Chempur).

Chemicals used for synthesis: 3-bromopropylamine hydrobromide (#B1263, TCI), 4-diethylaminobenzaldehyde (# D86256-100G, Sigma Aldrich), n-butylamine (#B0707, TCI), 9-julolidinecarboxaldehyde (# J0008, TCI), 8-hydroxyjulolidine-9-carboxaldehyde (# H1225, TCI), piperidine (# 721 SC486524, Merck), 2,3,3-trimethylindolenine (# T76805, Sigma Aldrich), 4-(diethylamino)salicylaldehyde (# 225681, Sigma Aldrich), 4-nitrobenzaldehyde (# 130176, Sigma Aldrich), 2-hydroxy-5-nitrobenzaldehyde (# 275352, Sigma Aldrich), 4-nitrobenzyl bromide (# N13054, Sigma Aldrich), diethyl malonate (# W237507, Sigma Aldrich), piperidine (# 411027, Sigma Aldrich), 1-ethyl-3-(3-dimethylaminopropyl)carbodiimide hydrochloride (EDC·HCl, # 8009070001, Sigma Aldrich), N-hydroxysuccinimide (# 130672, Sigma Aldrich), N,N-diisopropylethylamine (DIPEA, # 496219, Sigma Aldrich).

All metal ion salts for fluorescent measurements were from commercial sources were of analytical grade. Iron(III) chloride hexahydrate (# 236489), iron(II) sulfate heptahydrate (#215422), lead(II) nitrate (# 228621), manganese (II) sulfate monohydrate (# M7899), magnesium sulfate (# 746452), potassium nitrate (# 221295), potassium phosphate (# P5379), silver nitrate (# 209139), tetrakis(acetonitrile)copper(I) tetrafluoroborate (# 677892), tin(II) chloride (# 208256), Trizma base (# T6066) from Sigma-Aldrich. Sodium chloride (# 54447) from Warchem. Calcium nitrate tetrahydrate from Chmes. Cesium carbonate (# C2160) from TCI. Potassium tetrachloroplatinate(II) (# 11396315), zinc nitrate hexahydrate (# 10036103), aluminium nitrate nonahydrate (# 15269686), copper(II) nitrate trihydrate (#10124790), nickel(II) nitrate hexahydrate (# 10401651), iron(II) chloride (# 10401251), sodium nitrate (# 11904281) from ThermoScientific Acros. Potassium carbonate (# 427465708), sodium sulfate (# 118078707) from Chempur. Ammonium iron(II) sulfate hexahydrate (# 10087291), cobalt(II) nitrate

hexahydrate (# 10529380), lithium nitrate (# 10568620) from Fisher Chemical. Cadmium nitrate tetrahydrate (# 11351579), gallium nitrate monohydrate (# ALF-032116-14) from Alfa Aesar. DMSO (# 83673.290) from VWR. PBS (# 10010-015) and EDTA (# AM9260G) from ThermoFisher Scientific. NaOH (# 810981424) from POCH.

Phosphate buffer saline (PBS, # E0282-01 from EURX Sp. z o.o., or #10010023 from ThermoFisher Scientific), citric acid (# 145382101, Chempur), disodium hydrogen phosphate (# NIST2186II, Sigma Aldrich), sodium phosphate monobasic dihydrate (# 71500, Sigma Aldrich), HEPES (# H3375-25G) from Sigma Aldrich. Buffered solutions were brought to the correct pH with Mettler Toledo™ FiveEasy F20 pH-meter. Viscosity and polarity studies were carried out with glycerol (# G7893, Sigma Aldrich), and 1,4-dioxane (#PA-06-292300418, POCH).

DMSO for molecular biology (# 327182500) was used for dissolving and diluting the hemicyanine derivatives as well as the probe samples. A549, DU145, HEK cell lines were cultured in DMEM High Glucose (# 11965092, ThermoFisher Scientific; or # DMEM-HPA, Capricorn Scientific) supplemented with 10% fetal bovine serum (FBS, # E5050, EURx), 1% penicillin-streptomycin (# 17-745E, Lonza^{TM} BioWhittaker^{TM}). Staurosporine (# T6680, TargetMol) was used as positive control for cell viability studies.

Deuterated NMR solvents for NMR spectroscopy were purchased from Sigma Aldrich: chloroform-d ($CDCl_3$, # 151858), methanol-d_4 (MeOD, # 151947), dimethylsulfoxide-d_6 (d_6-DMSO, # 156914), acetonitrile-d_3 (or CD_3CN, # 233323).

5.2. Synthesis and characterisation

All reactions were monitored by thin-layer chromatography (TLC). Column chromatography was performed using silica gel 60 mesh. ^{1}H NMR and ^{13}C NMR analysis were performed using Spectrometer NMR 400 MHz (9.39 T) AVANCE II Bruker, 500 MHz (11.74 T) NMR Spectrometer AVANCE III Bruker, and Spectrometer NMR 700 MHz (16.44 T) AVANCE III Bruker. Chemical shifts are given in parts per million (ppm) units and coupling constants are given in Hz. Multiplicity of signals is described with abbreviations: s, d, dd, t, q, m standing for, respectively, singlet, doublet,

double of doublets, triplet, quartet, multiplet. Calibration of the spectra was done with the residual peak of the solvent.

High Resolution Mass Spectrometry analysis of samples was performed on Q-Exactive Orbitrap mass spectrometer (Thermo Fisher Scientific, Bremen, Germany) equipped with TriVersa NanoMate robotic nanoflow ESI ion source (Advion BioSciences ltd., Ithaca, USA). The nanoelectrospray chips with nozzles' diameter of 5.5 µm were used in order to obtain stable ion spray and Chipsoft software (ver. 8.3.1.1018) was applied to control ESI ion source. 5 µL of sample were infused directly into mass spectrometer, after ion current stabilization, sample was measured for 1 minute. The source was operated at gas pressure of 1.25 psi and ionization voltage was set to 1.05 kV. MS data were acquired in positive ion mode within the range of m/z 150 – 1500 at the resolution of 140,000 (at m/z 200, FWHM). Automatic gain control was set to target value of $3 \cdot 10^6$ and ion injection time (IT) was 100 ms. Raw data were analysed in Thermo Xcalibur Qual Browser 3.1 software.

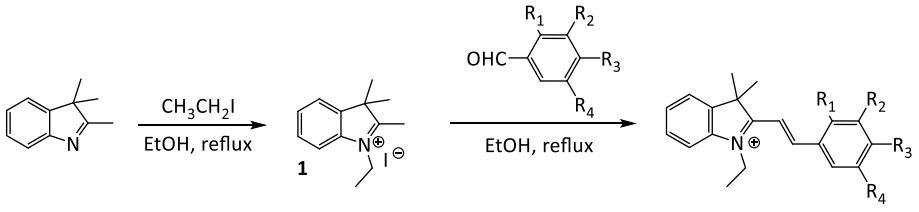

2 R_1,R_2,R_4: H, R_3: OMe
3 R_1,R_2,R_4: H, R_3: NEt_2
4 R_1: H, R_2: CH_2R, R_3: NCH_2R'
5 R_1: OH, R_2: CH_2R, R_3: NCH_2R'

Scheme A1*. Synthetic scheme of compound **1** and subsequent hemicyanine derivatives **2-5**. Yields: **1**, 48.8%; **2**, 34.2%; **3**, 98.5%; **4**, 99.2%; **5**, 23.5%.*

1,2,3,3-tetramethyl-3H-indolium iodide (1)

1 has been synthesized by using an adapted procedure from [174]. 2,3,3-trimethylindolenine (2.008 g, 12.6 mmol) and iodoethane (2.006 g, 12.6 mmol) were dissolved in anhydrous acetonitrile (20 mL) and heated at reflux for 6 h. The solvent was removed by rotatory evaporation and the crude product was dispersed in acetone (25 mL), resulting in the formation of the pink precipitate **1** (1.941 g, 48.8%), was isolated by vacuum filtration and washed with cold diethyl ether (5 mL).

δ_H(400 MHz; $CDCl_3$): 7.71 (m, 1H), 7.59 (m, 3H), 4.77 (q, ^3J = 7.0 Hz, 2H), 3.16 (s, 3H), 1,62 (m, 9H) ppm.

(E)-1-ethyl-2-(4-methoxystyryl)-3,3-dimethyl-3H-indol-1-ium iodide (HCy-OMe, 2)

Adapted procedure from [117]. 1,2,3,3-tetramethyl-3H-indolium iodide (237 mg, 0.752 mmol), p-anisaldehyde (102 mg, 0.749 mmol) and piperidine were dissolved in EtOH (25 mL) and the reaction mixture was refluxed with stirring for 10 h and then evaporated in vacuo. The crude product was purified by column chromatography DCM by increasing MeOH percentage and the solvent of the collected fractions was evaporated to give **2** as a brown solid (81 mg, 34.2%). δ_H(400 MHz; CD_3CN): 8.31 (d, 1H, J = 16.0 Hz), 8.11 (d, 2H, ^3J = 9.0 Hz), 7.74-7.72 (m, 2H), 7.60 (q, 2H, ^3J = 3.5 Hz), 7.36 (d, 1H, ^3J = 16.0 Hz), 7.12 (d, 2H, ^3J =9.0 Hz), 4.63-4.58 (m, 2H), 3.91 (s, 3H), 1.79 (s, 6H), 1.52 (t, 3H, ^3J = 7.0 Hz) ppm.

(E)-2-(4-(diethylamino)styryl)-1-ethyl-3,3-dimethyl-3H-indol-1-ium iodide (HCy-NEt_2, 3)

3 has been synthesized by using an adapted procedure from [175]. **1** (89 mg, 0.29 mmol) and 4-diethylaminobenzaldehyde (104 mg, 0.86 mmol) were dissolved in EtOH (10 mL) and heated at reflux for 5 h. The crude product was purified by column chromatography DCM by increasing MeOH percentage and the solvent of the collected fractions was evaporated to give **3** as a dark purple solid (133 mg, 98.5%). δ_H(400 MHz; $CDCl_3$): 8.13-8.00 (m, 2H), 7.53-7.45 (m, 3H), 7.39 (m, 2H), 6.81 (d, ^3J = 8.5 Hz, 2H), 4.79 (q, ^3J = 7.0 Hz, 2H), 3.53 (q, ^3J = 7.0 Hz, 4H), 1.77 (s, 6H), 1.57 (t, ^3J = 7.0 Hz, 6H) ppm. m/z (ESI) calculated for $[C_{24}H_{31}N_2]^+ = [M^+]$: 347.25, found 347.25.

(E)-1-ethyl-3,3-dimethyl-2-(2-(2,3,6,7-tetrahydro-1H,5H-pyrido[3,2,1-ij]quinolin-9-yl)vinyl)-3H-indol-1-ium iodide (HCy-Jul, 4)

4 has been synthesized by using an adapted procedure from [175]. **1** (319 mg, 1.02 mmol) and 9-julolidinecarboxaldehyde (206 mg, 1.02 mmol) were dissolved in absolute EtOH (15 mL) and heated at reflux for 6 h. The crude product was purified by column chromatography with DCM by increasing diethyl ether percentage, then back to DCM and with increasing MeOH percentage. The solvent of the collected fractions was evaporated to give **4** as a dark purple solid (504 mg, 99.2%). δ_H(400 MHz; d_6-DMSO): 8.16 (d, 1H, ^3J = 15.0 Hz), 7.74-7.62 (m, 4H), 7.51 (t, 1H, ^3J = 7.0

Hz), 7.42 (d, 1H, ^3J = 7.5 Hz), 7.08 (d, 1H, ^3J = 15.0 Hz), 4.47 (d, 2H, ^3J = 7.0 Hz), 3.44 (t, 4H, ^3J = 5.5 Hz), 2.76 (t, 4H, ^3J = 6.0 Hz), 1.91 (t, 4H, ^3J = 5.0 Hz), 1.71 (s, 6H), 1.36 (t, 3H, ^3J = 7.0) ppm. δ_C(500 MHz; d_6-DMSO): 177. 01, 153.78, 149.36, 142.27, 140.85, 128.65, 126.60, 122.57, 121.59, 112.60, 102.19, 50.24, 49.94, 26.75, 26.59, 20.40, 12.94 ppm. m/z (ESI) calculated for $[C_{26}H_{31}N_2]^+$ = $[M^+]$: 371.25, found 371.25.

(E)-1-ethyl-2-(2-(8-hydroxy-2,3,6,7-tetrahydro-1H,5H-pyrido[3,2,1-ij]quinolin-9-yl)vinyl)-3,3-dimethyl-3H-indol-1-ium iodide (5)

5 has been synthesized by using an adapted procedure from [175]. **1** (288 mg, 0.92 mmol) and 8-hydroxyjulolidine-9-carboxaldehyde (202 mg, 0.92 mmol) were dissolved in EtOH (10 mL) and heated at reflux for 4.5 h. The crude product was purified by column chromatography with DCM by increasing MeOH percentage and the solvent of the collected fractions was evaporated to give **5** as a dark purple solid (111 mg, 23.5%). δ_H(500 MHz, d_6-DMSO): 9.89 (s, 1H), 8.44 (d, 1H, ^3J = 14.0 Hz), 7.68 (m, 2H), 7.53 (d, 1H, ^3J = 8.0 Hz), 7.47 (t, 1H, ^3J = 7.0 Hz), 7.34 (t, 1H, ^3J = 7.5 Hz), 6.97 (s, 1H), 4.35 (q, 2H, ^3J = 7.0 Hz), 3.44- 3.41 (m, 4H), 2.70 (t, 2H, ^3J = 6.0 Hz), 2.61 (t, 2H, ^3J = 6.0 Hz), 1.89-1.85 (m, 4H), 1.33 (t, 3H, ^3J = 7.0 Hz) ppm. m/z (ESI) calculated for $[C_{26}H_{31}N_2O]^+$ = $[M]^+$: 387.24, found 387.24.

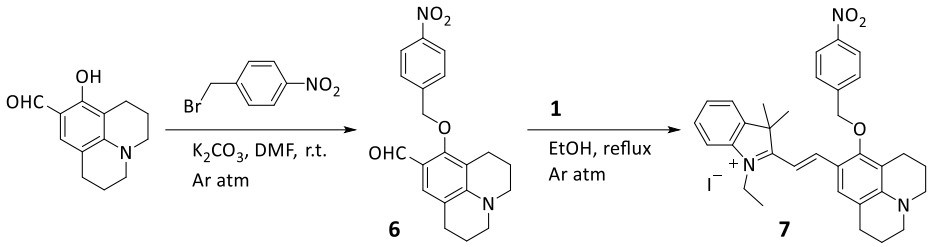

***Scheme A2**. Synthesis of protected salicylaldehyde **6** and **NHCy** probe **7**. Yields: **6**, 91.0%; **7**, 33.0%.*

8-((4-nitrobenzyl)oxy)-2,3,6,7-tetrahydro-1H,5H-pyrido[3,2,1-ij]quinoline-9-carbaldehyde (6)

6 has been synthesized by using an adapted procedure from [118]. 9-Formyl-8-hydroxyjulolidine (217 mg, 2.21 mmol), K_2CO_3 (610 mg, 4.42 mmol), 1-(bromomethyl)-4-nitrobenzene (582 mg, 2.70 mmol) were dissolved in anhydrous DMF (13 mL). The reaction mixture was stirred at r.t. under Ar atm for 24 h. Distilled water (20 mL) and $NaHCO_3$ 0.2 M (20 mL) were added and the reaction mixture was extracted with EtOAc (6x20 mL). The organic phase was then extracted with

brine (3x30 mL), dried over Na_2SO_4 and the solvent evaporated under reduced pressure. The crude was purified by column chromatography in silica gel from Hex/DCM (2:8) to DCM increasing MeOH percentage. The collected fractions were evaporated under reduced pressure and **6** was obtained as an ochre precipitate (764 mg, 98.1%). δ_H(400 MHz; $CDCl_3$): 9.88 (s, 1H), 8.26 (m, 2H), 7.65 (d,^3J = 7.0 Hz, 2H), 7.34 (s, 1H), 5.02 (s, 2H), 3.30 (q, ^3J = 6.0 Hz, 4H), 2.74 (dt, ^3J = 10.0, 6.5 Hz, 4H) 1.96 (m, 4H) ppm. δ_C(400 MHz; $CDCl_3$): 187.17, 128.63, 127.94, 123.69, 117.40, 116.61, 112.45, 75.13, 50.00, 49.60, 27.25, 21.23, 21.03, 20.62 ppm. m/z (ESI) calculated for $[C_{20}H_{20}N_2O_4]^+ = [M+H]^+$: 352.14, found 352.14.

NHCy (7)

7 has been synthesized by using an adapted procedure from [117]. **6** (152 mg, 0.43 mmol) and **1** (135 mg, 0.43 mmol) were dispersed in EtOH (10 mL). The reaction mixture was set at reflux under Ar atm for 5 h. A dark precipitate appeared while the reaction mixture was cooling down. It was left to crystallize overnight. The precipitate was vacuum filtered and washed with EtOH (5 mL). The collected fractions were evaporated under reduced pressure and the crude was purified by column chromatography in alumina gel 50% Acetone/DCM to 100% Acetone. **7** was obtained as an ochre precipitate (92 mg, 33.0%). δ_H(400 MHz; $CDCl_3$): 8.36 (m, 2H), 8.16 (d, ^3J = 15.5 Hz, 1H), 7.90 (s, 1H), 7.86-7.80 (m, 2H), 7.68-7.58 (m, 2H), 7.49 (td, ^3J = 7.5, 1.0 Hz, 1H), 7.38 (dd, ^3J = 8.0, 7.0 Hz, 1H),7.10 (d, ^3J = 15.5 Hz, 1H), 5.11 (s, 2H), 4.38 (q, ^3J = 7.0 Hz, 2H), 3.52-3.41 (m, 4H), 2.78 (t, ^3J = 6.0 Hz, 4H), 1.98-1.84 (m, 4H), 1.45 (s, 6H), 1.30 (t, ^3J = 7.0 Hz, 3H) ppm. δ_C(500 MHz; d_6-DMSO): 163.12, 161.18, 154.37, 152.30, 148.50, 143.10, 140.03, 130.17, 130.10, 123.06, 123.04, 119.77, 113.78, 113.61, 113.43, 113.27, 87.89, 85.85, 73.46, 70.59, 61.60, 42.45, ppm. m/z (ESI) calculated for $[C_{33}H_{36}N_3O_3]^+ = [M^+]$: 522.28, found 522.28.

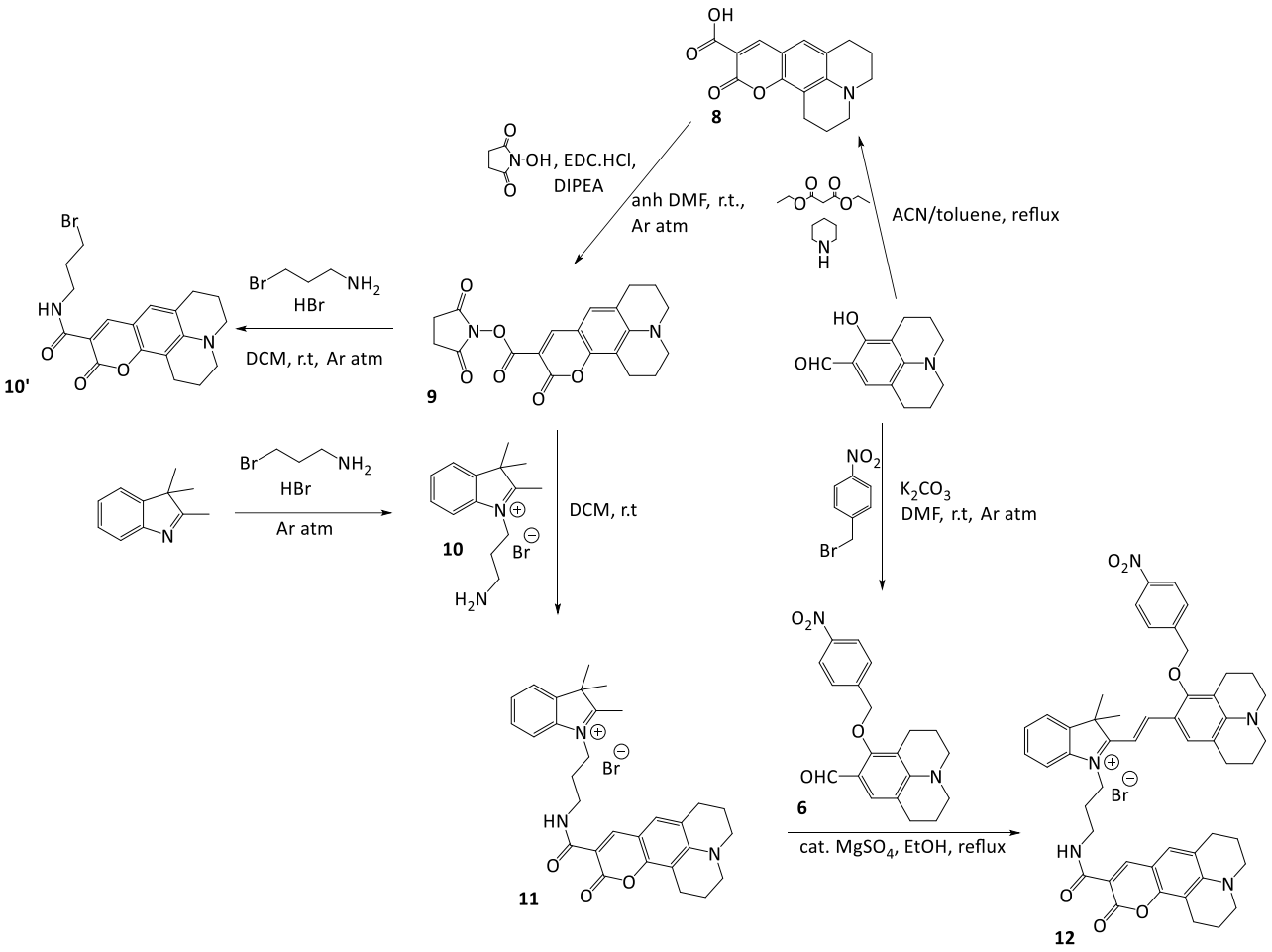

***Scheme A3**. Synthesis of pH and NTR activity responsive ratiometric fluorescent probe **NHCy-C, 12**. Yields: **6**, 98.1%; **8**, 48.5%; **9**, 71.9; **10'**: 47.1%;**10**, 78.2%; **12**, 3.0%.*

11-oxo-2,3,6,7-tetrahydro-1H,5H,11H-pyrano[2,3-f]pyrido[3,2,1-ij]quinoline-10-carboxylic acid (8, coumarin 343)

8 (coumarin 343) has been synthesized by using an adapted procedure from [167]. 9-Formyl-8-hydroxyjulolidine (1.993 mg, 9.2 mmol) and diethylmalonate (4.545 g, 28.4 mmol) were dissolved in a mixture of acetonitrile (18.5 mL) and toluene (37 mL). Then, piperidine was added (3.986 g, 46.8 mmol) and the reaction mixture was heated at reflux for 25 h. The solvent was removed by rotatory evaporation and the crude product was dissolved in conc. HCl (34.5 mL) and was left stirring overnight, resulting in a dark red solution. Distilled water was added (10 mL) and **8** was obtained as an ochre precipitate, which was isolated by vacuum filtration and dried in air (1.270 g, 48.5%). Distilled water (2 mL) was added to the filtrate to check that the process of

precipitation had been completed. δ_H(400 MHz; $CDCl_3$): 12.48 (s, 1H), 8.48 (s, 1H), 7.00 (s, 1H), 3.38 (m, 4H), 2.88 (t, ^3J = 6.5 Hz, 2H), 2.79 (t, ^3J = 6.0 Hz, 2H), 1.99 (m, 4H) ppm.

2,5-dioxopyrrolidin-1-yl 11-oxo-2,3,6,7-tetrahydro-1H,5H,11H-pyrano[2,3-f]pyrido[3,2,1-ij]quinoline-10-carboxylate (9)

9 has been synthesized by using an adapted procedure from [56]. **8** (499 mg, 1.75 mmol), EDC·HCl (511 mg, 2.63 mmol), DIPEA (500 µL, 2.65 mmol) were dissolved in a mixture of anhydrous DCM (5 mL) and anhydrous DMF (10 mL). A solution of N-hydroxysuccinimde (301 mg, 2.63 mmol) in anh. DMF (10 mL), was then added and the reaction mixture was stirred at r.t. under Ar atm for 27 h. The yellow precipitate was isolated by vacuum filtration and dried in air (481 mg, 71.9%). δ_H(400 MHz; DMSO-d_6): 8.59 (s, 1H), 7.30 (s, 1H), 3.40 (br, 6H), 2.87 (br, 4H), 2.71 (br, 4H), 1.89 (br, 4H) ppm.

N-(3-bromopropyl)-11-oxo-2,3,6,7-tetrahydro-1H,5H,11H-pyrano[2,3-f]pyrido[3,2,1-ij]quinoline-10-carboxamide (10')

10' has been synthesized by an adapted procedure from [37]. **9** (347 mg, 0.92 mmol) was dissolved with a mixture of DCM (25 mL) and triethylamine (194 µL, 1.39 mmol). 3-Bromopropan-1-amine hydrobromide was added (304 mg, 1.39 mmol) and the reaction mixture was stirred at r. t. overnight. The reaction mixture was then diluted with DCM (25 mL) and extracted with $NaHCO_3$ (0.2 M, 3x25 mL), HCl (0.2 M, 3x25 mL) and brine (3x25 mL), subsequently. The resulting organic phase was dried over Na_2SO_4 and the solvent was removed by rotatory evaporation resulting in **3** as a yellow powder (99 mg, 47.1%). δ_H(400 MHz; $CDCl_3$): 8.94 (m, 1H), 8.59 (s, 1H), 7.00 (s, 1H), 3.58 (q, ^3J = 6.5 Hz, 2H), 3.48 (t, ^3J = 6.5, 2H), 3.33 (m, 4H), 2.89 (t, ^3J = 6.5 Hz, 2H), 2.77 (t, ^3J = 6.5 Hz, 2H), 2.18 (quint, ^3J = 6.5 Hz, 2H), 1.98 (m, 4H) ppm. δ_C(400 MHz; $CDCl_3$): 164.06, 163.24, 152.80, 148.25, 127.19, 119.85, 108.89, 108.41, 105.86 ppm.

1-(3-aminopropyl)-2,3,3-trimethyl-3H-indol-1-ium bromide (10)

10 has been synthesized by using an adapted procedure from[176]. 3-Bromopropylamine hydrobromide (1.000 g, 4.59 mmol) and 2,3,3-trimethylindolenine (0.736 mL, 4.59 mmol) were dissolved in ACN (15 mL) and the reaction mixture was refluxed at 120 ^oC with stirring for 22 h in

inert conditions. KI (0.1 eq) was added to the reaction mixture and it was stirred at r.t. for 1 h, then refluxed for 3 h. A purple precipitate appeared, which was isolated by vacuum filtration, washed with Et_2O and $Et_2O/CHCl_3$ (1:1) and dried, to give **10** as a purple crude (1.067 g, 78.2%), which was used in the following step without further purification. m/z (ESI) calculated for $[C_{14}H_{21}N_2]^+ = [M^+]$: 217.17, found 217.17.

2,3,3-trimethyl-1-(3-(11-oxo-2,3,6,7-tetrahydro-1H,5H,11H-pyrano[2,3-f]pyrido[3,2,1-ij]quinoline-10-carboxamido)propyl)-3H-indol-1-ium (11)

11 has been synthesized by using an adapted procedure from[167]. **10** (468 mg, 1.57 mmol) and **9** (400 mg, 1.05 mmol), triethylamine (330 µL, 2.36 mmol) were dispersed in DCM (40 mL) and left stirring over night at r.t. Addition of **9** (62 mg, 0.21 mmol) and trimethylamine (30 µL, 0.21 mmol) and were left stirring over night at r.t. The solvent was removed by rotatory evaporation and the crude treated with diethyl ether (40 mL) and the walls of the flask scratched vigorously until obtaining a precipitate (964 mg), which was isolated by vacuum filtration and used in the following step without further purification. m/z (ESI) calculated for $[C_{30}H_{34}N_3O_3]^+ = [M^+]$: 484.26, found 484.26.

8-((4-nitrobenzyl)oxy)-2,3,6,7-tetrahydro-1H,5H-pyrido[3,2,1-ij]quinoline-9-carbaldehyde (6)

6 has been synthesized by using an adapted procedure from [118]. 9-Formyl-8-hydroxyjulolidine (217 mg, 2.21 mmol), K_2CO_3 (610 mg, 4.42 mmol), 1-(bromomethyl)-4-nitrobenzene (582 mg, 2.70 mmol) were dissolved in anhydrous DMF (13 mL). The reaction mixture was stirred at r.t. under Ar atm for 24 h. Distilled water (20 mL) and $NaHCO_3$ 0.2 M (20 mL) were added and the reaction mixture was extracted with EtOAc (6x20 mL). The organic phase was then extracted with brine (3x30 mL), dried over Na_2SO_4 and the solvent evaporated under reduced pressure. The crude was purified by column chromatography in silica gel from Hex/DCM (2:8) to DCM increasing MeOH percentage. The collected fractions were evaporated under reduced pressure and **6** was obtained as an ochre precipitate (764 mg, 98.1%). δ_H(400 MHz; $CDCl_3$): 9.88 (s, 1H), 8.26 (m, 2H), 7.65 (d, ^3J = 7.0 Hz, 2H), 7.34 (s, 1H), 5.02 (s, 2H), 3.30 (q, ^3J = 6.0 Hz, 4H), 2.74 (dt, ^3J = 10.0, 6.5 Hz, 4H) 1.96 (m, 4H) ppm. δ_C(400 MHz; $CDCl_3$): 187.17, 128.63, 127.94, 123.69, 117.40, 116.61,

112.45, 75.13, 50.00, 49.60, 27.25, 21.23, 21.03, 20.62 ppm. m/z (ESI) calculated for $[C_{20}H_{20}N_2O_4]^+ = [M+H]^+$: 352.14, found 352.14.

NHCy-C (12)

12 has been synthesized by using an adapted procedure from [117]. **11** (304 mg, 0.54 mmol), **6** (190 mg, 0.54 mmol), cat. $MgSO_4$ (3.76 mg, 5%) were dissolved in EtOH (30 mL). The reaction mixture was set at reflux under Ar atm for 20 h. The solvent was removed by rotatory evaporation and the crude product was purified in alumina gel with DCM/Acetone (1:1). The crude still contained a few impurities, so a purification with Preparative Layer Chromatography (PLC) was carried out (62 mg crude), followed by column chromatography DCM/MeOH (95:5) to give **12** as a dark blue precipitate (14.3 mg, 3.0% considering that 11 has 100% purity, which is not the case). δ_H(400 MHz; MeOD): 9.07 (t, 1H, ^3J = 5.5 Hz), 8.35 (d, 2H, ^3J = 9.0 Hz), 8.31 (s, 1H), 8.22 (d, 1H, ^3J = 15.5 Hz), 7.80 (d, 2H, ^3J = 9.0 Hz), 7.53-7.46 (m, 4H), 7.39-7.36 (m, 1H) 7.06 (s, 1H), 6.96 (d, 1H, ^3J = 15.5 Hz), 5.06 (s, 2H), 4.42 (t, 2H, ^3J = 6.5 Hz), 3.43-3.36 (m, 10H), 2.82-2.78 (m, 4H), 2.75-2.67 (m, 4H), 2.29-2.27 (q, 3H, ^3J = 3.0 Hz), 2.02-1.95 (m, 4H), 1.89 (m, 4H), 1.52 (s, 6H) ppm. δ_C(400 MHz; MeOD): 209.96, 171.63, 158.07, 147.39, 144.20, 141.79, 141.01, 135.60, 128.67, 127.52, 126.73, 124.85, 123.49, 122.25, 122.07, 115.28, 112.36, 109.60, 107.82, 106.76, 69.33, 69.10, 36.55, 55.53, 54.58,, 51.77, 50.29, 49.90, 49.81, 49.31, 39.40, 38.99, 30.65, 29.16, 28.11, 28.07, 27.00, 26.67, 23.50, 22.04, 20.68, 20.53, 19.84, 19.69, 17.84 ppm. m/z (ESI) calculated for $[C_{50}H_{52}N_5O_6]^+ = [M^+]$: 818.39, found 818.39.

5.3. NMR analysis of nucleophilic addition to hemicyanine derivatives

To solutions of styrylindolium salts (0.0125 mmol) in DMSO-d_6/D_2O (85:15) (500 µL) in NMR tubes were added solutions of potassium cyanide, sodium methanethiolate or glutathione (all 0.25 M in D_2O). Additions were made in 0.25 eq. increments (i.e. 12.5 µL of 0.25 M solution, 0.00313 mmol) up to 1 eq. total (with a final 20% D_2O), allowing 30 minutes between additions. ^{1}H NMR spectra were recorded right after each addition, and again preceding the subsequent addition.

^{1}H NMR, ^{13}C NMR, COSY, HSQC, HMBC spectra were also recorded 24 h after the final addition, but no changes were observed, so they have not been added to the appendix.

5.4. Fluorescence measurements

Fluorescent measurements were performed in either 96- or 384-well plate formats with flat-bottom wells. The 96-well plates used were polystyrene (PS) with either transparent bottom (#655906) or black bottom (#655076) from Greiner Bio-One (Greiner). Only in the case of viscosity and polarity plates, experiments were carried out in polypropylene (PP) well plates (#655209). The 384 well-plates used were polystyrene (PS) with transparent bottom (#781096) from Greiner Bio-One (Greiner).

Fluorescent measurements from samples prepared in 96-well plates were recorded with Cytation 3 Imaging Reader (BioTek Instruments, Inc.) while the ones prepared in 384-well plates were recorded with ClarioStar (BMG Labtech) plate reader unless otherwise stated. Generally, measurements consisted of 3 repeats (N = 3), each with 3 technical repeats, unless otherwise stated.

Quantum yield measurements

The molar extinction coefficients (ε), fluorescence quantum yields (Φ_F), and brightness (B) for compounds **HCy-NEt$_2$** (**3**), **HCy-Jul** (**4**), and **NHCy**, were determined using a comparative method developed by Williams et al. [123] This method utilizes samples with known ΦF values. Data collection was conducted using a multi-well plate reader with 96-well plates that had a transparent bottom, allowing for simultaneous measurements of absorbance and fluorescence for each sample. Typically, the procedure involves obtaining absorption spectra for 5 different concentrations (ensuring absorbances are below 0.1 to avoid inner filter effects) at the excitation wavelength, followed by the collection of fluorescence spectra at the same excitation wavelength (516 nm). Molar extinction coefficients were calculated by performing linear fits of absorbance data across 5 concentrations for each compound. The coefficient obtained from the linear regression (a) was then used to calculate the molar extinction coefficient using the formula ε = a / l, where l is the light path length (0.56 cm for 200 µL in a standard 96-well plate). In the case of

384 well-plate measurements with a final volume of 40 µL, an estimation of the path length was carried out (explained in the section below) and the chosen estimated path length was 0.31.

To calculate fluorescence quantum yields, integrated fluorescence was plotted against absorbance at the excitation wavelength for both the compound of interest and a reference standard (Rhodamine 6G in EtOH). The experimental points were fit with linear regression), and the resulting coefficient (a) was used to determine the fluorescence QY relative to the standard (Rhodamine 6G in EtOH with Φ_F = 0.95[124] with the use of equation $\Phi_X = \Phi_{ST}[(Grad_X/Grad_{ST})(\eta_X^2/\eta_{ST}^2)]$, Where Φ_X is the quantum yield of examined fluorophore; Φ_{ST} is the fluorescence quantum yield of the standard fluorophore; $Grad_X$ is the gradient obtained from the plot of integrated fluorescence intensity against absorbance of the sample fluorophore; $Grad_{ST}$ is the gradient obtained from the plot of integrated fluorescence intensity against absorbance of the standard fluorophore; η_X is the refractive index for sample solution, η_{ST} is the refractive index for standard solution.Refractive indices used in the calculations were η_{ST} = 1.36 for EtOH[177] and approximately η_x = 1.48 for DMSO[177].

Estimation of path length in different well-plates and volumes of solutions

Considering a known path length of 0.56 cm for 200 µL in 96 well-plates, estimation was done for 40 µL in 384 well-plates. Three different solutions of Rhodamine 6G (with concentrations 0.4, 0.8, and 1 µM in EtOH) and the blank sample (EtOH) were prepared in 96 well-plates (200 µL final volume) and 384 well-plates (40 µL final volume), with 5 replicates for each sample in the same experiment. Absorbance spectra were collected with ClarioStar (BMG Labtech) plate reader. Then slope of a linear fit was calculated for the plot of absorbance vs concentration for 96 wp 200 µL (a-96) and then also for the plot of absorbance vs concentration for 384 well-plate 40 µL (a-384). Path length for 384 well-plate was calculated via the obtained slopes with the following equation l-384 = (a-384 / a-96) · L-96, as well as l (384wp) = l (96wp) · [averageAbs(384wp)/averageAbs(96wp)] for each of three concentrations. The path length that was estimated was 0.31 and 0.33, via the obtained slope and the obtained averages, respectively. For quantum yield measurements, the value used was the one obtained from the slope.

Fluorescence measurements of hemicyanine derivatives in different buffers (same pH with a range of concentrations)

Several buffer solutions of certain concentrations (50, 100, 150, 200, 250, and 500 µM) of PB, TRIS·HCl, HEPES buffers at pH 7.5 were prepared and their conductivity was measured with METTLER TOLEDO™ SevenExcellence™ S470 pH/Conductivity Benchtop Meter. To the previously mentioned buffered solutions were added **HCy-OMe** (5 µM), **HCy-NEt$_2$** (2.5 µM), **HCy-Jul** (2.5 µM) hemicyanines to give a final 1% DSMO and a final volume of 200 µL. The blank samples consisted in the corresponding solution of glycerol/water of a given ratio with the same final %DMSO. Experiments were carried out in polypropylene 96 well-plates (#655209, Greiner Bio-One). Fluorescent measurements were recorded with Cytation 3 Imaging Reader (BioTek Instruments, Inc.). Emission spectra were recorded at λ_{exc} = 430 nm and λ_{em} = 490-700 nm for **HCy-OMe**. For **HCy-NEt$_2$** and **HCy-Jul**, emission spectra were collected at λ_{exc} = 530 nm, λ_{em} = 560-700 nm.

Fluorescence measurements of hemicyanine derivatives in different buffer solutions (same buffer concentration with 3 different pH values)

Three different buffer solutions of 100 mM with different pH values were prepared: phosphate buffer (PB, pH = 6, 7.5), TRIS·HCl (TRIS, pH = 7.5, 8, 9), HEPES (pH = 7.5, 8, 9). To the previously mentioned buffered solutions were added **HCy-OMe** (5 µM), HCy-NEt$_2$ (2.5 µM), **HCy-Jul** (2.5 µM) hemicyanines to give a final 1% DSMO and a final volume of 200 µL. The blank samples consisted in the corresponding solution of glycerol/water of a given ratio with the same final %DMSO. Experiments were carried out in polypropylene 96 well-plates (#655209, Greiner Bio-One). Fluorescent measurements were recorded with Cytation 3 Imaging Reader (BioTek Instruments, Inc.). Emission spectra were recorded at λ_{exc} = 430 nm and λ_{em} = 490-700 nm for **HCy-OMe**. For **HCy-NEt$_2$** and **HCy-Jul**, emission spectra were collected at λ_{exc} = 530 nm, λ_{em} = 560-700 nm.

Fluorescence measurements of hemicyanine derivatives in solutions of different polarity

To 1,4-dioxane/water solutions of different ratios (10:0, 9:1, 8:2, 7:3, 6:4, 1:1, 4:6, 3:7, 2:8, 1:9, 0:10) were added DMSO-based solutions of **HCy-OMe** (5 µM), **HCy-NEt$_2$** (2.5 µM), **HCy-Jul** (2.5 µM) hemicyanines to give a final 1% DSMO and a final volume of 200 µL. The blank samples consisted in the corresponding solution of 1,4-dioxane/water of a given ratio with the same final

%DMSO. Experiments were carried out in polypropylene 96 well-plates (#655209, Greiner Bio-One). Fluorescent measurements were recorded with Cytation 3 Imaging Reader (BioTek Instruments, Inc.). For **HCy-OMe**, excitation spectra were collected at λ_{em} = 530 nm, λ_{exc} = 300-500 nm, and emission spectra at λ_{exc} = 430 nm, λ_{em} = 460-700 nm. For **HCy-NEt$_2$**, excitation spectra were collected at λ_{em} = 610 nm, λ_{exc} = 300-580 nm, and emission spectra at λ_{exc} = 550 nm, λ_{em} = 580-700 nm. For **HCy-Jul**, excitation spectra were collected at λ_{em} = 635 nm, λ_{exc} = 300-605 nm, and emission spectra at λ_{exc} = 570 nm, λ_{em} = 600-700 nm.

Fluorescence measurements of hemicyanine derivatives in solutions of different viscosity

To glycerol/water solutions of different ratios (10:0, 9:1, 8:2, 7:3, 6:4, 1:1, 4:6, 3:7, 2:8, 1:9, 0:10) were added DMSO-based solutions of **HCy-OMe** (5 µM), **HCy-NEt$_2$** (2.5 µM), **HCy-Jul** (2.5 µM) hemicyanines to give a final 1% DSMO and a final volume of 200 µL. The blank samples consisted in the corresponding solution of glycerol/water of a given ratio with the same final %DMSO. Experiments were carried out in polypropylene 96 well-plates (#655209, Greiner Bio-One). Fluorescent measurements were recorded with Cytation 3 Imaging Reader (BioTek Instruments, Inc.). For **HCy-OMe**, excitation spectra were collected at λ_{em} = 530 nm, λ_{exc} = 300-500 nm, and emission spectra at λ_{exc} = 430 nm, λ_{em} = 460-700 nm. For **HCy-NEt$_2$**, excitation spectra were collected at λ_{em} = 610 nm, λ_{exc} = 300-580 nm, and emission spectra at λ_{exc} = 550 nm, λ_{em} = 580-700 nm. For **HCy-Jul**, excitation spectra were collected at λ_{em} = 635 nm, λ_{exc} = 300-605 nm, and emission spectra at λ_{exc} = 570 nm, λ_{em} = 600-700 nm.

Fluorescence measurements of hemicyanine derivatives cyanide anion

Studies were carried out for **HCy-OMe** (5 µM), **HCy-NEt$_2$** (2.5 µM), **HCy-Jul** (2.5 µM) in DMSO/HEPES (80:20) at different pH values (7.4, 8, and 9) with or without cyanide treatment (25 and 250 µM). Experiments were done in polypropylene 96 well-plates (#655209, Greiner Bio-One). Fluorescent measurements were recorded at several timepoints with Cytation 3 Imaging Reader (BioTek Instruments, Inc.). For **HCy-OMe**, excitation spectra were collected at λ_{em} = 530 nm, λ_{exc} = 300-500 nm, and emission spectra at λ_{exc} = 430 nm, λ_{em} = 460-700 nm. For **HCy-NEt$_2$**, excitation spectra were collected at λ_{em} = 610 nm, λ_{exc} = 300-580 nm, and emission spectra at λ_{exc}

= 550 nm, λ_{em} = 580-700 nm. For **HCy-Jul**, excitation spectra were collected at λ_{em} = 635 nm, λ_{exc} = 300-605 nm, and emission spectra at λ_{exc} = 570 nm, λ_{em} = 600-700 nm.

Fluorescence measurements of hemicyanine derivatives glutathione

Studies were carried out for **HCy-OMe** (5 μM), **HCy-NEt$_2$** (2.5 μM), **HCy-Jul** (2.5 μM) in DMSO/HEPES (80:20) at different pH values (7.4, 8, and 9) with or without GSH treatment (2 mM). Experiments were done in polypropylene 96 well-plates (#655209, Greiner Bio-One). Fluorescent measurements were recorded at several timepoints with Cytation 3 Imaging Reader (BioTek Instruments, Inc.). For **HCy-OMe**, excitation spectra were collected at λ_{em} = 530 nm, λ_{exc} = 300-500 nm, and emission spectra at λ_{exc} = 430 nm, λ_{em} = 460-700 nm. For **HCy-NEt$_2$**, excitation spectra were collected at λ_{em} = 610 nm, λ_{exc} = 300-580 nm, and emission spectra at λ_{exc} = 550 nm, λ_{em} = 580-700 nm. For **HCy-Jul**, excitation spectra were collected at λ_{em} = 635 nm, λ_{exc} = 300-605 nm, and emission spectra at λ_{exc} = 570 nm, λ_{em} = 600-700 nm.

Fluorescence measurements of hemicyanine derivatives in the presence of metal ion salts

Milli-Q water was used to prepare solutions of 1 and 10 equivalents to the corresponding hemicyanine derivative of the following metal io salts: iron(II) chloride, ammonium iron(II) sulfate hexahydrate, iron(III) chloride, magnesium nitrate, potassium chloride, sodium nitrate, copper(II) nitrate trihydrate, calcium nitrate, cobalt(II) nitrate hexahydrate, zinc nitrate hexahydrate, manganese(II) nitrate, tetrakis(acetonitrile) copper(I) tetrafluoroborate, nickel(II) nitrate.

Experiments were performed in polypropylene 384 well-plates (# 781096, Greiner Bio-One). To Milli-Q water-based solutions were added **HCy-OMe** (5 μM), **HCy-NEt$_2$** (2.5 μM), **HCy-Jul** (2.5 μM) hemicyanines to give a final 1% DSMO and a final volume of 40 μL. The blank samples consisted in the corresponding solution of a metal ion salt of a given concentration with the same final %DMSO. Fluorescent measurements were recorded with ClarioStar (BMG Labtech) plate reader.

Fluorescence measurements of hemicyanine derivatives and probes

The hemicyanine derivatives or probes (2.5 μM) in PBS buffer pH 7.4 received various treatments by addition of NTR (10 μg mL^{-1}), NADH (500 μM), and NTR+NADH (10 μg mL^{-1} and 500 μM, respectively), to give a final 1% DMSO. The fluorescence emission is also recorded from samples

containing the same %DMSO, for NTR (10 µg mL^{-1}), NADH (500 µM), and NTR+NADH (10 µg mL^{-1} and 500 µM, respectively) in the absence of hemicyanine derivative or probe. The measurements were carried out at times t_1 (≈5 min) and t_2 (≈1h).

pKa determination

The experiment was repeated in triplicates. pK_a value of **NHCy** was obtained by linear regression analysis of the fluorescence titration curve to fit the derived Henderson-Hasselbach equation[178]: pK_a - pH =log[(I_{max}-I)/(I-I_{min})], where I is the fluorescence intensity at 600 nm at different pH values (CPB: 4.5, 5, 5.5; PB: 6.5, 7), I_{max} and I_{min} are the fluorescence intensity measured at pH 4.0 and 7.5 at 600, respectively. The pK_a value was determined from the resulting intercept in the linear trend obtained from the plot pH vs log[(I_{max}-I)/(I-I_{min})].

5.5. Biology

5.5.1. General cell lines information and cell culture conditions

Cell lines used were from American Type Culture Collection (ATCC): A549 (# CCL-185), DU145 (# HTB-81), HEK (HEK-293, # CRL-1573™), MCF7 (HTB-22 ™).

Dulbecco's Modified Eagle's Medium (DMEM), supplemented with 10% fetal bovine serum (FBS) and 1% penicillin-streptomycin was used for 2D culture of cell lines (A549, DU145, HEK). Cell detachment for passaging was carried out via trypsin 0.25%+EDTA.

5.5.2. Fluorescence Confocal Microscopy experiments

5.5.2.1. Normoxic conditions in 2D cell culture

7500 cells/well of a given cell line (DU145, A549, HEK) in supplemented DMEM High Glucose (300 µL) were seeded into in CellView cell culture dish PS, 4 compartments (#627870, from Greiner Bio-One). After 48 h incubation, cells were incubated with the given compound, probe or tracker (to yield the corresponding final concentration, 1% DMSO). After 15 min of incubation time, the wells were then washed three times with 300 µL of PBS, followed by the addition of Fluorobrite™ and the imaging process right after that. The well containing blank contained the same final

%DMSO and was treated the same way. Imaging of prepared samples (5 z-stacks with 0.25 µm thickness per sample, and spectral scans of selected samples) was carried out with different exc/em fluorescent and brightfield channels via Confocal microscope Leica TCS SP5 II with white laser and intravital chamber with LAS AF SP5 software and LAS X SP8 software with deconvolution. The corresponding generated images (bright field and fluorescence images) were exported as .tiff format and analysed with ImageJ, Fiji. [179] Simple scripts were created for automation of the images' thresholding process, as well as simple KNIME pipeline[180] was created to facilitate the data analysis process. Co-localisation of the compounds with trackers was determined by JaCoP with ImageJ, Fiji. [179]

Script for data analysis of HCy-OMe, HCy-NEt$_2$, and HCy-Jul

```
/*
 * Script to process multiple images in a folder and set thresholds at 1-255 and 1-254
 */
input = getDirectory("Choose input directory ");
output = getDirectory("Choose output directory ");
File.makeDirectory(output);
suffix = ".tif"
processFolder(input);
// function to scan folders/subfolders/files to find files with correct suffix
function processFolder(input) {
	list = getFileList(input);
	list = Array.sort(list);
	for (i = 0; i < list.length; i++) {
		// switch off recursion
```

```
                    //      if(File.isDirectory(input + File.separator + list[i]))
                    //      processFolder(input + File.separator + list[i]);
                    if(endsWith(list[i], suffix))
                            processFiles_2(input, list[i]);
            }
    }
    function processFile(input, file) {
            open(input+file);
run("Measure");
run("Duplicate...", " ");
run("Duplicate...", " ");
setAutoThreshold("Default");
//run("Threshold...");
setThreshold(1, 255);
//setThreshold(1, 255);
setOption("BlackBackground", false);
run("Create Selection");
roiManager("Add");
close();
setAutoThreshold("Default");
//run("Threshold...");
setThreshold(1, 254);
```

```
//setThreshold(1, 254);
setOption("BlackBackground", false);
run("Create Selection");
roiManager("Add");
close();
roiManager("Select", newArray(0,1));
roiManager("Measure");
saveAs("Results", output + "Results"+file+".csv");
                run("Clear Results");
                print("Processing: " + input + File.separator + file);
    }
    function processFiles_2(input, file) {
                open(input+file);
run("Measure");
run("Duplicate...", " ");
run("Duplicate...", " ");
setAutoThreshold("Default");
//run("Threshold...");
setThreshold(1, 255);
//setThreshold(1, 255);
setOption("BlackBackground", false);
run("Create Selection");
```

```
	roiManager("Add");
	close();
	setAutoThreshold("Default");
	//run("Threshold...");
	setThreshold(1, 254);
	//setThreshold(1, 254);
	setOption("BlackBackground", false);
	run("Create Selection");
	roiManager("Add");
	close();
	roiManager("Select", newArray(0,1));
	roiManager("Measure");
	saveAs("Results", output + "Results"+file+"_2.csv");
		run("Clear Results");
		print("Processing: " + input + File.separator + file);
	roiManager("Deselect");
	roiManager("Delete");
	close();
	}
result_for_first_file = ""
result_for_second_file = ""
result_for_last_file = ""
```

```
function macro_for_first_file(input_1){
	run("Measure");
	run("Duplicate...", " ");
	setAutoThreshold("Default");
	//run("Threshold...");
	setThreshold(1, 255);
	//setThreshold(1, 255);
	setOption("BlackBackground", false);
	run("Create Selection");
	result_for_first_file = roiManager("Add");
	close();
	close();
}
function macro_for_second(input_2) {
	run("Duplicate...", " ");
	setAutoThreshold("Default");
	//run("Threshold...");
	setThreshold(1, 254);
	//setThreshold(1, 254);
	setOption("BlackBackground", false);
	run("Create Selection");
	result_for_first_file = roiManager("Add");
```

```
	close();
	close();
}
function summary(){
	print (result_for_first_file)
}
```

Script for data analysis of NHCy and NHCy-C

```
	/*
	 * Script to process multiple images in a folder and set Autothreshold Mean and AutoLocal Threshold Otsu
	 */
  input = getDirectory("Choose input directory ");
  output = getDirectory("Choose output directory ");
  File.makeDirectory(output);
	suffix = ".tif"
	processFolder(input);
	// function to scan folders/subfolders/files to find files with correct suffix
	function processFolder(input) {
		list = getFileList(input);
		list = Array.sort(list);
		for (i = 0; i < list.length; i++) {
			// switch off recursion
```

```
                    //      if(File.isDirectory(input + File.separator + list[i]))
                    //      processFolder(input + File.separator + list[i]);
                    if(endsWith(list[i], suffix))
                            processFiles_2(input, list[i]);
            }
    }
    function processFile(input, file) {
            open(input+file);
run("Measure");
run("Duplicate...", " ");
run("Duplicate...", " ");
run("Duplicate...", " ");
setAutoThreshold("Default");
//run("Threshold...");
setThreshold(1, 255);
//setThreshold(1, 255);
setOption("BlackBackground", false);
run("Create Selection");
run("Create Selection");
roiManager("Add");
close();
run("Auto Threshold...", "method=Mean ignore_black white");
```

```
	run("Create Selection");
	roiManager("Add");
	close();
	run("Auto Local Threshold...", "method=Otsu radius=15 parameter_1=0 parameter_2=0 white");
	run("Create Selection");
	roiManager("Add");
	close();
	roiManager("Select", newArray(0,1,2));
	roiManager("Measure");
	saveAs("Results", output + "Results"+file+".csv");
		run("Clear Results");
		print("Processing: " + input + File.separator + file);
	}
	function processFiles_2(input, file) {
		open(input+file);
	   run("Measure");
	run("Duplicate...", " ");
	run("Duplicate...", " ");
	run("Duplicate...", " ");
	setAutoThreshold("Default");
	//run("Threshold...");
```

```
setThreshold(1, 255);
//setThreshold(1, 255);
setOption("BlackBackground", false);
run("Create Selection");
roiManager("Add");
close();
 run("Auto Threshold...", "method=Mean ignore_black white");
run("Create Selection");
roiManager("Add");
close();
run("Auto Local Threshold...", "method=Otsu radius=15 parameter_1=0 parameter_2=0 white");
run("Create Selection");
roiManager("Add");
close();
roiManager("Select", newArray(0,1,2));
roiManager("Measure");
saveAs("Results", output + "Results"+file+"_2.csv");
                run("Clear Results");
                print("Processing: " + input + File.separator + file);
roiManager("Deselect");
roiManager("Delete");
```

```
        close();
            }
result_for_first_file = ""
result_for_second_file = ""
result_for_last_file = ""
function macro_for_first_file(input_1){
            run("Measure");
            run("Duplicate...", " ");
            setAutoThreshold("Default");
            //run("Threshold...");
            setThreshold(1, 255);
            //setThreshold(1, 255);
            setOption("BlackBackground", false);
            run("Create Selection");
            result_for_first_file = roiManager("Add");
            close();
            close();
}
function macro_for_second(input_2) {
            run("Duplicate...", " ");
            run("Auto Threshold...", "method=Mean ignore_black white");
            run("Create Selection");
```

```
	result_for_second_file = roiManager("Add");
	close();
	close();
}
function macro_for_last_file(input_3) {
	run("Duplicate...", " ");
	run("Auto Local Threshold...", "method=Otsu radius=15 parameter_1=0 parameter_2=0 white");
	run("Create Selection");
	result_for_last_file = roiManager("Add");
	close();
	close();
}
function summary(){
	print (result_for_first_file)
}
```

5.5.2.2. Hypoxic conditions in 2D cell culture

7500 cells/well of a given cell line (DU145, A549, HEK) in supplemented DMEM High Glucose (300 µL) were seeded into in CellView cell culture dish PS, 4 compartments (#627870), from Greiner Bio-One. Hypoxia in cells was induced by low oxygen percentage in the cell incubator chamber for x h before incubation with the probe.

After 48 h incubation, cells were incubated with the given probe (final concentration 2 µM, final 1% DMSO). After 15 min of incubation time, the wells were then washed three times with 300 µL

of PBS, followed by the addition of Fluorobrite™ and the imaging process right after that. The well containing blank contained the same final %DMSO and was treated the same way. Imaging of prepared samples (5 z-stacks with 0.25 µm thickness per sample, and spectral scans of selected samples) was carried out with different exc/em fluorescent and brightfield channels via Confocal microscope Leica TCS SP5 II with white laser and intravital chamber with LAS AF SP5 software and LAS X SP8 software with deconvolution. The corresponding generated images (bright field and fluorescence images) were exported as .tiff format and analysed with ImageJ, Fiji. [179] The same scripts used in image analysis for normoxic conditions were then used for hypoxic conditions for the automation of the images' thresholding process, as well as simple KNIME[180] pipeline was created to facilitate the data analysis process. Co-localisation of the compounds with trackers was determined by JaCoP with ImageJ, Fiji. [179]

5.5.2.3. Hypoxic conditions in 3D cell culture: spheroids

For homogenous 3D culture spheroids from tumour cells (LNCaP and DU145 cell lines), 1000 cells/well were seeded in 96-well plates (Nunclon Sphera U-bottom plate, # 174925 from ThermoFisher Scientific). The plates with seeded cells were centrifuged for 5 min at 300g, ensuring all cells within the well were pelleted at the bottom. 14 days after cell seeding, cells were treated with DMSO (blank) and **NHCy** (1 µM), 8 independent repeats for each sample, with final 1% DMSO. Imaging (25 z-stacks of 15 µm thickness) was performed via Opera Phenix High Content Screening System, using 5x or 10x air objective, with different exc/em fluorescent and brightfield channels. The corresponding generated images (bright field and fluorescence images) were exported as .tiff format and analysed with ImageJ, Fiji. [179] Due to the amount of images, 3 independent repeats for each sample were considered for analysis and scripts for re-scaling and plotting profiles were created (see below). For the intensity-based analysis, selection of ROIs were done manually: each spheroid was segmented into three distinct regions of interest - ROI 1 whole spheroid (ROI 1), inner core (ROI 2), and outer part of the spheroid (ROI 3, with approximately 100 µm of width). The average grey value was measured with Image J, Fiji. [179] Co-localisation of the compounds with trackers was determined by JaCoP with ImageJ, Fiji. [179]

Script for re-scaling the images

```
// Define the main folder path
mainFolderPath = "C:/Users/X";
// Define the cell lines, sample types, and channels
cellLines = newArray("DU145", "LNCaP");
sampleTypes = newArray("DMSO", "FC105 1 uM", "FC105 2 uM", "FC103 10 uM");
channels = newArray("ch1 8-bit", "ch2 8-bit", "ch3 8-bit", "ch4 8-bit", "ch5 8-bit");
// Function to process each channel folder
function processChannelFolder(channelPath, newChannelPath) {
   // Get list of .tiff files in the channel folder
   fileList = getFileList(channelPath);
   // Loop through each file in the channel folder
   for (f = 0; f < fileList.length; f++) {
      // Only process .tiff files
      if (endsWith(fileList[f], ".tiff")) {
         // Open the image
         open(channelPath + "/" + fileList[f]);
         // Get the image title (for naming the duplicated image)
         imageTitle = getTitle();
         // Duplicate the image
         run("Duplicate...", "title=" + imageTitle + "_duplicate");
         // Close the original image
         run("Close", imageTitle);
```

```
            // Set the scale
            run("Set Scale...", "distance=1 known=1.19595 unit=micron");
            // Save the duplicated image in the new subfolder
            saveAs("Tiff", newChannelPath + "/" + imageTitle + "_rescaled.tiff");
            // Close the duplicated image
            run("Close");
        }
    }
}
// Loop through each cell line
for (c = 0; c < cellLines.length; c++) {
    cellLinePath = mainFolderPath + "/" + cellLines[c];
    // Loop through each sample type
    for (s = 0; s < sampleTypes.length; s++) {
        sampleTypePath = cellLinePath + "/" + sampleTypes[s];
        // Loop through each channel
        for (ch = 0; ch < channels.length; ch++) {
            channelPath = sampleTypePath + "/" + channels[ch];
            newChannelPath = sampleTypePath + "/" + channels[ch] + " rescaled";
            // Create new subfolder if it doesn't exist
            File.makeDirectory(newChannelPath);
            // Process the channel folder
```

```
            processChannelFolder(channelPath, newChannelPath);
        }
    }
}
```

Script for plotting profiles on Image J

```
// Set the main folder path
mainFolder = "C:/Users/X/";
// Array of cell lines
cellLines = newArray("DU145", "cellLine2");
// Loop through each cell line
for (cellLineIndex = 0; cellLineIndex < lengthOf(cellLines); cellLineIndex++) {
    // Set the cell line
    cellLine = cellLines[cellLineIndex];
    // Set the cell line folder path
    cellLineFolder = mainFolder + cellLine + "/";
    // Array of sample types
    sampleTypes = newArray("DMSO", "NHCy 1 uM");
    // Loop through each sample type
    for (sampleTypeIndex = 0; sampleTypeIndex < lengthOf(sampleTypes); sampleTypeIndex++) {
        // Set the sample type
        sampleType = sampleTypes[sampleTypeIndex];
        // Set the sample type folder path
```

```
    sampleTypeFolder = cellLineFolder + sampleType + "/";
    // Array of channels
    channels = newArray("ch1 8-bit rescaled", "ch2 8-bit rescaled", "ch3 8-bit rescaled", "ch4 8-bit rescaled", "ch5 8-bit rescaled");
    // Loop through each channel
    for (channelIndex = 0; channelIndex < lengthOf(channels); channelIndex++) {
      // Set the channel
      channel = channels[channelIndex];
      // Set the channel folder path
      channelFolder = sampleTypeFolder + channel + "/";
      // Get a list of files in the channel folder
      list = getFileList(channelFolder);
      // Create profile folder if it doesn't exist
      profileFolder = channelFolder + "profile/";
      File.makeDirectory(profileFolder);
      // Loop through each file
      for (fileIndex = 0; fileIndex < lengthOf(list); fileIndex++) {
        // Open images containing same "r##c##f##" in .tiff format
        open(channelFolder + list[fileIndex]);
        // Get the title of the opened image
        imageTitle = getTitle();
        // Duplicate the image
```

```
            run("Duplicate...", "title=" + imageTitle + "_duplicate");
            // Close the original image
            run("Close", imageTitle);
            // Draw a line at specific coordinates for duplicated images
            makeLine(54, 394, 1048, 394);
            // Run plot profiler
            run("Plot Profile");
            // Get the name of the plot
            plotName = getTitle();
            // Save plot as tiff with the name of the original image
            saveAs("Tiff", profileFolder + File.nameWithoutExtension(imageTitle) +
"_plotprofile.tif");
            // Close all open images, plots, profiles
            close("*");
        }
    }
  }
}
```

5.5.3. Flow cytometry

MCF7 cells seeding in the 12-well plates (# 83.3921, Sarstedt) 59375 cells/well cells in supplemented DMEM High Glucose (1 mL). Incubation in normoxic and hypoxic (1% of oxygen for 24 h in specific chamber Invivo2 400 before addition of probe). 24 h after cell seeding, cells were incubated with the probe (2.5 µM) for 30 min. The wells were washed three times with PBS

1x (# SH30028.02, Cytiva; 700 µL). Cells were then manually scrapped and Fluorobrite™ (700 µL) was added. The obtained cell solutions were then injected to the flow cytometer CytoFlex S Berckman Coulter and analysed with CytExpert 2.3 software.

5.5.4. Cytotoxicity

5.5.4.1. DU145, A549, and HEK cell lines

2500 cells/well of a given cell line (HEK, DU145) were seeded cells in supplemented DMEM High Glucose (20 µL) in PhenoPlate (formerly CellCarrier Ultra) poly-D-lysine-coated 384-well plates (# 6057500, from Revvity). After 48 h incubation, cells were treated with solutions (10 µL, in DMEM High Glucose supplemented) containing the hemicyanine derivatives to yield final concentrations (0.01, 0.1, 0.2, 0.3, 0.4, 0.5, 0.74. 1, 2.5, 5, 10 µM) and a final 1% DMSO in the wells. DMSO and staurosporine[149] were added as negative and positive controls to the corresponding columns of each plate to yield 1% and 5 µM final concentration, respectively. After 1h of incubation time, the wells were rinsed with PBS 1x with HydroSpeed™ plate washer (Tecan Life Sciences), followed by the addition of supplemented DMEM High Glucose (30 µL). After 48 h, a resazurin solution (10 µL, in PBS) was added to yield a final concentration of 600 µM in the well. The plate was then incubated at 37 ^{o}C for 30 min and its fluorescent emission was recorded at exc/em = 550/585 with Cytation 3 Imaging Reader (BioTek Instruments, Inc.).

5.5.4.2. MCF7 breast cancer cell line

MCF7 cell line (HEK, DU145) were seeded (1562.5 cells/well) in supplemented DMEM High Glucose (50 µL) in 384 well-plates (# 732-2907, VWR). 24 h after cells seeding, treatment with fluorescent probe was performed to yield the following final concentrations: 5 µM, 2.5 µM, 1.25 µM, 0.625 µM, 0.3125 µM, 0.156 µM. MTS test (# G1111, Promega) was used following the manufacturer's instructions and absorbance was recorded with Ensight PerkinElmer at 490 nm after and 24h.

6. Appendix

6.1. NMR spectroscopy

6.1.1. NMR spectra of synthesised compounds

^{1}H NMR spectra are attached for all compounds, while ^{13}C NMR spectra only for novel compounds.

^{1}H NMR spectrum of **1**, $CDCl_3$.

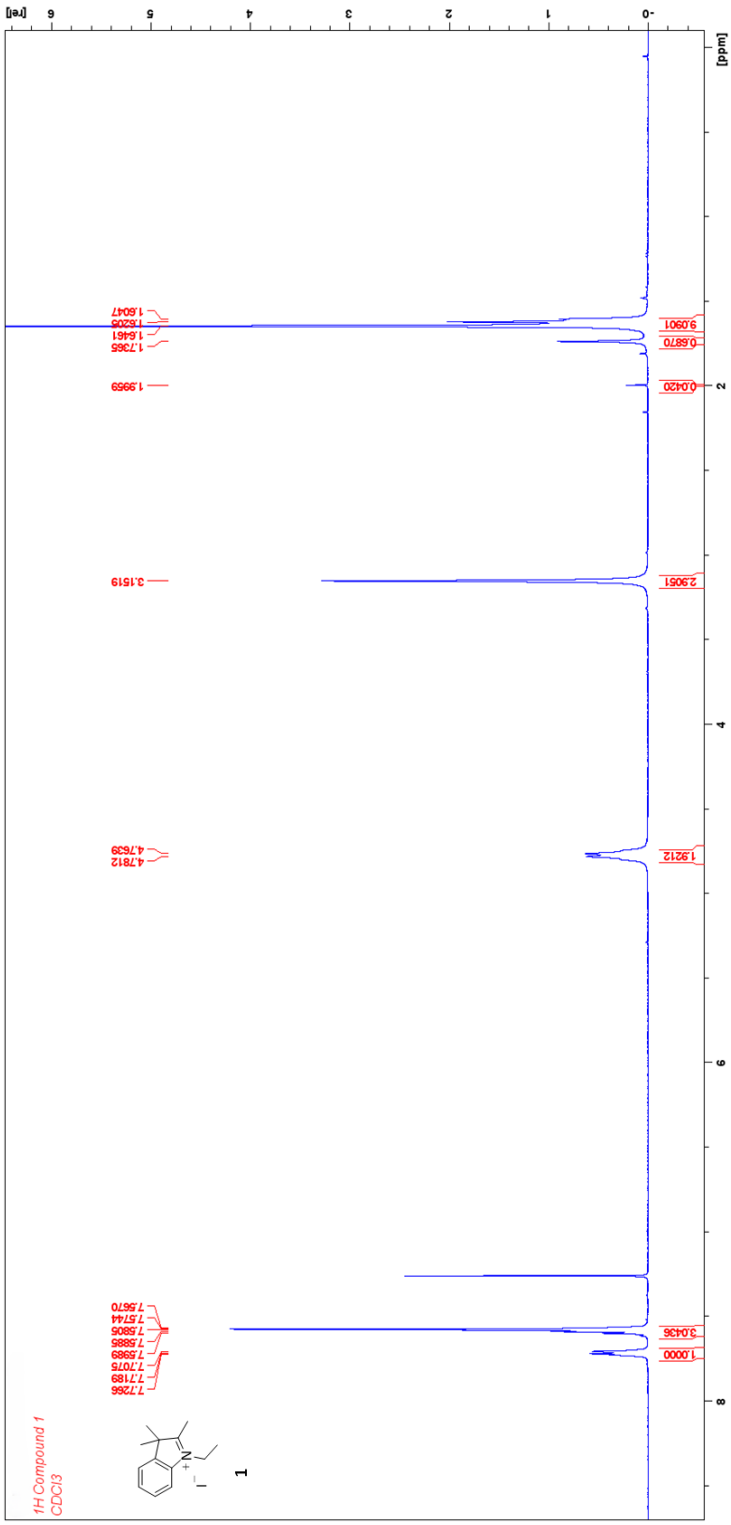

^{1}H NMR spectrum of **HCy-OMe** (**2**), CD_3CN.

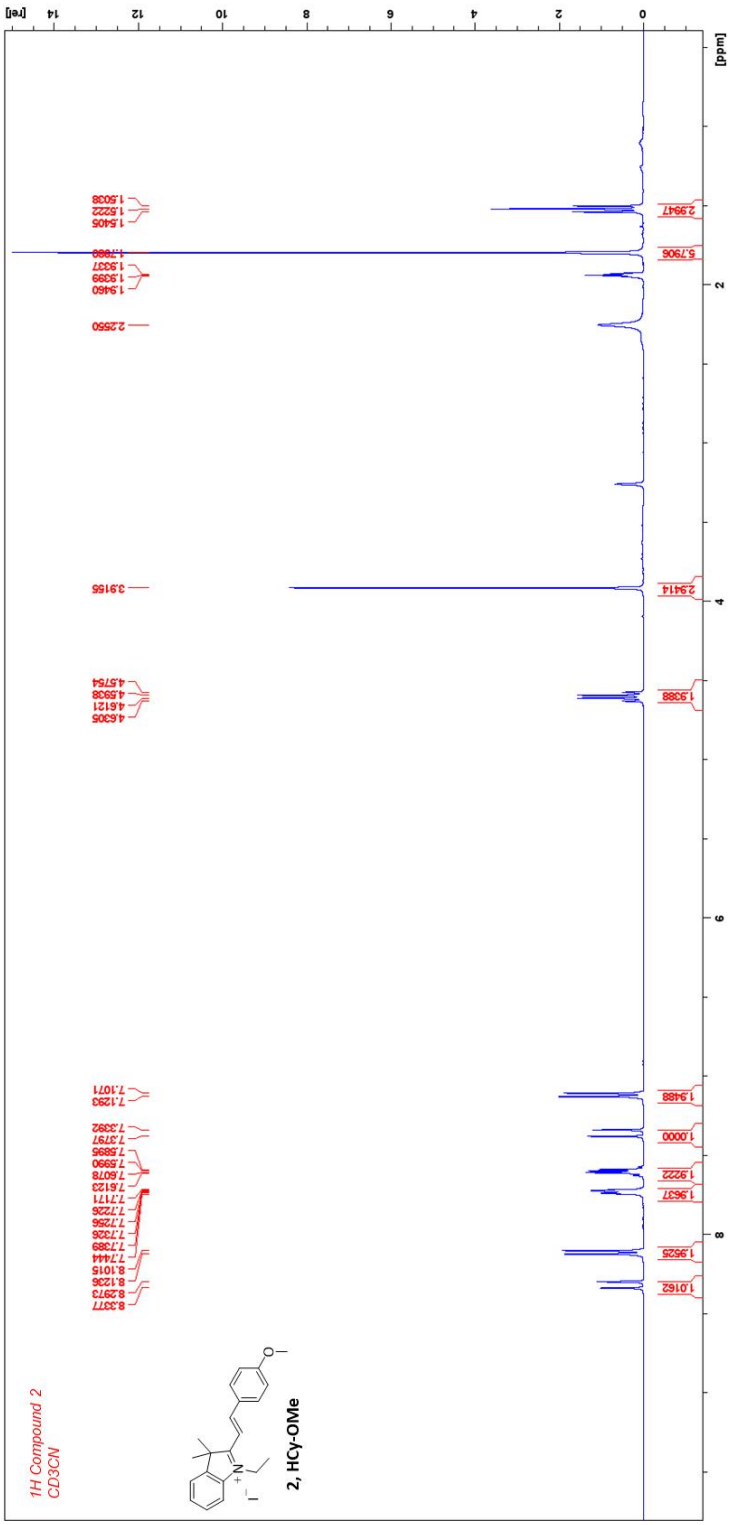

^{1}H NMR spectrum of **HCy-NEt$_2$** (**3**), d_6-DMSO.

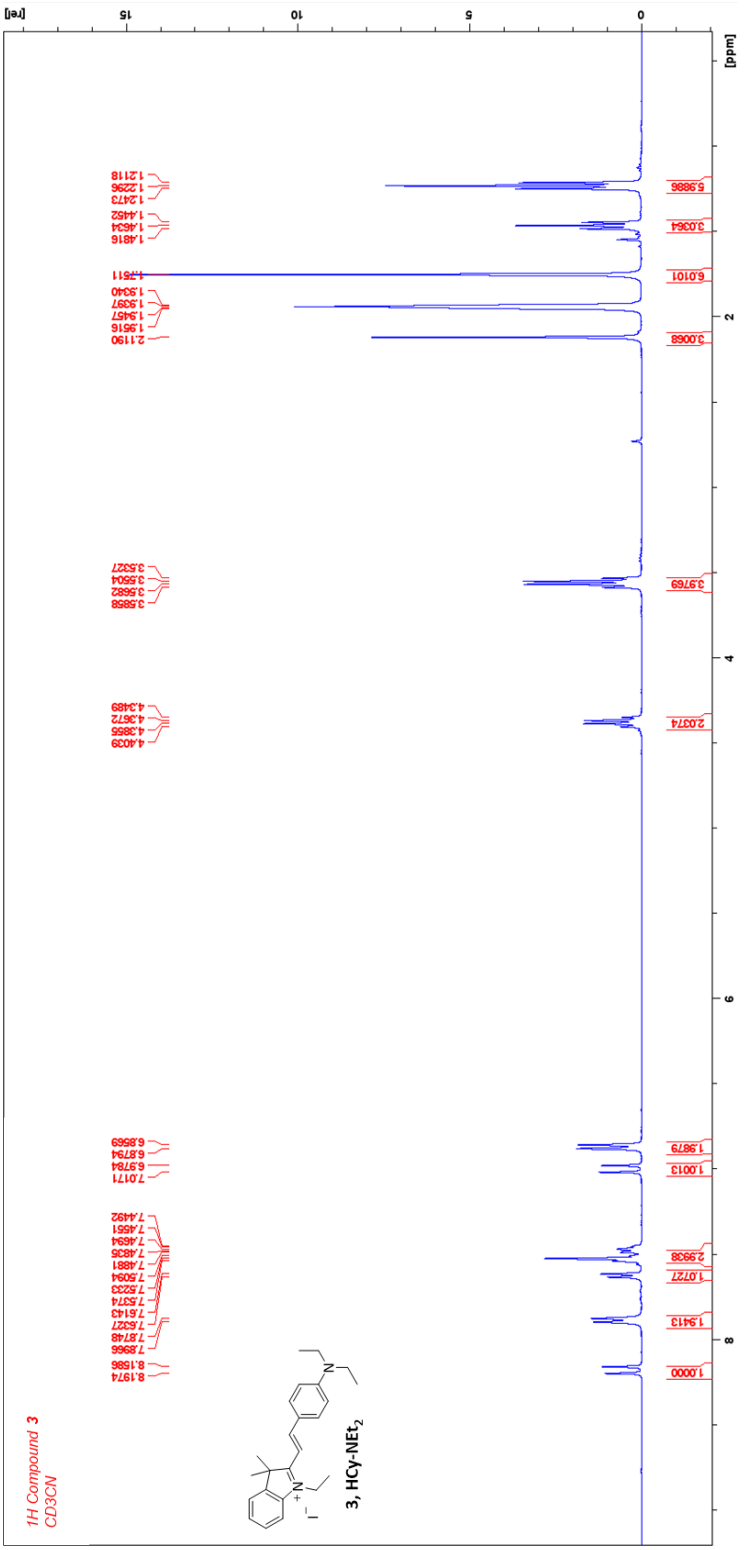

^{1}H NMR spectrum of **HCy-Jul** (**4**), d_6-DMSO.

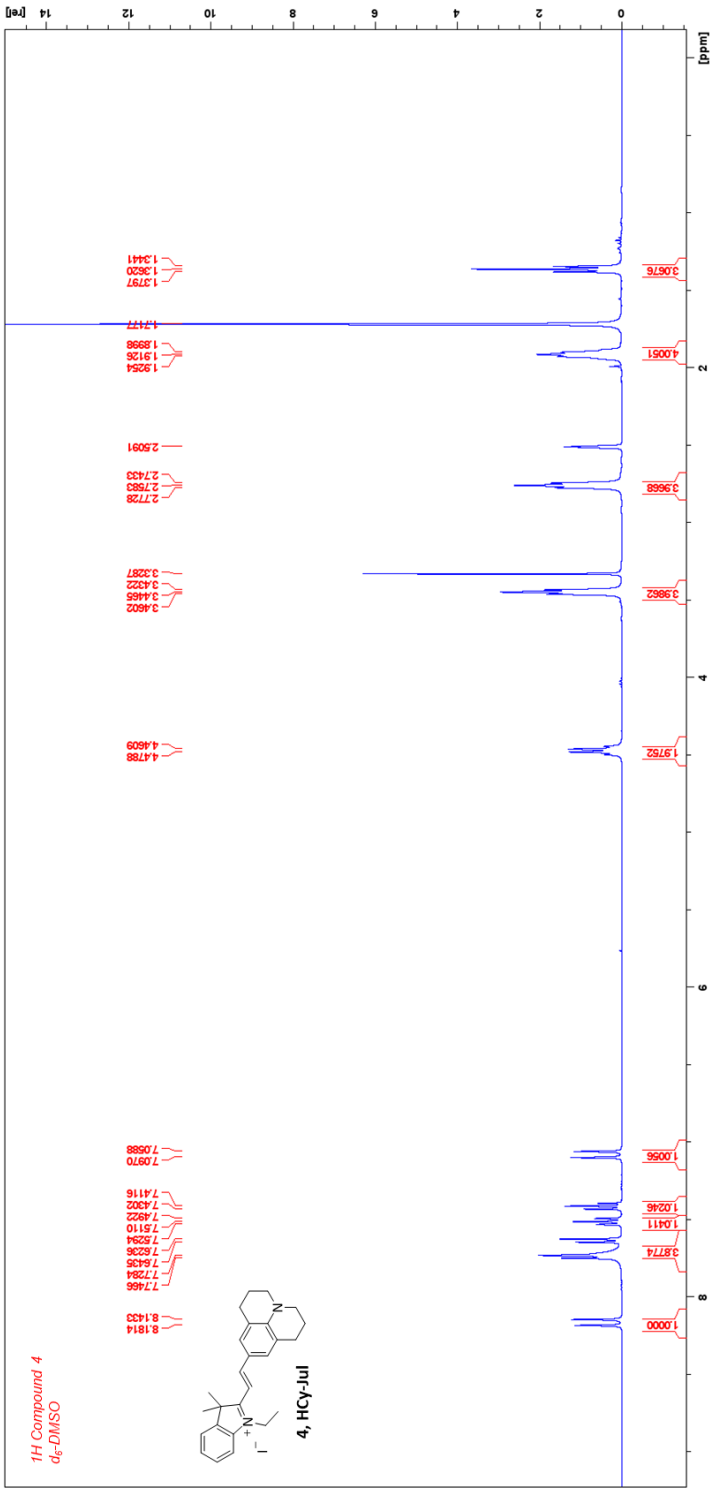

^{13}C NMR spectrum of **HCy-Jul** (**4**), d_6-DMSO.

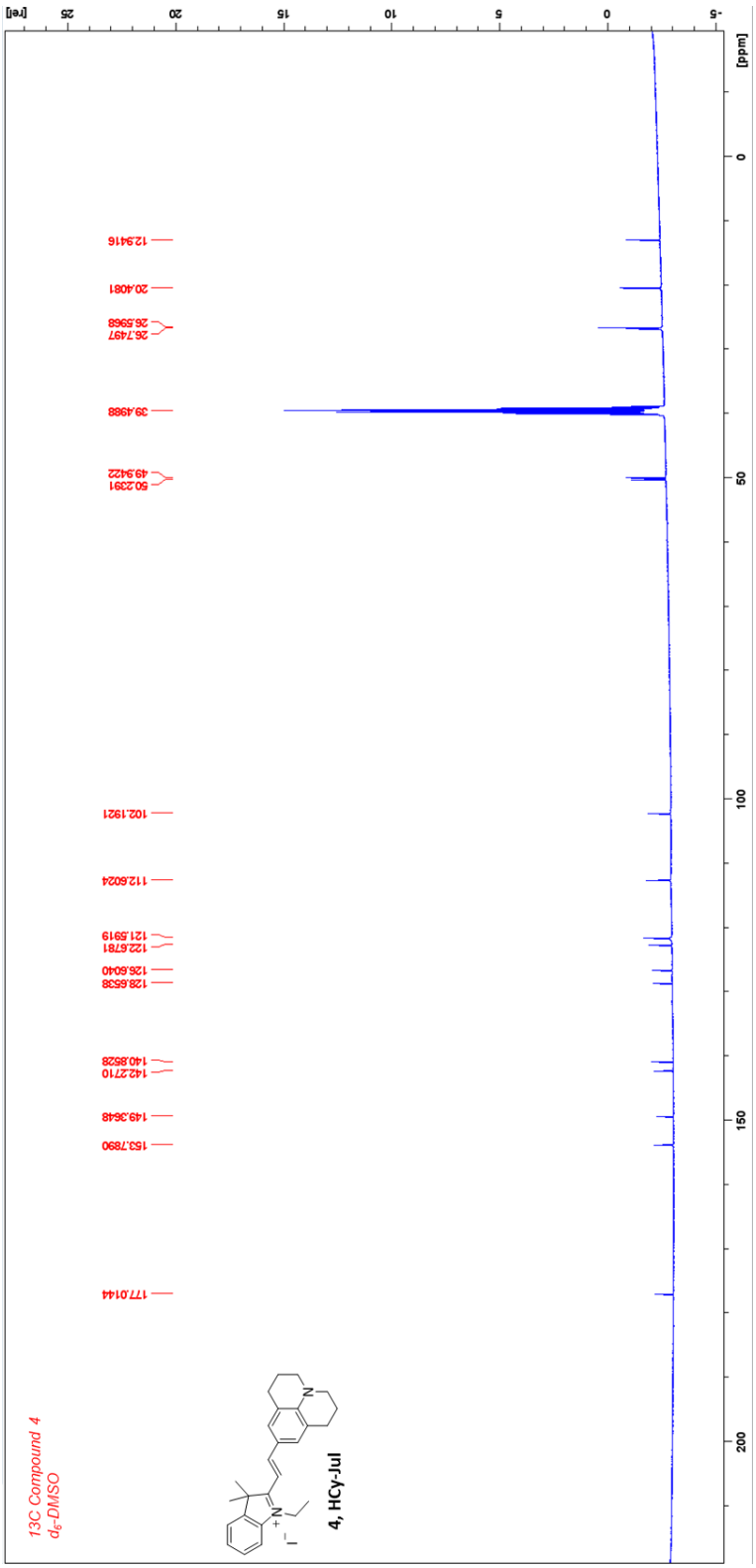

^{1}H NMR spectrum of **5**, d_6-DMSO.

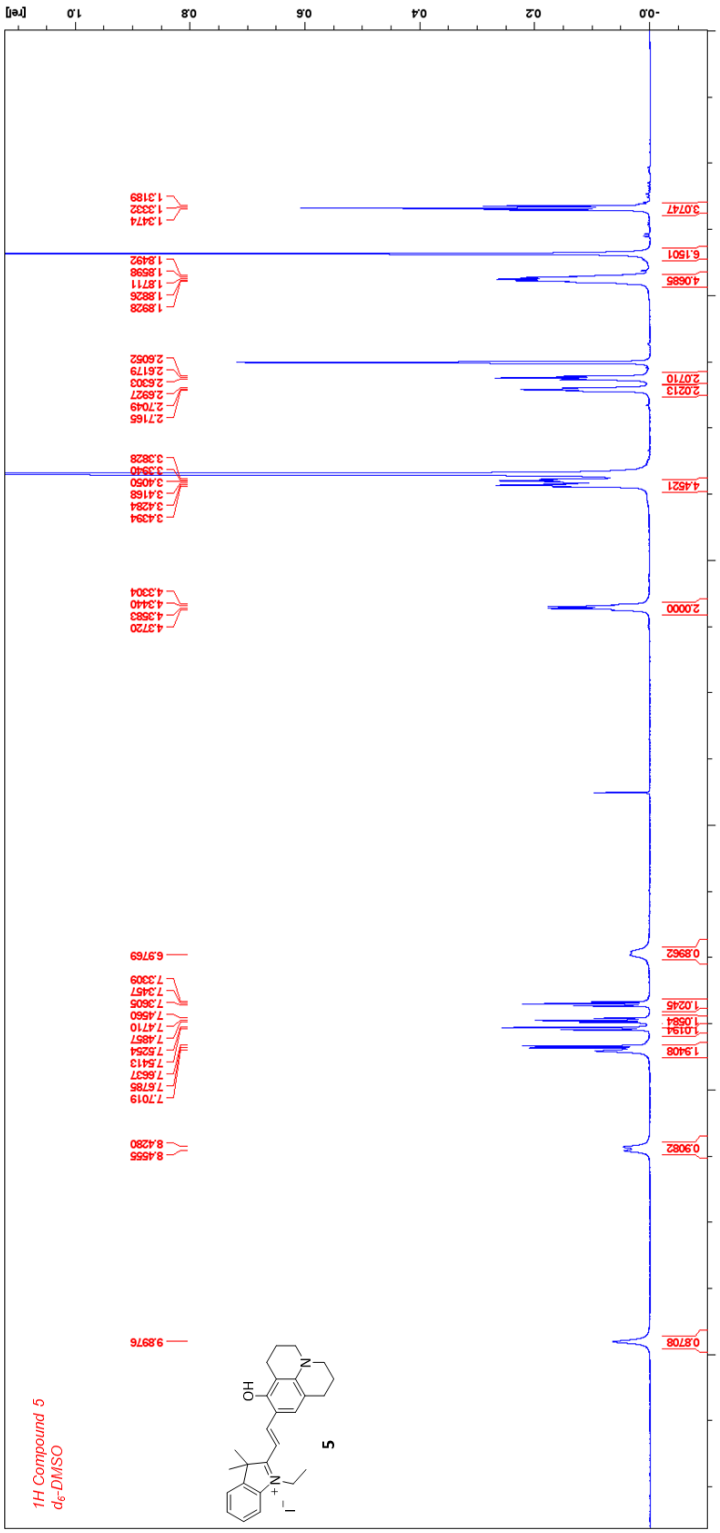

^{1}H NMR spectrum of **6**, $CDCl_3$.

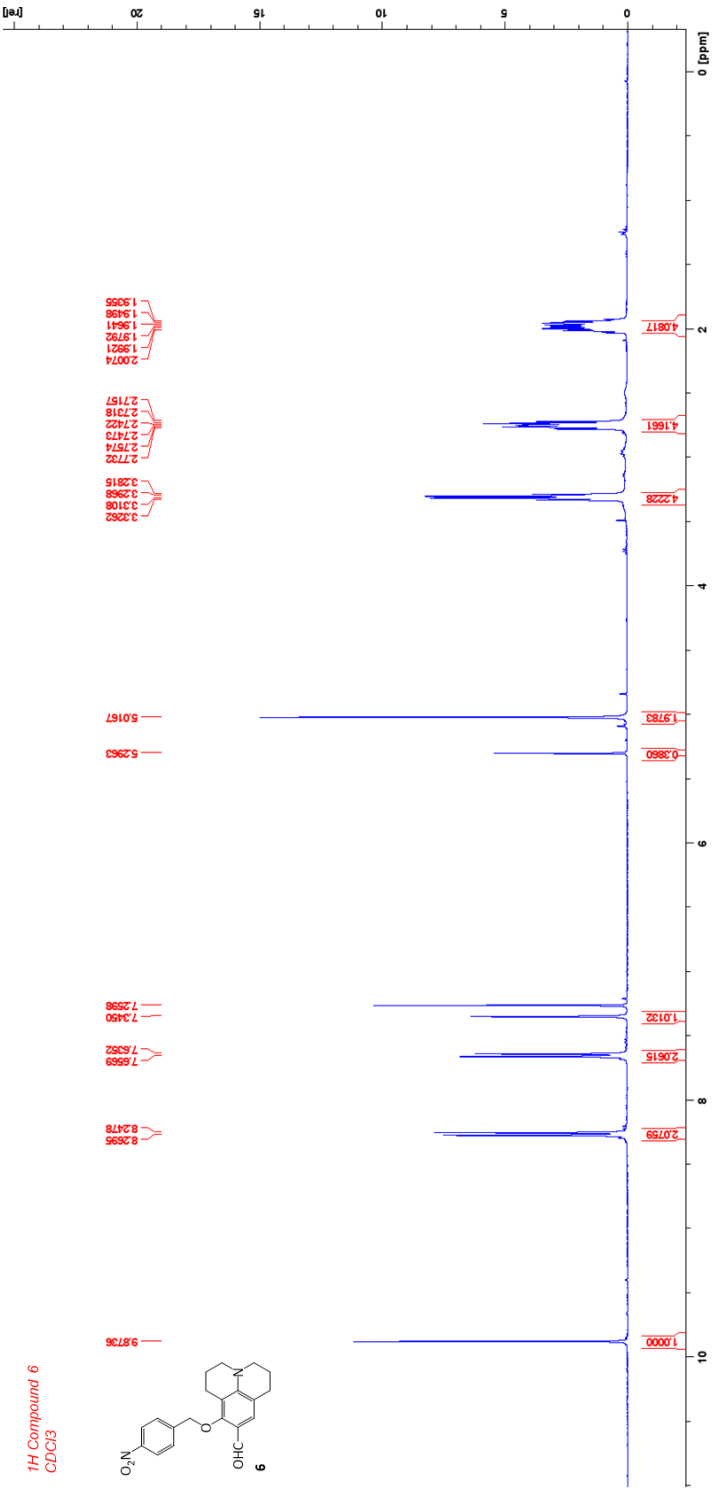

^{13}C NMR spectrum of **6**, $CDCl_3$.

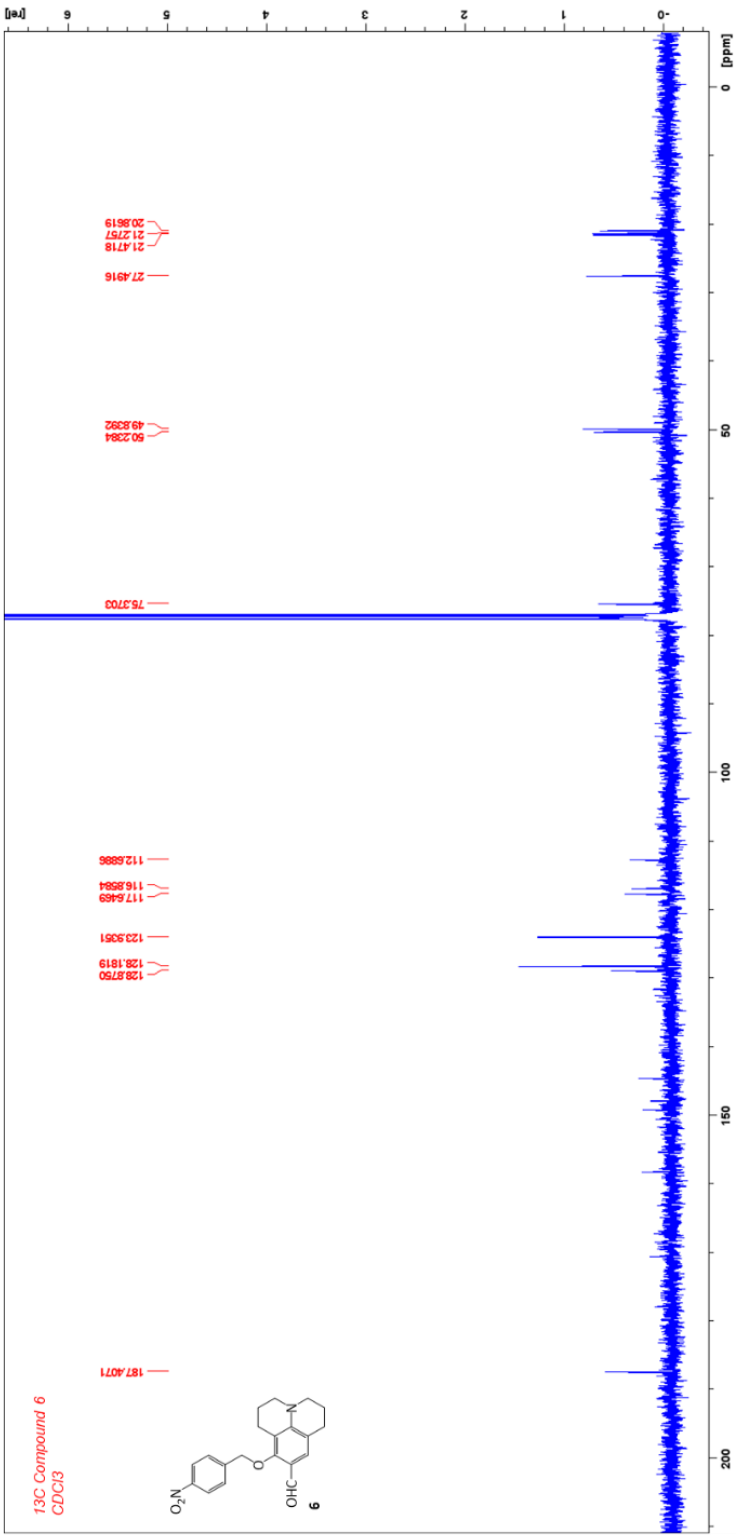

^{1}H NMR spectrum of **7**, d_6-DMSO.

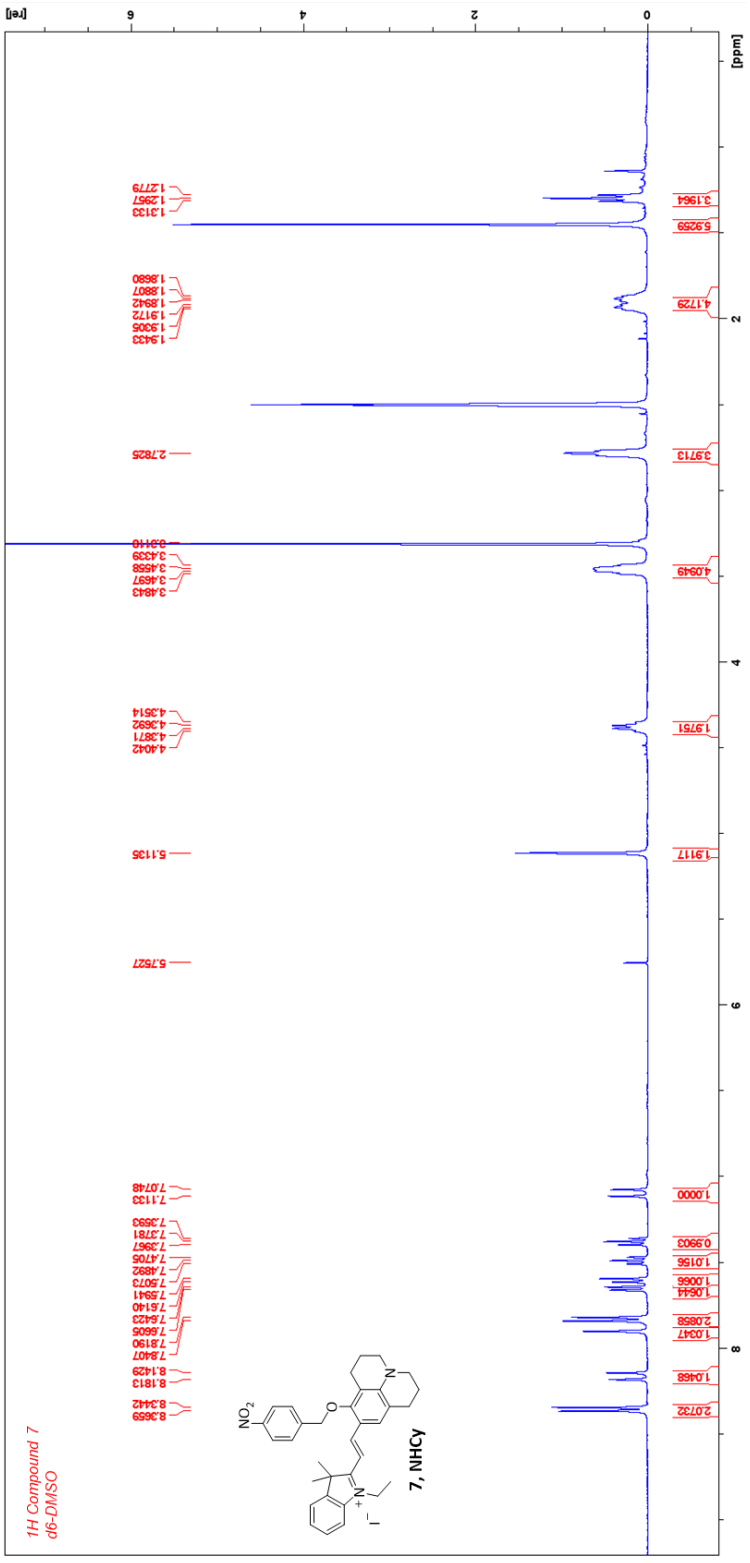

^{13}C NMR spectrum of **7**, d_6-DMSO.

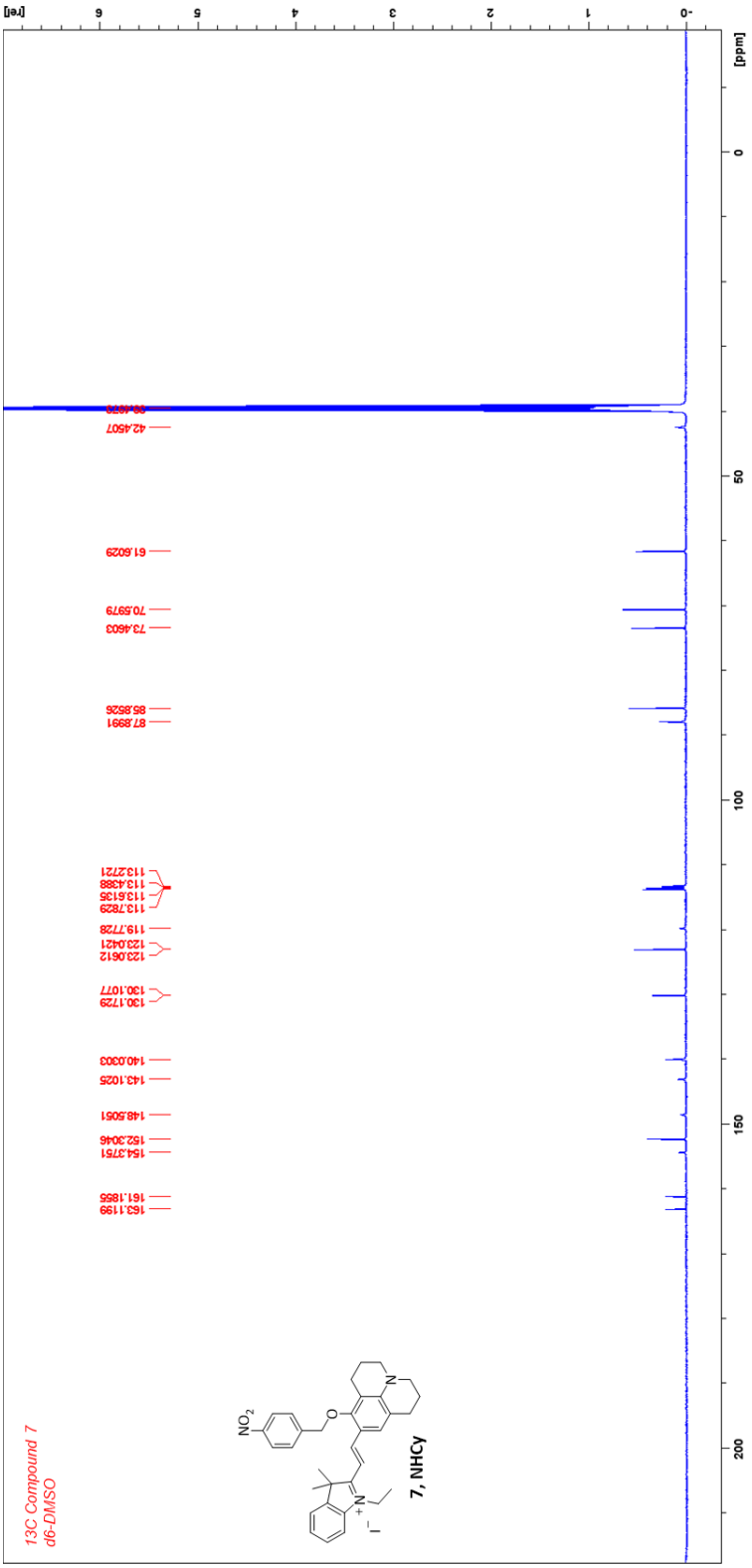

^{1}H NMR spectrum of **8**, $CDCl_3$.

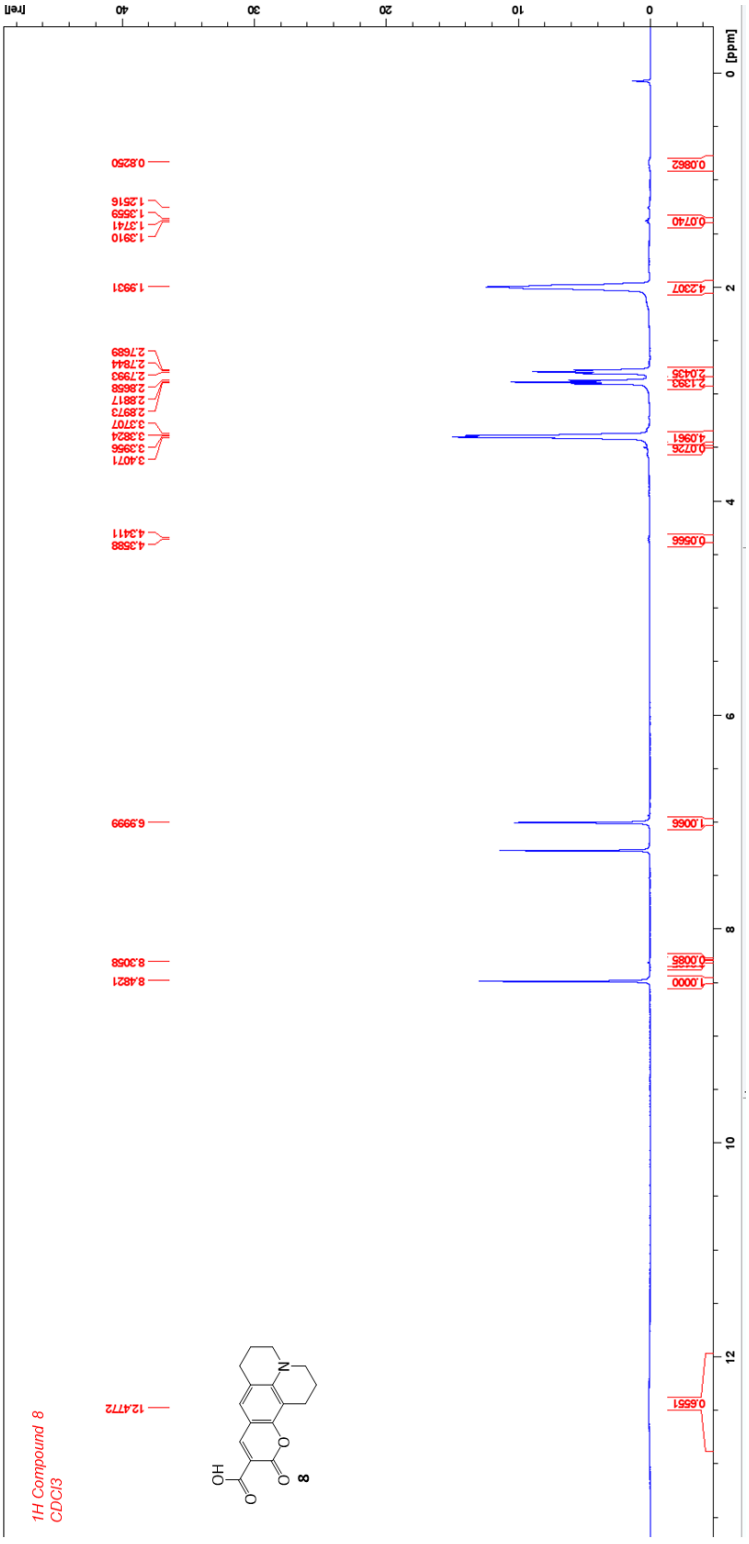

^{1}H NMR spectrum of **9**, d_6-DMSO.

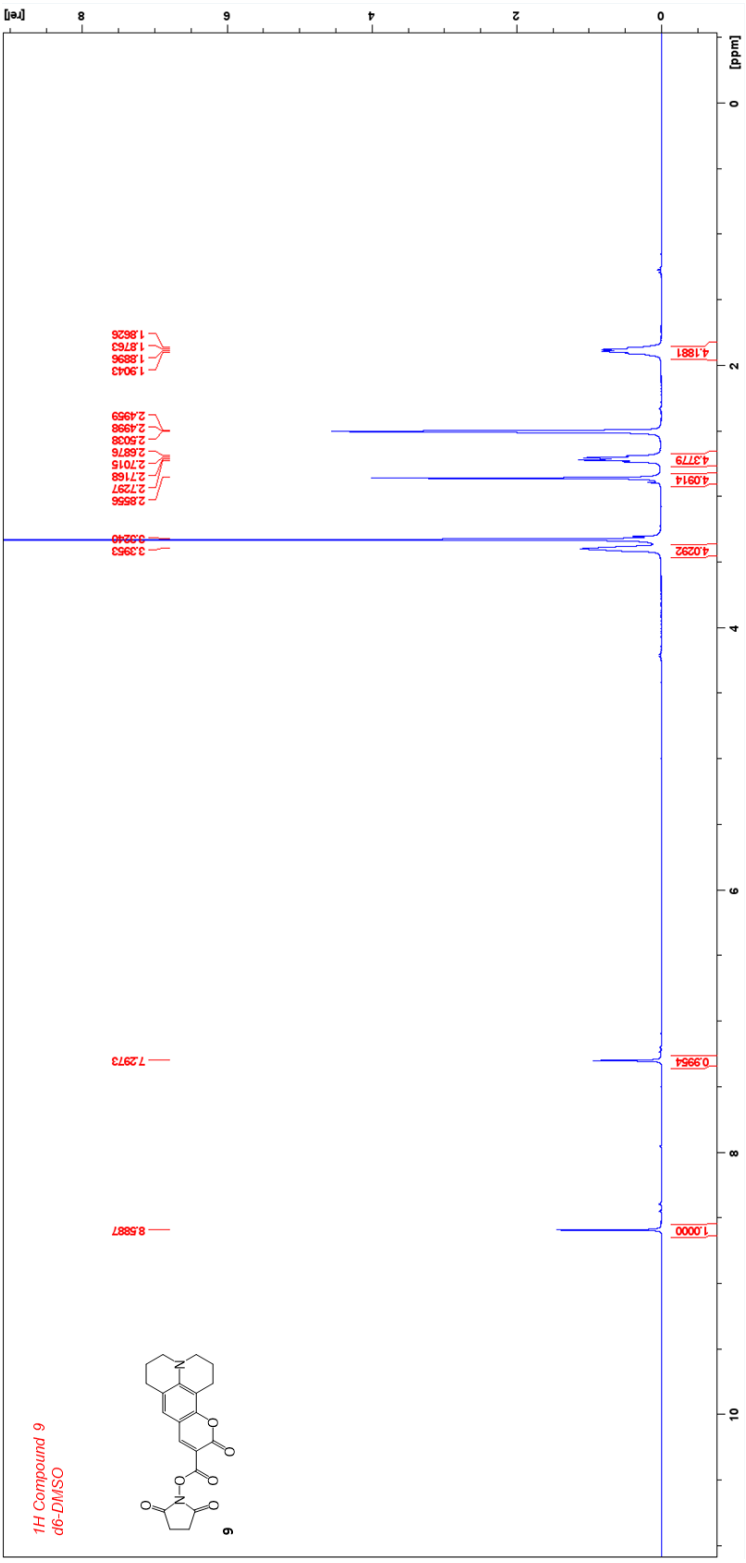

^{1}H NMR spectrum of **10'**, $CDCl_3$.

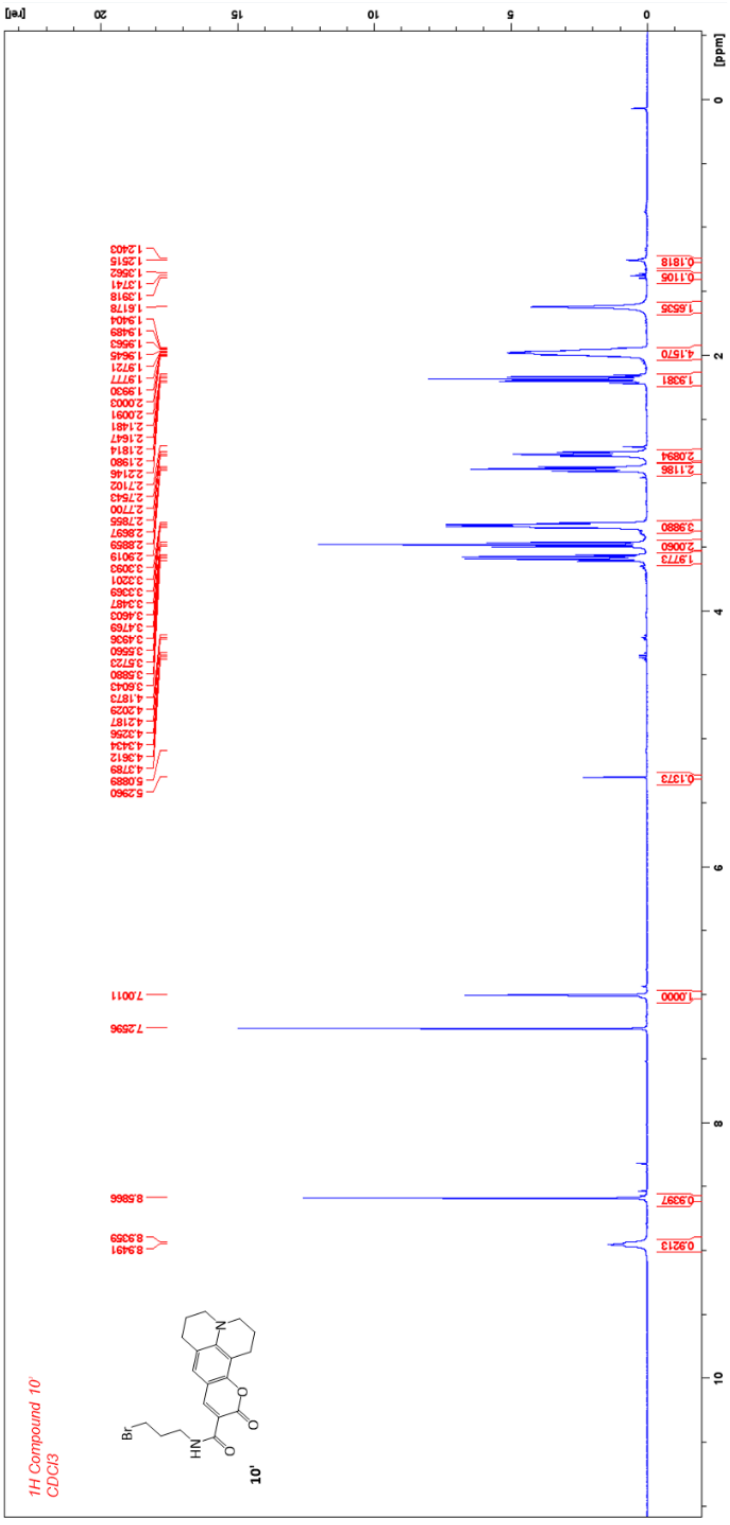

^{13}C NMR spectrum of **10'**, $CDCl_3$.

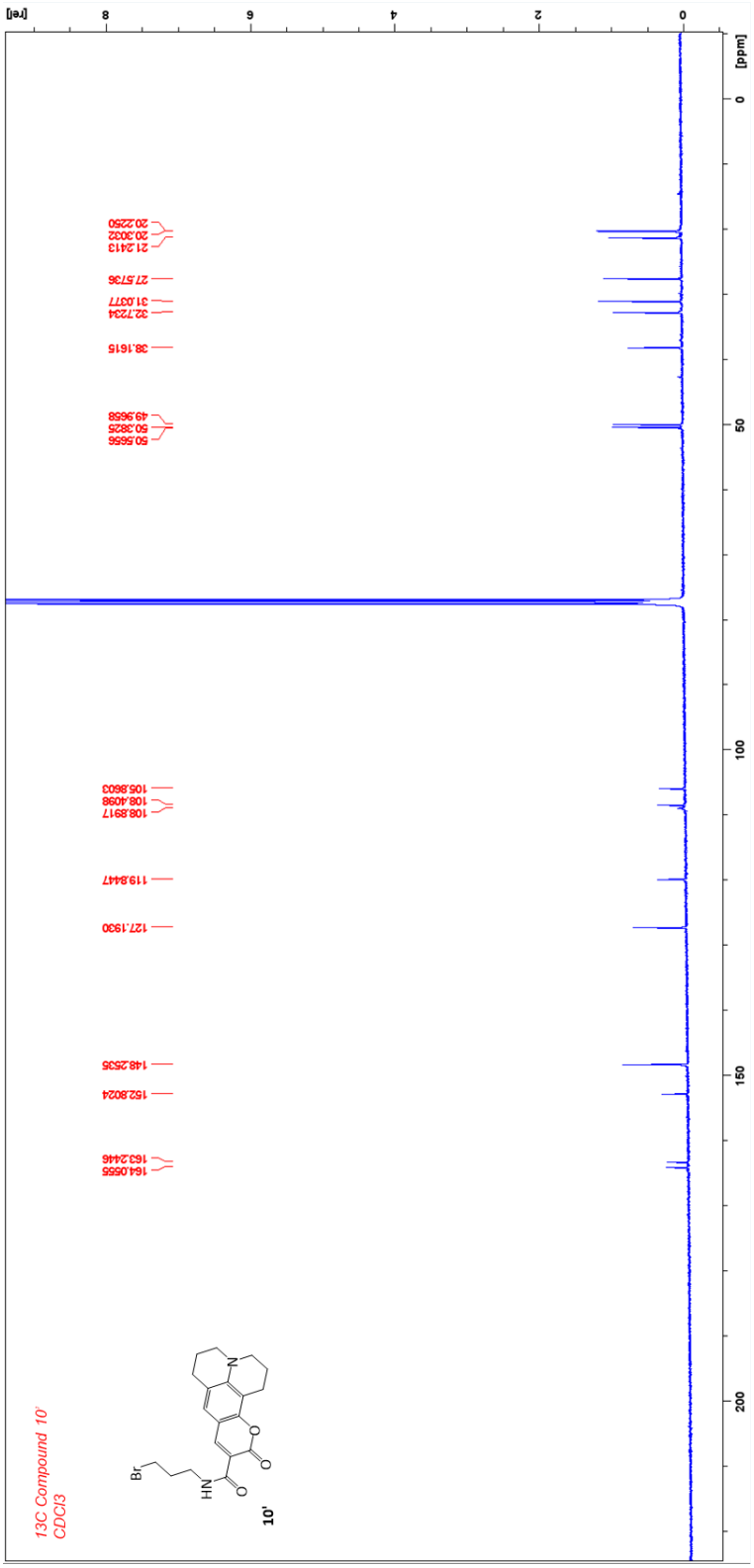

^{1}H NMR spectrum of **NHCy-C** (**12**) in MeOD.

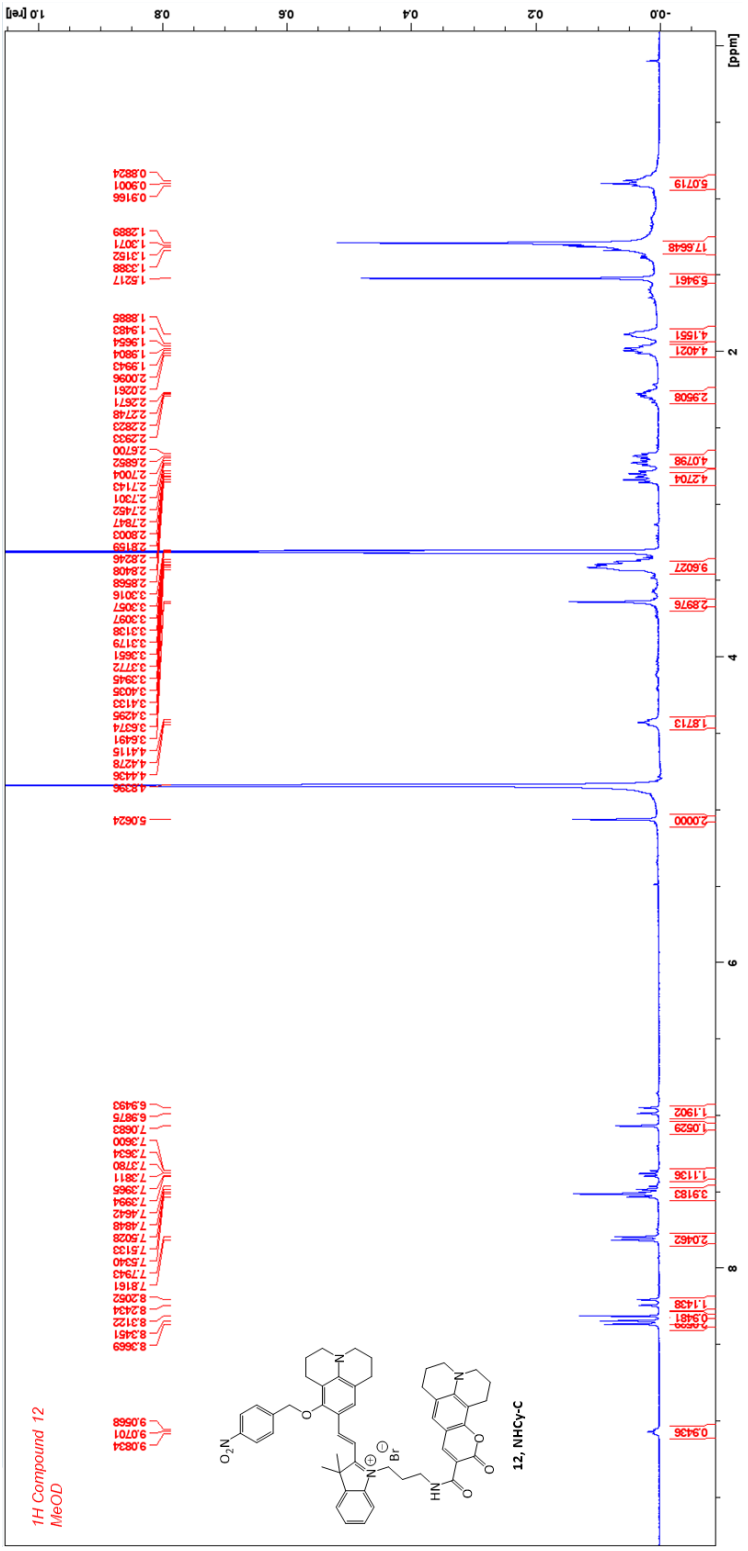

^{13}C NMR spectrum of **NHCy-C, 12**, MeOD.

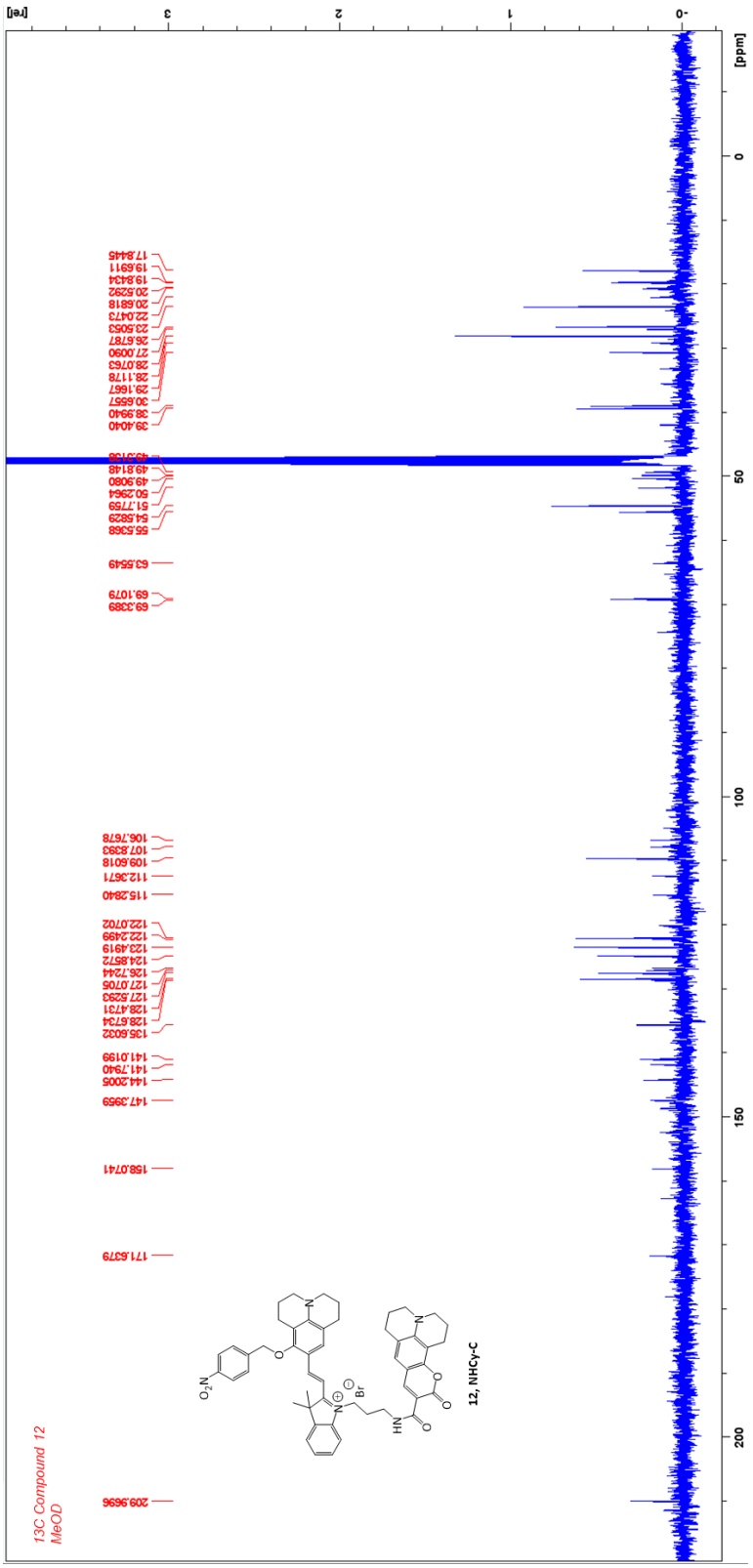

6.1.2. NMR spectra of titrations

^{1}H, ^{13}C, COSY, HMBC, and HSQC, spectra of treated (1 eq nucleophile) hemicyanine derivatives **HCy-OMe**, **HCy-NEt$_2$**, and **HCy-Jul** are attached in this subchapter

Cyanide titration yielded 1,2-adducts of **HCy-OMe** and **HCy-Jul** in full conversion. Basic elucidation for those was attempted.

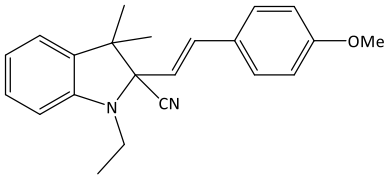

1,2-adduct of **HCy-OMe**: δ_H(500 MHz; d_6-DMSO/D_2O (80:20)): 7.49 (d, 2H, ^{3}J = 8.5 Hz), 7.10 (t, 2H, ^{3}J = 7.5 Hz), 6.92 (d, 2H, ^{3}J = 8.5 Hz), 6.87 (d, 1H, ^{3}J = 16.0 Hz), 6.79 (d, 1H, ^{3}J = 7.5 Hz), 6.66 (d, 1H, ^{3}J = 8.0 Hz), 6.22 (d, 1H, ^{3}J = 16.0 Hz), 3.72 (s, 3H), 3.13-3.00 (m, 2H),1.37 (s, 3H), 1.18 (t, 3H, ^{3}J = 7.0 Hz), 1.05 (s, 3H) ppm. δ_C(500 MHz; d_6-DMSO/D_2O (80:20)): 160.50, 148.43, 137.04, 135.12, 129.28, 129.09, 128.36, 122.79, 121.50, 120.50, 119.93, 115.14, 80.37, 56.02, 49.62, 41.22, 24.88, 22.96, 14.70 ppm.

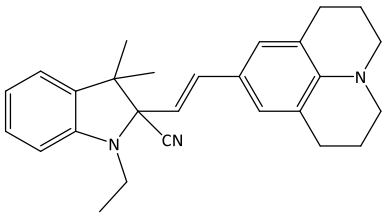

1,2-adduct of **HCy-Jul**: δ_H(500 MHz; d_6-DMSO/D_2O (80:20)): 7.10 (q, 2H, ^{3}J = 7.0 Hz), 6.88 (s, 2H), 6.77 (t, 1H, ^{3}J = 7.5 Hz), 6.69-6.63 (m, 2H), 5.94 (d, 1H, ^{3}J = 16.0 Hz), 3.09-3.02 (m, 6H), 2.62 (t, 4H, ^{3}J = 6.5 Hz), 1.80 (t, 4H, ^{3}J = 6.0 Hz), 1.34 (s, 3H), 1.18 (t, 3H, ^{3}J = 7.0 Hz), 1.03 (s, 3H) ppm. δ_C(500 MHz; d_6-DMSO/D_2O (80:20)): 148.20,143.60, 136.79, 135.88, 128.57, 126.17, 125.523, 122.16, 121.25, 119.85, 119.54, 116.77, 108.56, 80.25, 49.67, 49.05, 40.67, 40.43, 40.26, 40.10, 39.93, 39.76, 27.64, 27.53, 24.66, 22.8, 21.92, 21.81,14.51 ppm.

Methanethiolate titration yielded 1,4-adduct of **HCy-OMe** in full conversion.

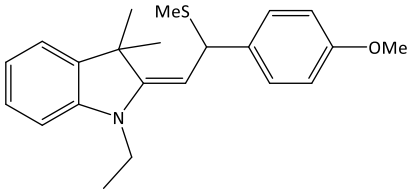

1,4-adduct of **HCy-OMe**: δ_H(500 MHz; d_6-DMSO/D_2O (80:207.32 (d, 2H, J = 8.5 Hz), 7.06-7.00 (m, 2H), 6.86 (t, 2H, ^3J = 6.5 Hz), 6.65 (t, 1H, ^3J = 7.5 Hz), 6.52 (d, 1H, ^3J = 8.0 Hz), 4.98 (d, 1H, ^3J = 11.0 Hz), 4.57 (d, 1H, ^3J = 11.0 Hz), 3.68 (s, 3H), 3.51-3.47 (m, 2H), 1.86 (s, 3H), 1.48 (s, 3H), 1.27 (s, 3H), 0.99 (t, 3H, ^3J = 7.0 Hz) ppm. δ_C(500 MHz; d_6-DMSO/D_2O (80:20)): 158.16, 152.51, 144.80, 138.08, 135.54, 128.86, 128.22, 121.90, 118.70, 114.2, 105.44, 94.74, 55.44, 46.63, 44.40, 36.09, 28.77, 27.95, 14.79, 10.56 ppm

^{1}H NMR spectra of **HCy-OMe** treated with 1 eq of KCN in DMSO-d_6/D_2O (80:20).

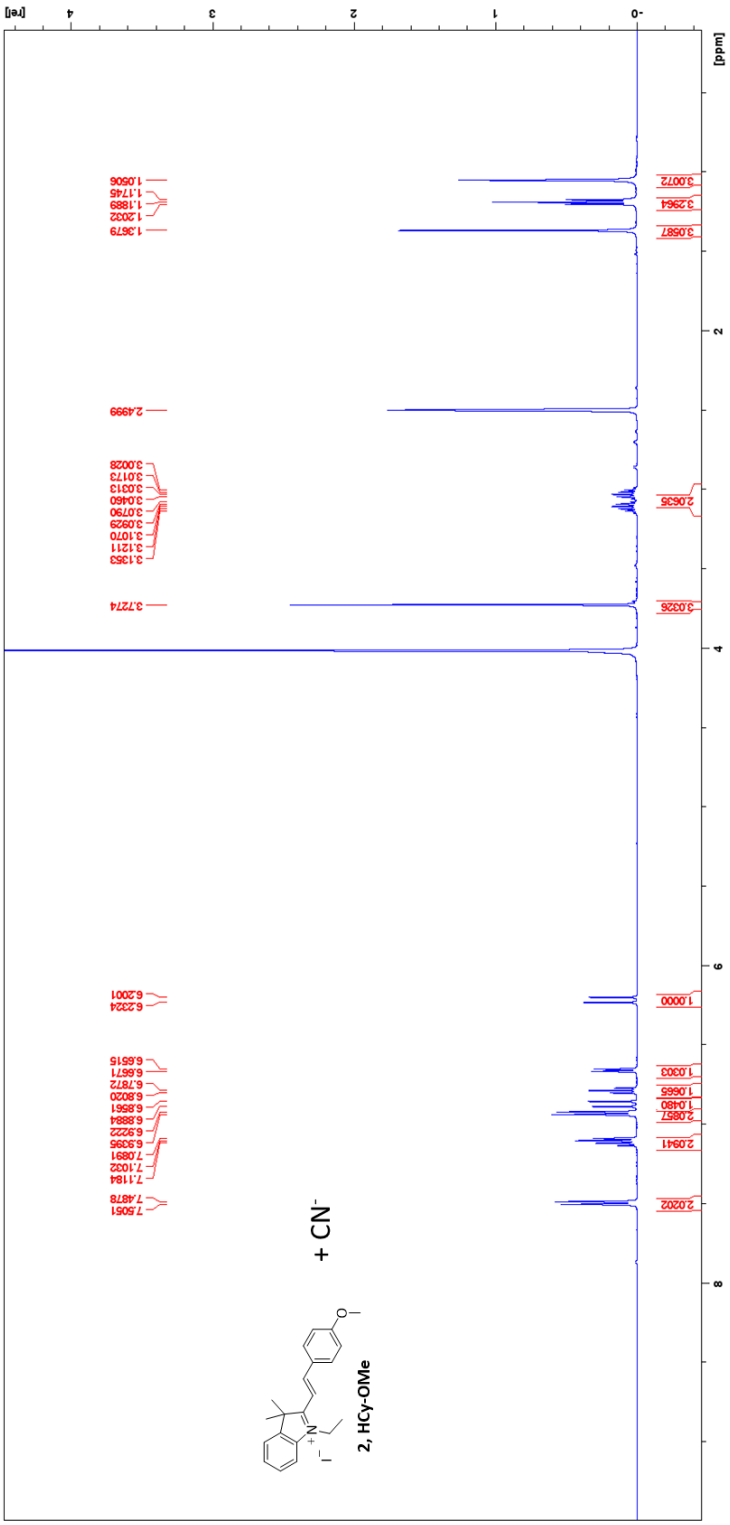

^{13}C NMR spectra of **HCy-OMe** treated with 1 eq of KCN in DMSO-d_6/D_2O (80:20).

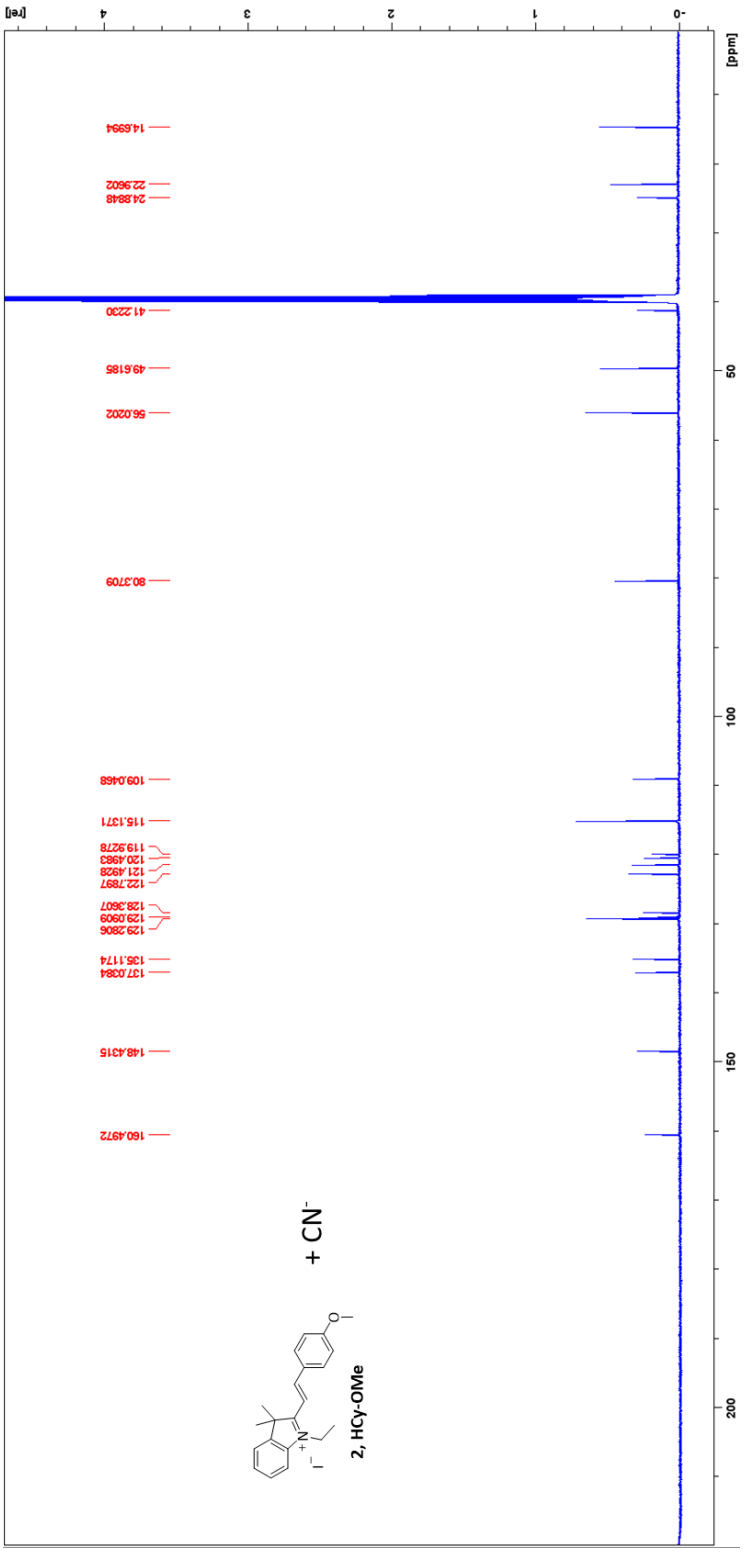

COSY spectra of **HCy-OMe** treated with 1 eq of KCN in DMSO-d_6/D_2O (80:20).

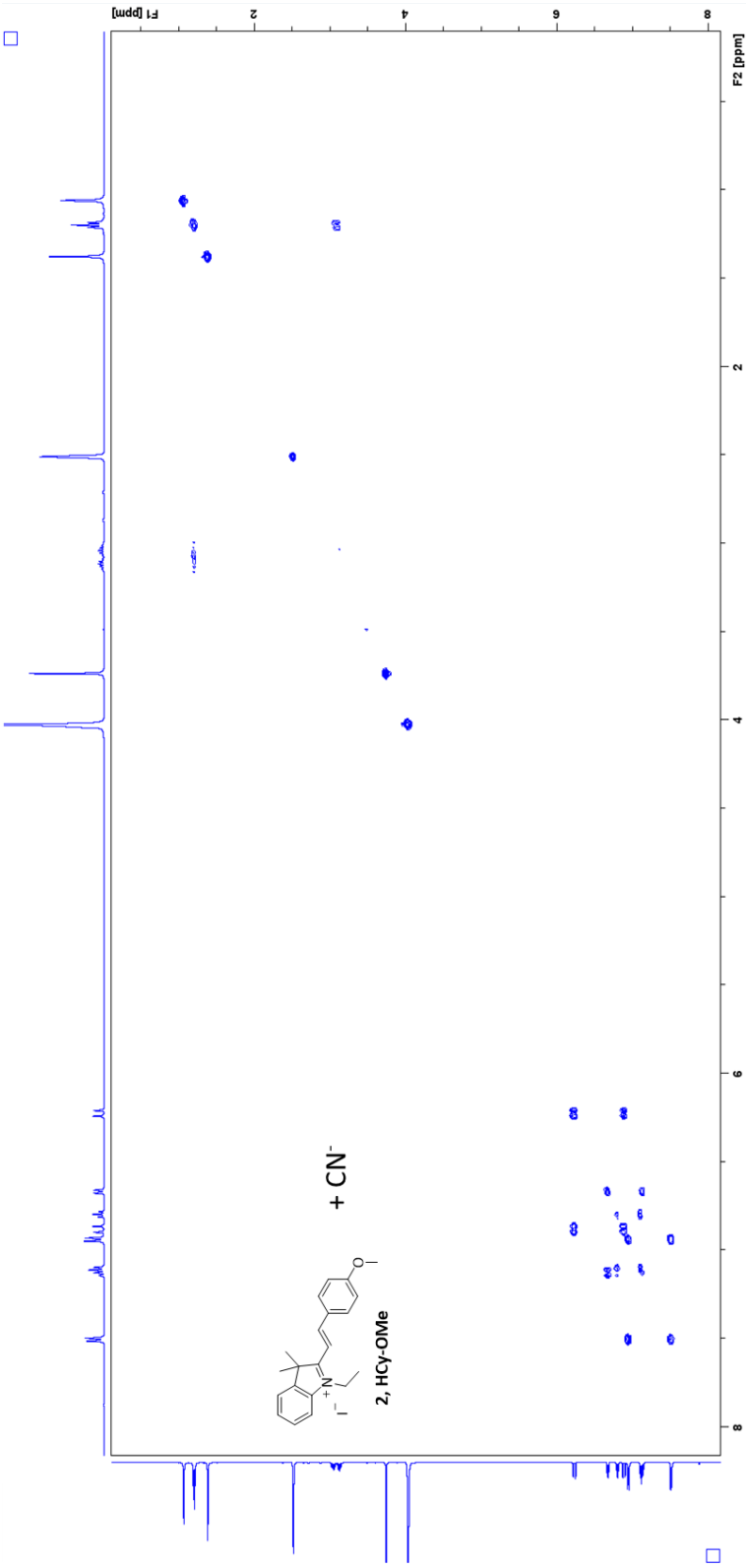

HMBC spectra of **HCy-OMe** treated with 1 eq of KCN in DMSO-d_6/D_2O (80:20).

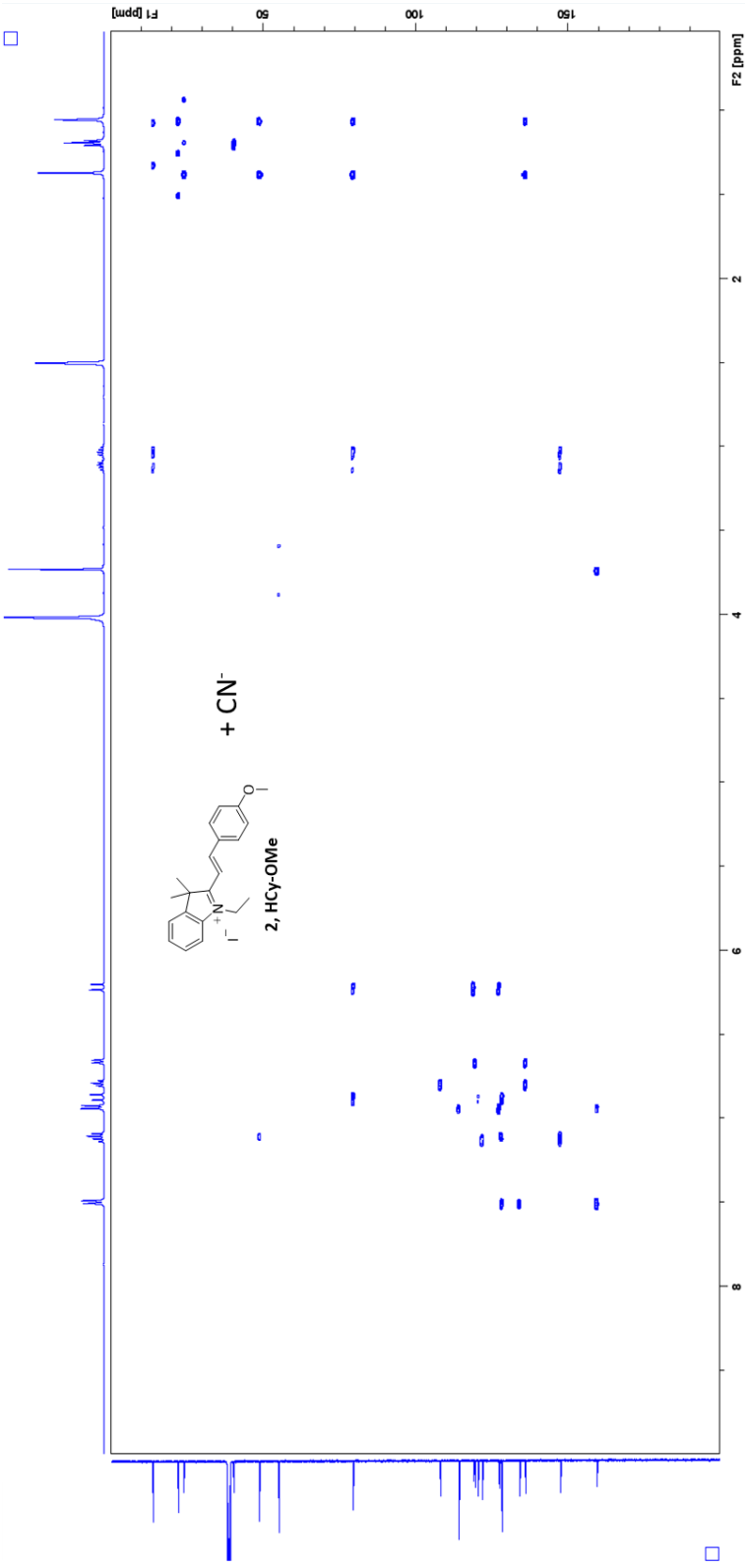

HSQC spectra of **HCy-OMe** treated with 1 eq of KCN in DMSO-d_6/D_2O (80:20).

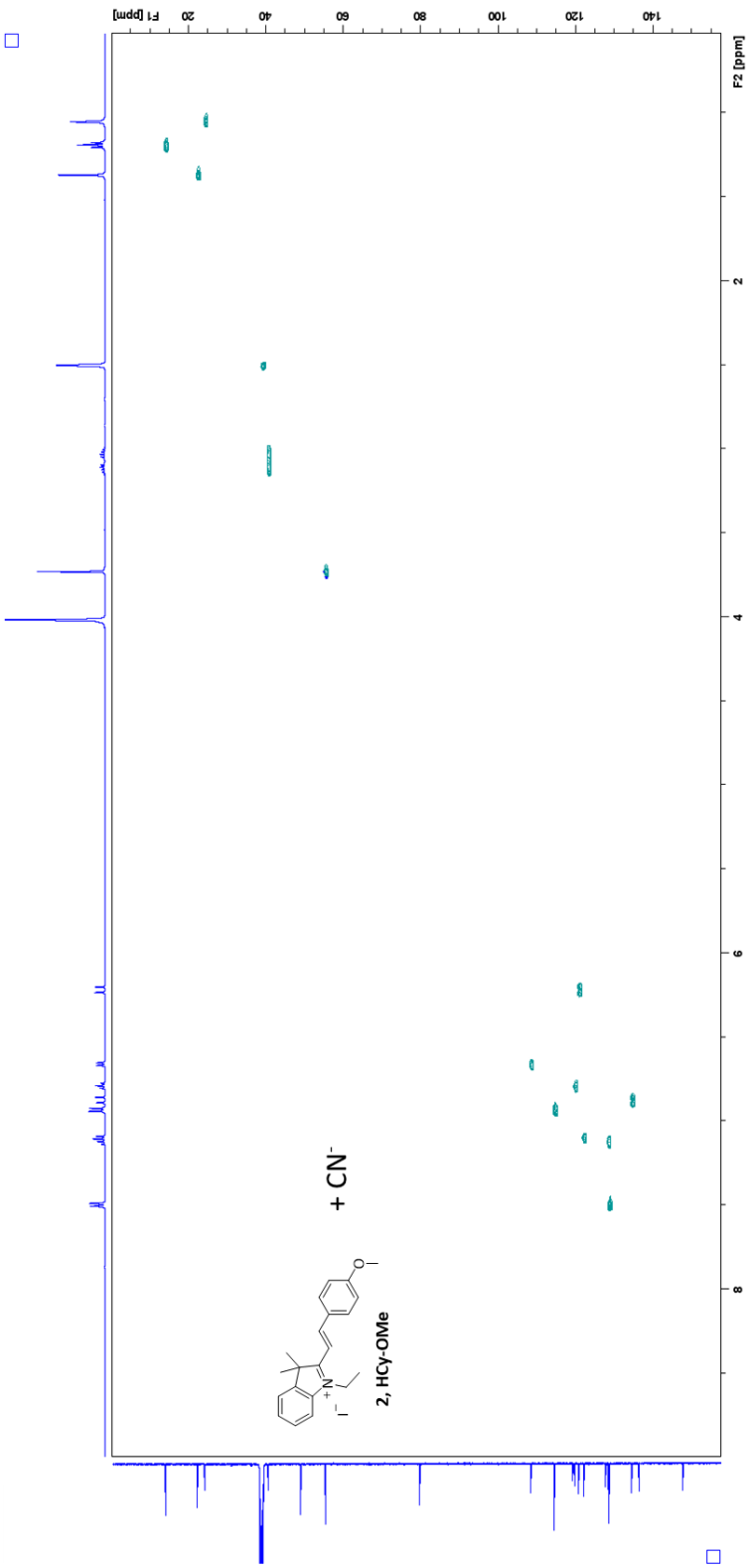

^{1}H NMR spectra of **HCy-NEt$_2$** treated with 1 eq of KCN in DMSO-d$_6$/D$_2$O (80:20).

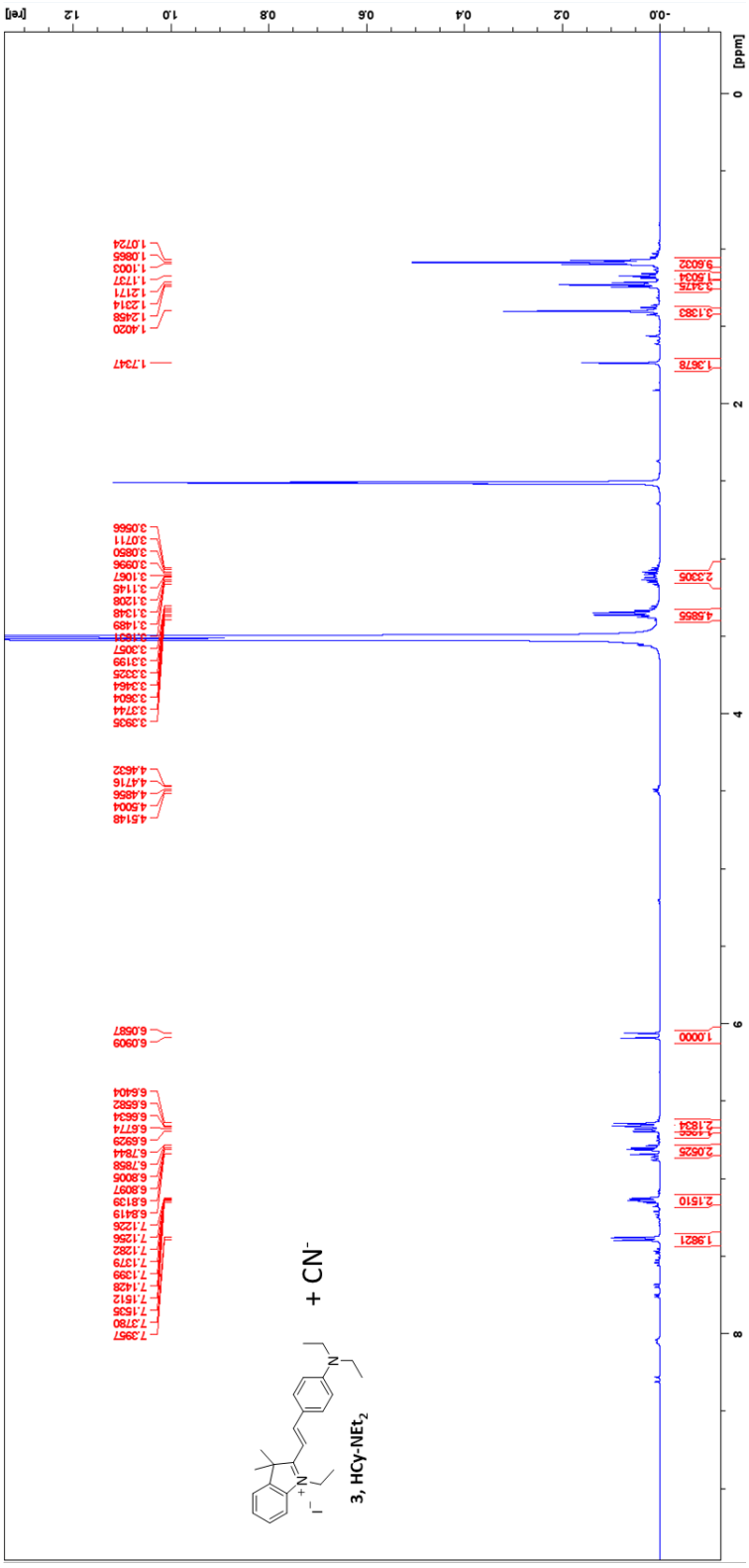

^{13}C NMR spectra of **HCy-NEt$_2$** treated with 1 eq of KCN in DMSO-d_6/D_2O (80:20).

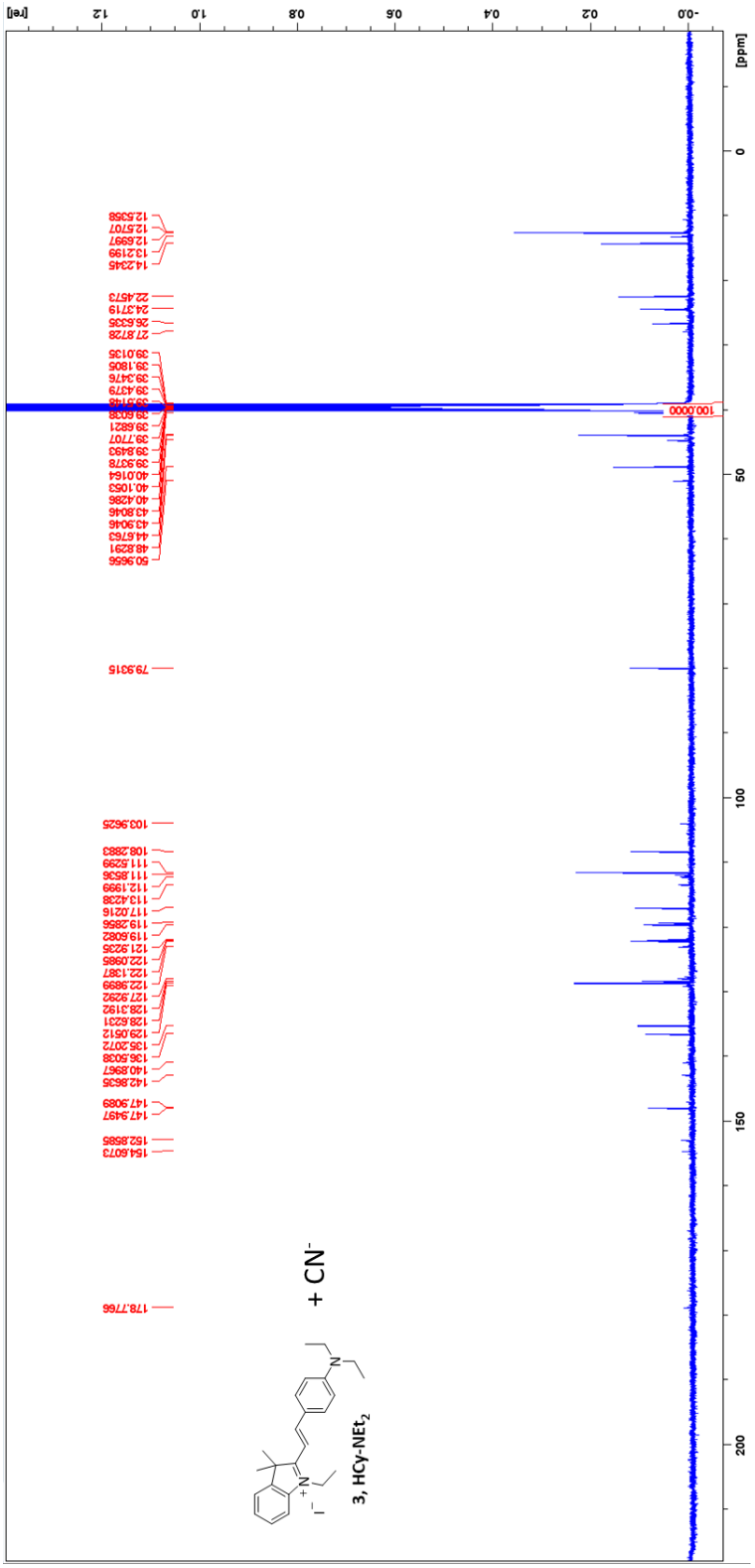

COSY spectra of **HCy-NEt$_2$** treated with 1 eq of KCN in DMSO-d$_6$/D$_2$O (80:20).

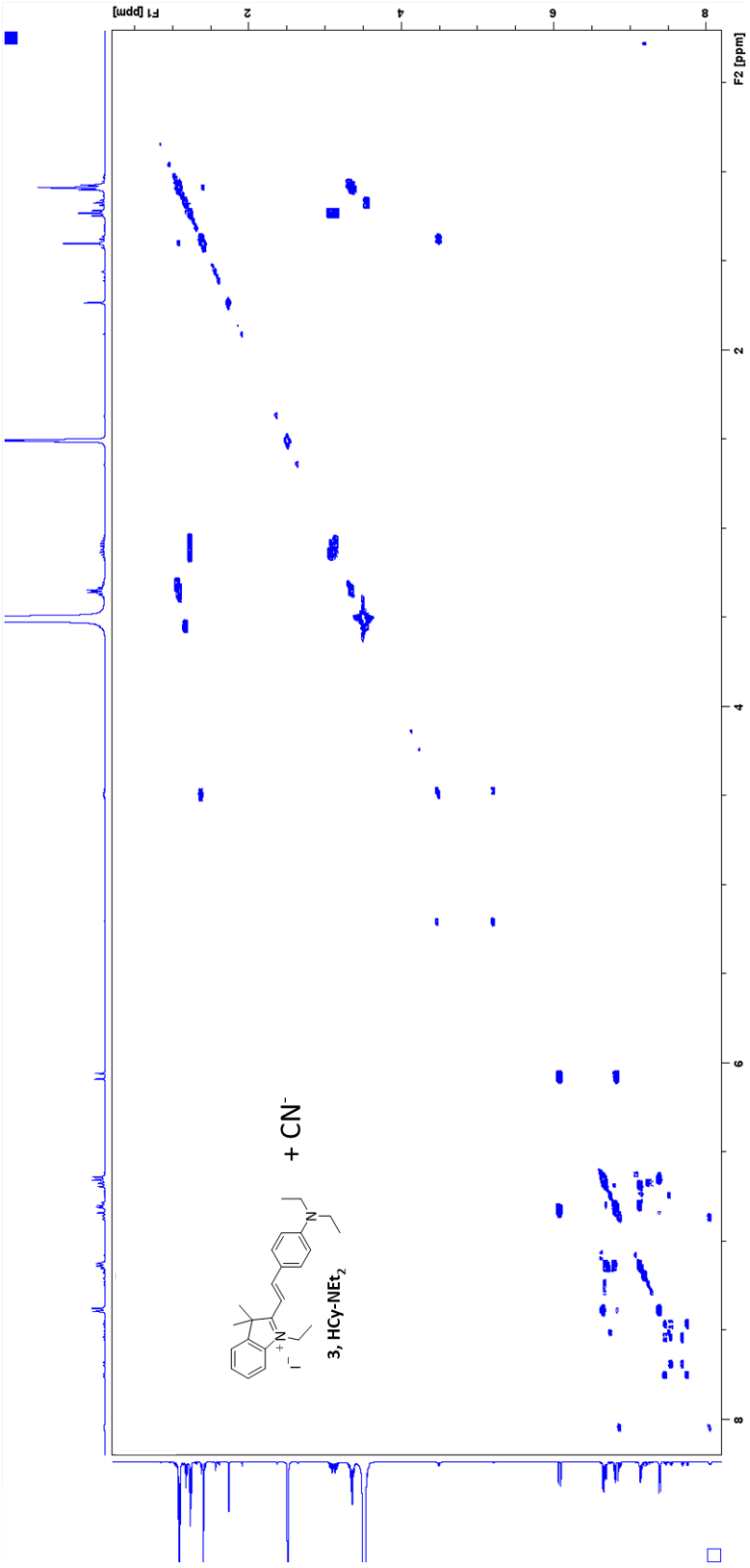

HMCB spectra of **HCy-NEt$_2$** treated with 1 eq of KCN in DMSO-d_6/D_2O (80:20).

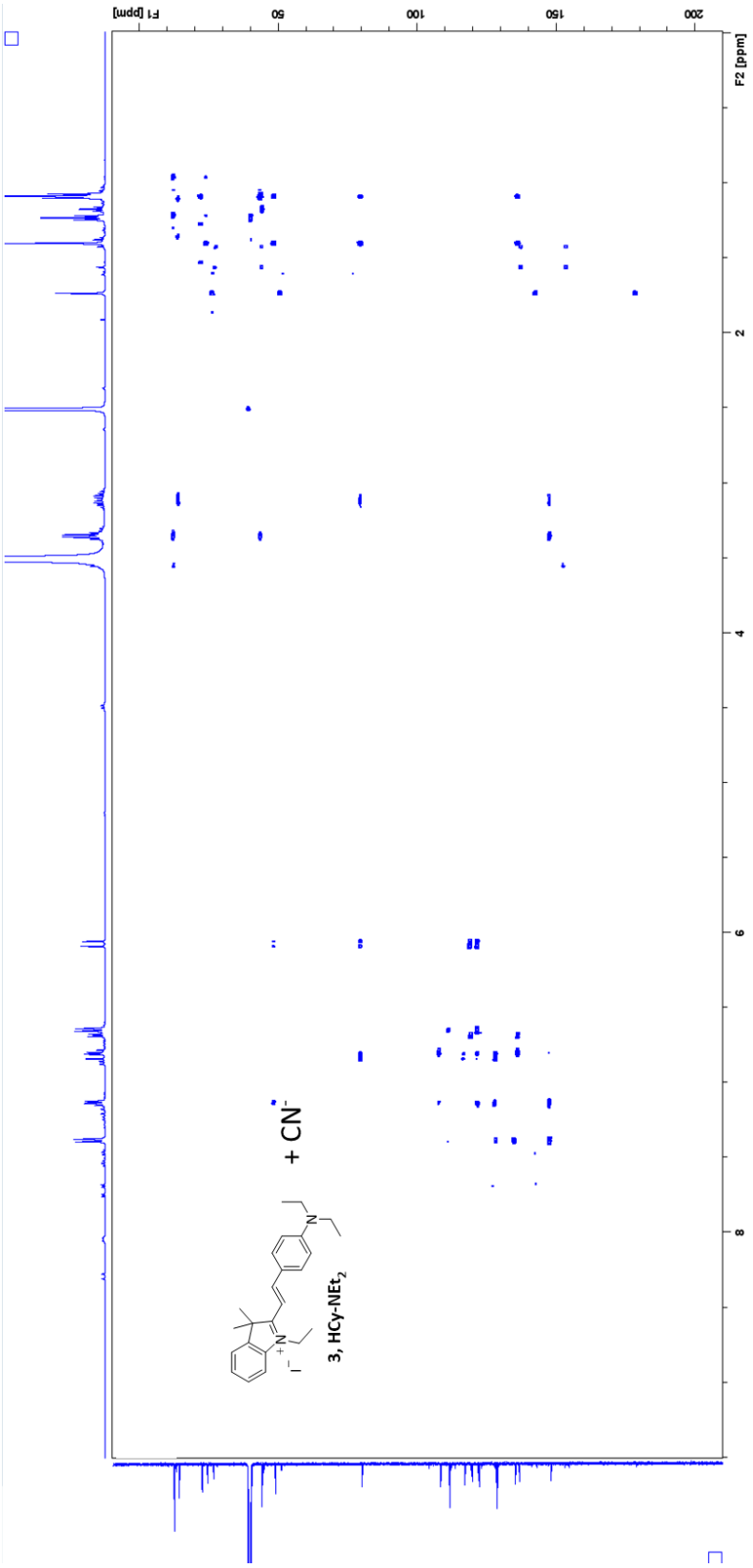

HSQC spectra of **HCy-NEt$_2$** treated with 1 eq of KCN in DMSO-d_6/D_2O (80:20).

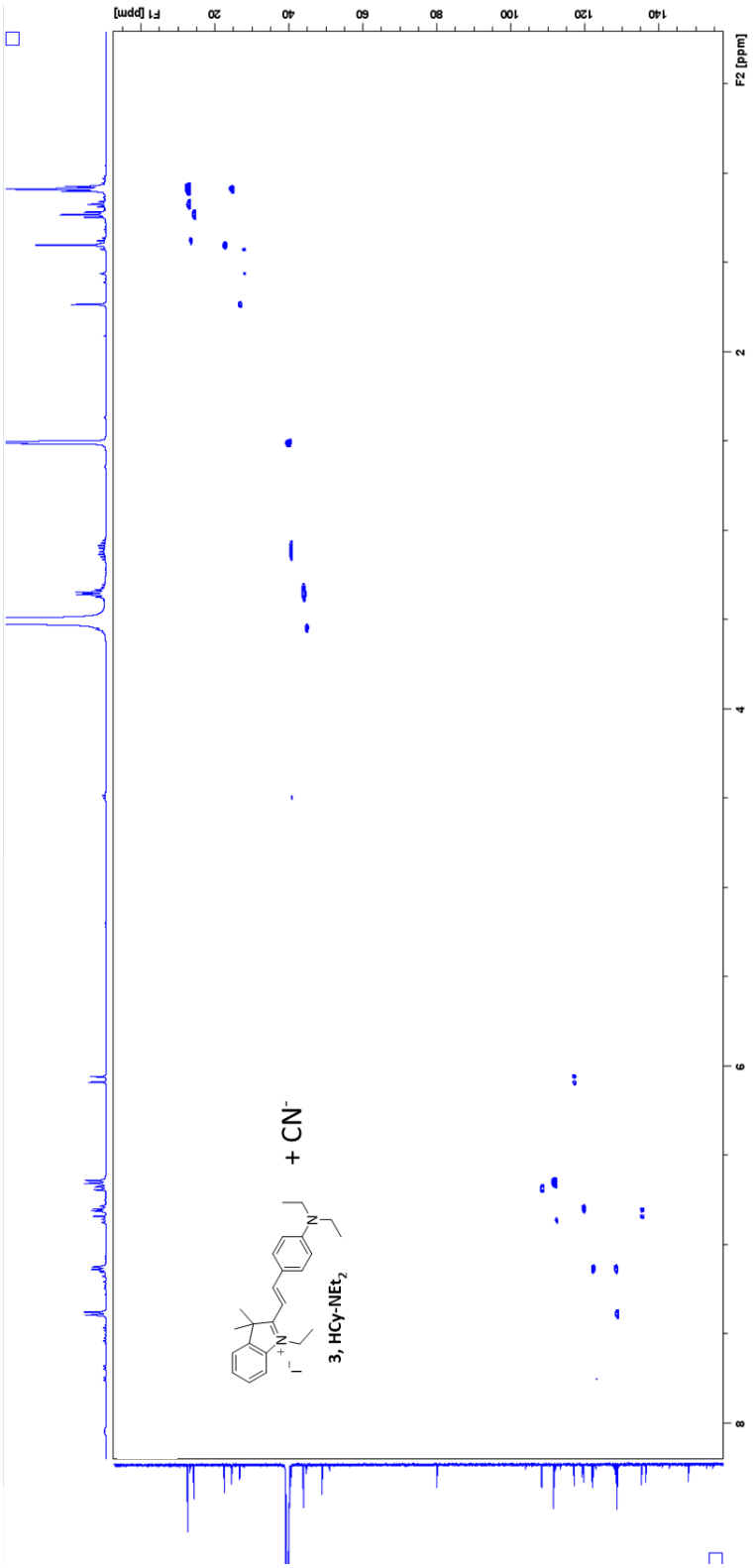

^{1}H NMR spectra of **HCy-Jul** treated with 1 eq of KCN in DMSO-d_6/D_2O (80:20).

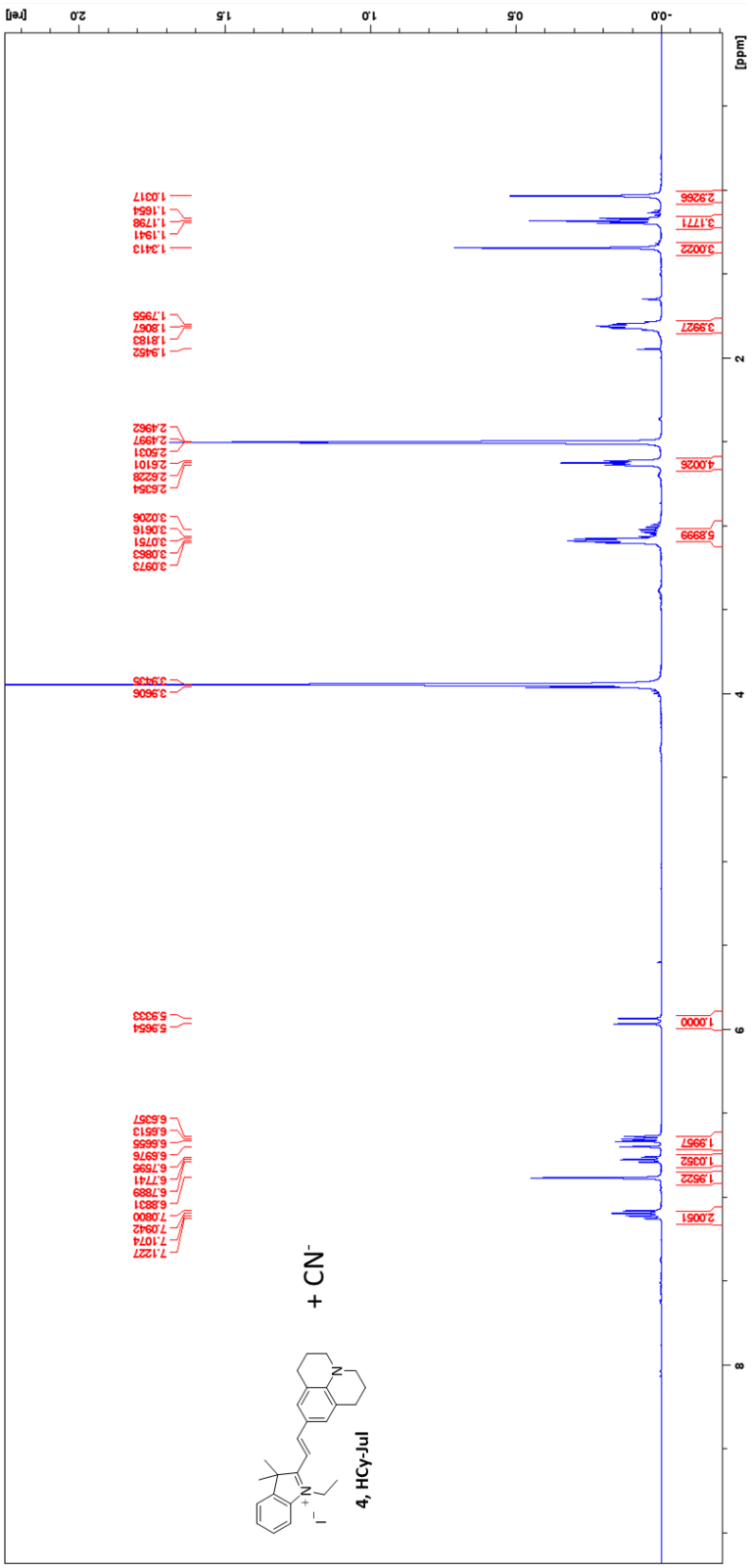

^{13}C NMR spectra of **HCy-Jul** treated with 1 eq of KCN in DMSO-d_6/D_2O (80:20).

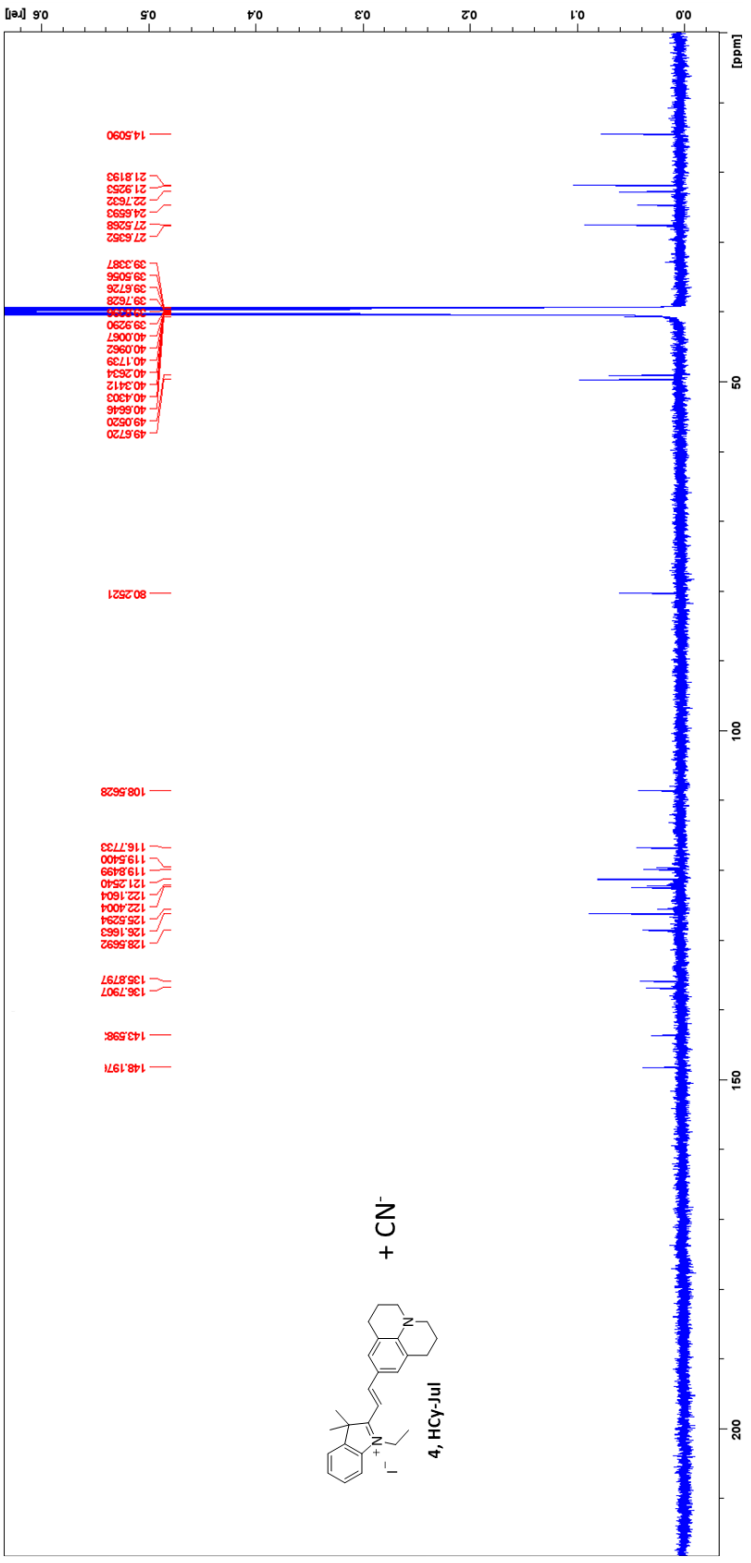

COSY spectra of **HCy-Jul** treated with 1 eq of KCN in DMSO-d_6/D_2O (80:20).

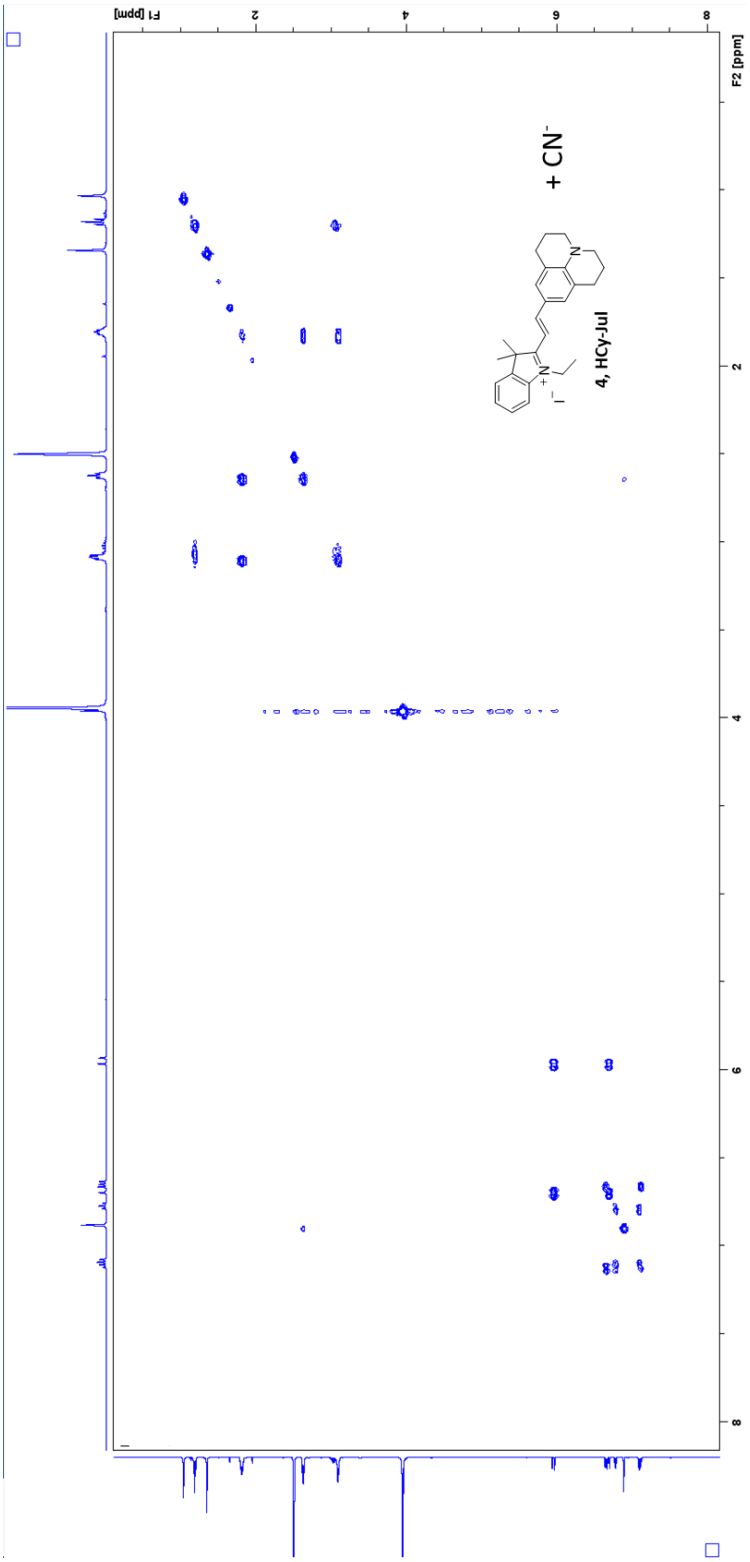

HMBC spectra of **HCy-Jul** treated with 1 eq of KCN in DMSO-d_6/D_2O (80:20).

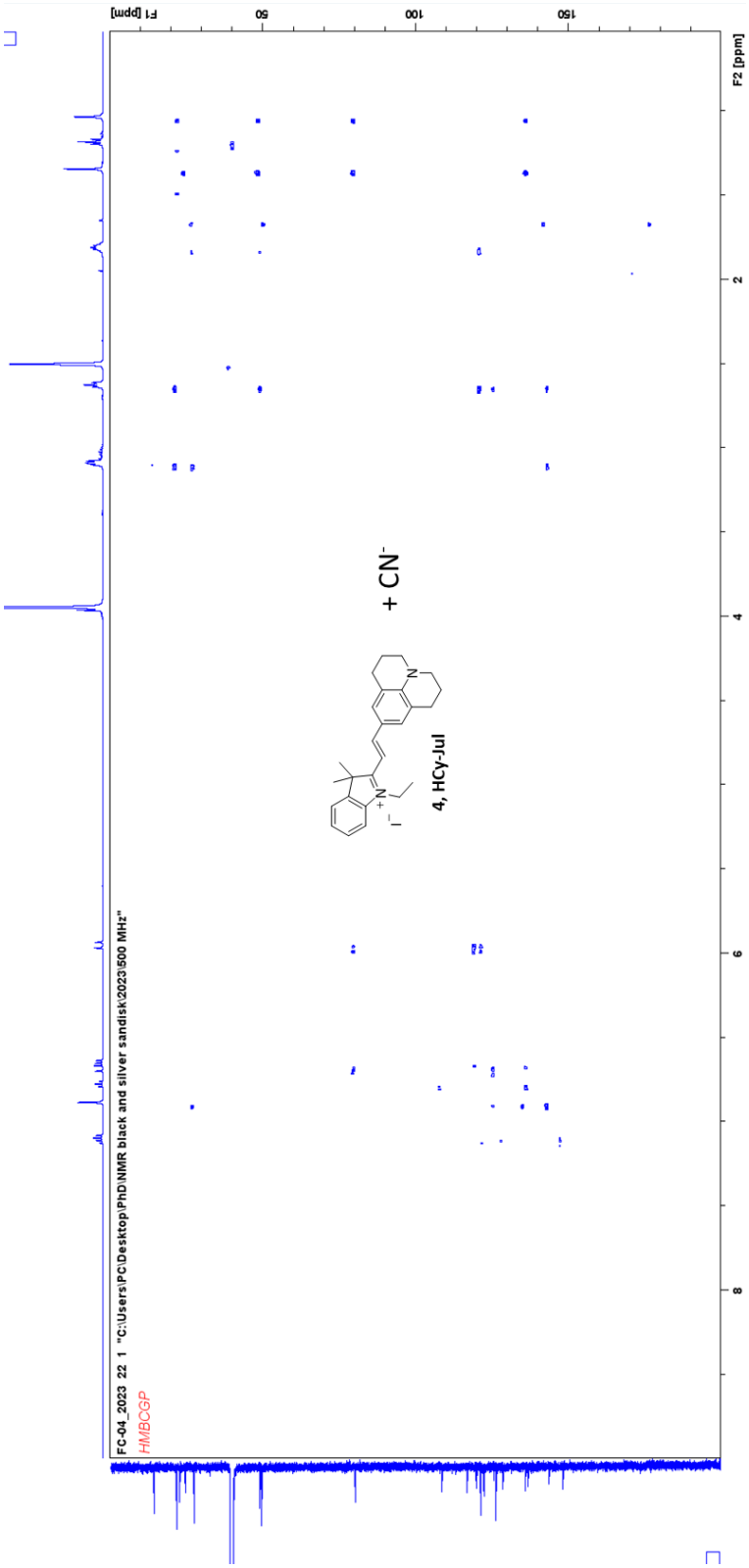

HSQC spectra of **HCy-Jul** treated with 1 eq of KCN in DMSO-d_6/D_2O (80:20).

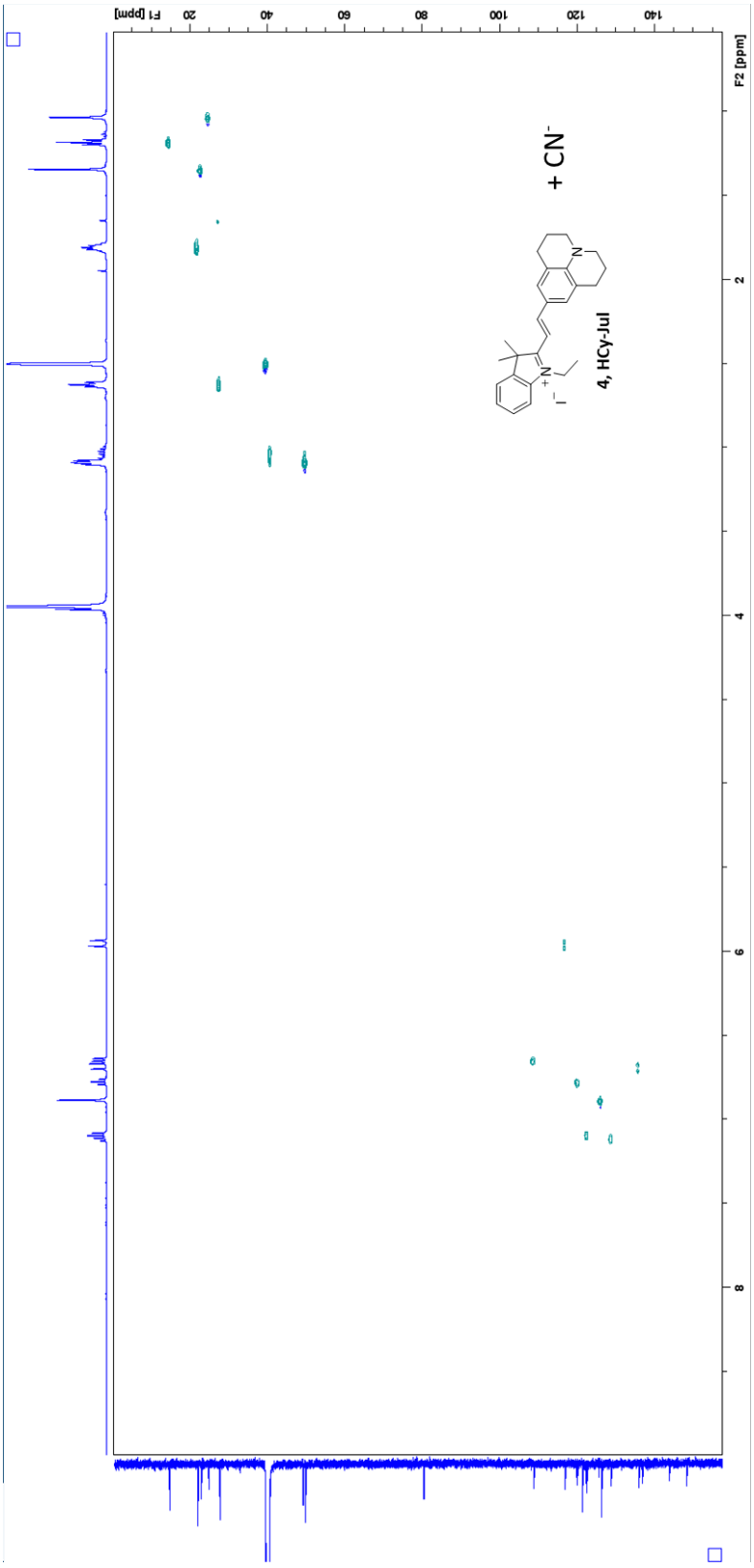

^{1}H NMR spectra of **HCy-OMe** treated with 1 eq of CH_3SNa in DMSO-d_6/D_2O (80:20).

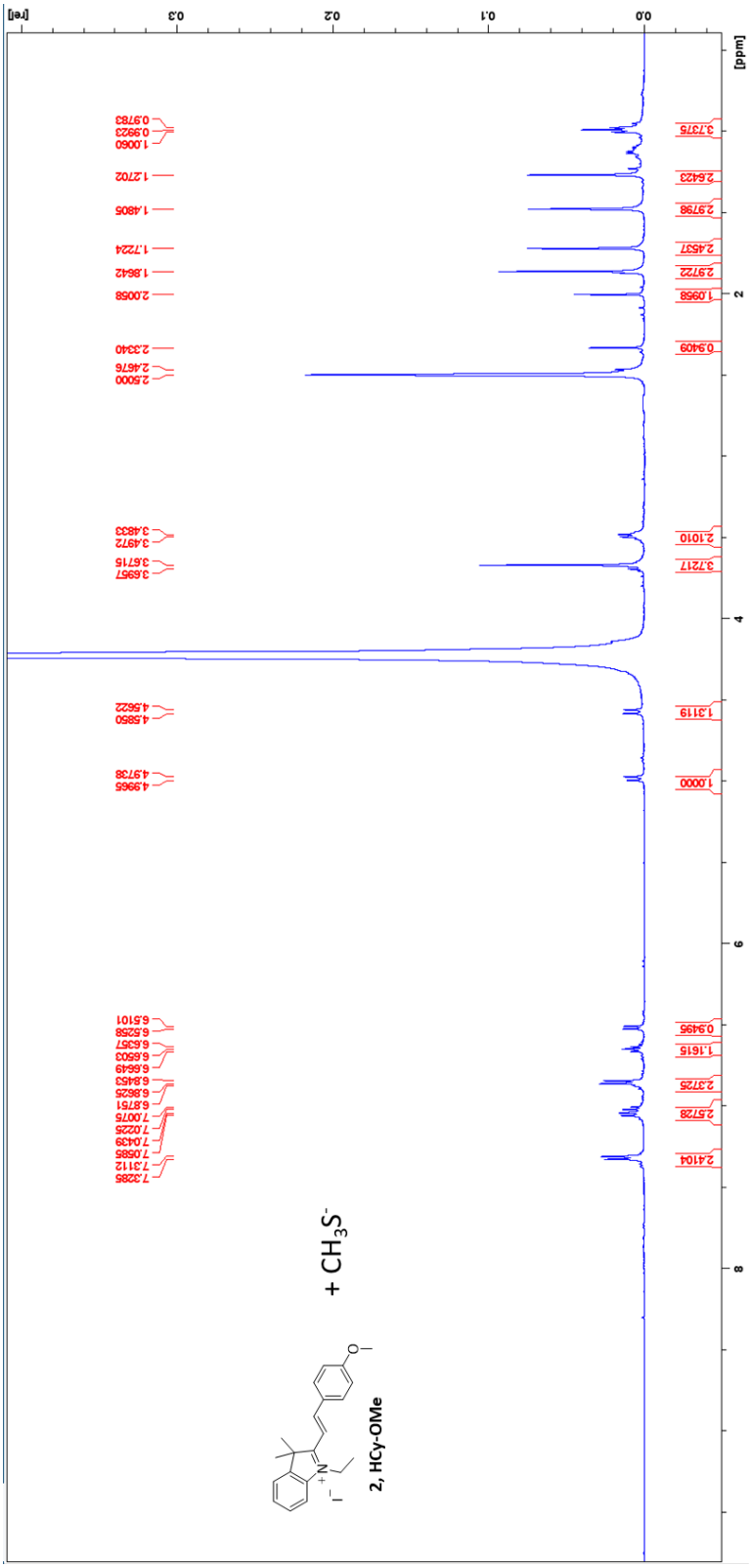

^{13}C NMR spectra of **HCy-OMe** treated with 1 eq of CH_3SNa in DMSO-d_6/D_2O (80:20).

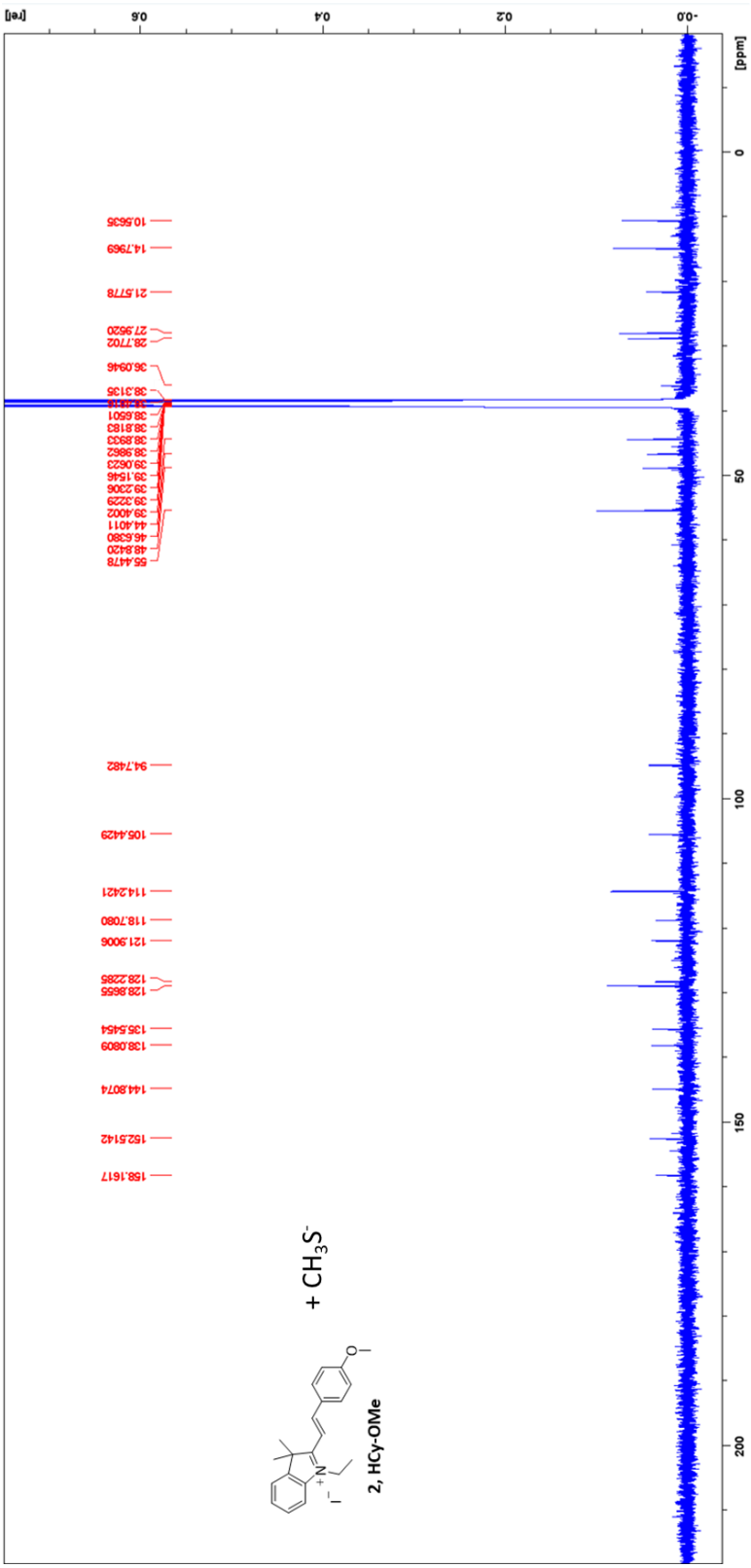

COSY spectra of **HCy-OMe** treated with 1 eq of CH_3SNa in DMSO-d_6/D_2O (80:20).

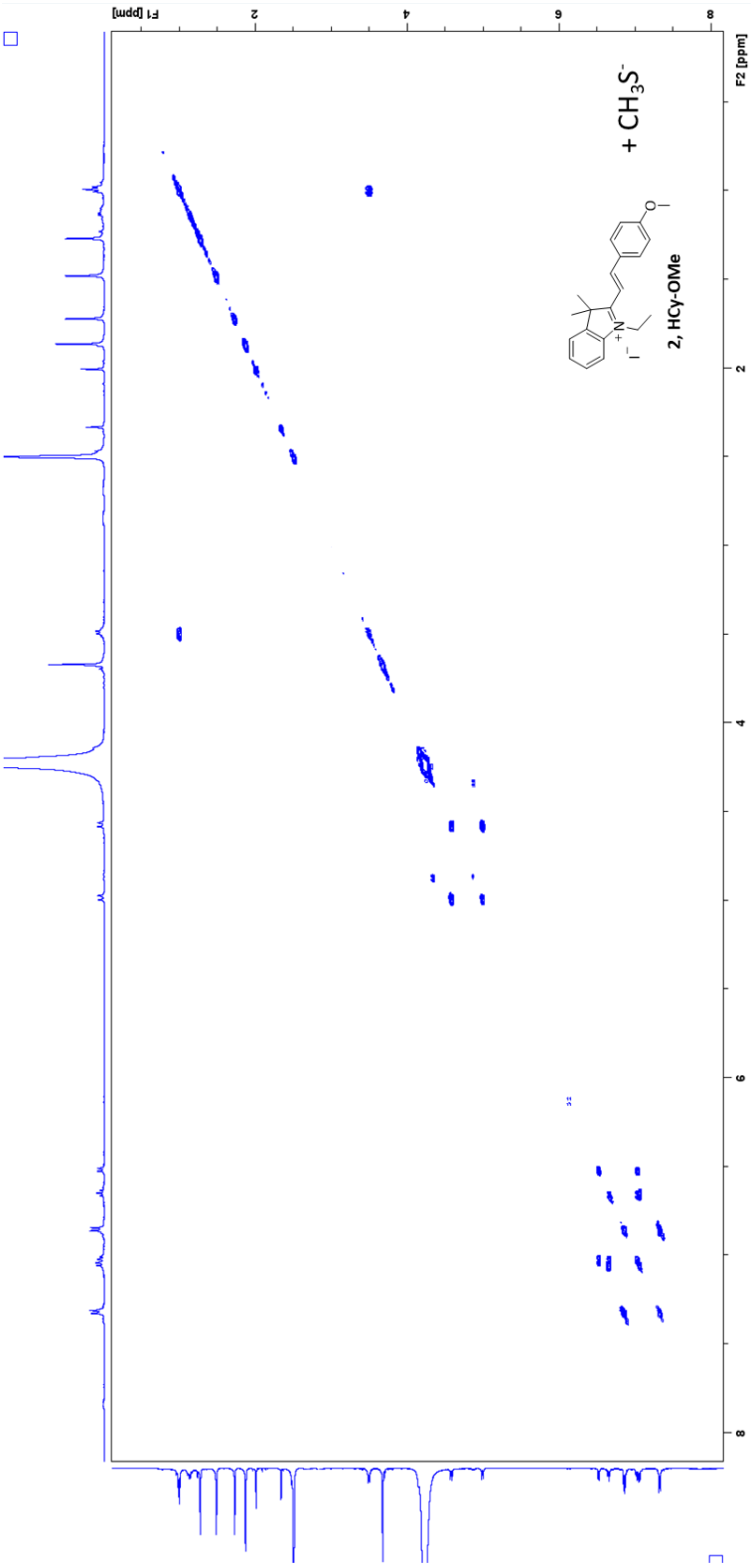

HMBC spectra of **HCy-OMe** treated with 1 eq of CH_3SNa in DMSO-d_6/D_2O (80:20).

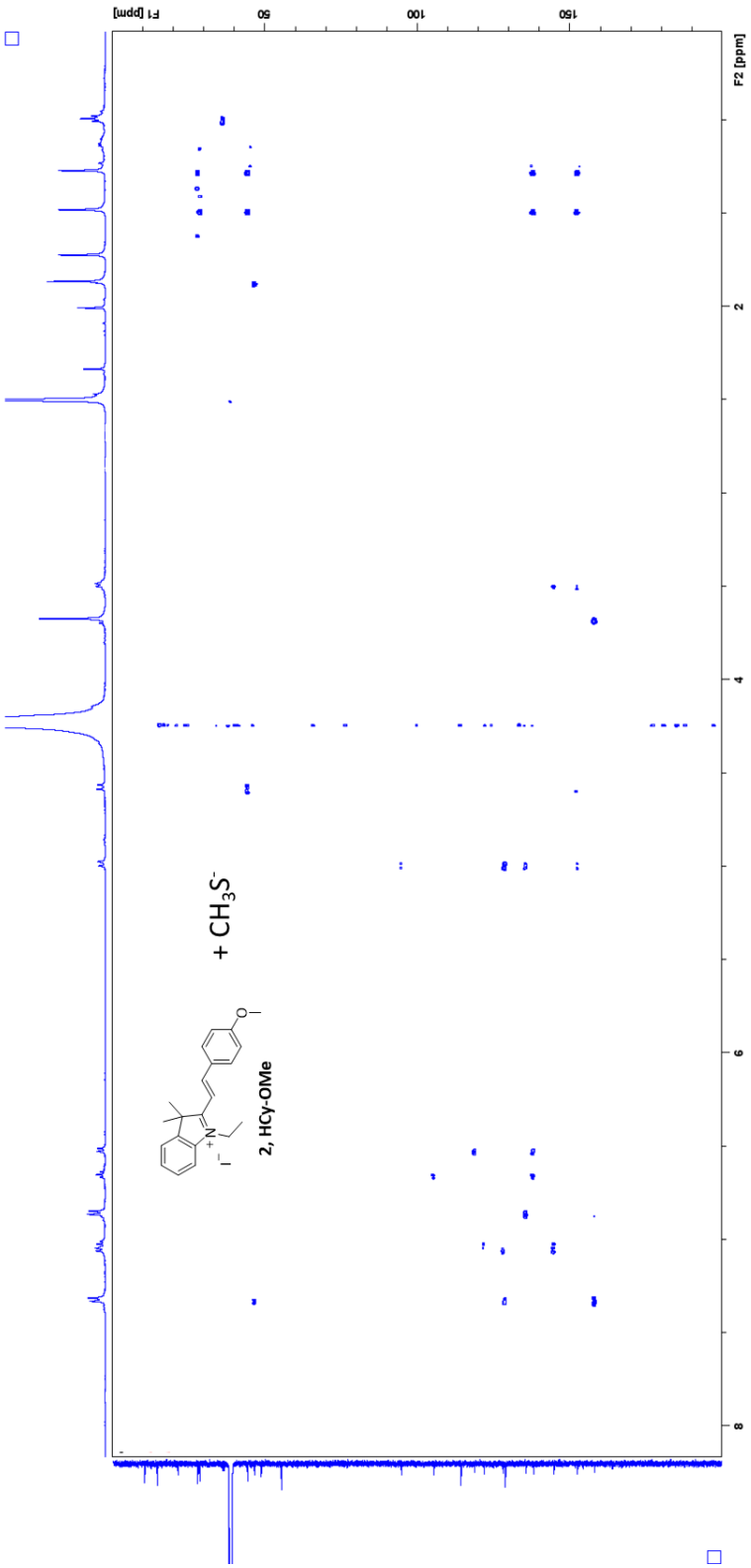

HSQC spectra of **HCy-OMe** treated with 1 eq of CH_3SNa in DMSO-d_6/D_2O (80:20).

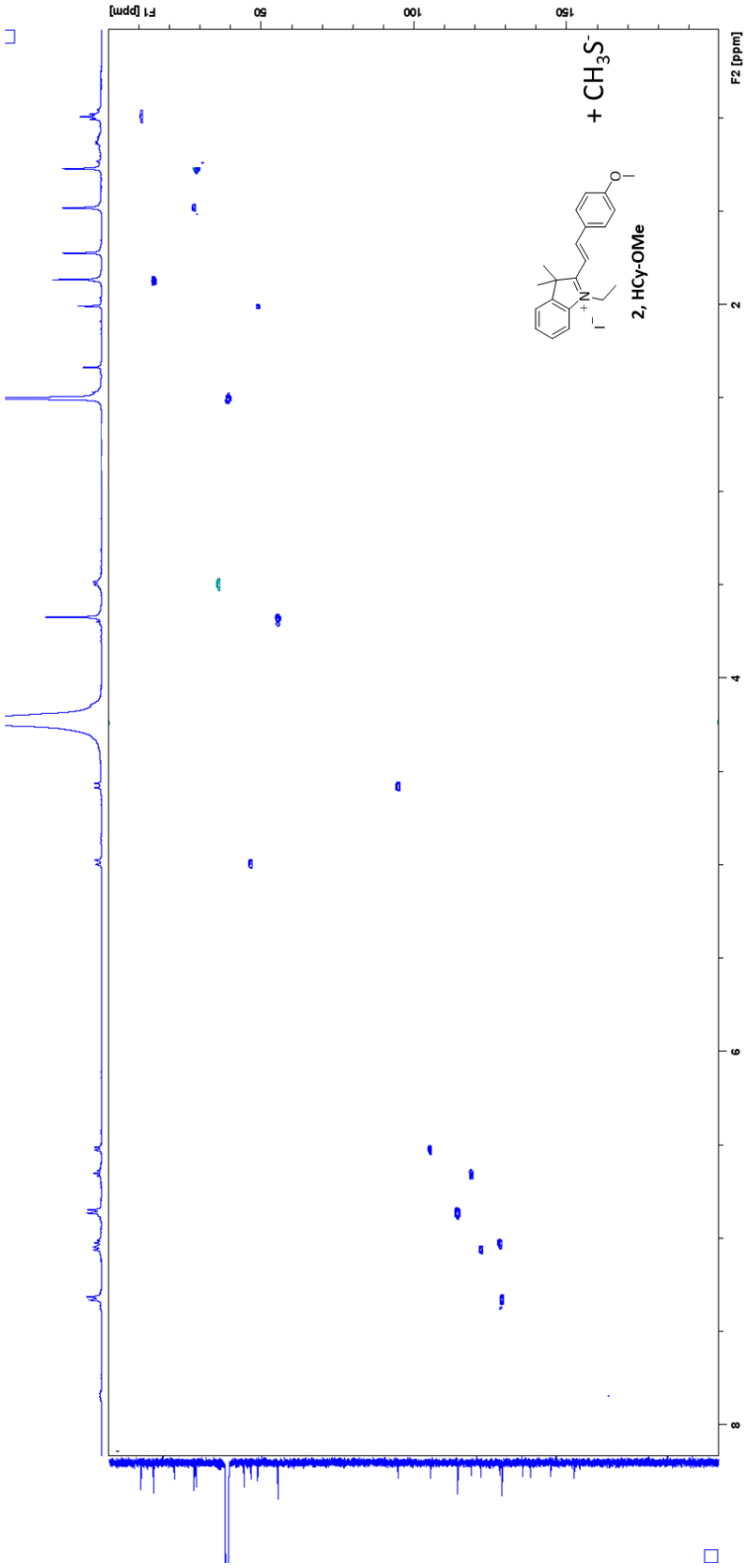

^{1}H NMR spectra of **HCy-NEt$_2$** treated with 1 eq of CH_3SNa in DMSO-d_6/D_2O (80:20).

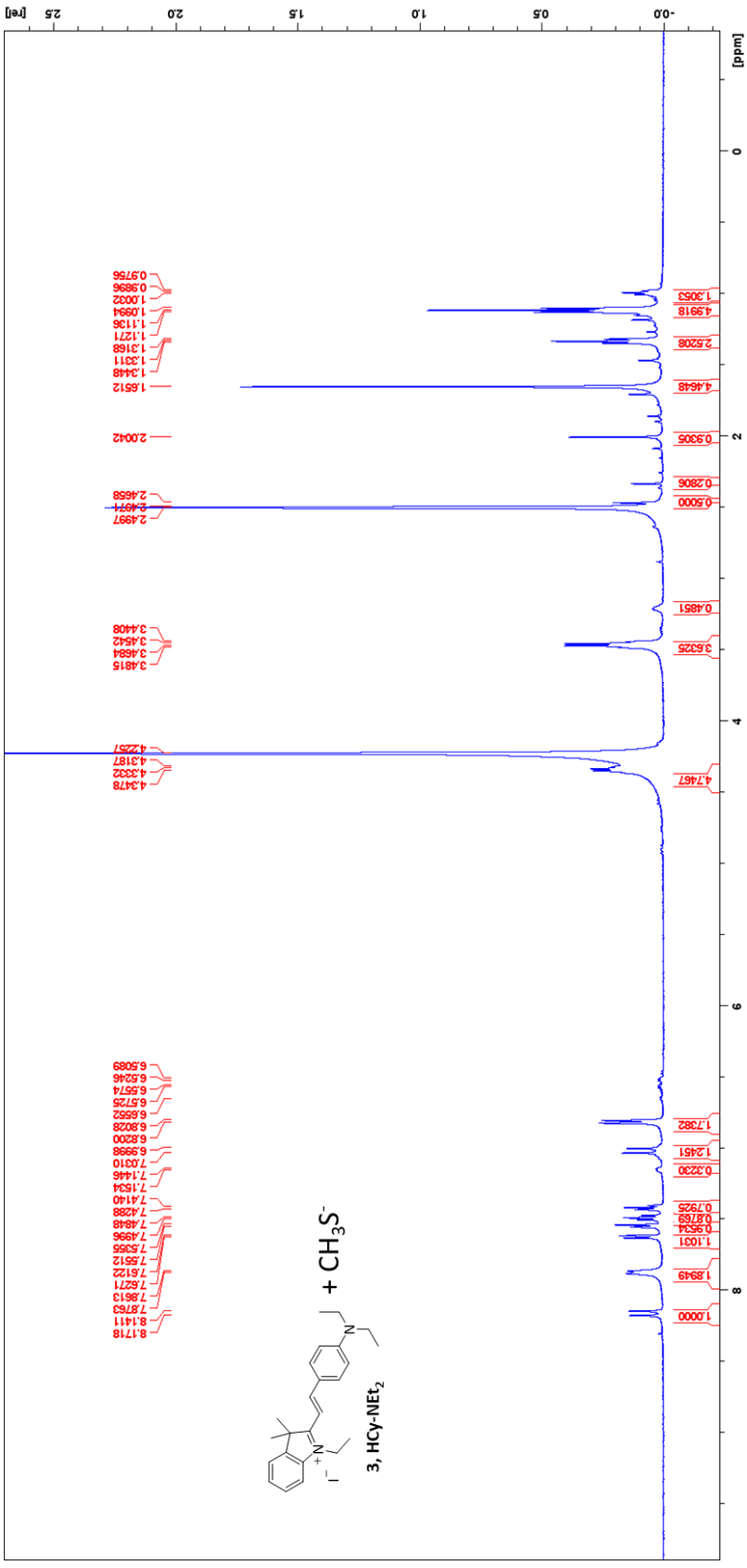

^{13}C NMR spectra of **HCy-NEt$_2$** treated with 1 eq of CH_3SNa in DMSO-d_6/D_2O (80:20).

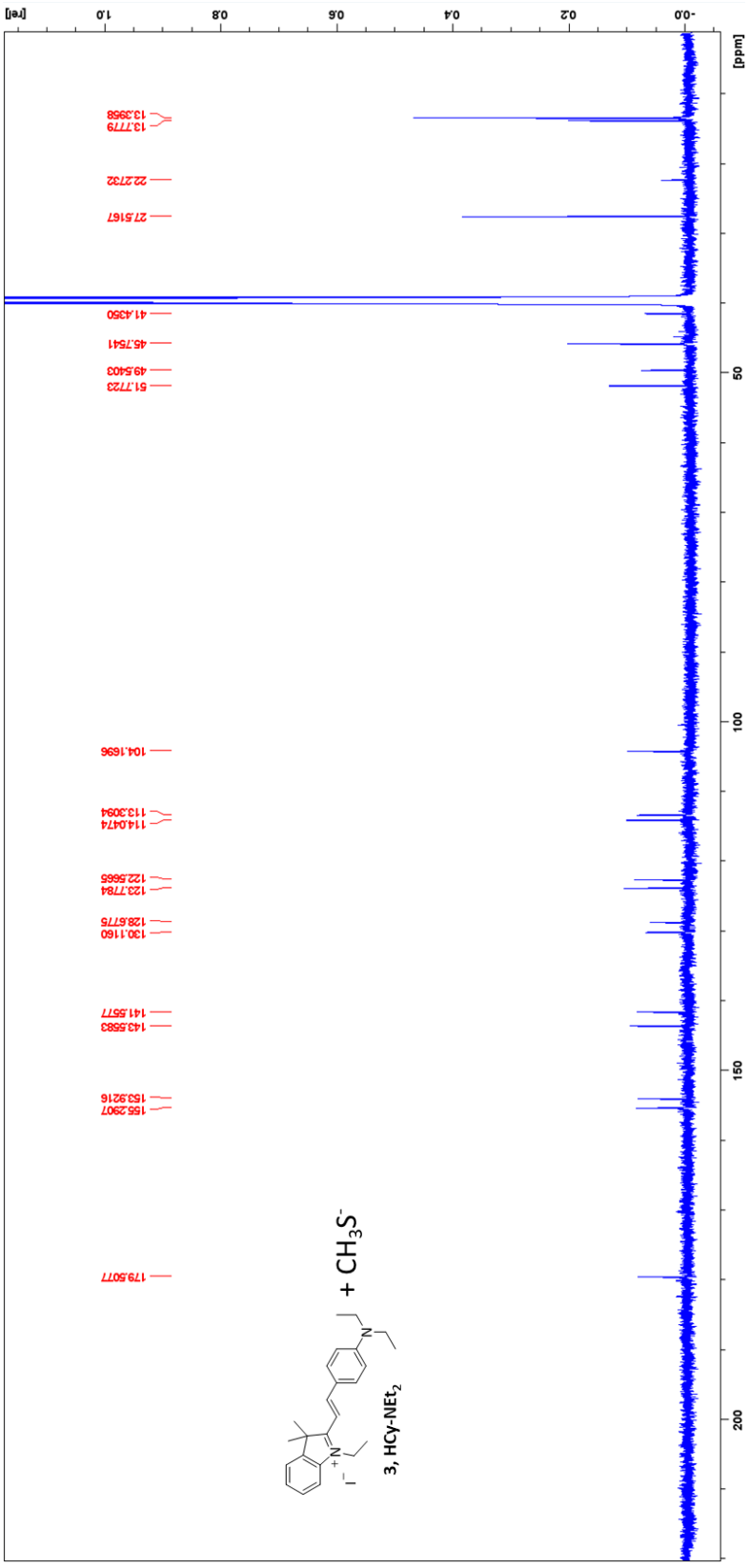

COSY spectra of **HCy-NEt$_2$** treated with 1 eq of CH_3SNa in DMSO-d_6/D_2O (80:20).

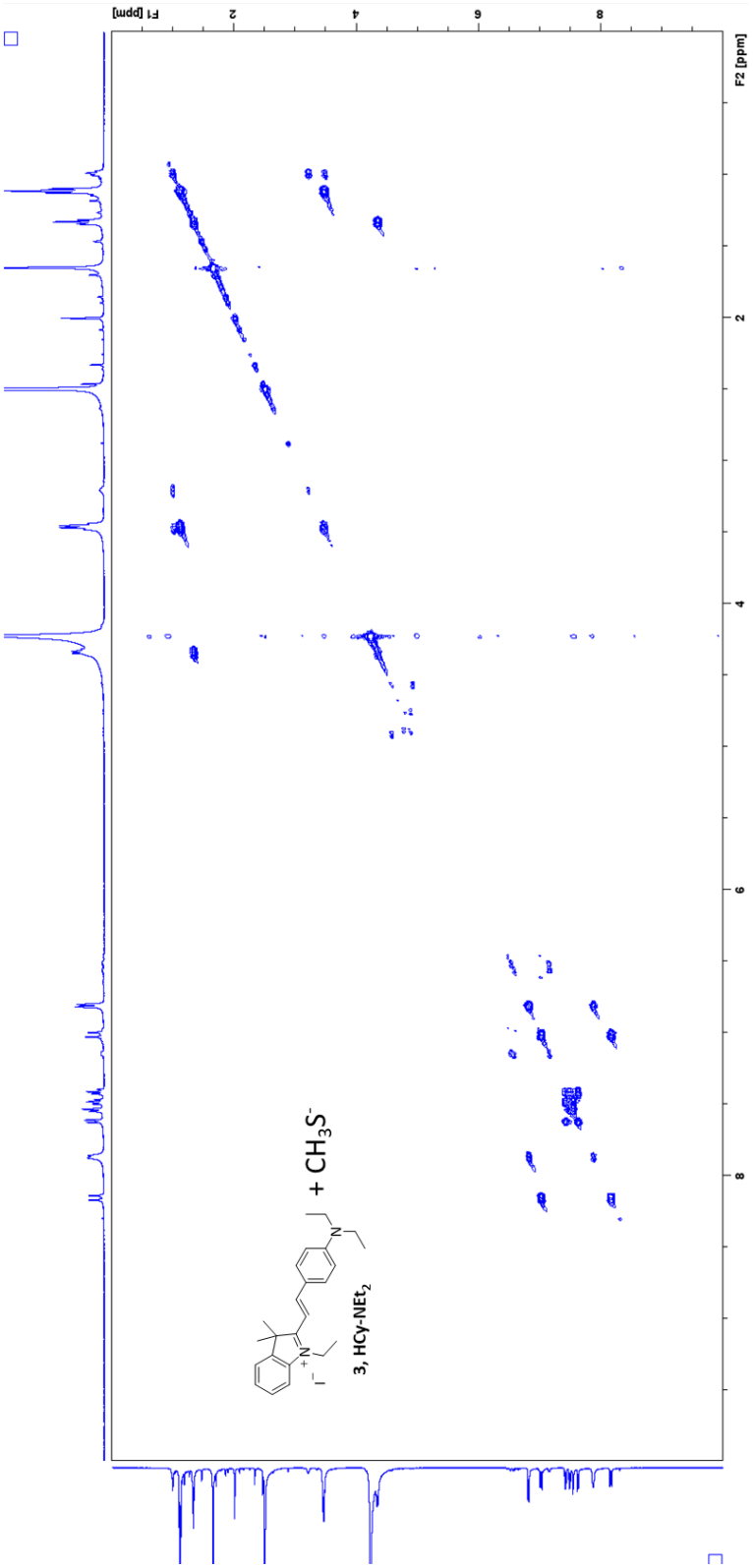

HMBC spectra of **HCy-NEt$_2$** treated with 1 eq of CH_3SNa in DMSO-d_6/D_2O (80:20).

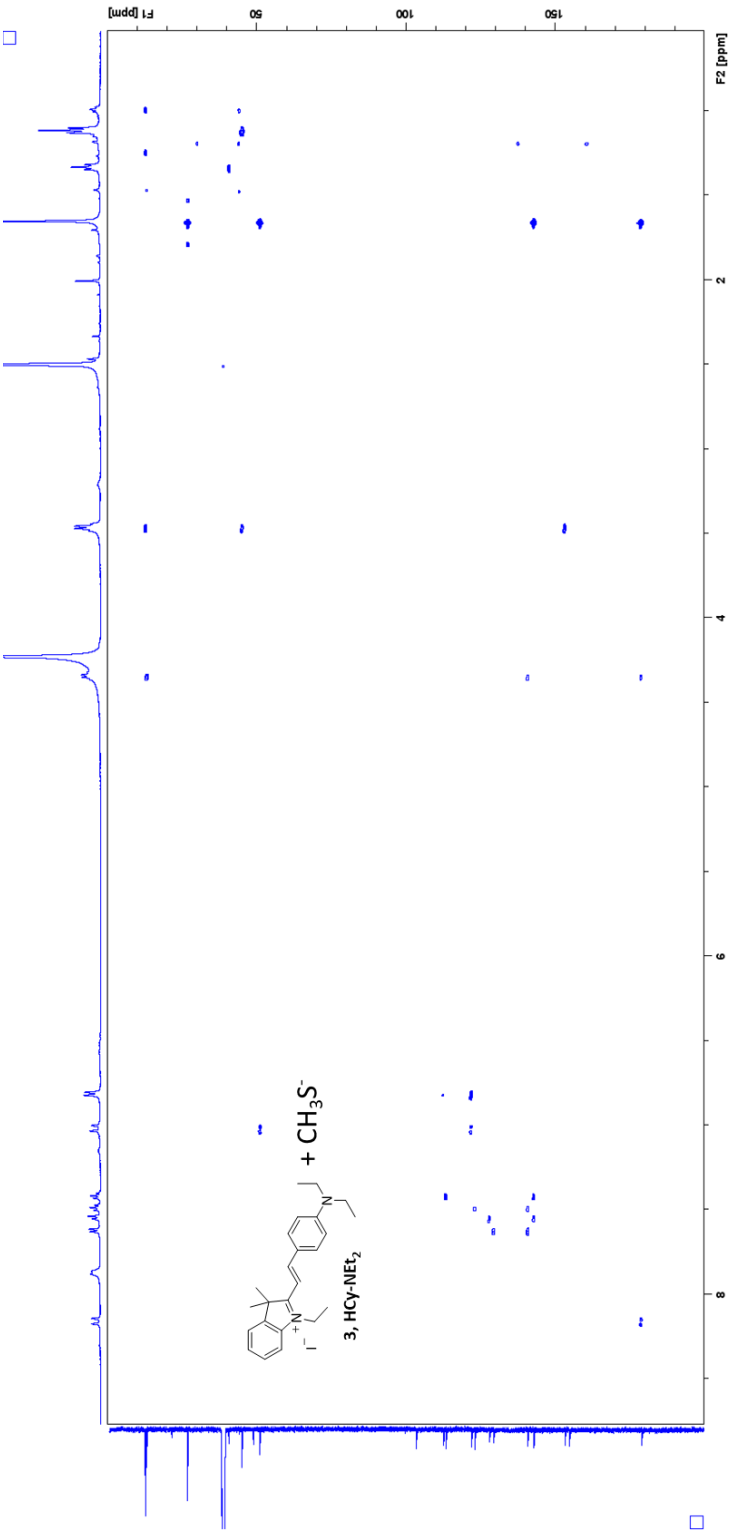

HSQC spectra of **HCy-NEt$_2$** treated with 1 eq of CH_3SNa in DMSO-d_6/D_2O (80:20).

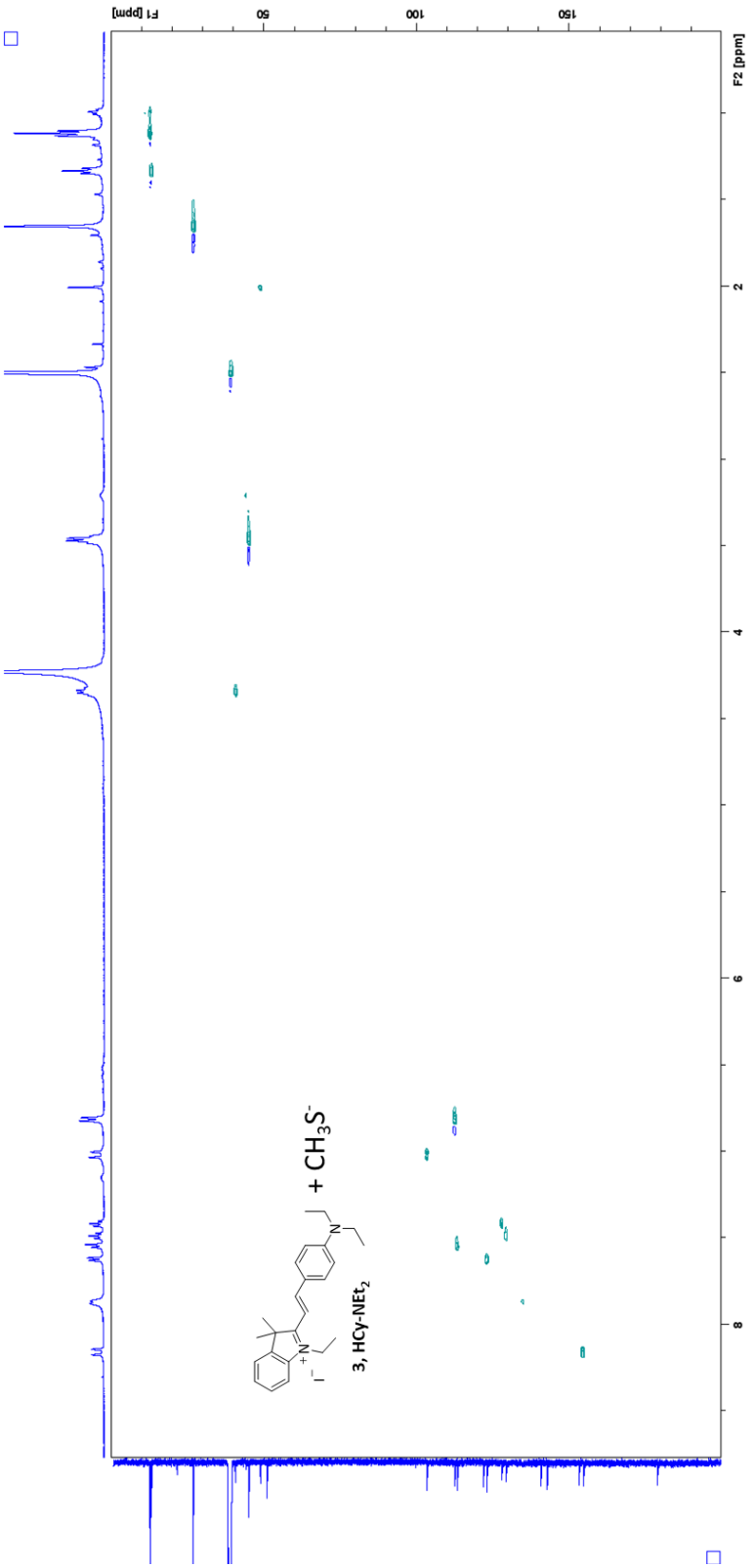

^{1}H NMR spectra of **HCy-Jul** treated with 1 eq of CH_3SNa in DMSO-d_6/D_2O (80:20).

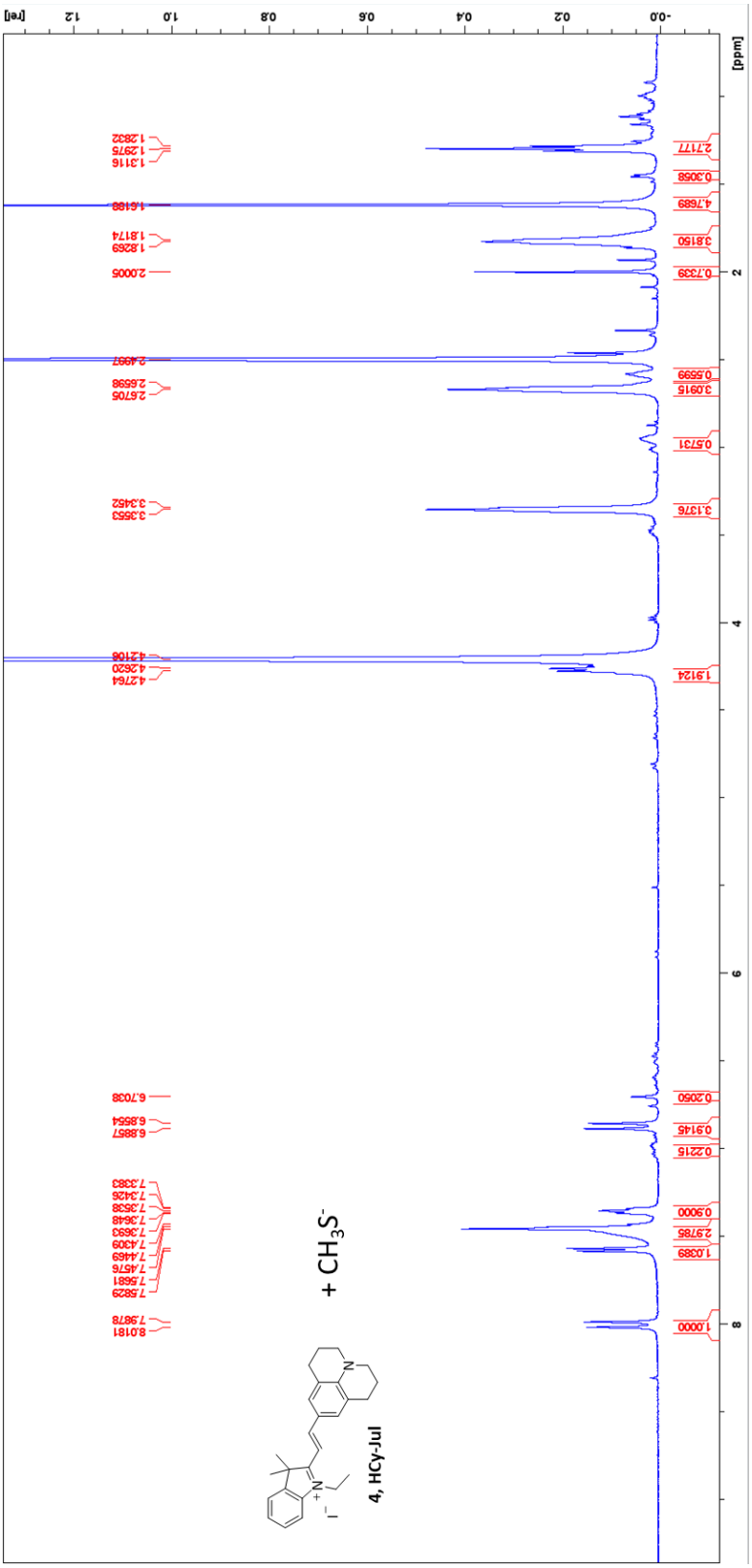

^{13}C NMR spectra of **HCy-Jul** treated with 1 eq of CH_3SNa in DMSO-d_6/D_2O (80:20).

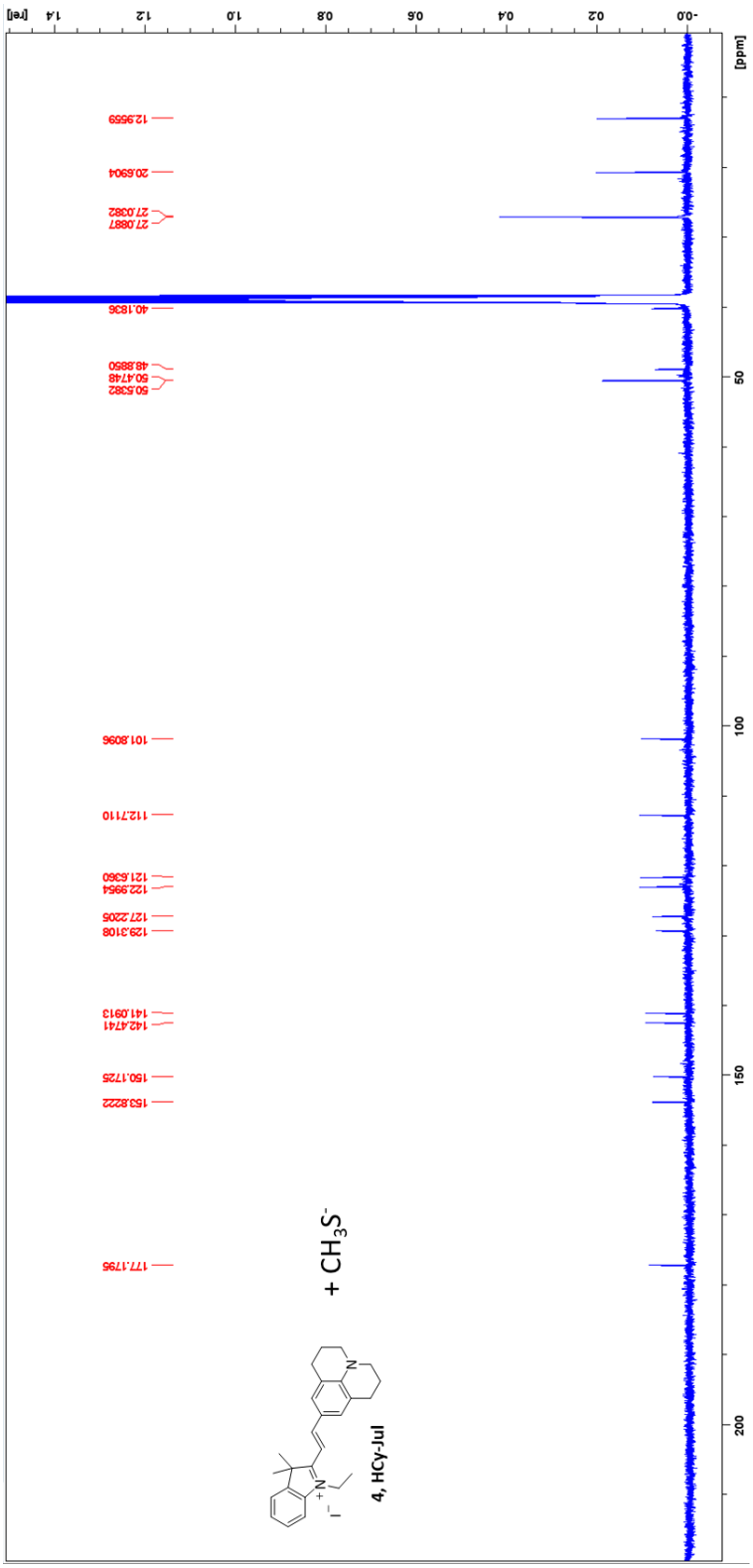

COSY spectra of **HCy-Jul** treated with 1 eq of CH_3SNa in DMSO-d_6/D_2O (80:20).

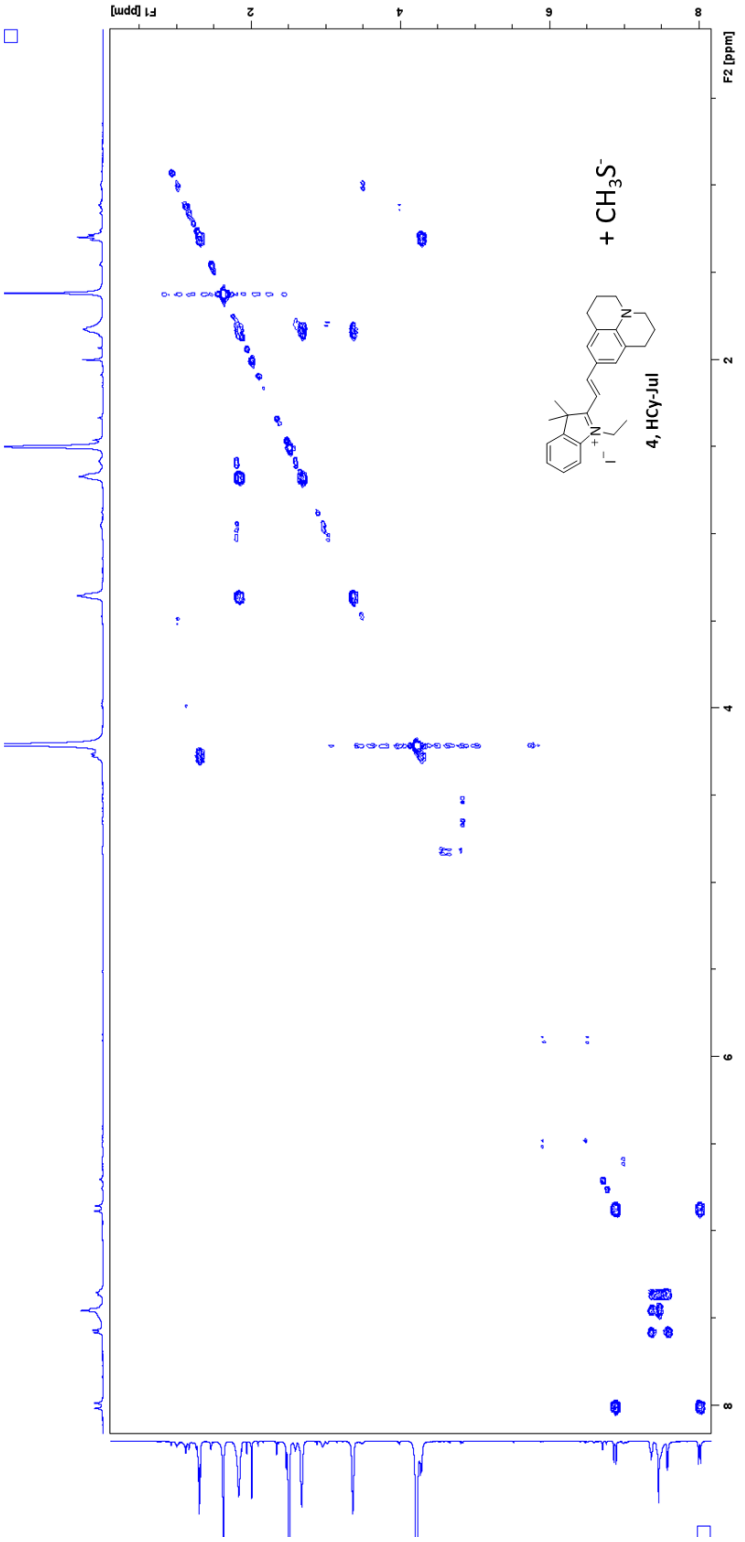

HMBC spectra of **HCy-Jul** treated with 1 eq of CH_3SNa in DMSO-d_6/D_2O (80:20).

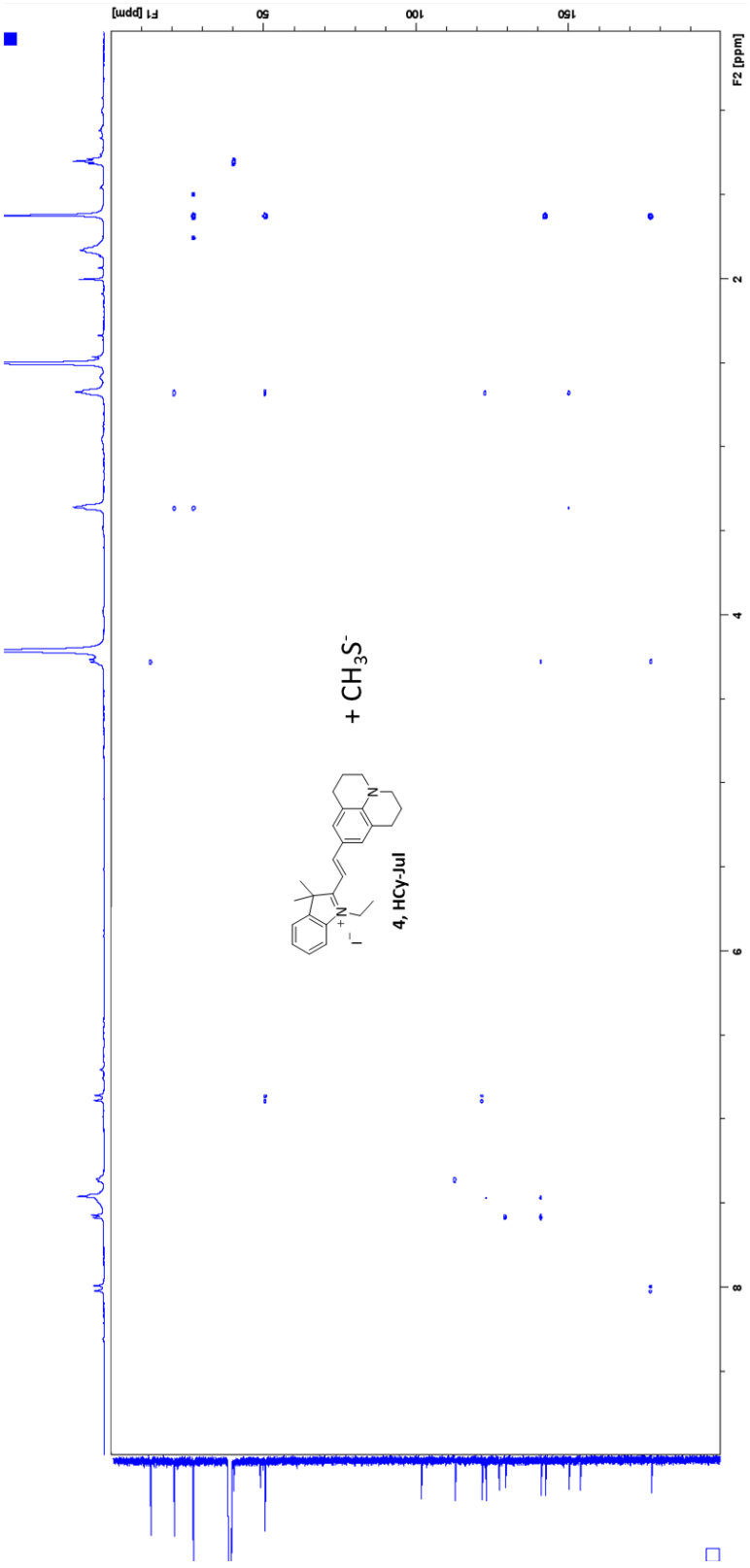

HSQC spectra of **HCy-Jul** treated with 1 eq of CH_3SNa in DMSO-d_6/D_2O (80:20).

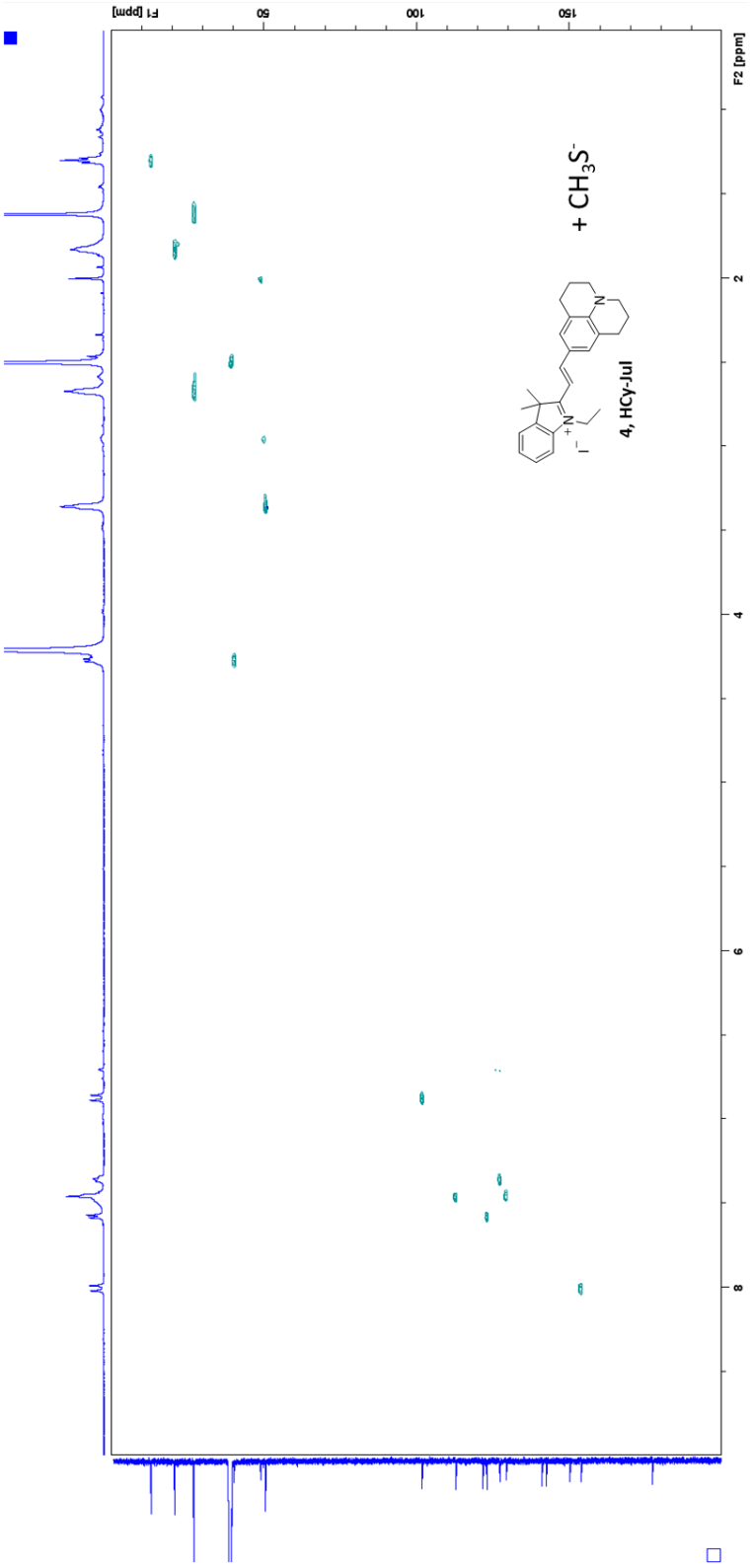

^{1}H NMR spectra of **HCy-OMe** treated with 1 eq of GSH in DMSO-d_6/D_2O (80:20).

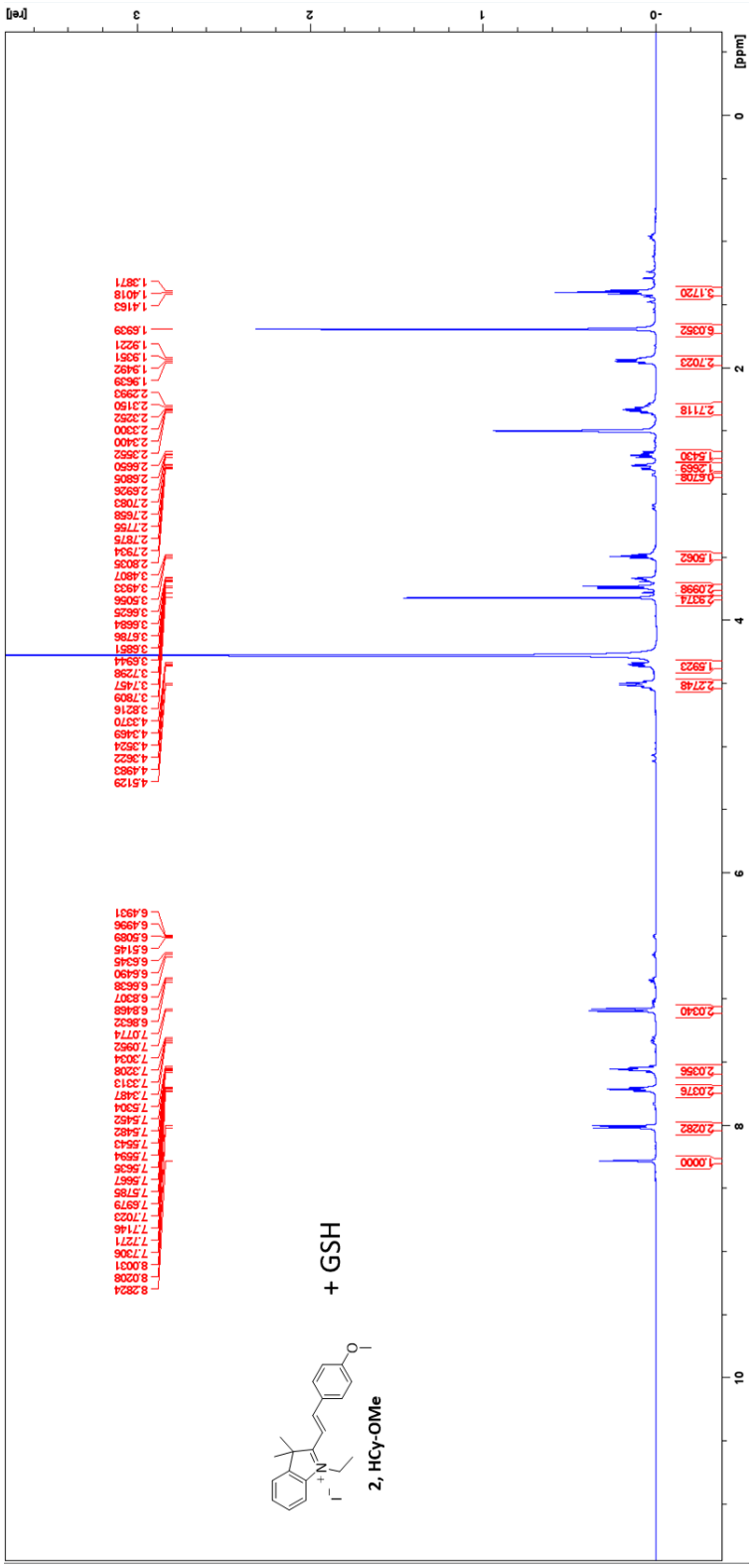

^{13}C NMR spectra of **HCy-OMe** treated with 1 eq of GSH in DMSO-d_6/D_2O (80:20).

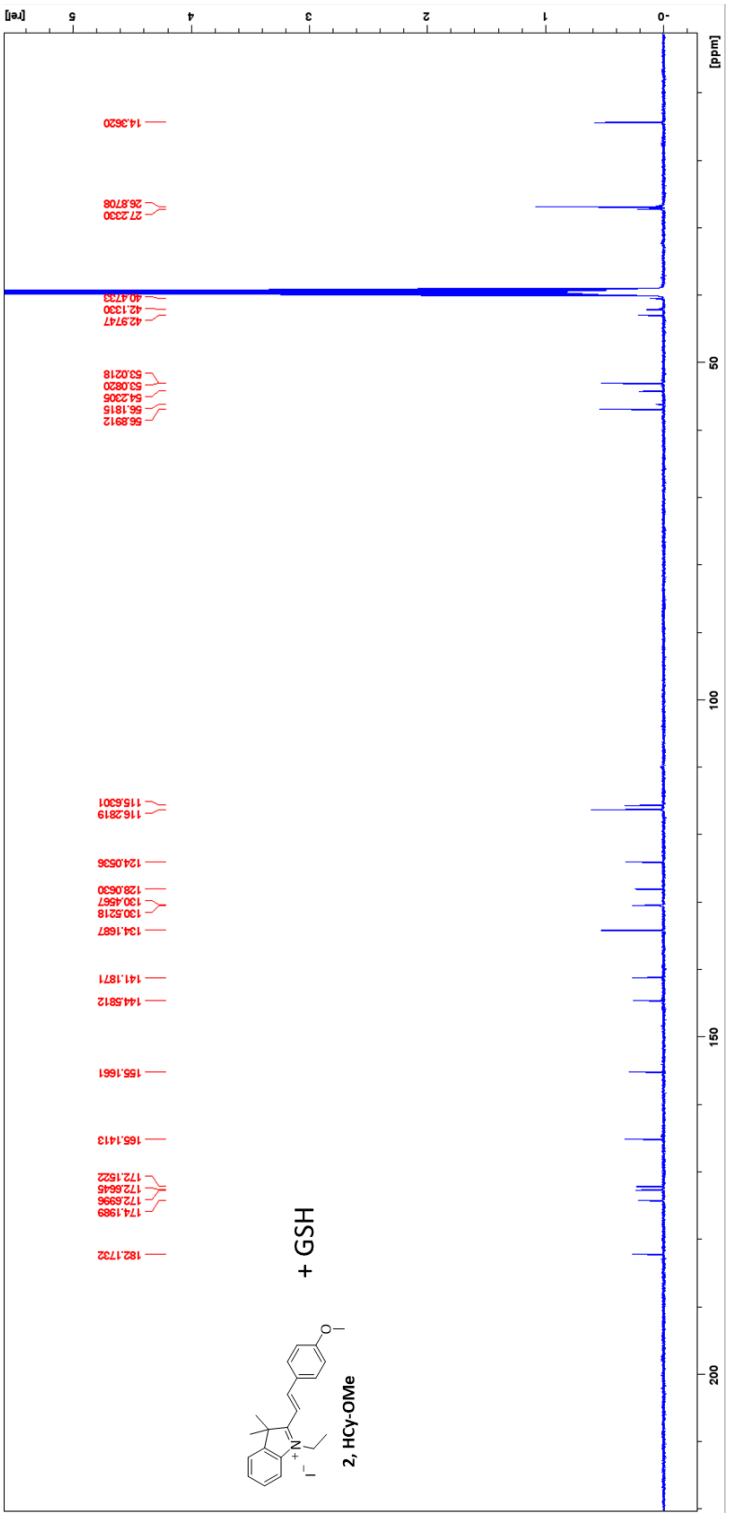

COSY spectra of **HCy-OMe** treated with 1 eq of GSH in DMSO-d_6/D_2O (80:20).

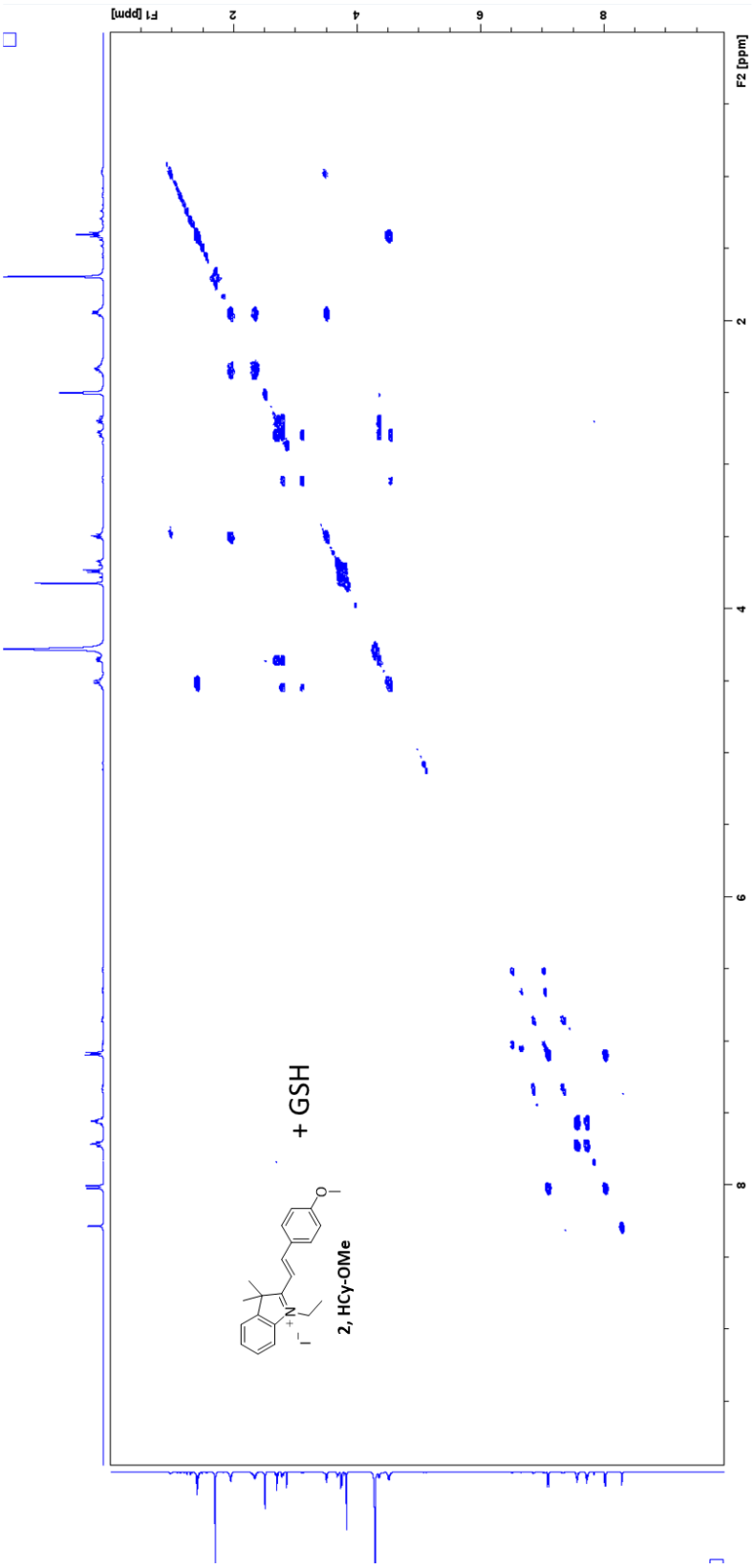

HMBC spectra of **HCy-OMe** treated with 1 eq of GSH in DMSO-d_6/D_2O (80:20).

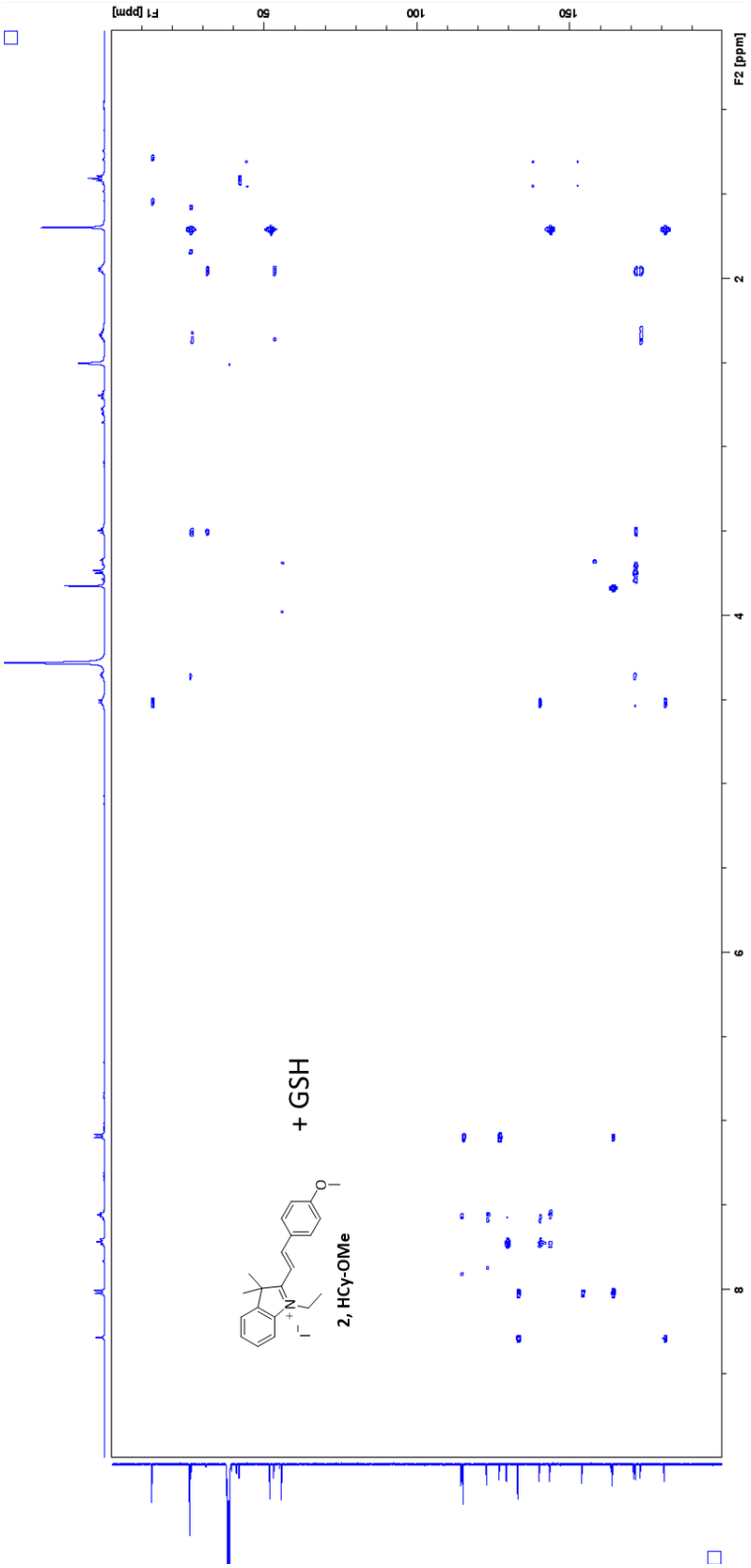

HSQC spectra of **HCy-OMe** treated with 1 eq of GSH in DMSO-d_6/D_2O (80:20).

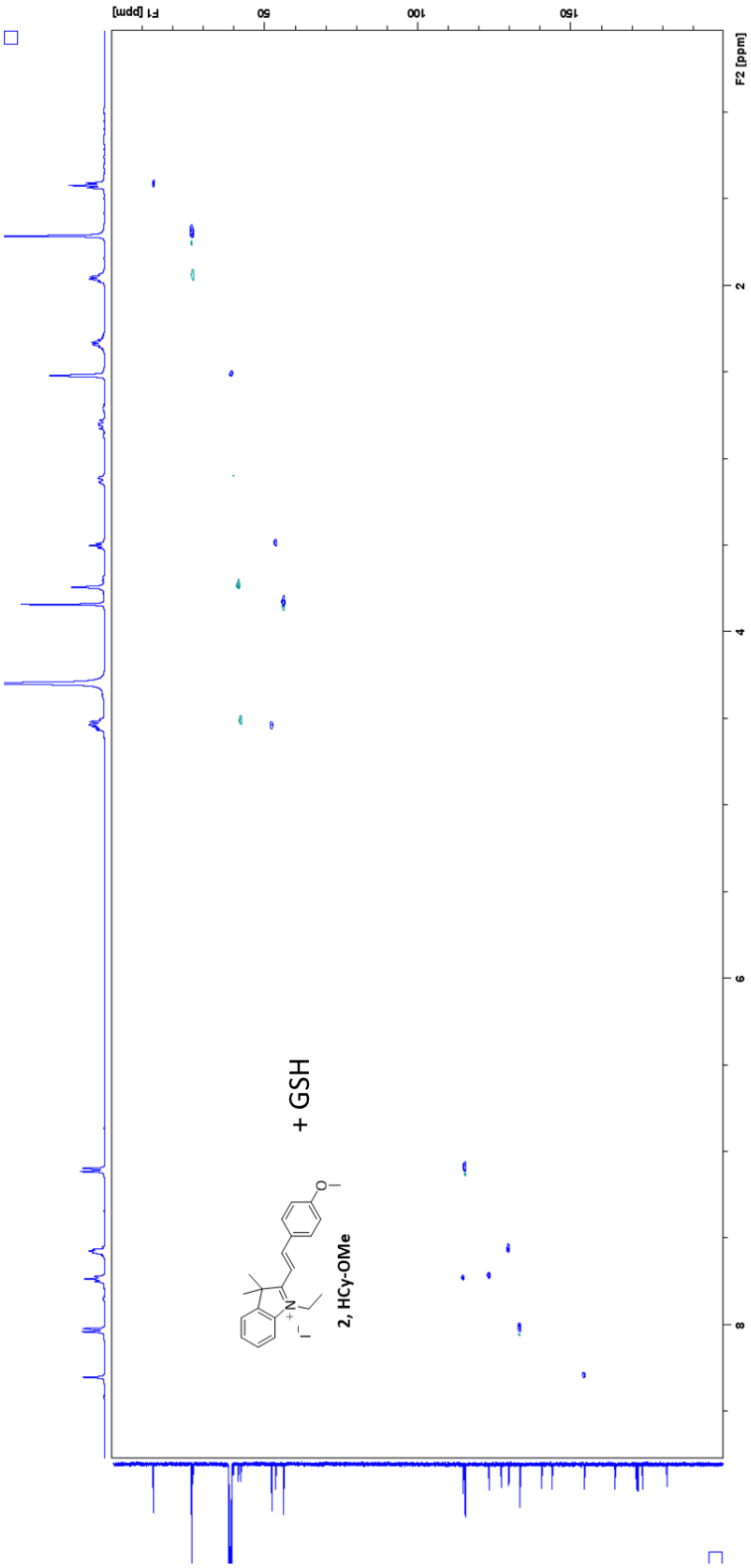

^{1}H NMR spectra of **HCy-NEt$_2$** treated with 1 eq of GSH in DMSO-d$_6$/D$_2$O (80:20).

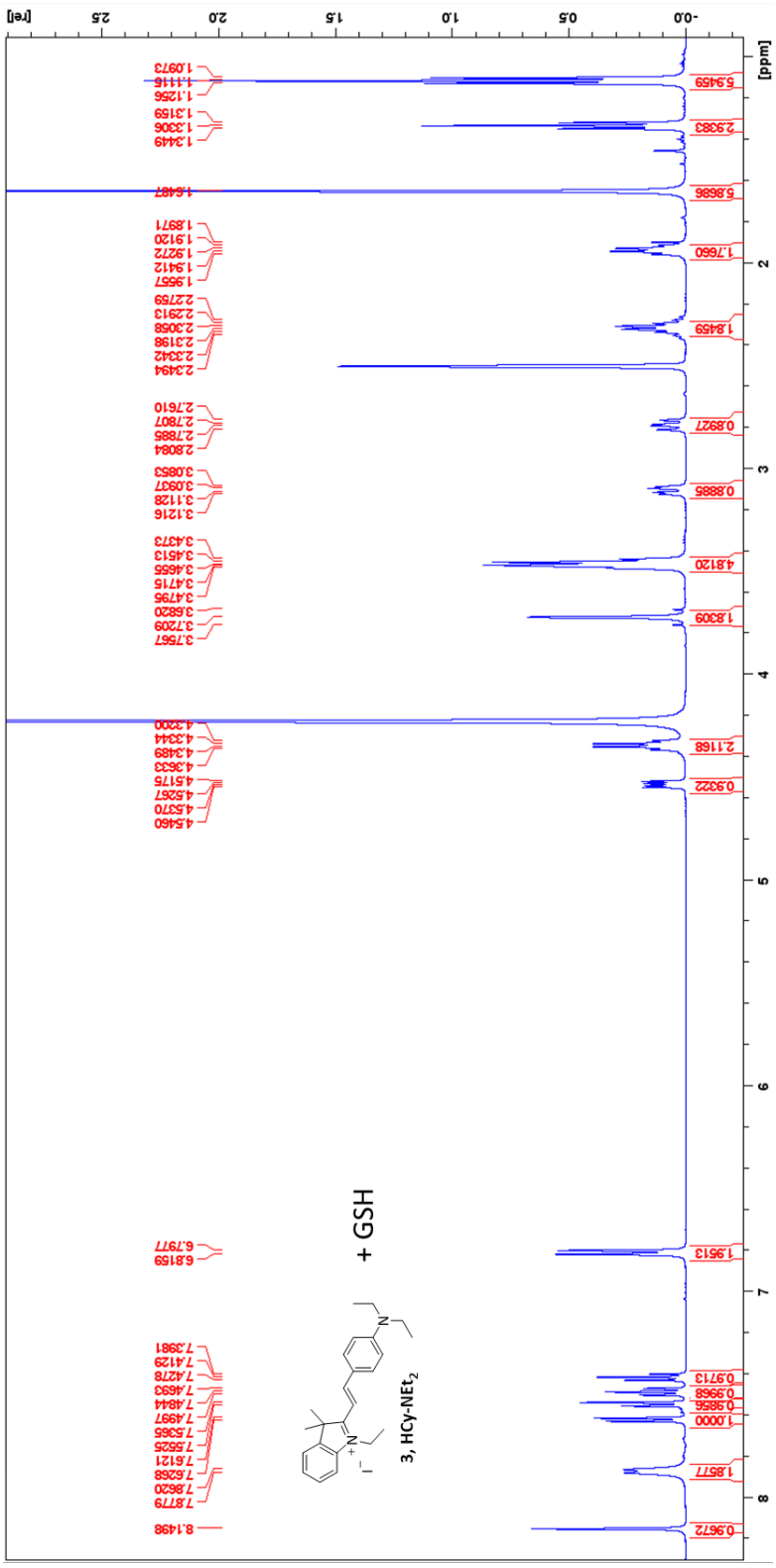

^{13}C NMR spectra of **HCy-NEt$_2$** treated with 1 eq of GSH in DMSO-d_6/D_2O (80:20).

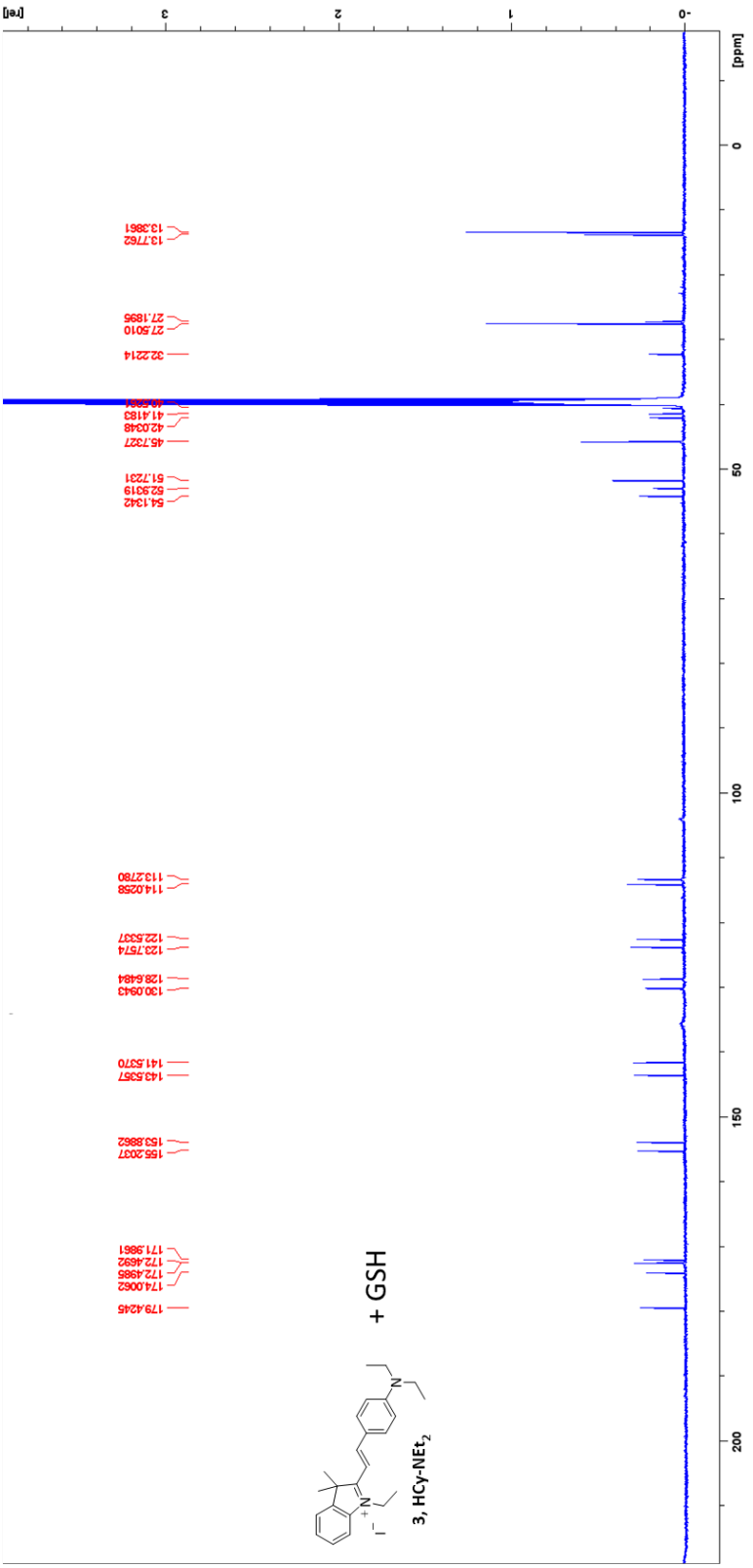

COSY spectra of **HCy-NEt$_2$** treated with 1 eq of GSH in DMSO-d_6/D_2O (80:20).

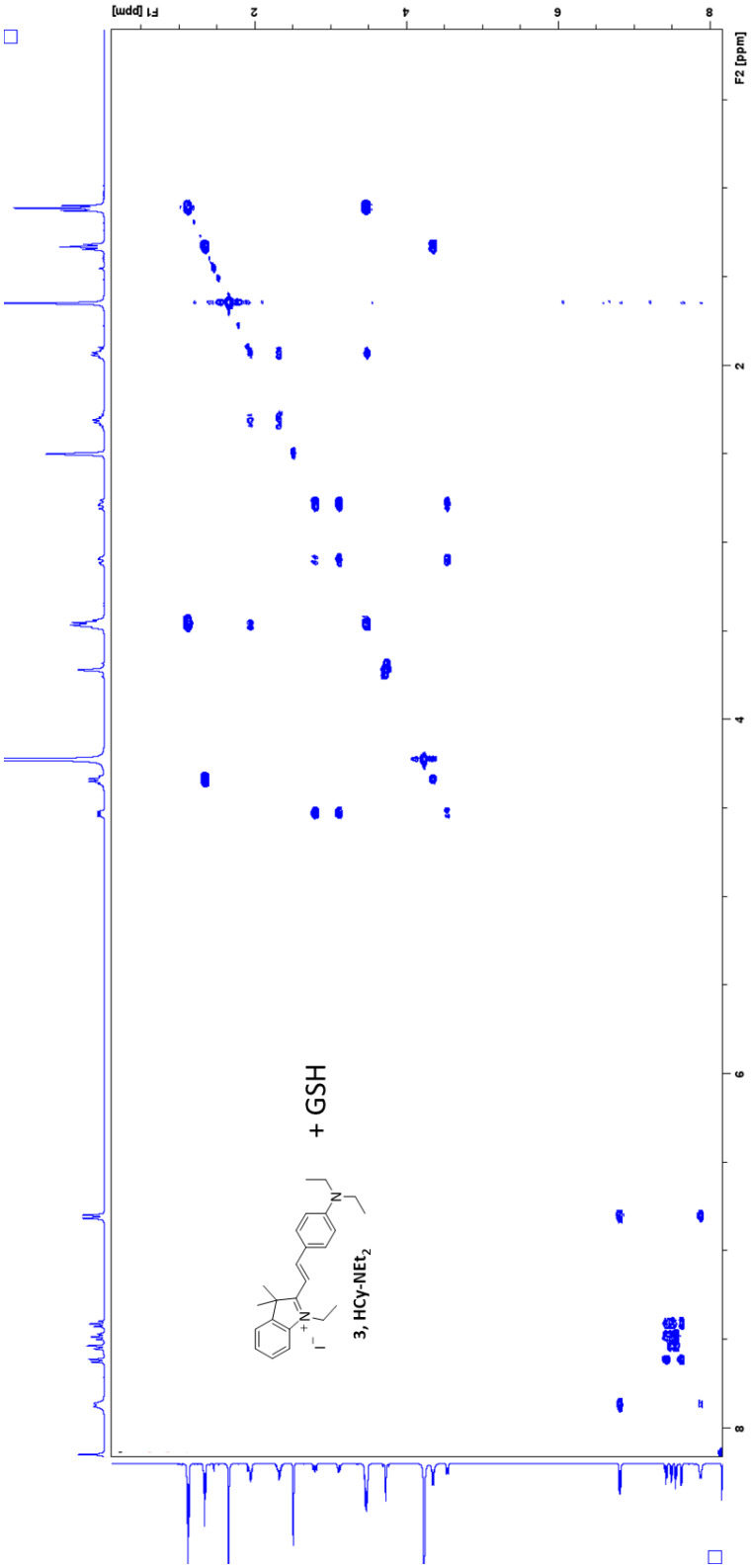

HMCB spectra of **HCy-NEt$_2$** treated with 1 eq of GSH in DMSO-d_6/D_2O (80:20).

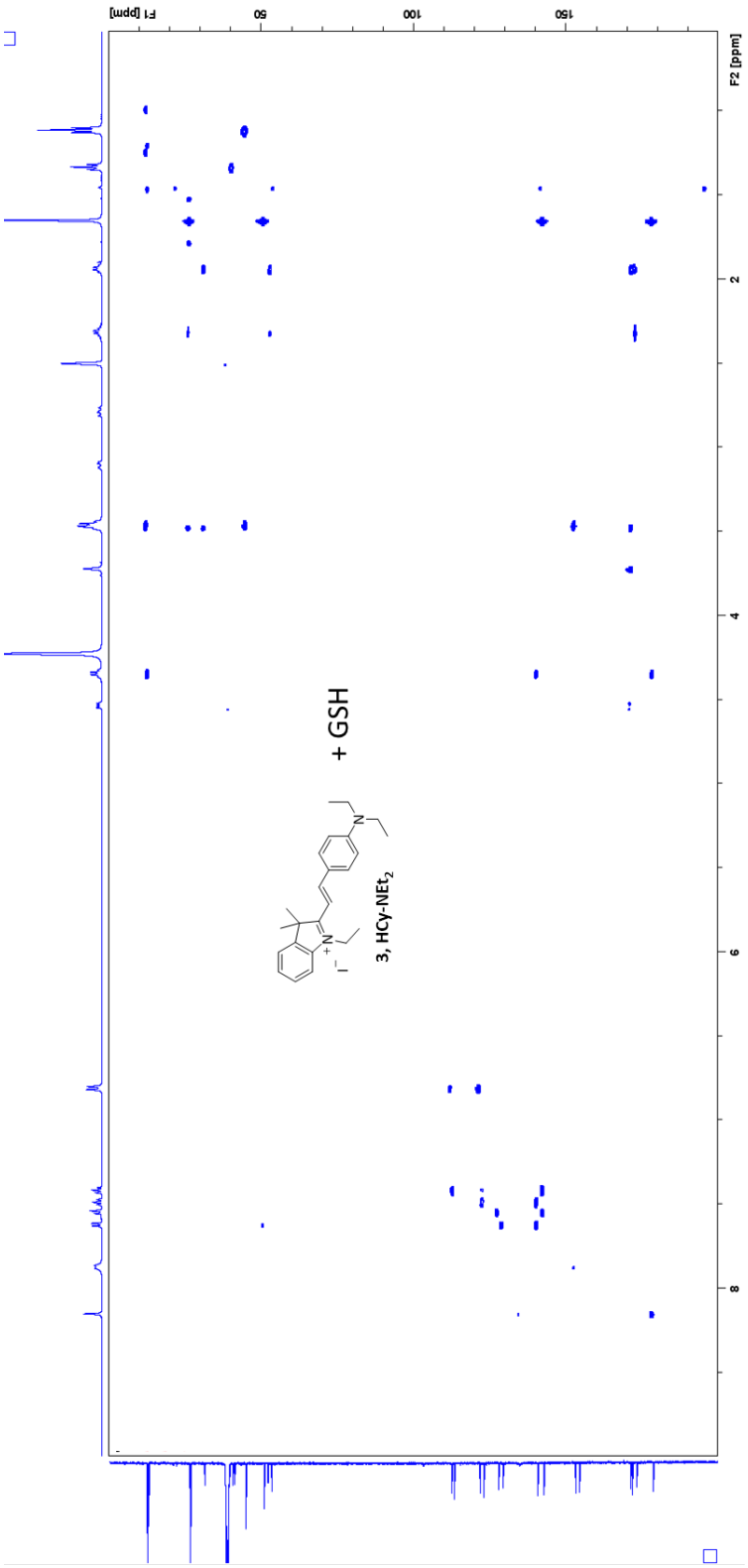

HSQC spectra of **HCy-NEt$_2$** treated with 1 eq of GSH in DMSO-d_6/D_2O (80:20).

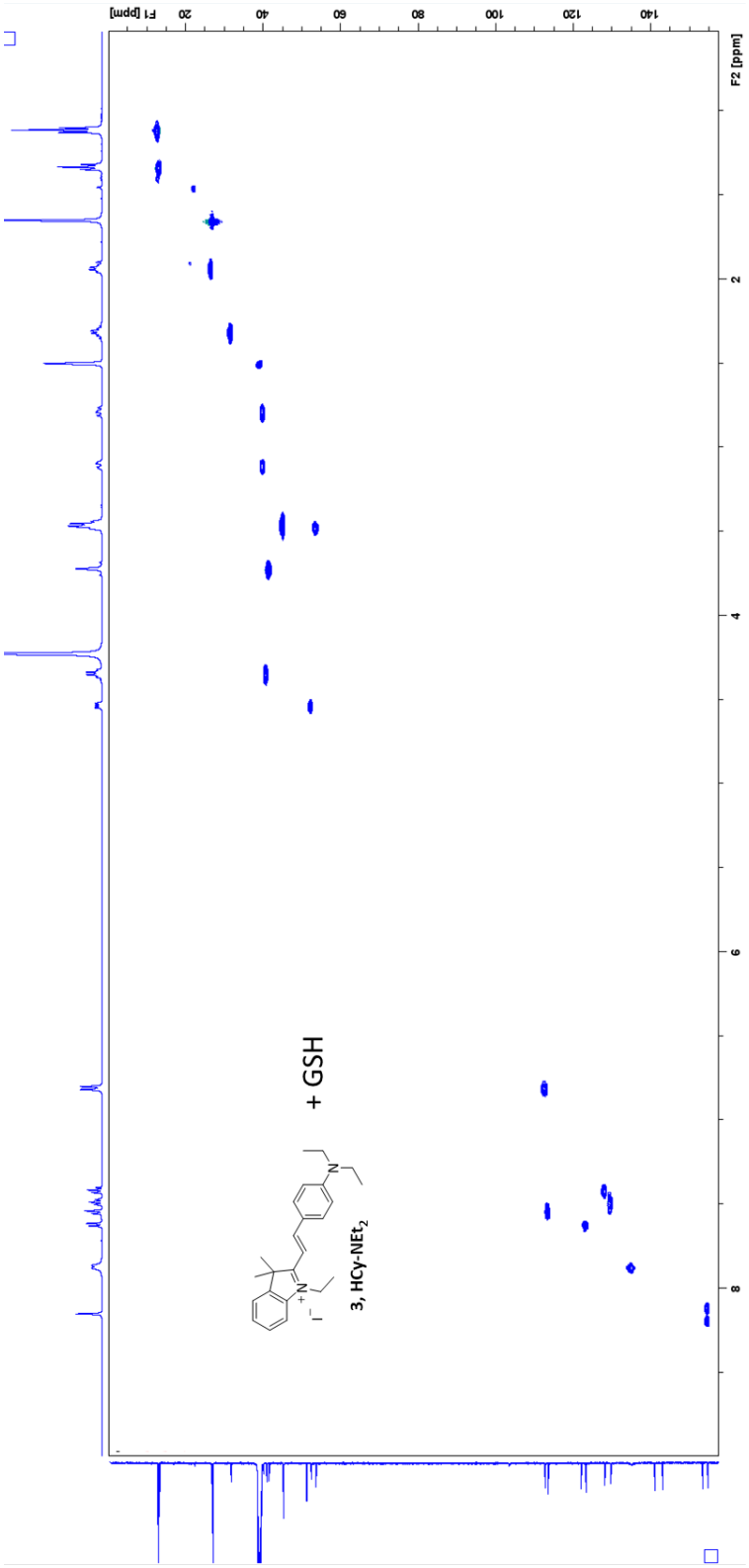

^{1}H NMR spectra of **HCy-Jul** treated with 1 eq of GSH in DMSO-d_6/D_2O (80:20).

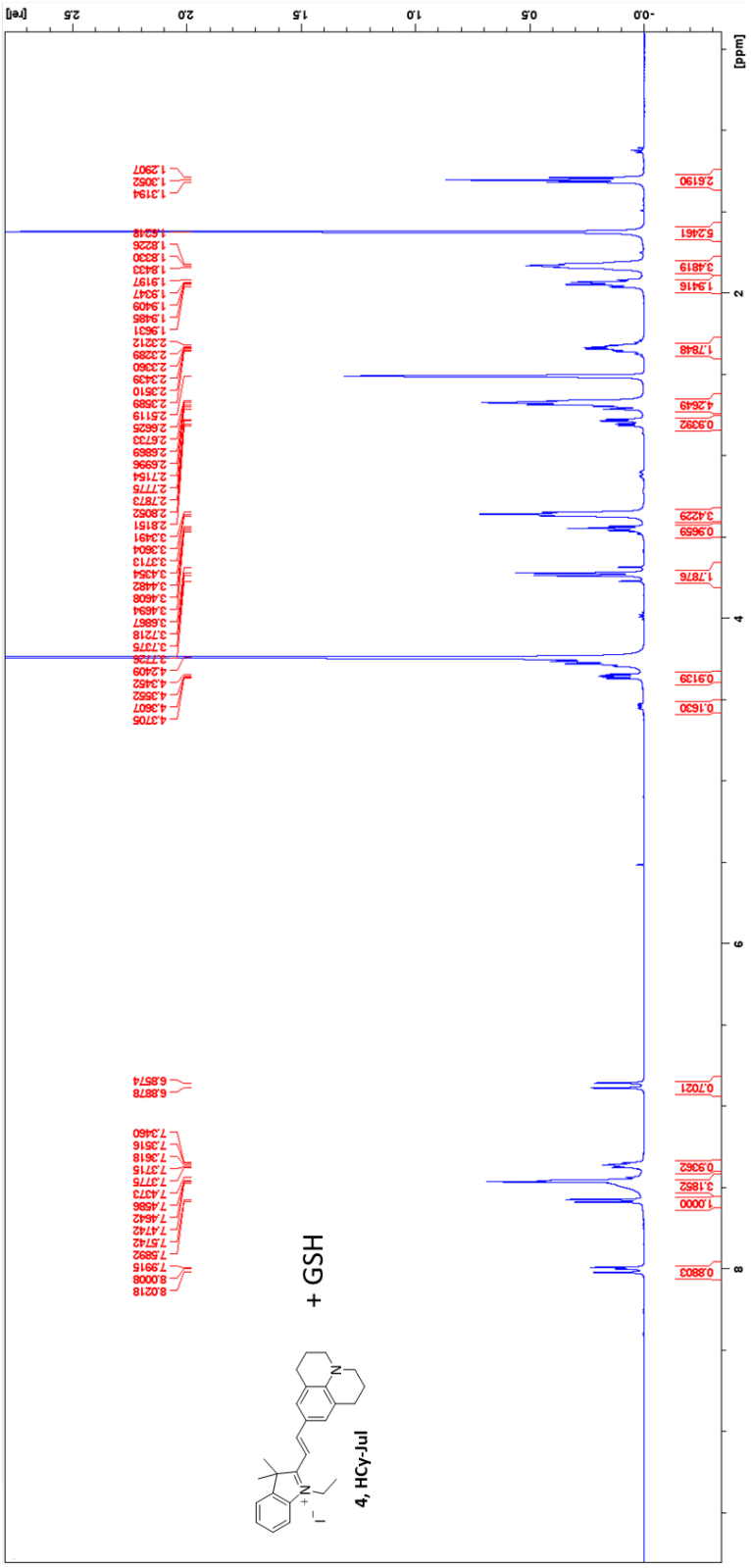

^{13}C NMR spectra of **HCy-Jul** treated with 1 eq of GSH in DMSO-d_6/D_2O (80:20).

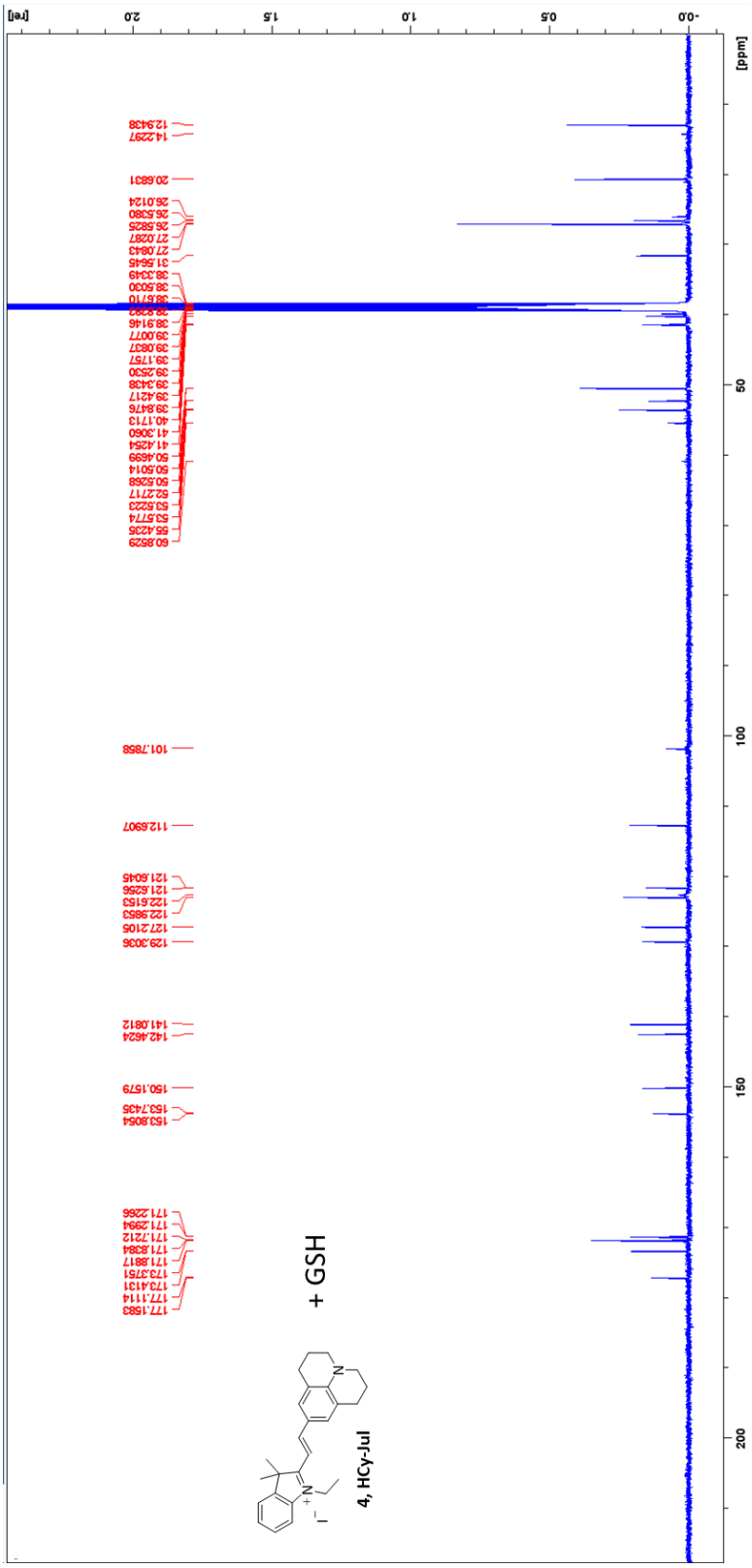

COSY spectra of **HCy-Jul** treated with 1 eq of GSH in DMSO-d_6/D_2O (80:20).

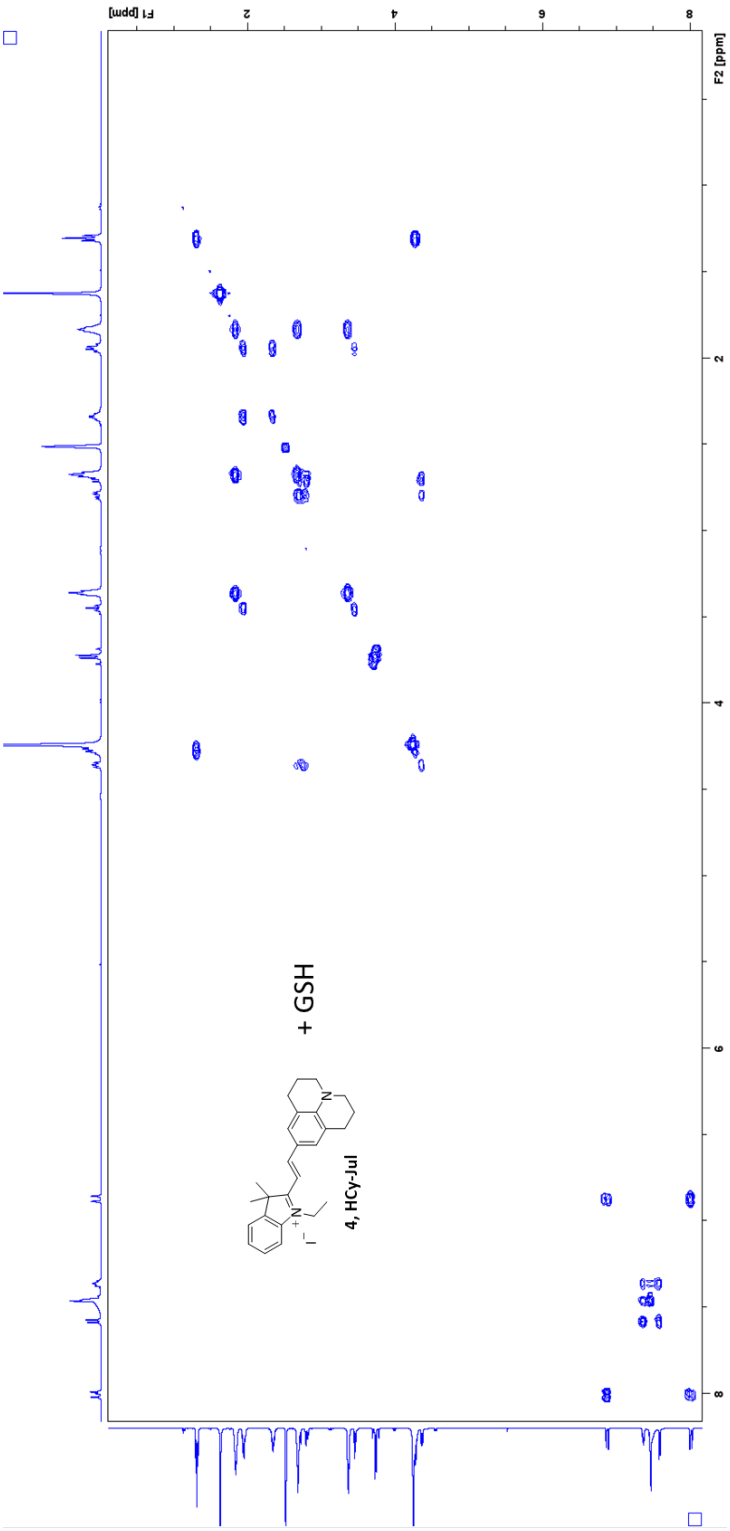

HMBC spectra of **HCy-Jul** treated with 1 eq of GSH in DMSO-d_6/D_2O (80:20).

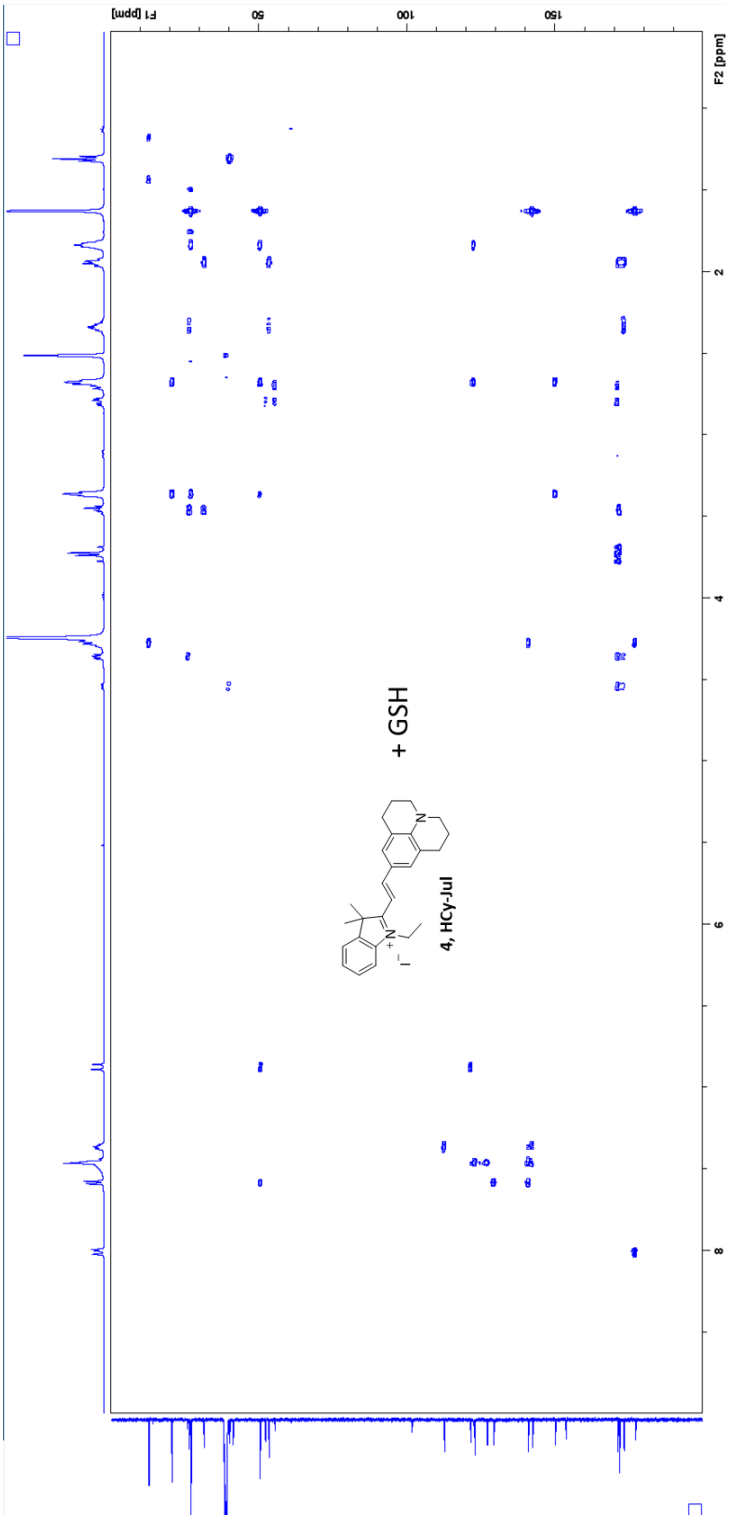

HSQC spectra of **HCy-Jul** treated with 1 eq of GSH in DMSO-d_6/D_2O (80:20).

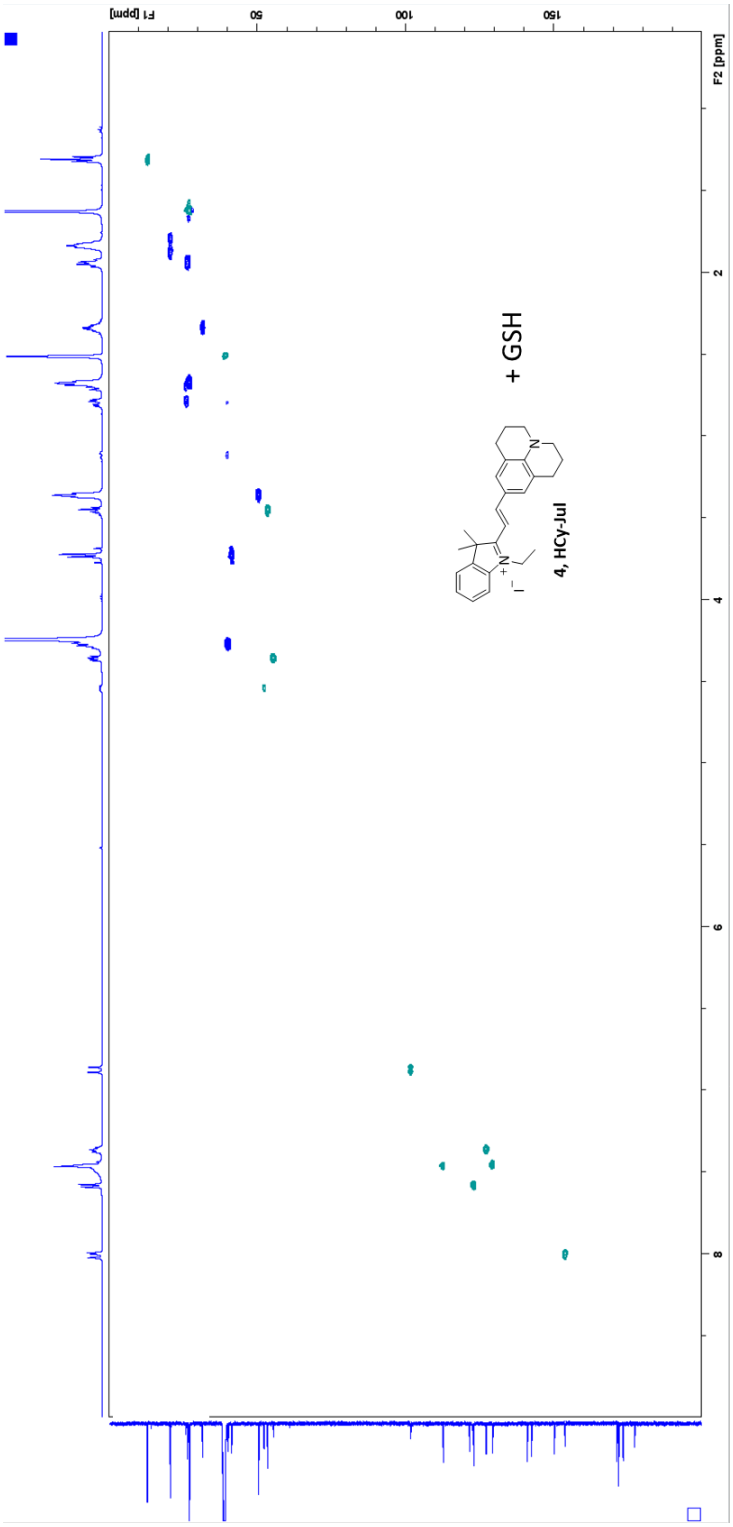

6.2 HR-MS spectra

HR-MS spectrum of compound **1**, DCM.

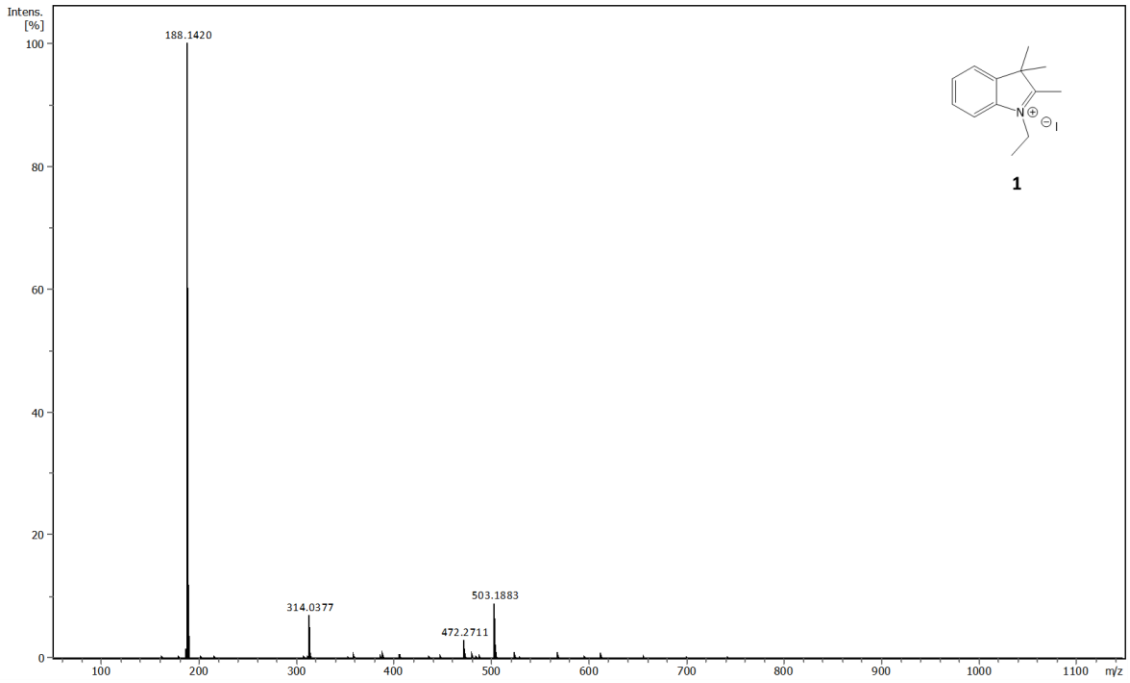

HR-MS spectrum of compound **HCy-NEt$_2$** (**3**), DCM.

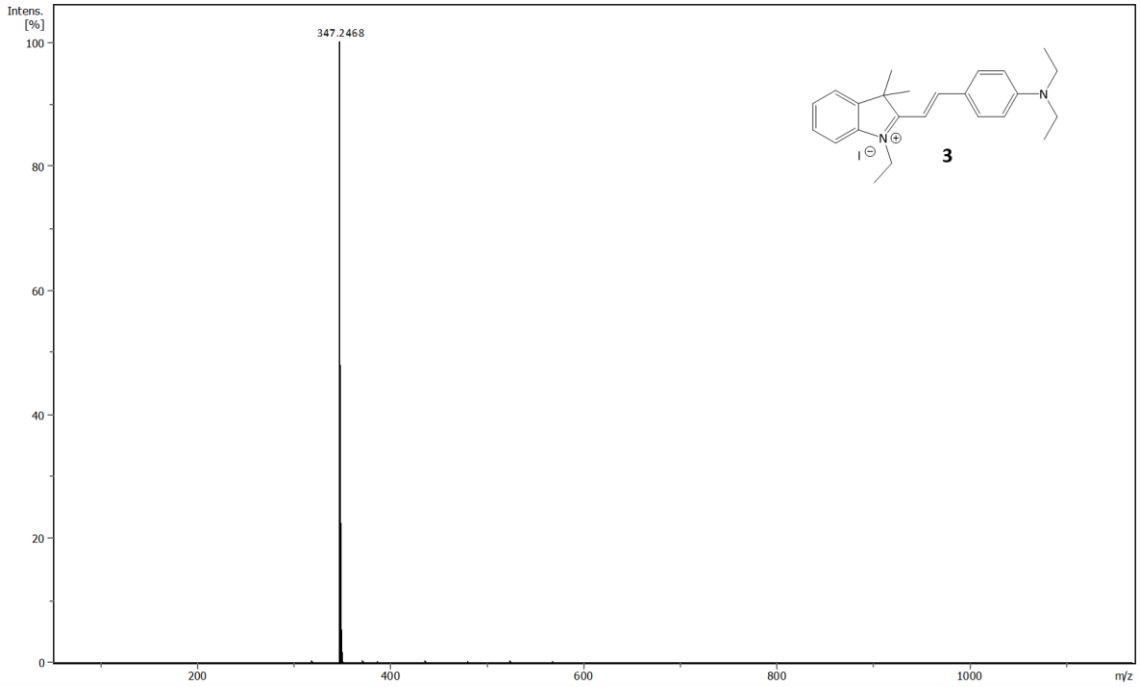

HR-MS spectrum of compound **HCy-Jul** (**4**), DCM.

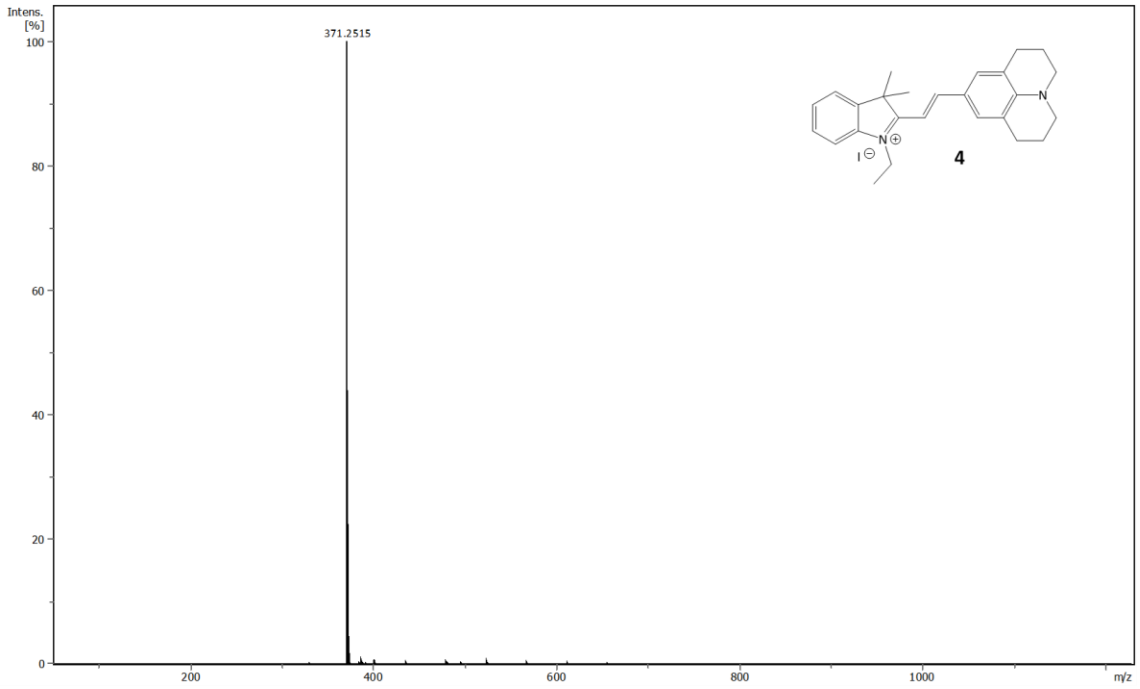

HR-MS spectrum of compound **5**, DCM.

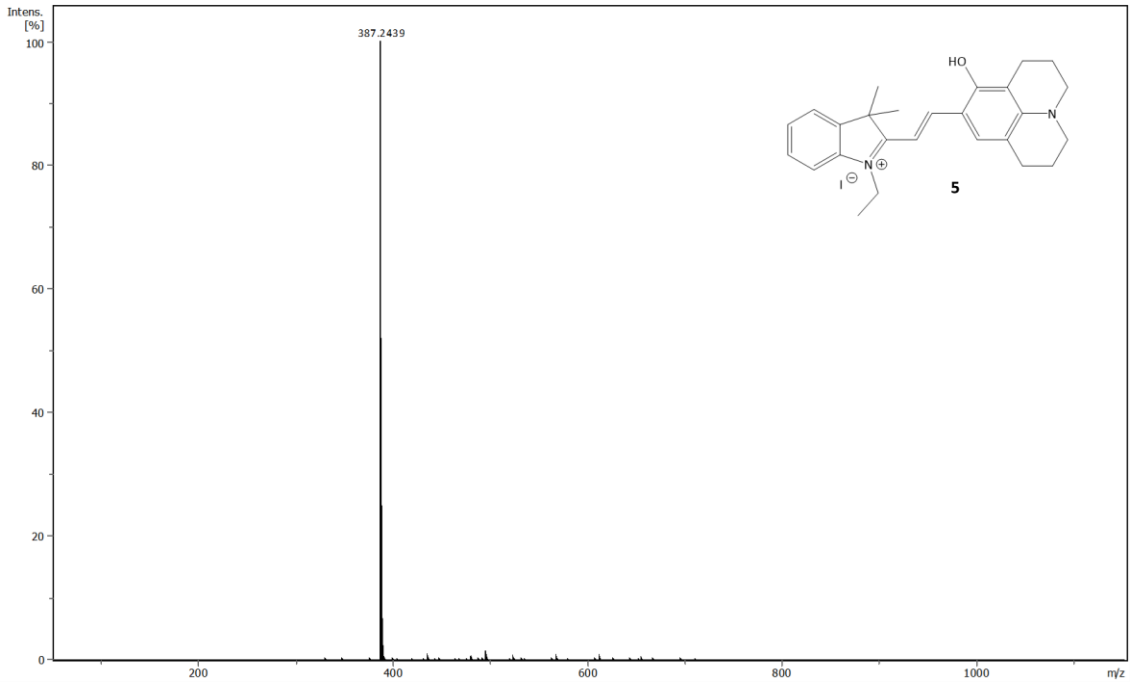

HR-MS spectrum of compound **6**, DCM.

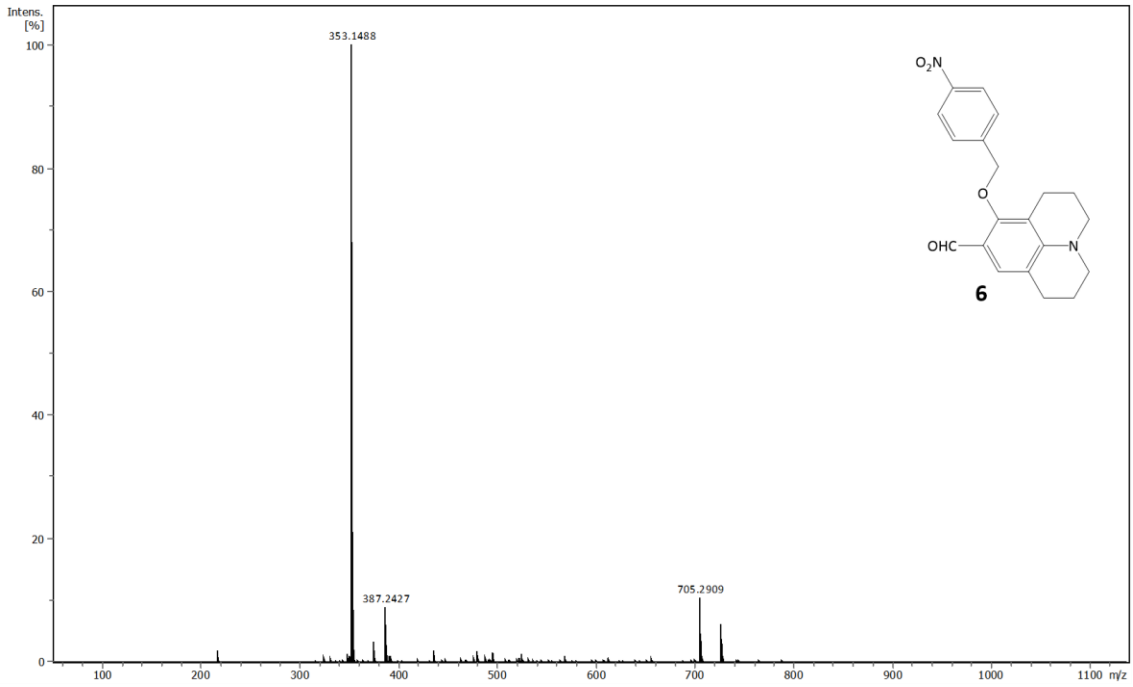

HR-MS spectrum of compound **NHCy** (**7**), DCM.

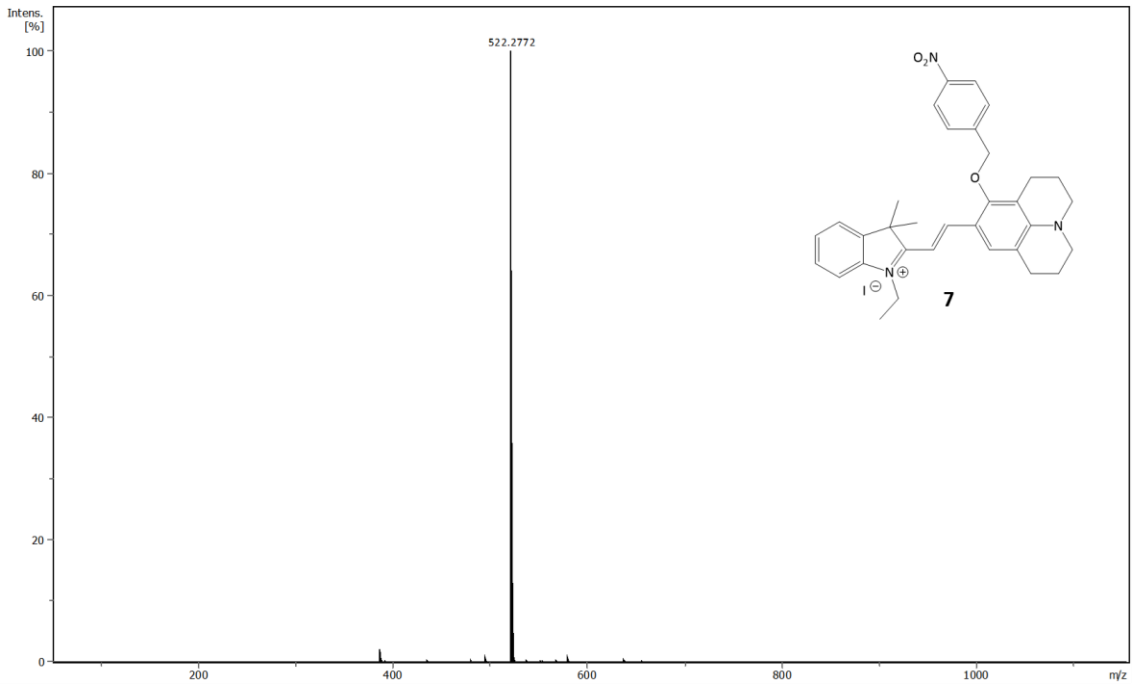

HR-MS spectrum of compound **10**, DCM.

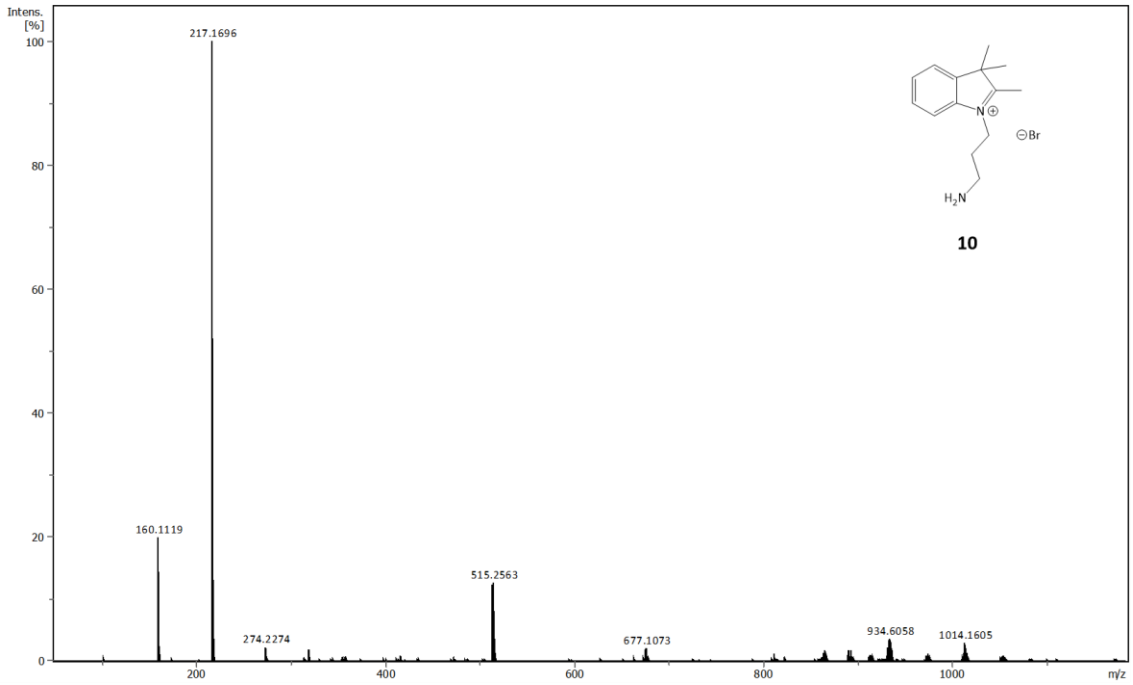

HR-MS spectrum of compound **11**, DCM.

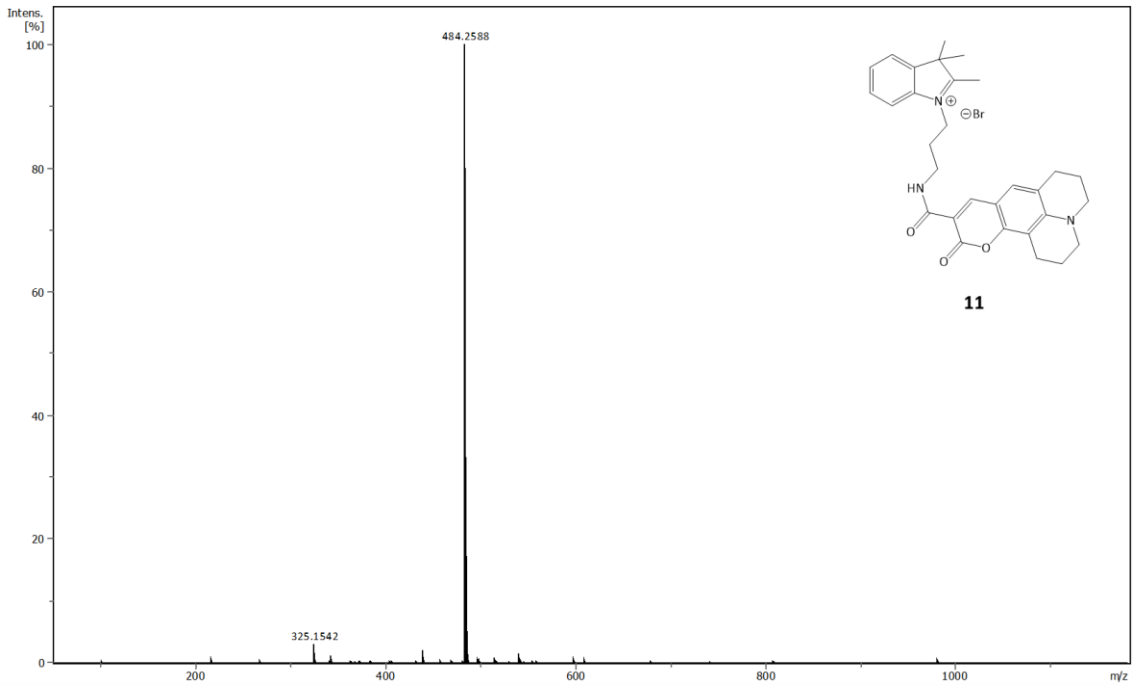

HR-MS spectrum of compound **NHCy-C** (**12**), DCM.

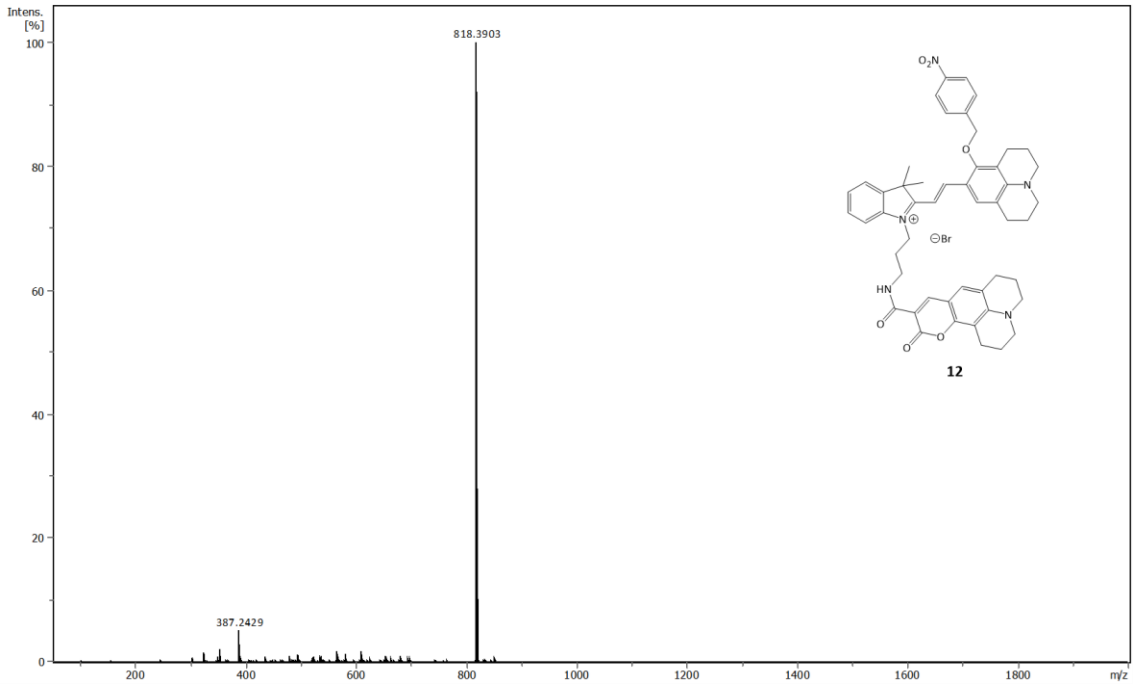

6.3 Fluorescence spectroscopic studies

Fluorescence studies of hemicyanine derivatives **HCy-OMe**, **HCy-NEt$_2$**, and **HCy-Jul** in different buffers for a given concentration range and a pH value of 7.4.

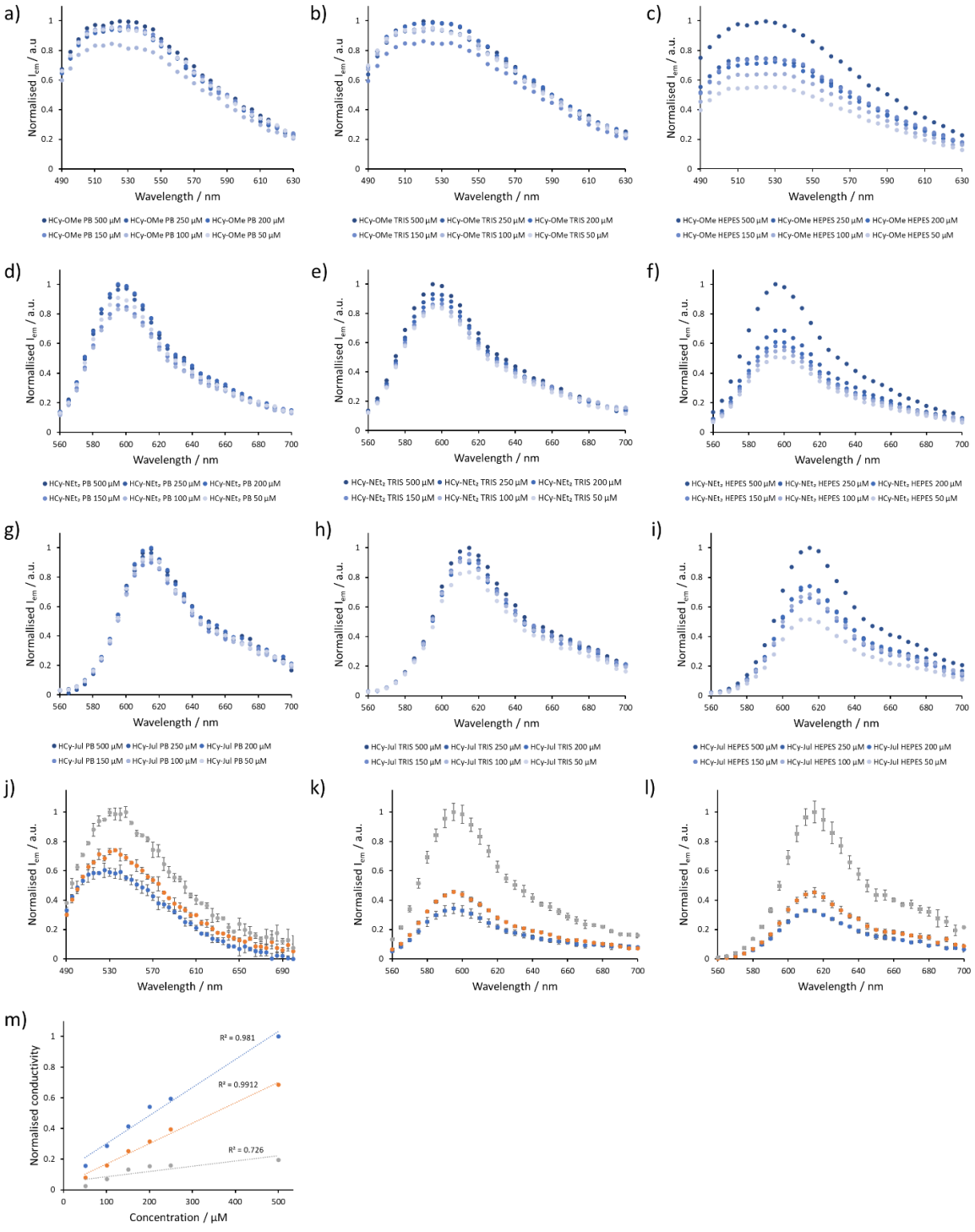

***Figure A1**. Fluorescence intensity of (a-c) **HCy-OMe** (5 µM), (d-f) **HCy-NEt₂** (2.5 µM), (g-i) **HCy-Jul** (2.5 µM) hemicyanine derivatives in three different buffer solutions: (a,d,g) phosphate buffer, (b,e,h) TRIS·HCl, and (c,f,i) HEPES; with concentration (50, 100, 150, 200, 250, and 500 µM) of pH 7.4, with a final 1% of DMSO. Normalisation of the fluorescent output signal was carried out within a given compound and buffer solution. Fluorescence intensity of (j) **HCy-OMe** (5 µM), (k) **HCy-NEt₂** (2.5 µM), (l) **HCy-Jul** (2.5 µM) hemicyanine derivatives in three different buffer solutions (phosphate buffer, blue dots; TRIS·HCl, orange dots; HEPES, grey dots; 100 mM) 100 mM at a pH value of 7.4, with a final 1% of DMSO. Normalisation of the fluorescent output signal was carried out within a given compound in PB solution (which consisted in the highest output signal). For **HCy-OMe** hemicyanine, spectra were collected at λ_{exc} = 430 nm, λ_{em} = 460-700 nm, and for **HCy-NEt₂** and **HCy-Jul** hemicyanines at λ_{exc} = 530 nm, λ_{em} = 560-700 nm, Gain 120. To be normalised within a given compound.For **HCy-OMe** hemicyanine, spectra were collected at λ_{exc} = 430 nm, λ_{em} = 460-700 nm, and for **HCy-NEt₂** and **HCy-Jul** hemicyanines at λ_{exc} = 530 nm, λ_{em} = 560-700 nm. (m) Plot of normalised electric conductivity vs concentration (50, 100, 150, 200, 250, and 500 µM) of PB (blue dots and trendline), TRIS·HCl (orange dots and trendline), HEPES (grey dots and trendline) buffers at pH 7.5. Conductivity was normalised to the output value given by 500 µM PB. N = 3*

Fluorescence studies of hemicyanine derivatives **HCy-OMe**, **HCy-NEt$_2$**, and **HCy-Jul** and their treatment with cyanide (5 µM) in DMSO/HEPES (80:20) with a pH value of 7.4.

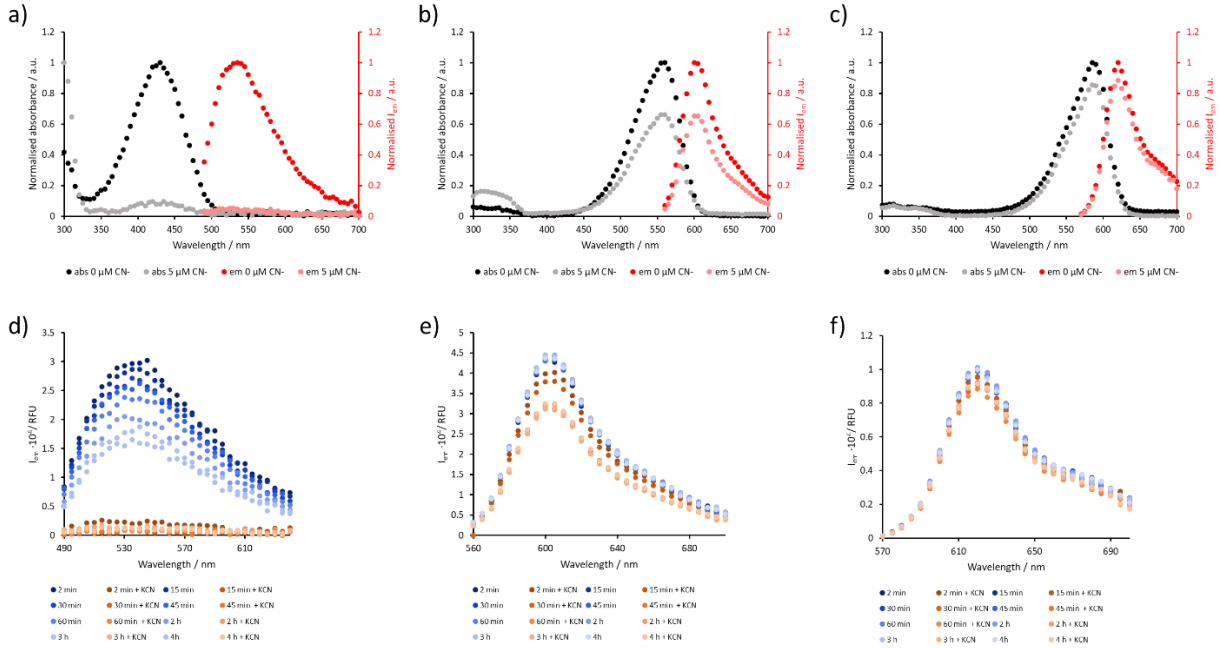

***Figure A2**. (a-c) Normalised absorbance (black and grey) and fluorescence emission (red) spectra of (a) **HCy-OMe** (5 µM), (b) **HCy-NEt$_2$** (2.5 µM), (c) **HCy-Jul** (2.5 µM) in the absence (dark colour) and presence (light colour) of GSH (2 mM) in DMSO/HEPES (80:20) with at pH value of 7.4 at 4 h after treatment. (d-e) Fluorescence emission spectra of (d) **HCy-OMe** (5 µM), (e) **HCy-NEt$_2$** (2.5 µM), (f) **HCy-Jul** (2.5 µM) in the absence (blue gradient dots) and presence (orange gradient dots) of GSH (2 mM) in DMSO/HEPES (80:20) with at pH value of 7.4 at different time points. Emission spectra collection: $\lambda_{exc/em}$ **HCy-OMe** = 430/490-700; $\lambda_{exc/em}$ HCy-NEt2 and **HCy-Jul** = 530/560-700. N = 3*

Fluorescence studies of hemicyanine derivatives **HCy-OMe**, **HCy-NEt$_2$**, and **HCy-Jul** and their treatment with GSH (2 mM) in DMSO/HEPES (80:20) with a pH value of 8.

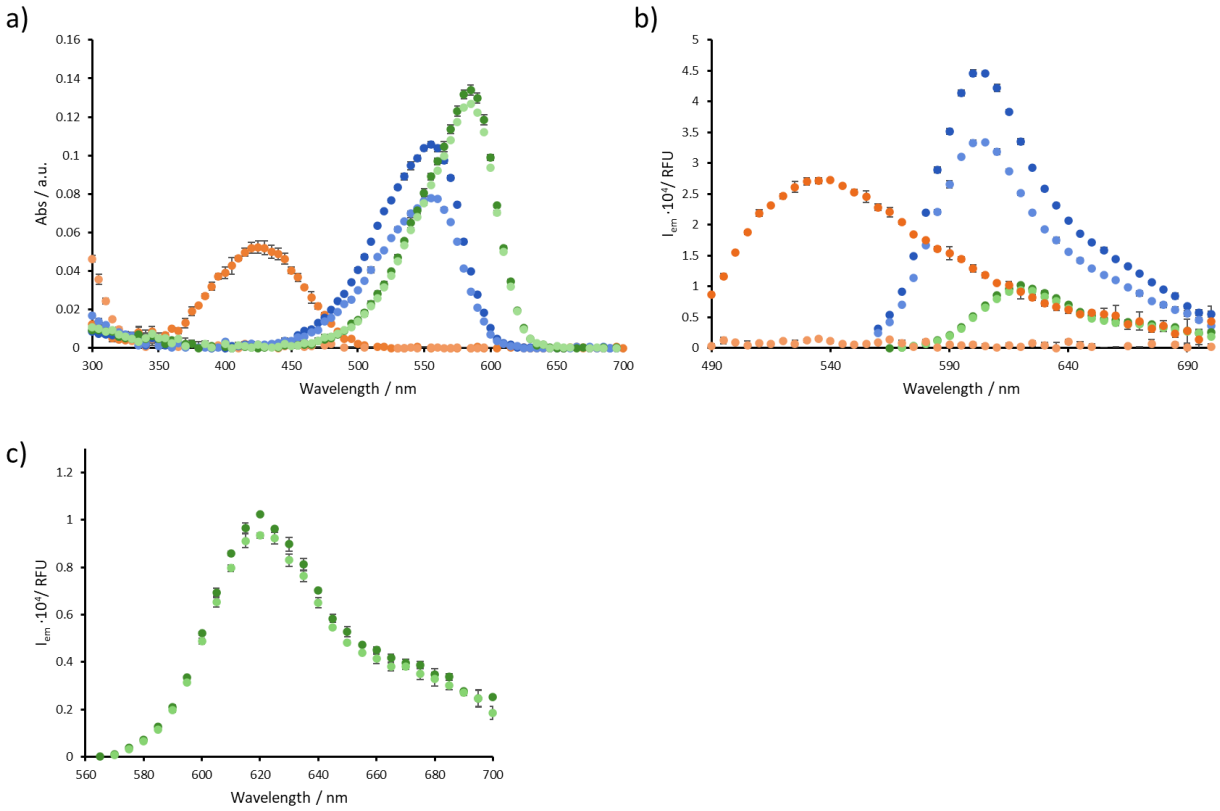

Figure A3. *(a) Absorbance and (b,c) fluorescence emission spectra of* ***HCy-OMe*** *(5 µM; orange dots),* ***HCy-NEt$_2$*** *(2.5 µM; blue dots),* ***HCy-Jul*** *(2.5 µM; green dots) in the absence (dark colour) and presence (light colour) of GSH (2 mM) in DMSO/HEPES (80:20) with a pH value of 8. Emission spectra collection 150 min upon GSH treatment: $\lambda_{exc/em}$* ***HCy-OMe*** *= 430/490-700; $\lambda_{exc/em}$* ***HCy-NEt2*** *and* ***HCy-Jul*** *= 530/560-700. N = 3*

Fluorescence studies of hemicyanine derivatives **HCy-OMe**, **HCy-NEt$_2$**, and **HCy-Jul** and their treatment with GSH (2 mM) in DMSO/HEPES (80:20) with a pH value of 7.4, 8, and 9.

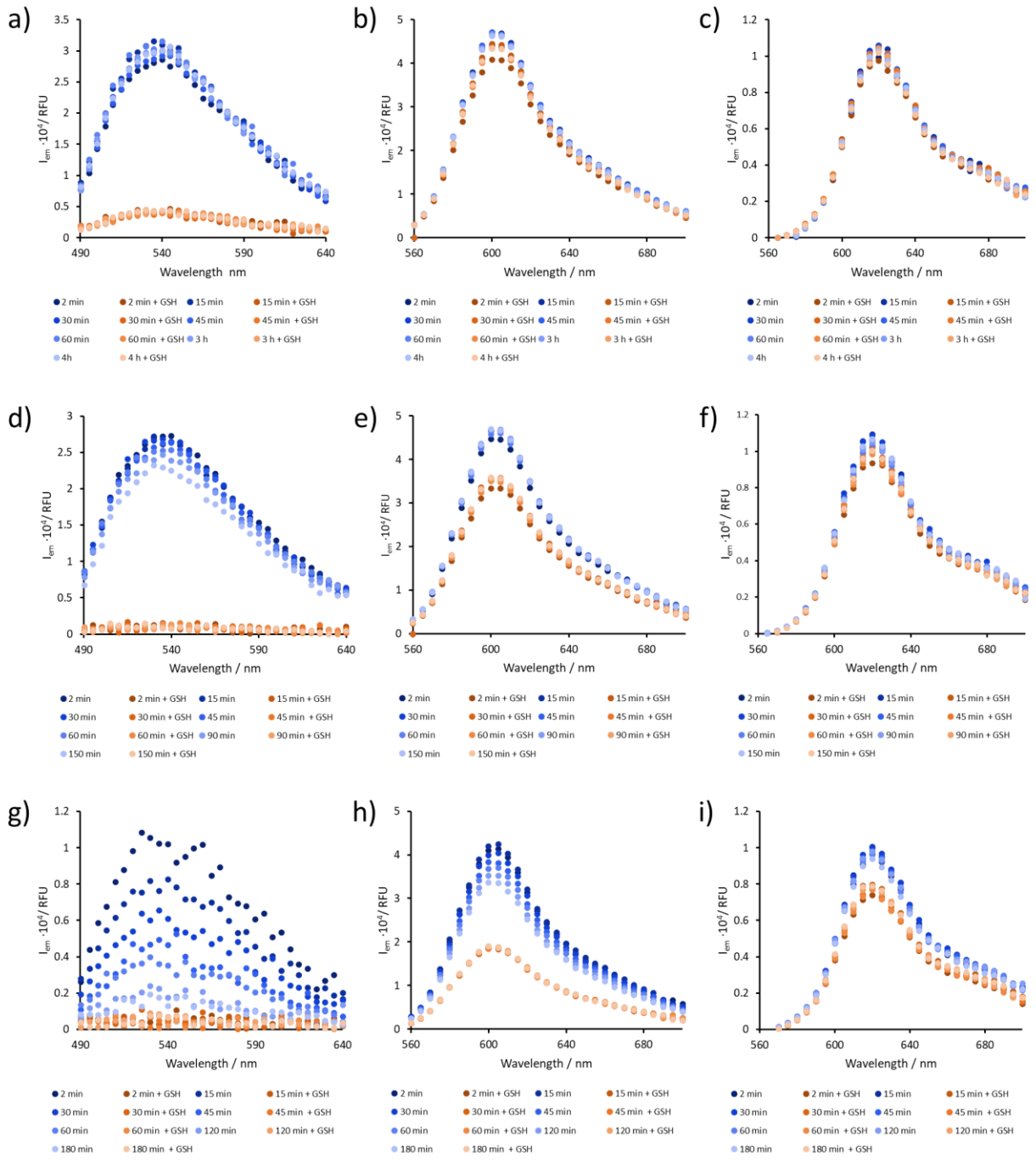

***Figure A4**. Fluorescence emission spectra of (a,d,g) **HCy-OMe** (5 µM), (b,e,h) **HCy-NEt$_2$** (2.5 µM), (c,f,i) **HCy-Jul** (2.5 µM) in the absence (blue gradient dots) and presence (orange gradient dots) of GSH (2 mM) in DMSO/HEPES (80:20) with at pH values of (a-c) 7.4, (d-f) 8, and (g-i) 9 at different time points. Emission spectra collection: $\lambda_{exc/em}$ **HCy-OMe** = 430/490-700; $\lambda_{exc/em}$ **HCy-NEt2** and **HCy-Jul** = 530/560-700. N = 3*

Estimation of path length

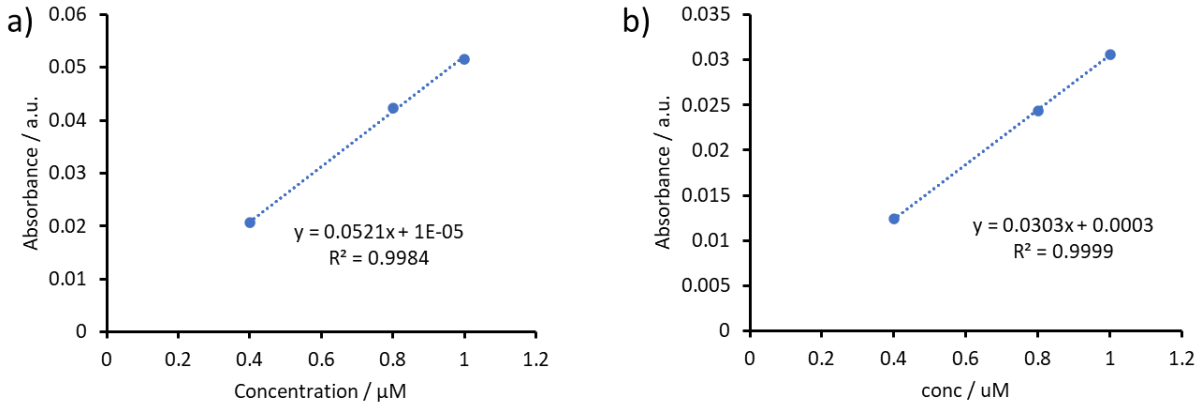

Figure A5. *Plots of absorbance vs concentration of Rhodaine 6G (0.4, 0.8, and 1 µM in EtOH) for (a) 96 well-plates with 200 µL volume solution per well and (b) 384 well-plates with 40 µL volume solution per well. The blank sample was pure EtOH in the respective volume.*

Fluorescence and absorbance plots for the determination of molar extinction coefficient, brightness, and ϕ_F in 96 well-plates

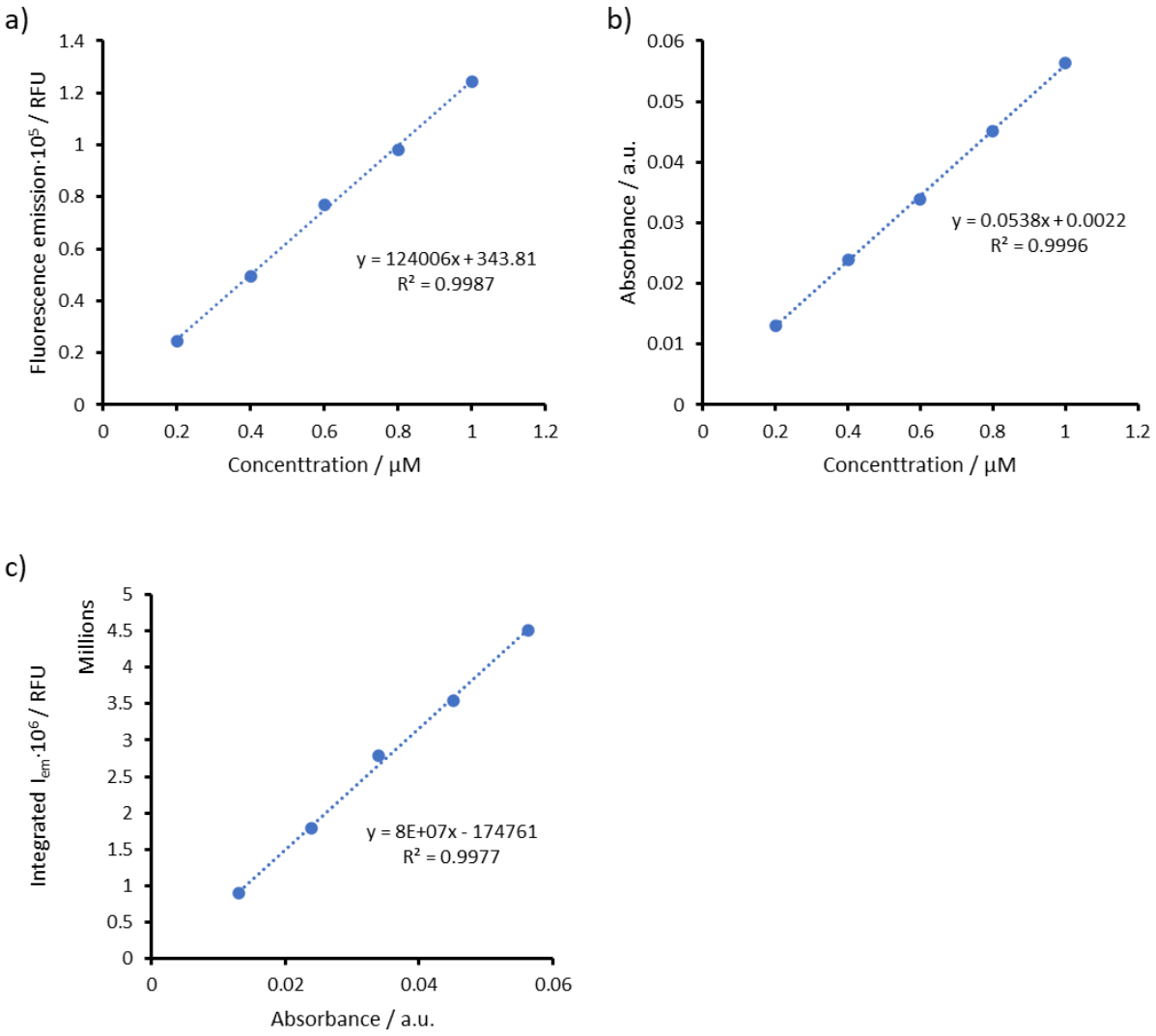

***Figure A6**. Plots of (a) fluorescence emission vs concentration (b) absorbance vs fluorescence integrated fluorescence emission vs concentration for Rhodamine 6G (range: 0.2 - 1.25 µM) in ethanol. N = 3*

Fluorescence and absorbance plots for the determination of molar extinction coefficient, brightness, and ϕ_F in 384 well-plates

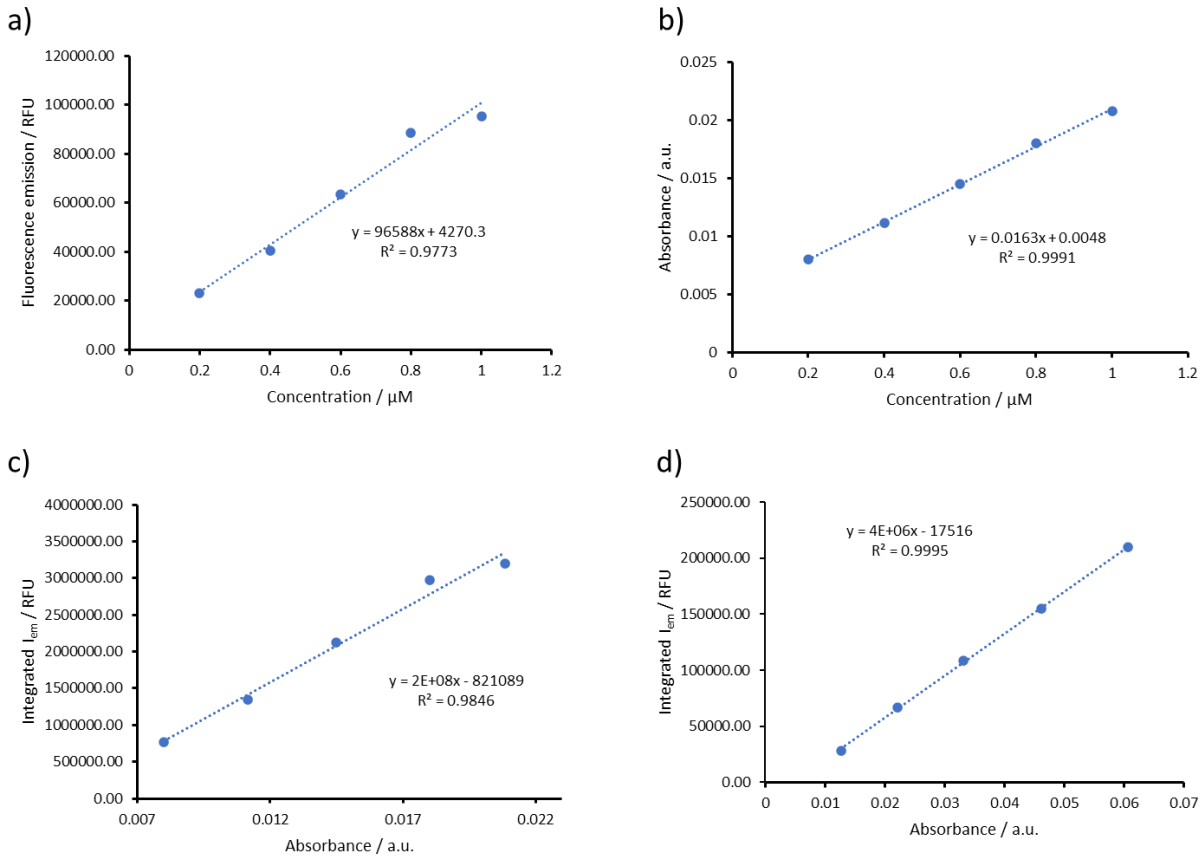

***Figure A7**. Plots of (a) fluorescence emission vs concentration (b) absorbance vs fluorescence integrated fluorescence emission vs concentration for Rhodamine 6G (range: 0.2 - 1.25 µM) in ethanol. (d) Plot of integrated fluorescence emission vs concentration for **NHCy** (range: 2 -10 µM) in DMSO. Emission spectra were collected in the following condition: $\lambda_{exc/em}$ = 515/545-700 nm. N = 3*

6.4 Cell viability studies

Table A1. Cell death (%) depending on derivatives **HCy-NEt$_2$** and **HCy-Jul** concentration (in µM) in DU145 and HEK cell lines 48 h after treatment. N = 3

	HCy-NEt$_2$		**HCy-Jul**	
	DU145	HEK	DU145	HEK
Concentration [µM]	Cell death [%]	Cell death [%]	Cell death [%]	Cell death [%]
10	22.6 ± 5.9	37.9 ± 9.6	77.9 ± 11.9	77.7 ± 0.8
5	12.6 ± 3.6	9.0 ± 14.0	71.4 ± 5.8	70.9 ± 1.0
2.5	20.6 ± 9.4	2.5 ± 9.0	50.2 ± 15.1	51.8 ± 6.2
0.74	14.4 ± 3.0	-3.2 ± 21.0	33.5 ± 17.7	20.7 ± 11.5
0.5	17.1 ± 9.6	-9.5 ± 15.1	40.6 ± 8.0	23.5 ± 18.4
0.4	15.9 ± 9.8	-2.3 ± 22.4	15.9 ± 9.5	-17.1 ± 7.5
0.25	32.1 ± 9.2	19.9 ± 12.7	27.9 ± 11.2	25.0 ± 11.8
0.2	13.1 ± 12.5	2.5 ± 21.1	21.7 ± 12.7	1.3 ± 8.6
0.1	15.8 ± 11.9	16.0 ± 11.2	27.0 ± 8.5	34.2 ± 8.9
0.01	20.6 ± 22.9	6.5 ± 12.8	18.6 ± 10.9	19.9 ± 9.5

Table A2. IC_{50}, lower and upper limits, slope values of **HCy-NEt$_2$** and **HCy-Jul** for resazurin assay in DU145 and HEK cell line. N = 3

HCy/Cell line	IC_{50} [µM]	Std. Error [µM]	Lower Limit [%]	Upper Limit [%]	Slope
HCy-NEt$_2$/DU145	>10	-	20.56	22.65	-
HCy-NEt$_2$/HEK	>10	-	6.50	37.90	-
HCy-Jul/DU145	3.09	1.67	9.04	81.47	1.32
HCy-Jul/HEK	2.04	0.74	14.7	78.36	2.31

Table A3. Cell death (%) depending on **NHCy** concentration (in µM) in DU145 and A549 cell lines 48 h after treatment. N = 3

	NHCy	
	DU145	A549
Concentration [µM]	Cell death [%]	Cell death [%]
10	88.3 ± 20.4	23.1 ± 14.2
5	85.2 ± 12.0	11.1 ± 9.1
2.5	69.4 ± 7.2	8.1 ± 3.1
0.74	33.2 ± 2.8	2.8 ± 1.7
0.5	24.7 ± 13.7	2.4 ± 3.2
0.4	10.6 ± 1.8	2.9 ± 1.5
0.25	10.3 ± 2.3	1.1 ± 3.1
0.2	-1.2 ± 6.4	0.6 ± 0.8
0.1	-1.3 ± 2.0	1.3 ± 2.5
0.01	7.0 ± 7.6	1.1 ± 0.5

Table A4. IC_{50}, lower and upper limits, slope values, and curves of **NHCy** for resazurin assay in DU145 and A549 cell lines. N = 3

Cell line	IC_{50} [µM]	Std. Error [µM]	Lower Limit [%]	Upper Limit [%]	Slope
DU145	1.09	0.19	0.54	90.13	1.67
A549	>10	-	1.07	23.05	-

Table A5. Cell death (%) depending on **NHCy** concentration (in µM) in DU145 and A549 cell lines 48 h after treatment, and MCF7 cell line 24 h after treatment. N = 3

	NHCy-C		
	DU145	A549	MCF7
Concentration [µM]	Cell death [%]	Cell death [%]	Cell death [%]
10	68.4 ± 2.9	21.1 ± 3.7	-
5	57.4 ± 1.7	4.4 ± 2.3	9.3 ± 7.7
2.5	39.2 ± 15.1	7.4 ± 4.6	2.6 ± 2.2
1.25	-	-	3.6 ± 6.8
0.74	27.2 ± 19.6	1.6 ± 1.0	-
0.625	-	-	1.0 ± 0.5
0.5	11.7 ± 4.2	0.9 ± 1.9	-
0.4	17.2 ± 11.0	1.7 ± 0.7	-
0.313	-	-	2.2 ± 3.5
0.25	6.3 ± 1.1	1.0 ± 2.0	-
0.2	10.8 ± 6.3	0.7 ± 0.9	-
0.156	-	-	2.2 ± 4.0
0.1	8.7 ± 1.5	1.4 ± 2.8	-
0.01	11.6 ± 8.5	2.4 ± 1.6	-

Table A6. IC_{50}, lower and upper limits, slope values, of **NHCy-C** for resazurin assay in DU145, A549, and MCF7 cell lines. N = 3

Cell line	IC_{50} [µM]	Std. Error [µM]	Lower Limit [%]	Upper Limit [%]	Slope
DU145	3.09	1.67	9.04	81.47	1.32
A549	>10	-	2.35	21.12	-
MCF7	>5	-	2.17	9.33	-

6.5 Flow cytometry scatter plots

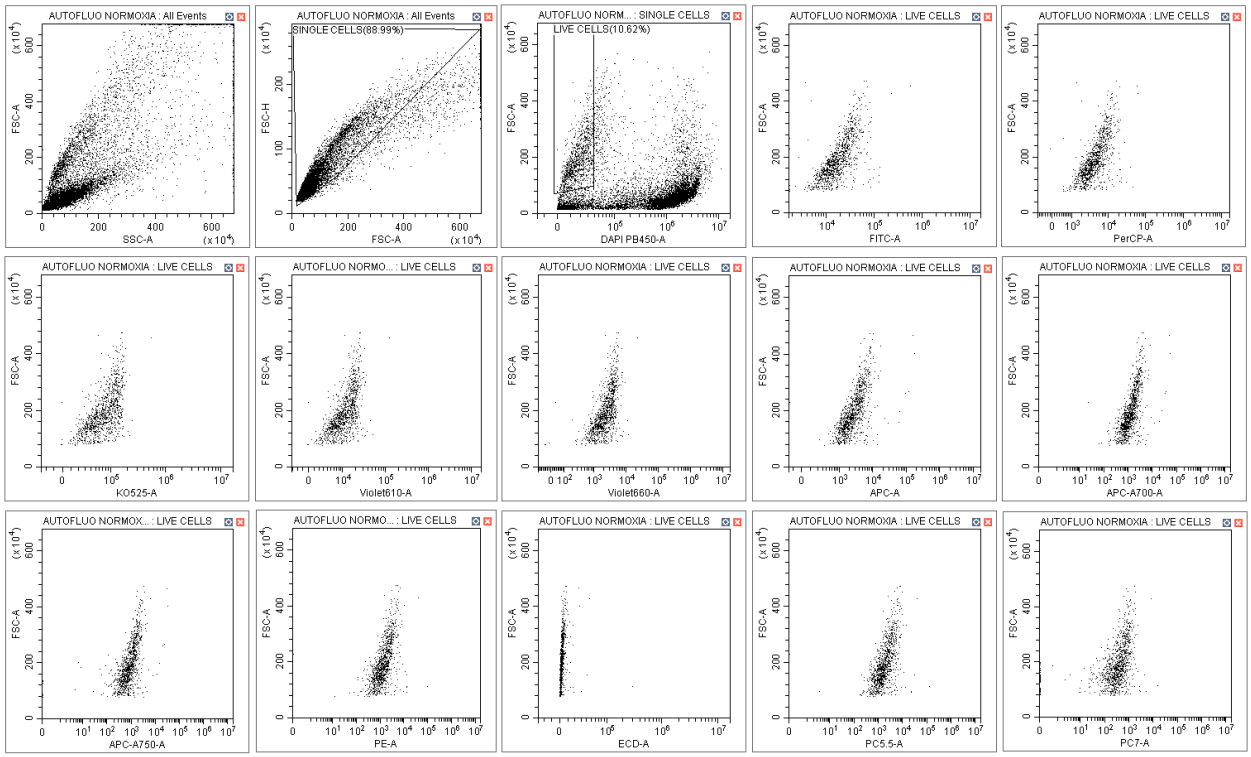

***Figure A8**. Flow cytometry scatter plots MCF7 cells in normoxic conditions treated with **NHCy-C** (2.5 µM) with a final 1% DMSO – normoxia autofluorescence sample.*

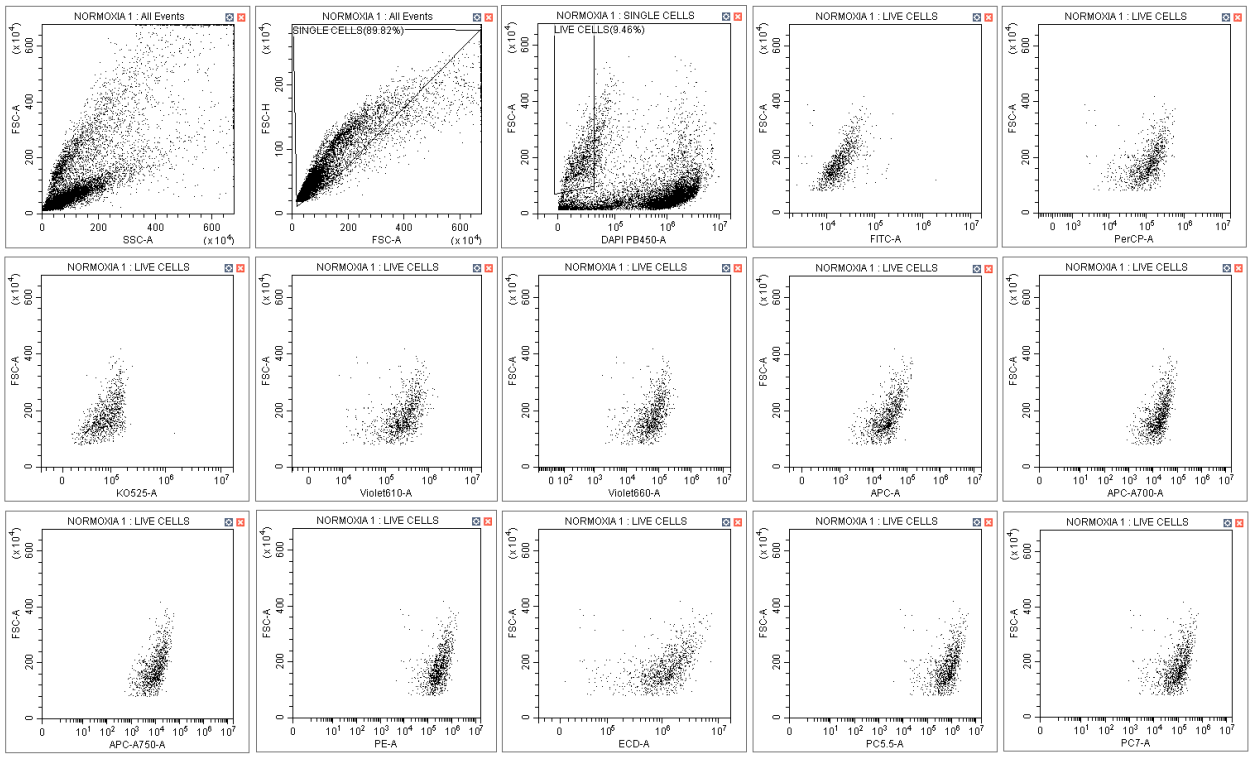

***Figure A9**. Flow cytometry scatter plots MCF7 cells in normoxic conditions treated with **NHCy-C** (2.5 µM) with a final 1% DMSO – normoxia sample 1.*

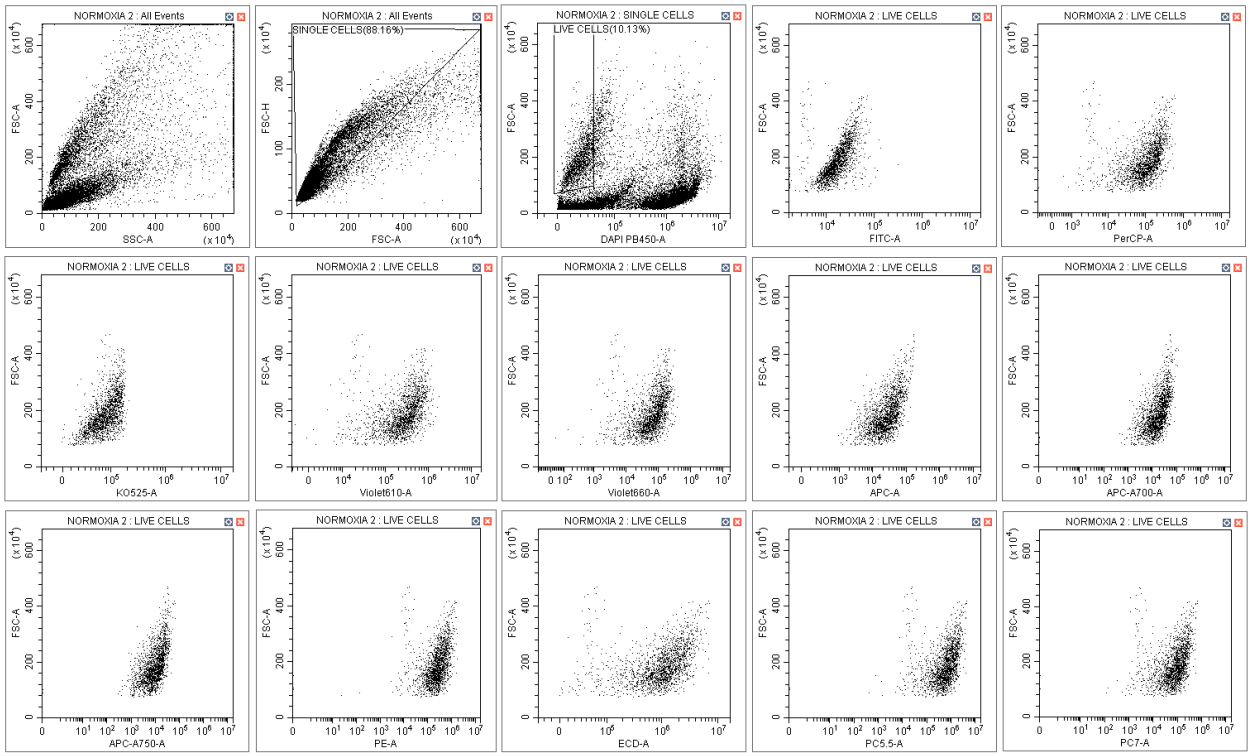

***Figure A10**. Flow cytometry scatter plots MCF7 cells in normoxic conditions treated with **NHCy-C** (2.5 µM) with a final 1% DMSO – normoxia sample 2.*

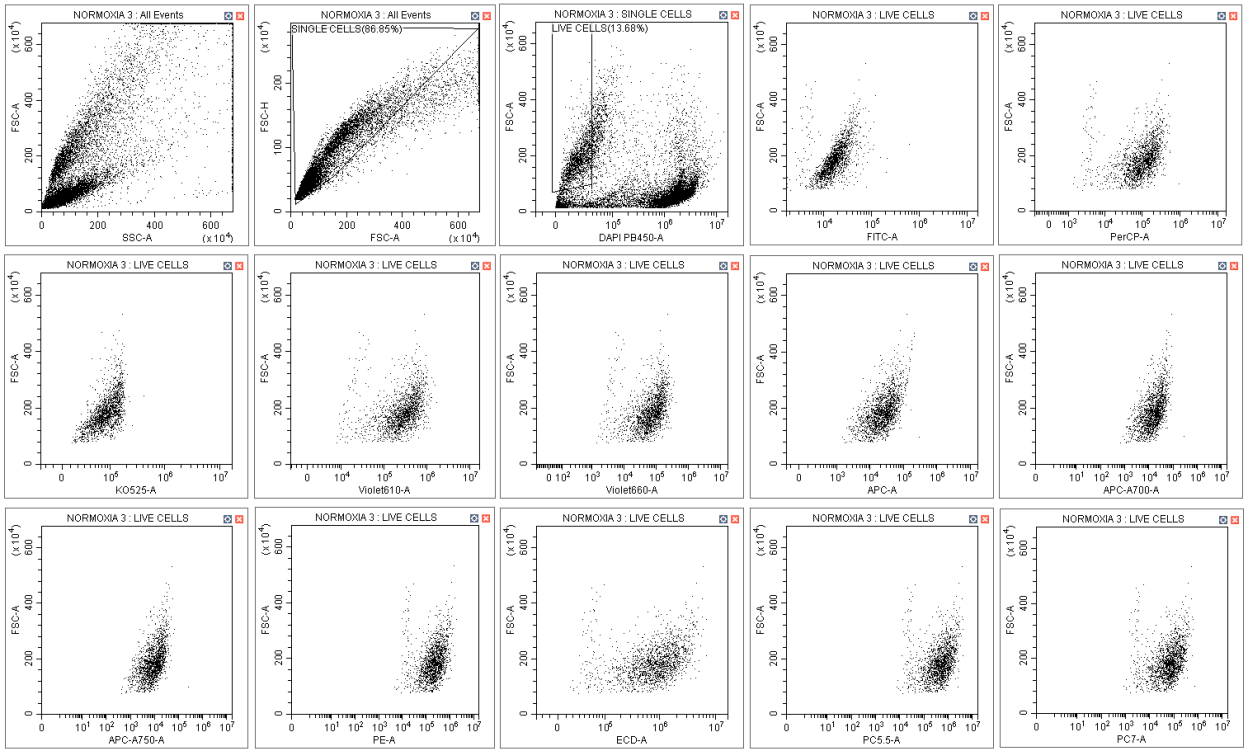

***Figure A11**. Flow cytometry scatter plots MCF7 cells in normoxic conditions treated with **NHCy-C** (2.5 µM) with a final 1% DMSO – normoxia sample 3.*

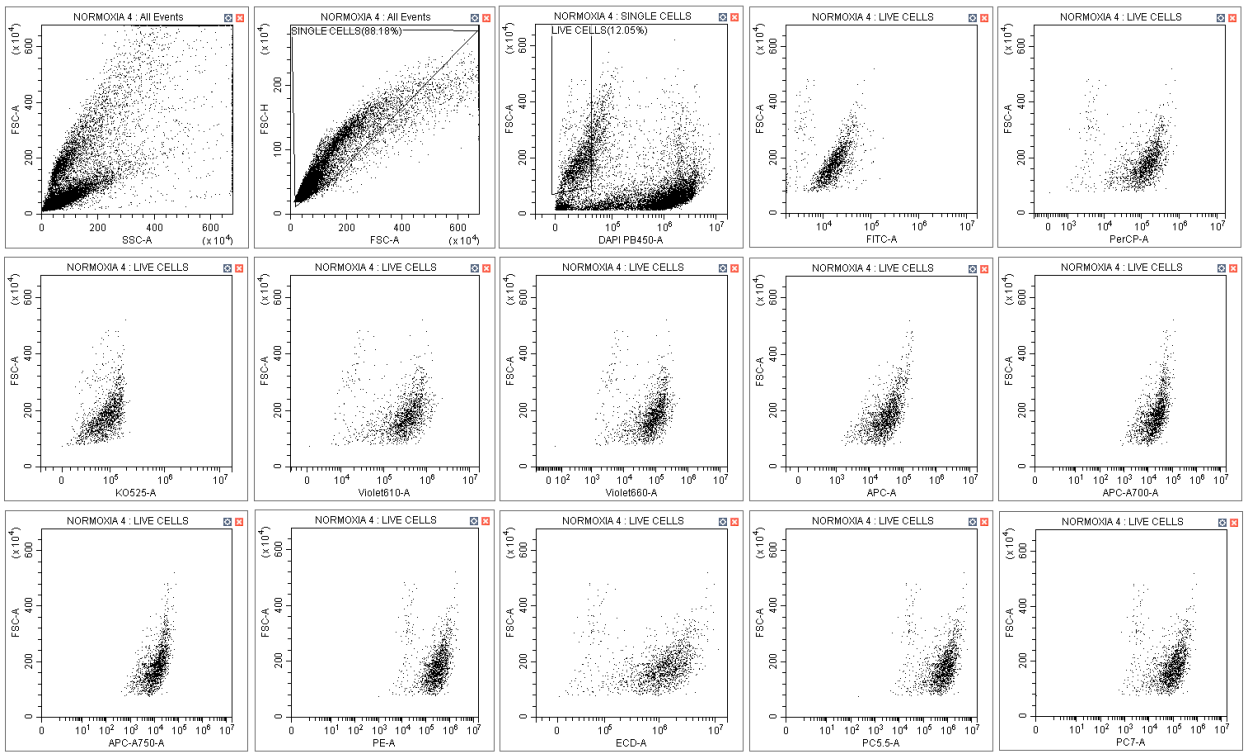

***Figure A12**. Flow cytometry scatter plots MCF7 cells in normoxic conditions treated with **NHCy-C** (2.5 µM) with a final 1% DMSO – normoxia sample 4.*

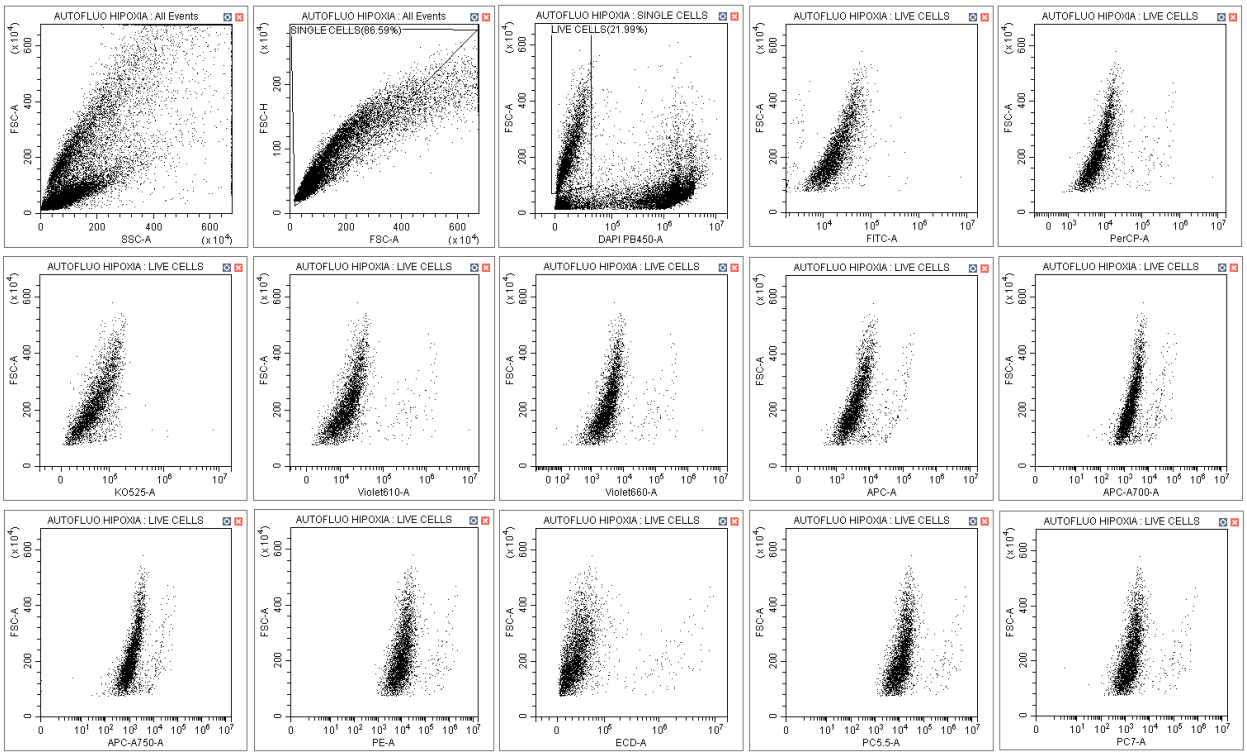

***Figure A13**. Flow cytometry scatter plots MCF7 cells in hypoxic conditions treated with **NHCy-C** (2.5 µM) with a final 1% DMSO – hypoxia autofluorescence sample.*

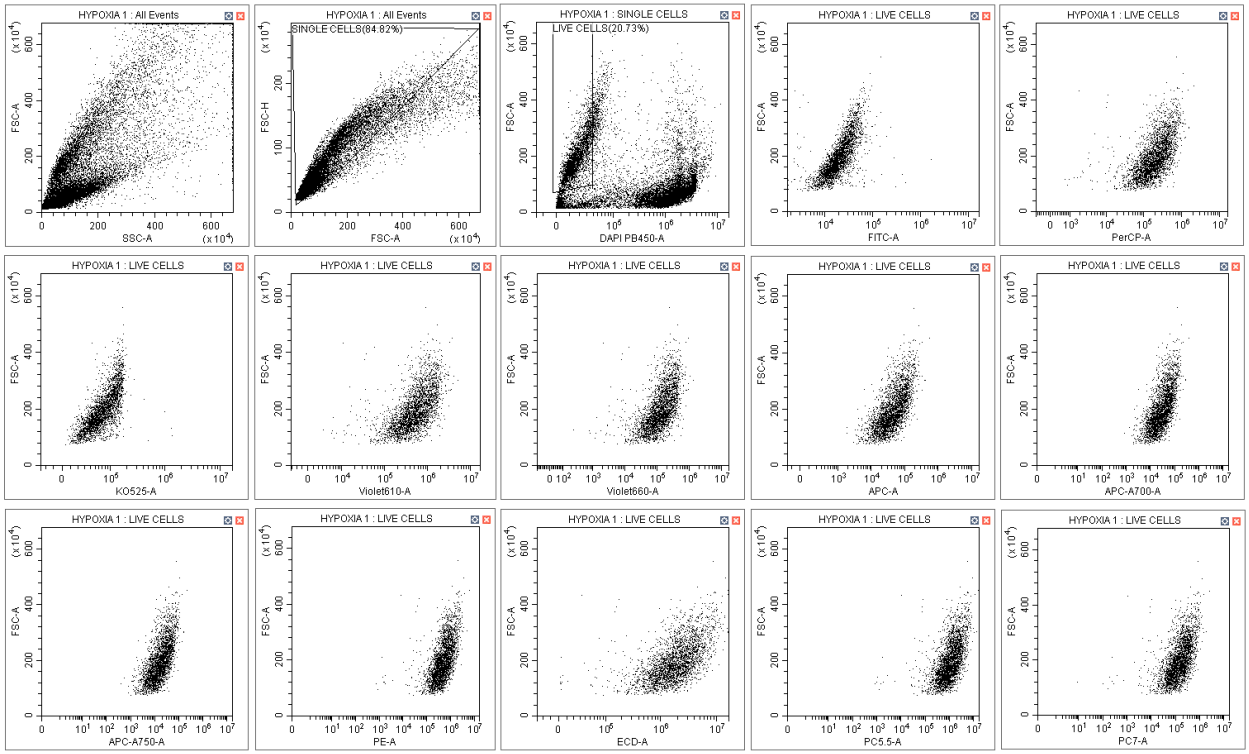

***Figure A14**. Flow cytometry scatter plots MCF7 cells in hypoxic conditions treated with **NHCy-C** (2.5 µM) with a final 1% DMSO – hypoxia sample 1.*

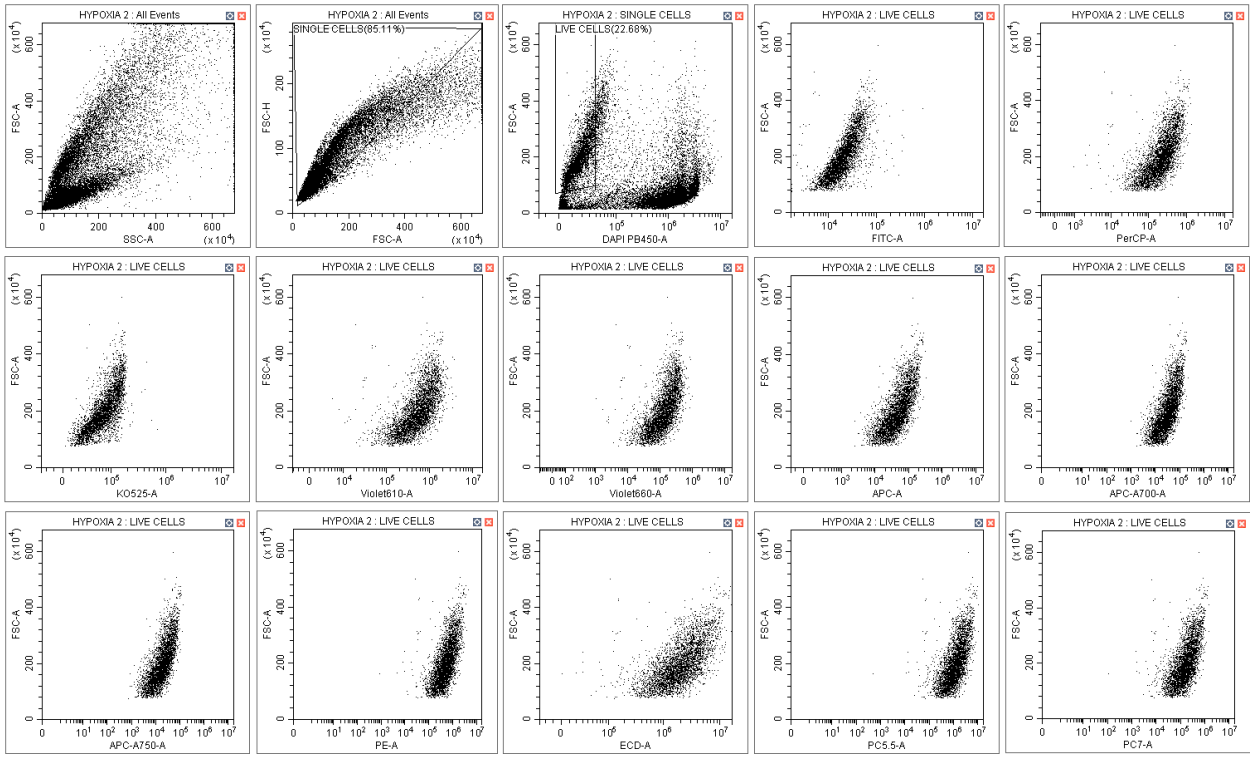

***Figure A15**. Flow cytometry scatter plots MCF7 cells in hypoxic conditions treated with **NHCy-C** (2.5 µM) with a final 1% DMSO – hypoxia sample 2.*

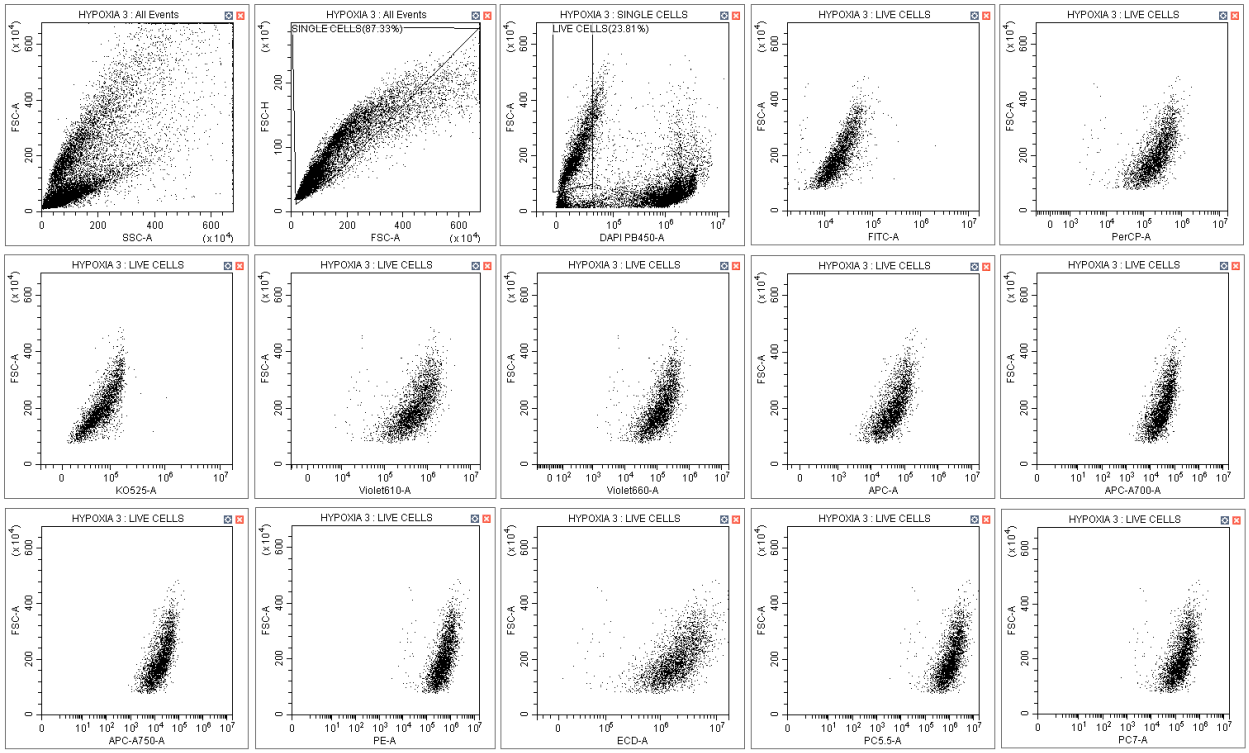

***Figure A16**. Flow cytometry scatter plots MCF7 cells in hypoxic conditions treated with **NHCy-C** (2.5 µM) with a final 1% DMSO – hypoxia sample 3.*

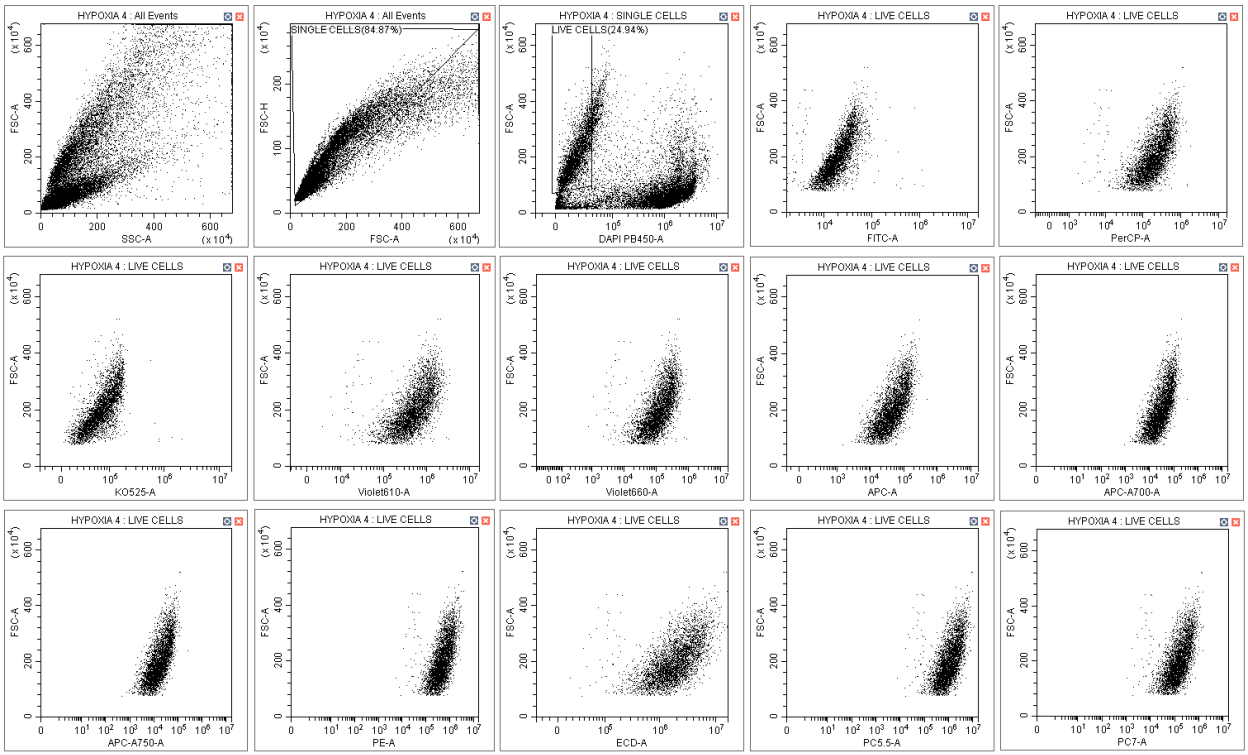

***Figure A17**. Flow cytometry scatter plots MCF7 cells in hypoxic conditions treated with **NHCy-C** (2.5 µM) with a final 1% DMSO – hypoxia sample 4.*

7. Bibliography

1. Adachi, J. *et al.* Dense and Acidic Organelle-Targeted Visualization in Living Cells: Application of Viscosity-Responsive Fluorescence Utilizing Restricted Access to Minimum Energy Conical Intersection. *Anal. Chem.* **95**, 5196–5204 (2023).

2. Yin, J. *et al.* Small molecule based fluorescent chemosensors for imaging the microenvironment within specific cellular regions. *Chem. Soc. Rev.* **50**, 12098–12150 (2021).

3. Kumari, R., Sunil, D., Ningthoujam, R. S. & Kumar, N. A. Azodyes as markers for tumor hypoxia imaging and therapy: An up-to-date review. *Chem. Biol. Interact.* **307**, 91–104 (2019).

4. Klymchenko, A. S. Solvatochromic and Fluorogenic Dyes as Environment-Sensitive Probes: Design and Biological Applications. *Acc. Chem. Res.* **50**, 366–375 (2017).

5. Gao, P., Pan, W., Li, N. & Tang, B. Fluorescent probes for organelle-targeted bioactive species imaging. *Chem. Sci.* **10**, 6035–6071 (2019).

6. Wang, H. *et al.* A water-soluble “turn-on” fluorescent probe for specifically imaging mitochondria viscosity in living cells. *Spectrochim. Acta - Part A Mol. Biomol. Spectrosc.* **203**, 127–131 (2018).

7. Ye, J. *et al.* Visualizing mitochondrial viscosity during ferroptosis by using solvatochromifc effect-decreased hemicyanine probe. *Microchem. J.* 109010 (2023).

8. Aron, A. T., Loehr, M. O., Bogena, J. & Chang, C. J. An Endoperoxide Reactivity-Based FRET Probe for Ratiometric Fluorescence Imaging of Labile Iron Pools in Living Cells. *J. Am. Chem. Soc.* **138**, 14338–14346 (2016).

9. Ren, J. *et al.* pH-Switchable Fluorescent Probe for Spatially-Confined Visualization of Intracellular Hydrogen Peroxide. *Anal. Chem.* **88**, 5865–5870 (2016).

10. Lakowicz, J. R. *Principles of Fluorescence Spectroscopy*. (Springer Science+Business Media, 2006). doi:10.1007/BF02629943.

11. Michael, K. Characterization of electronic transitions in complex molecules. *Discuss. Faraday Soc.* **9**, 14–19 (1950).

12. Stokes, G. G. On the change of refrangibility of light. *Philos. Trans. R. Soc. London* **142**, 463–562 (1852).

13. Dzebo, D. Photon Upconversion through Triplet-Triplet Annihilation: Towards Higher Efficiency and Solid State Applications. (2016). doi:10.13140/RG.2.2.34379.18722.

14. Demchenko, A. P. *Advanced Fluorescence Reporters in Chemistry and Biology I. Fundamentals and Molecular Design Volume*. *Springer Series on Fluorescence* (Springer-Verlag Berlin Heidelberg, 2010). doi:10.1007/978-3-642-04702-2.

15. Braslavsky, S. E. Glossary of terms used in photochemistry 3rd edition: (IUPAC Recommendations 2006). *Pure Appl. Chem.* **79**, 293–465 (2007).

16. Ueno, T. *et al.* Rational principles for modulating fluorescence properties of fluorescein. *J. Am. Chem. Soc.* **126**, 14079–14085 (2004).

17. Fox, M. A. Photoinduced Electron Transfer. *Photochem. Photobiol.* **52**, 617–627 (1990).

18. Doose, S., Neuweiler, H. & Sauer, M. Fluorescence quenching by photoinduced electron transfer: A reporter for conformational dynamics of macromolecules. *ChemPhysChem* **10**, 1389–1398 (2009).

19. Chen, Y., Tsao, K. & Keillor, J. W. Fluorogenic protein labelling: A review of photophysical quench mechanisms and principles of fluorogen design. *Can. J. Chem.* **93**, 389–398 (2015).

20. Meimetis, L. G., Carlson, J. C. T., Giedt, R. J., Kohler, R. H. & Weissleder, R. Ultrafluorogenic coumarin-tetrazine probes for real-time biological imaging. *Angew. Chemie - Int. Ed.* **53**, 7531–7534 (2014).

21. Nano, A. Towards optical memories: switchable optical systems for electron and energy transfer processes. (Université de Strasbourg, 2015).

22. *Volume 4. Probe Design and Chemical Sensing*. *Topics in Fluorescence Spectroscopy* (Kluwer Academic Publishers, 1994).

23. *Advanced Fluorescence Reporters in Chemistry and Biology I. Fundamentals and Molecular Design*. (Springer-Verlag Berlin Heidelberg, 2010). doi:10.1007/978-3-642-04702-2.

24. Liu, Z. *et al.* A charge transfer type pH responsive fluorescent probe and its intracellular application. *New J. Chem.* **34**, 656–660 (2010).

25. Wagnières, G. A., Star, W. M. & Wilson, B. C. In Vivo Fluorescence Spectroscopy and Imaging for

Oncological Applications. *Photochem. Photobiol.* **68**, 603–632 (1998).

26. Monici, M. Cell and tissue autofluorescence research and diagnostic applications. *Biotechnol. Annu. Rev.* **11**, 227–256 (2005).

27. Surre, J. *et al.* Strong increase in the autofluorescence of cells signals struggle for survival. *Sci. Rep.* **8**, 1–14 (2018).

28. Croce, A. C. & Bottiroli, G. Autofluorescence spectroscopy and imaging: A tool for biomedical research and diagnosis. *Eur. J. Histochem.* **58**, 320–337 (2014).

29. Stockert, J. C. & Blazquez-Castro, A. *Fluorescence Microscopy in Life Sciences*. (Bentham Science Publishers, 2017).

30. Hilderbrand, S. A. Labels and probes for live cell imaging: overview and selection guide. *Methods Mol. Biol.* **591**, 17–45 (2010).

31. Ji, Y. *et al.* Cell-Permeable Fluorogenic Probes for Identification and Imaging Nitroreductases in Live Bacterial Cells. *J. Org. Chem.* **84**, 1299–1309 (2019).

32. Dong, B. *et al.* Simultaneous Near-Infrared and Two-Photon In Vivo Imaging of H2O2 Using a Ratiometric Fluorescent Probe based on the Unique Oxidative Rearrangement of Oxonium. *Adv. Mater.* **28**, 8755–8759 (2016).

33. Chyan, W. & Raines, R. T. Enzyme-Activated Fluorogenic Probes for Live-Cell and in Vivo Imaging. *ACS Chem. Biol.* **13**, 1810–1823 (2018).

34. Kolanowski, J. L. & New, E. J. Fluorescent probes for the simultaneous detection of multiple analytes in biology. *Chem. Soc. Rev.* **47**, 195–208 (2017).

35. Zheng, J. *et al.* Near-infrared off-on fluorescence probe activated by NTR for in vivo hypoxia imaging. *Biosens. Bioelectron.* **119**, 141–148 (2018).

36. Hirayama, T., Tsuboi, H., Niwa, M., Miki, A. & Kadota, S. A universal fluorogenic switch for Fe (II) ion based on N-oxide chemistry permits the visualization of intracellular redox equilibrium shift towards labile iron in hypoxic tumor cells. *Chem. Sci.* 4858–4866 (2017) doi:10.1039/c6sc05457a.

37. Shen, C. *et al.* A ratiometric fluorescent sensor for the mitochondrial copper pool. *Metallomics* 915–919 (2016).

38. Hirayama, T., Okuda, K. & Nagasawa, H. A Highly Selective Turn-on Fluorescent Probe for Iron(II) to Visualize Labile Iron in Living Cells. *Chem. Sci.* **4**, 1250–1256 (2013).

39. Hirayama, T. Fluorescent probes for the detection of catalytic Fe(II) ion. *Free Radic. Biol. Med.* **133**, 38–45 (2019).

40. Zhu, H., Fan, J., Wang, B. & Peng, X. Fluorescent, MRI, and colorimetric sensors for the first-row d-block metal ions. *Chem. Soc. Rev.* **44**, 4337–4366 (2015).

41. Lavis, L. D. & Raines, R. T. Bright ideas for chemical biology. *ACS Chem. Biol.* **3**, 142–155 (2008).

42. Zeng, Z., Liew, S. S., Wei, X. & Pu, K. Hemicyanine-Based Near-Infrared Activatable Probes for Imaging and Diagnosis of Diseases. *Angew. Chemie* **133**, 26658–26679 (2021).

43. Li, H. *et al.* Activity-based NIR fluorescent probes based on the versatile hemicyanine scaffold: design strategy, biomedical applications, and outlook. *Chem. Soc. Rev.* **51**, 1795–1835 (2022).

44. Wang, W., Liu, Y., Niu, J. & Lin, W. Discriminating normal and inflammatory models by viscosity changes with a mitochondria-targetable fluorescent probe. *Analyst* **144**, 6247–6253 (2019).

45. Luo, P., Wang, M., Liu, W., Liu, L. & Xu, P. Activity-Based Fluorescent Probes Based on Hemicyanine for Biomedical Sensing. *Molecules* **27**, (2022).

46. Yin, C., Huo, F., Xu, M., Barnes, C. L. & Glass, T. E. A NIR, special recognition on HS−/CN− colorimetric and fluorescent imaging material for endogenous H2S based on nucleophilic addition. *Sensors Actuators, B Chem.* **252**, 592–599 (2017).

47. Perry, A. New mechanism, new chromophore: Investigating the electrophilic behaviour of styrylindolium dyes. *Org. Biomol. Chem.* **17**, 4825–4834 (2019).

48. Li, J., Chang, Z., Pan, X., Dong, W. & Jia, A. Q. A novel colorimetric and fluorescent probe based on indolium salt for detection of cyanide in 100% aqueous solution. *Dye. Pigment.* **168**, 175–179 (2019).

49. Lin, X., Hu, Y., Yang, D. & Chen, B. Cyanine-coumarin composite NIR dye based instantaneous -response probe for biothiols detection and oxidative stress assessment of mitochondria. *Dye. Pigment.* **174**, 107956 (2020).

50. Zhang, Y. *et al.* A ratiometric fluorescent probe for imaging enzyme dependent hydrogen sulfide

variation in the mitochondria and in living mice. *Analyst* **145**, 5123–5127 (2020).

51. Lin, X. *et al.* Imaging of intracellular bisulfate based on sensitive ratiometric fluorescent probes. *Spectrochim. Acta - Part A Mol. Biomol. Spectrosc.* **265**, 120335 (2022).

52. Park, J. H., Manivannan, R., Jayasudha, P. & Son, Y. A. Selective detection of cyanide ion in 100 % water by indolium based dual reactive binding site optical sensor. *J. Photochem. Photobiol. A Chem.* **397**, 112571 (2020).

53. Yu, Q. *et al.* Dual-emissive nanohybrid for ratiometric luminescence and lifetime imaging of intracellular hydrogen sulfide. *ACS Appl. Mater. Interfaces* **7**, 5462–5470 (2015).

54. Park, H. J. *et al.* A caveat to common hemicyanine dye components and their resolution. *Chem. Commun.* **56**, 7025–7028 (2020).

55. Matos, M. J. *et al.* Coumarins — An Important Class of Phytochemicals. in *Phytochemicals - Isolation, Characterisation and Role in Human Health* (ed. Rao, V.) 113–140 (IntechOpen, 2015). doi:10.5772/58648.

56. Xie, X. *et al.* Topology-Selective, Fluorescent "Light-Up" Probes for G-Quadruplex DNA Based on Photoinduced Electron Transfer. *Chem. - A Eur. J.* **24**, 12638–12651 (2018).

57. Wu, Z., Feng, Y., Geng, B., Liu, J. & Tang, X. Fluorogenic sensing of H2S in blood and living cells via reduction of aromatic dialkylamino N-oxide. *RSC Adv.* **4**, 30398–30401 (2014).

58. Cao, D. *et al.* Coumarin-Based Small-Molecule Fluorescent Chemosensors. *Chem. Rev.* **119**, 10403–10519 (2019).

59. Wychowaniec, A. *et al.* Multi-analyte responsive luminescent probes for the detection of biochemical targets in cell models. *Adv. Biochem.* (2024) doi:10.18388/pb.2021_538.

60. Kolanowski, J. L., Liu, F. & New, E. J. Fluorescent probes for the simultaneous detection of multiple analytes in biology. *Chem. Soc. Rev.* **47**, 195–208 (2018).

61. Guo, J. *et al.* Dual/Multi-responsive fluorogenic probes for multiple analytes in mitochondria: From design to applications. *TrAC - Trends Anal. Chem.* **155**, 1–23 (2022).

62. Yue, Y. *et al.* Functional synthetic probes for selective targeting and multi-analyte detection and imaging. *Chem. Soc. Rev.* **48**, 4155–4177 (2019).

63. Winterbourn, C. C. Biological production, detection, and fate of hydrogen peroxide. *Antioxidants Redox Signal.* **29**, 541–551 (2018).

64. Kehrer, J. P. The Haber-Weiss reaction and mechanisms of toxicity. *Toxicology* **149**, 43–50 (2000).

65. Chen, H. Y. Why the Reactive Oxygen Species of the Fenton Reaction Switches from Oxoiron(IV) Species to Hydroxyl Radical in Phosphate Buffer Solutions? A Computational Rationale. *ACS Omega* **4**, 14105–14113 (2019).

66. Fujiwara, O. *et al.* Peroxynitrite decomposition catalyst reduces vasopressin requirement in ovine MRSA sepsis. *Intensive Care Med. Exp.* **7**, (2019).

67. Wang, Z., Yeo, J. H. & New, E. J. Elucidating the Roles of Fenton Reactants in Drug-Treated Cells by Using a Selective Rhodamine-Thiophenol Fluorogenic Sensor. *Anal. Sens.* **1**, 90–94 (2021).

68. Andrés Juan, C., Manuel Pérez de la Lastra, J., Plou, F. J., Pérez-Lebeña, E. & Reinbothe, S. Molecular Sciences The Chemistry of Reactive Oxygen Species (ROS) Revisited: Outlining Their Role in Biological Macromolecules (DNA, Lipids and Proteins) and Induced Pathologies. *Int. J. Mol. Sci* **22**, 4642 (2021).

69. Mailloux, R. J. An update on methods and approaches for interrogating mitochondrial reactive oxygen species production. *Redox Biol.* **45**, (2021).

70. Collin, F. Chemical basis of reactive oxygen species reactivity and involvement in neurodegenerative diseases. *Int. J. Mol. Sci.* **20**, (2019).

71. Sies, H. & Jones, D. P. Reactive oxygen species (ROS) as pleiotropic physiological signalling agents. *Nat. Rev. Mol. Cell Biol.* **21**, 363–383 (2020).

72. Heid, M. E. *et al.* Mitochondrial Reactive Oxygen Species Induces NLRP3-Dependent Lysosomal Damage and Inflammasome Activation. *J. Immunol.* **191**, 5230–5238 (2013).

73. Ito, F., Sono, Y. & Ito, T. Measurement and clinical significance of lipid peroxidation as a biomarker of oxidative stress: Oxidative stress in diabetes, atherosclerosis, and chronic inflammation. *Antioxidants* **8**, (2019).

74. Yan, L. L. & Zaher, H. S. How do cells cope with RNA damage and its consequences? *J. Biol. Chem.* **294**, 15158–15171 (2019).

75. Hawkins, C. L. & Davies, M. J. Detection, identification, and quantification of oxidative protein modifications. *J. Biol. Chem.* **294**, 19683–19708 (2019).

76. Guzy, R. D. *et al.* Mitochondrial complex III is required for hypoxia-induced ROS production and cellular oxygen sensing. *Cell Metab.* **1**, 401–408 (2005).

77. López-Lázaro, M. Dual role of hydrogen peroxide in cancer: Possible relevance to cancer chemoprevention and therapy. *Cancer Lett.* **252**, 1–8 (2007).

78. Vaupel, P., Kallinowski, F. & Okunieff, P. Blood Flow, Oxygen and Nutrient Supply, and Metabolic Microenvironment of Human Tumors: A Review. *Cancer Res.* **49**, 6449–6465 (1989).

79. Brown, J. M. & Wilson, W. R. Exploiting tumour hypoxia in cancer treatment. *Nat. Rev. Cancer* **4**, 437–447 (2004).

80. Dewhirst, M. W., Cao, Y. & Moeller, B. Cycling hypoxia and free radicals regulate angiogenesis and radiotherapy response. *Nat. Rev. Cancer* **8**, 425–437 (2008).

81. Vaupel, P. & Höckel, M. Tumor hypoxia and therapeutic resistance. in *Recombinant Human Erythropoietin (rhEPO) in Clinical Oncology: Scientific and Clinical Aspects of Anemia in Cancer* (ed. Nowrousian, M. R.) 127–146 (Springer Vienna, 2002).

82. Lendahl, U., Lee, K. L., Yang, H. & Poellinger, L. Generating specificity and diversity in the transcriptional response to hypoxia. *Nat. Rev. Genet.* **10**, 821–832 (2009).

83. Rohwer, N. & Cramer, T. Hypoxia-mediated drug resistance: Novel insights on the functional interaction of HIFs and cell death pathways. *Drug Resist. Updat.* **14**, 191–201 (2011).

84. Chang, Q., Jurisica, I., Do, T. & Hedley, D. W. Hypoxia predicts aggressive growth and spontaneous metastasis formation from orthotopically grown primary xenografts of human pancreatic cancer. *Cancer Res.* **71**, 3110–3120 (2011).

85. Wilson, W. R. & Hay, M. P. Targeting hypoxia in cancer therapy. *Nat. Rev. Cancer* **11**, 393–410 (2011).

86. Sharma, A. *et al.* Hypoxia-targeted drug delivery. *Chem. Soc. Rev.* **48**, 771–813 (2019).

87. Zhang, J. *et al.* Efficient Two-Photon Fluorescent Probe for Nitroreductase Detection and Hypoxia Imaging in Tumor Cells and Tissues. *Anal. Chem.* **87**, 11832–11839 (2015).

88. Miller, A. F., Park, J. T., Ferguson, K. L., Pitsawong, W. & Bommarius, A. S. Informing efforts to develop nitroreductase for amine production. *Molecules* **23**, (2018).

89. Roldán, M. D., Pérez-Reinado, E., Castillo, F. & Moreno-Vivián, C. Reduction of polynitroaromatic compounds: The bacterial nitroreductases. *FEMS Microbiol. Rev.* **32**, 474–500 (2008).

90. Christofferson, A. & Wilkie, J. Mechanism of CB1954 reduction by Escherichia coli nitroreductase. *Biochem. Soc. Trans.* **37**, 413–418 (2009).

91. Mason, R. P. & Holtzman, J. L. The role of catalytic superoxide formation in the O2 inhibition of nitroreductase. *Biochem. Biophys. Res. Commun.* **67**, 1267–1274 (1975).

92. Whitmore, G. F. & Varghese, A. J. The biological properties of reduced nitroheterocyclics and possible underlying biochemical mechanisms. *Biochem. Pharmacol.* **35**, 97–103 (1986).

93. Streeter, A. J. & Hoener, B. ann. Evidence for the Involvement of a Nitrenium Ion in the Covalent Binding of Nitrofurazone to DNA. *Pharmaceutical Research: An Official Journal of the American Association of Pharmaceutical Scientists* vol. 5 434–436 (1988).

94. Handley, M. G., Medina, R. A., Nagel, E., Blower, P. J. & Southworth, R. PET imaging of cardiac hypoxia: Opportunities and challenges. *J. Mol. Cell. Cardiol.* **51**, 640–650 (2011).

95. Liu, J. N., Bu, W. & Shi, J. Chemical Design and Synthesis of Functionalized Probes for Imaging and Treating Tumor Hypoxia. *Chem. Rev.* **117**, 6160–6224 (2017).

96. Takahashi, S. *et al.* Reversible off-on fluorescence probe for hypoxia and imaging of hypoxia-normoxia cycles in live cells. *J. Am. Chem. Soc.* **134**, 19588–19591 (2012).

97. Fang, Y., Shi, W., Hu, Y., Li, X. & Ma, H. A dual-function fluorescent probe for monitoring the degrees of hypoxia in living cells: Via the imaging of nitroreductase and adenosine triphosphate. *Chem. Commun.* **54**, 5454–5457 (2018).

98. Gatenby, R. A. & Gillies, R. J. Why do cancers have high aerobic glycolysis? *Nat. Rev. Cancer* **4**, 891–899 (2004).

99. Chiche, J., Brahimi-Horn, M. C. & Pouysségur, J. Tumour hypoxia induces a metabolic shift causing acidosis: A common feature in cancer. *J. Cell. Mol. Med.* **14**, 771–794 (2010).

100. Kato, Y. *et al.* Acidic extracellular microenvironment and cancer. *Cancer Cell Int.* **13**, (2013).

101. Zeng, Y. *et al.* Estimation of pKa values for carboxylic acids, alcohols, phenols and amines using changes in the relative Gibbs free energy. *Fluid Phase Equilib.* **313**, 148–155 (2012).

102. K. C. Gross, R. G. S. Structure and pKa of Benzoic Acid. *Int. J. Quantum chem.* **85**, 569–579 (2001).

103. Lavis, L. D. Teaching Old Dyes New Tricks: Biological Probes Built from Fluoresceins and Rhodamines. *Annu. Rev. Biochem.* **86**, 825–843 (2017).

104. Chernyshev, A. V., Chernov'yants, M. S., Voloshina, E. N. & Voloshin, N. A. To estimation of pKa for spiropyrans of the indoline series. *Russ. J. Gen. Chem.* **72**, 1468–1472 (2002).

105. Beija, M., Afonso, C. A. M. & Martinho, J. M. G. Synthesis and applications of Rhodamine derivatives as fluorescent probes. *Chem. Soc. Rev.* **38**, 2410–2433 (2009).

106. Zheng, H., Shang, G. Q., Yang, S. Y., Gao, X. & Xu, J. G. Fluorogenic and chromogenic rhodamine spirolactam based probe for nitric oxide by spiro ring opening reaction. *Org. Lett.* **10**, 2357–2360 (2008).

107. Tian, M., Peng, X., Fan, J., Wang, J. & Sun, S. A fluorescent sensor for pH based on rhodamine fluorophore. *Dye. Pigment.* **95**, 112–115 (2012).

108. Iwatate, R. J. *et al.* Silicon Rhodamine-Based Near-Infrared Fluorescent Probe for γ-Glutamyltransferase. *Bioconjug. Chem.* **29**, 241–244 (2018).

109. Kolmakov, K. *et al.* Red-emitting rhodamine dyes for fluorescence microscopy and nanoscopy. *Chem. - A Eur. J.* **16**, 158–166 (2010).

110. Wang, L. *et al.* Hybrid Rhodamine Fluorophores in the Visible/NIR Region for Biological Imaging. *Angew. Chemie - Int. Ed.* **58**, 14026–14043 (2019).

111. Tian, X., Li, Z., Sun, Y., Wang, P. & Ma, H. Near-Infrared Fluorescent Probes for Hypoxia Detection via Joint Regulated Enzymes: Design, Synthesis, and Application in Living Cells and Mice. *Anal. Chem.* **90**, 13759–13766 (2018).

112. Zhai, B. *et al.* A two-photon fluorescent probe for nitroreductase imaging in living cells, tissues and zebrafish under hypoxia conditions. *Analyst* **142**, 1545–1553 (2017).

113. Tian, X. *et al.* Coumarin-based fluorescent probe for the detection of glutathione and nitroreductase. *Tetrahedron* **82**, 131890 (2021).

114. Perry, A. New mechanism, new chromophore: Investigating the electrophilic behaviour of styrylindolium dyes. *Org. Biomol. Chem.* **17**, 4825–4834 (2019).

115. Shiraishi, Y., Itoh, M. & Hirai, T. Colorimetric response of spiropyran derivative for anions in aqueous or organic media. *Tetrahedron* **67**, 891–897 (2011).

116. Hansch, C., Leo, A. & Taft, R. W. A Survey of Hammett Substituent Constants and Resonance and Field Parameters. *Chem. Rev.* **91**, 165–195 (1991).

117. Tian, W. & Tian, J. An insight into the solvent effect on photo-, solvato-chromism of spiropyran through the perspective of intermolecular interactions. *Dye. Pigment.* **105**, 66–74 (2014).

118. Feng, W. *et al.* A novel anticancer theranostic pro-prodrug based on hypoxia and photo sequential control. *Chem. Commun.* **52**, 9434–9437 (2016).

119. Wang, L. *et al.* Unraveling the Hydrolysis of Merocyanine-Based Probes in Biological Assay. *Anal. Chem.* **88**, 9136–9142 (2016).

120. Sangsuwan, W. *et al.* Design, Synthesis, and Characterization of Novel Styryl Dyes as Fluorescent Probes for Tau Aggregate Detection in Vitro and in Cells. *Chem. - An Asian J.* **19**, 1–8 (2024).

121. Petinova, A., Metsov, S., Petkov, I. & Stoyanov, S. Photophysical behaviours of some 2-styrylindolium dyes in aqueous solutions and in the presence of cyclodextrins. *J. Incl. Phenom. Macrocycl. Chem.* **59**, 183–190 (2007).

122. Zhang, Y. *et al.* A hemicyanine fluorescent probe with intramolecular charge transfer (ICT) mechanism for highly sensitive and selective detection of acidic pH and its application in living cells. *Anal. Chim. Acta* **1098**, 155–163 (2020).

123. Rhys Williams, A. T., Winfield, S. A. & Miller, J. N. Relative fluorescence quantum yields using a Computer-controlled luminescence spectrometer. *Analyst* **108**, 1067–1071 (1983).

124. Magde, D., Wong, R. & Seybold, P. G. Fluorescence Quantum Yields and Their Relation to Lifetimes of Rhodamine 6G and Fluorescein in Nine Solvents: Improved Absolute Standards for Quantum Yields¶. *Photochem. Photobiol.* **75**, 327 (2002).

125. Brooke, D., Movahed, N. & Bothner, B. Universal buffers for use in biochemistry and biophysical experiments. *AIMS Biophys.* **2**, 336–342 (2015).

126. Pielak, G. J. Buffers, Especially the Good Kind. *Biochemistry* **60**, 3436–3440 (2021).

127. Taha, M. & Coutinho, J. A. P. Organic-phase biological buffers for biochemical and biological research in organic media. *J. Mol. Liq.* **221**, 197–205 (2016).

128. Salis, A. & Monduzzi, M. Not only pH. Specific buffer effects in biological systems. *Curr. Opin. Colloid Interface Sci.* **23**, 1–9 (2016).

129. Stoll, V. S. & Blanchard, J. S. Buffers: Principles and Practice. *Methods Enzymol.* **182**, 24–38 (1990).

130. Stoughton, R. W. & Rollefson, G. K. The Influence of Ionic Strength on the Quenching of Fluorescence in Aqueous Solutions. *J. Am. Chem. Soc.* **61**, 2634–2638 (1939).

131. Liu, T. *et al.* Quantitatively mapping cellular viscosity with detailed organelle information via a designed PET fluorescent probe. *Sci. Rep.* **4**, 1–7 (2014).

132. Wang, K. *et al.* Characterization of cytoplasmic viscosity of hundreds of single tumour cells based on micropipette aspiration. *R. Soc. Open Sci.* **6**, (2019).

133. Segur, J. B. & Oderstar, H. E. Viscosity of Glycerol and Its Aqueous Solutions. *Ind. Eng. Chem.* **43**, 2117–2120 (1951).

134. Li, H. *et al.* Ferroptosis Accompanied by •OH Generation and Cytoplasmic Viscosity Increase Revealed via Dual-Functional Fluorescence Probe. *J. Am. Chem. Soc.* **141**, 18301–18307 (2019).

135. Spange, S. Polarity of organic solvent/water mixtures measured with Reichardt's B30 and related solvatochromic probes—A critical review. *Liquids* **4**, 191–230 (2024).

136. Spange, S., Weiß, N., Schmidt, C. H. & Schreiter, K. Reappraisal of empirical Solvent polarity scales for organic solvents. *Chemistry-Methods* **1**, 42–60 (2021).

137. Yao, T. & Asayama, Y. Animal-cell culture media: History, characteristics, and current issues. *Reprod. Med. Biol.* **16**, 99–117 (2017).

138. Spencer, V. A., Kumar, S., Paszkiet, B., Fein, J. & Zmuda, J. F. Cell culture media for fluorescence imaging. *Genet. Eng. Biotechnol. News* **34**, 0–4 (2014).

139. Tantipanjaporn, A. & Wong, M. K. Development and Recent Advances in Lysine and N-Terminal Bioconjugation for Peptides and Proteins. *Molecules* **28**, (2023).

140. Al Temimi, A. H. K. *et al.* The nucleophilic amino group of lysine is central for histone lysine methyltransferase catalysis. *Commun. Chem.* **2**, 1–14 (2019).

141. Dos Santos, A. P. A. *et al.* Nucleophilicity of cysteine and related biothiols and the development of fluorogenic probes and other applications. *Org. Biomol. Chem.* **18**, 9398–9427 (2020).

142. Bak, D. W. *et al.* Cysteine Reactivity Across the Sub-Cellular Universe¡. *Curr Opin Chem Biol.* 96–105 (2019) doi:10.1016/j.cbpa.2018.11.002.Cysteine.

143. Shipman, C. Evaluation of 4-(2-hydroxyphenyl)-1-piperazineethanesulfonic acid (HEPES) as a Tissue CUlture Buffer. *Proc Soc Exp Biol Med* .. **130**, 305–310 (1969).

144. Graham, F. L. & van der Eb, A. J. A new technique for the assay of infectivity of human adenovirus 5 DNA. *Virology* **52**, 456–467 (1973).

145. Stepanenko, A. A. & Dmitrenko, V. V. HEK293 in cell biology and cancer research: Phenotype, karyotype, tumorigenicity, and stress-induced genome-phenotype evolution. *Gene* **569**, 182–190 (2015).

146. Stone, K. R., Mickey, D. D., Wunderli, H., Mickey, G. H. & Paulson, D. F. Isolation of a human prostate carcinoma cell line (DU 145). *Int. J. Cancer* **21**, 274–281 (1978).

147. Yang, X. *et al.* A novel ICT-based two photon and NIR fluorescent probe for labile Fe2+ detection and cell imaging in living cells. *Sensors Actuators, B Chem.* **288**, 217–224 (2019).

148. Cai, Q., Yu, T., Zhu, W., Xu, Y. & Qian, X. A turn-on fluorescent probe for tumor hypoxia imaging in living cells. *Chem. Commun.* **51**, 14739–14741 (2015).

149. Galluzzi, L. *et al.* Essential versus accessory aspects of cell death: Recommendations of the NCCD 2015. *Cell Death Differ.* **22**, 58–73 (2015).

150. Yong, L. *et al.* CN117603206A Mitochondrial fluorescent probe as well as preparation method and application thereof. (2024).

151. Steinegger, A., Wolfbeis, O. S. & Borisov, S. M. Optical Sensing and Imaging of pH Values: Spectroscopies, Materials, and Applications. *Chem. Rev.* **120**, 12357–12489 (2020).

152. Chen, L. *et al.* Highly photostable wide-dynamic-range pH sensitive semiconducting polymer dots enabled by dendronizing the near-IR emitters. *Chem. Sci.* **8**, 7236–7245 (2017).

153. Zeng, J., Shirihai, O. S. & Grinstaff, M. W. Modulating lysosomal pH: a molecular and nanoscale materials design perspective. *J. Life Sci.* **2**, (2020).

154. McKinnon, K. M. Flow cytometry: an overview. *Curr. Protoc. Immunol.* **120**, 5.1.1–5.1.11 (2019).

155. Putzke, A. P. *et al.* Metastatic progression of prostate cancer and E-cadherin: Regulation by ZEB1 and Src family kinases. *Am. J. Pathol.* **179**, 400–410 (2011).

156. Heerlein, K., Schulze, A., Hotz, L., Bärtsch, P. & Mairbäurl, H. Hypoxia decreases cellular ATP demand and inhibits mitochondrial respiration of A549 cells. *Am. J. Respir. Cell Mol. Biol.* **32**, 44–51 (2005).

157. Luo, F. M. *et al.* Hypoxia-inducible transcription factor-1α promotes hypoxia-induced A549 apoptosis via a mechanism that involves the glycolysis pathway. *BMC Cancer* **6**, 1–10 (2006).

158. Li, M. *et al.* Hypoxia inducible factor-1α-dependent epithelial to mesenchymal transition under hypoxic conditions in prostate cancer cells. *Oncol. Rep.* **36**, 521–527 (2016).

159. Higgins, L. H. *et al.* Hypoxia and the metabolic phenotype of prostate cancer cells. *Biochim. Biophys. Acta - Bioenerg.* **1787**, 1433–1443 (2009).

160. Riffle, S. & Hegde, R. S. Modeling tumor cell adaptations to hypoxia in multicellular tumor spheroids. *J. Exp. Clin. Cancer Res.* **36**, 1–10 (2017).

161. Khaitan, D., Chandna, S., Arya, M. B. & Dwarakanath, B. S. Establishment and characterization of multicellular spheroids from a human glioma cell line; implications for tumor therapy. *J. Transl. Med.* **4**, 1–13 (2006).

162. Ghisla, S. Fluorescence and Optical Characteristics of Reduced Flavins and Flavoproteins. *Methods Enzymol.* **66**, 360–373 (1980).

163. Raczyńska, E. D., Kosińska, W., Ośmiałowski, B. & Gawinecki, R. Tautomeric equilibria in relation to Pi-electron delocalization. *Chem. Rev.* **105**, 3561–3612 (2005).

164. Allegretti, P. E., Castro, E. A. & Furlong, J. J. P. Tautomeric equilibrium of amides and related compounds: Theoretical and spectral evidences. *J. Mol. Struct. THEOCHEM* **499**, 121–126 (2000).

165. Mujika, J. I., Matxain, J. M., Eriksson, L. A. & Lopez, X. Resonance structures of the amide bond: The advantages of planarity. *Chem. - A Eur. J.* **12**, 7215–7224 (2006).

166. Montalbetti, C. A. G. N. & Falque, V. Amide bond formation and peptide coupling. *Tetrahedron* **61**, 10827–10852 (2005).

167. Liu, S., Wang, W., Dang, Y., Fu, Y. & Sang, R. Rational design and efficient synthesis of a fluorescent-labeled jasmonate. *Tetrahedron Lett.* **53**, 4235–4239 (2012).

168. Dai, X., Cheng, H., Bai, Z. & Li, J. Breast cancer cell line classification and Its relevance with breast tumor subtyping. *J. Cancer* **8**, 3131–3141 (2017).

169. Alizadeh, E. *et al.* Cellular morphological features are predictive markers of cancer cell state. *Comput. Biol. Med.* **126**, 104044 (2020).

170. Slavik, J. *Fluorescence Microscopy and Fluorescent Probes*. (1995).

171. Jonkman, J., Brown, C. M., Wright, G. D., Anderson, K. I. & North, A. J. Tutorial: guidance for quantitative confocal microscopy. *Nat. Protoc.* **15**, 1585–1611 (2020).

172. Mukhopadhyay, P. *et al.* Simultaneous detection of apoptosis and mitochondrial superoxide production in live cells by flow cytometry and confocal microscopy. *Nat. Protoc.* **2**, 2295–2301 (2007).

173. Sharrow, S. O. Overview of Flow Cytometry. *Curr. Protoc. Immunol.* **50**, 5.1.1-5.1.8 (1991).

174. Collot, M. *et al.* Bright fluorogenic squaraines with tuned cell entry for selective imaging of plasma membrane vs. endoplasmic reticulum. *Chem. Commun.* **51**, 17136–17139 (2015).

175. Yuan, J. *et al.* A highly selective turn-on fluorescent probe based on semi-cyanine for the detection of nitroreductase and hypoxic tumor cell imaging. *RSC Adv.* 56207–56210 (2014) doi:10.1039/c4ra10044a.

176. Song, G. *et al.* Photoactivated In Situ Generation of Near Infrared Cyanines for Spatiotemporally Controlled Fluorescence Imaging in Living Cells. *Angew. Chemie - Int. Ed.* **60**, 16889–16893 (2021).

177. Shelton, D. P. Refractive index measured by laser beam displacement at λ = 1064nm for solvents and deuterated solvents. *Appl. Opt.* **50**, 4091–4098 (2011).

178. Po, H. N. & Senozan, N. M. The Henderson-Hasselbalch equation: Its history and limitations. *J. Chem. Educ.* **78**, 1499–1503 (2001).

179. Schindelin, J. *et al.* Fiji - an Open platform for biological image analysis. *Nat. Methods* **9**, (2009).

180. Fillbrunn, A. *et al.* KNIME for reproducible cross-domain analysis of life science data. *J. Biotechnol.* **261**, 149–156 (2017).